AFIT/GE/ENG/95J-02

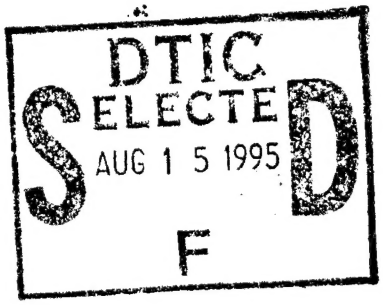

DESIGN AND DEVELOPMENT OF MICROSWITCHES FOR MICRO-ELECTRO-MECHANICAL RELAY MATRICES

THESIS

Mark W. Phipps, BS PHYS
2nd Lieutenant, USAF

AFIT/GE/ENG/95J-02

19950811 047

Approved for public release; distribution unlimited.

AFIT/GE/ENG/95J-02

DESIGN AND DEVELOPMENT OF MICROSWITCHES FOR MICRO-ELECTRO-MECHANICAL RELAY MATRICES

THESIS

Presented to the Faculty of the Graduate School of Engineering

of the Air Force Institute of Technology

Air University

In Partial Fulfillment of the

Requirements for the Degree of

Master of Science in Electrical Engineering

Accesion For	
NTIS CRA&I	☒
DTIC TAB	☐
Unannounced	☐
Justification	
By	
Distribution /	
Availability Codes	
Dist	Avail and / or Special
A-1	

Mark W. Phipps, BS PHYS

2nd Lieutenant, USAF

June 1995

Approved for public release; distribution unlimited.

Acknowledgments

I would like to the thank the many people who helped me get through this thesis project. First, I'd like to thank my advisor, Dr. Victor Bright, who helped me make it this far. I'd also like to thank Mr. Chris O'Brien and Mr. Bill Trop for all their help down in the microelectronics lab. A special thanks goes out to Capt. John Comtois for all the time and effort he has put in for getting all the MUMPs and LIGA fabrication runs together. Lastly, I would like to thank my wife for all the understanding she has given during the times of great stress.

Table of Contents

Page

Acknowledgments ii

List of Figures vii

List of Tables xi

Abstract xiii

1. Introduction 1-1

    1.1. Background 1-1

    1.2. Problem Statement 1-4

    1.3. Scope 1-4

    1.4. Assumptions 1-5

    1.5. Approach 1-6

        1.5.1. Cantilever and Microbridge 1-10

        1.5.2. Comb-Drive Actuator 1-10

        1.5.3. Heat-Drive Actuator 1-11

        1.5.4. Hinge Switch Design 1-11

    1.6. Switch and Relay Characterization Effort 1-12

    1.7. Plan of Development 1-12

2. Literature Review of Micro-Electro-Mechanical Technology Applicable to Microswitch Development 2-1

    2.1. Fabrication Techniques 2-1

        2.1.1. Bulk Micromachining of Crystalline Silicon 2-1

2.1.2. Surface Micromachining 2-8

2.1.3. Deep X-ray Lithography, Electroforming, Molding 2-13

2.2. Micro-Electro-Mechanical Actuation 2-20

2.2.1. Thermal Actuation 2-20

2.2.1.1. Bimetallic Actuators 2-21

2.2.1.2. Thermally Activated Beam Flexure 2-21

2.2.2. Electrostatic Actuation 2-23

2.2.2.1. Electrostatic Cantilever Actuators 2-25

2.2.2.2. Electrostatic Microbridge Actuators 2-27

2.2.2.3. Electrostatic Comb-Drive Actuators 2-32

2.2.3. Magnetic and Piezoelectric Actuation 2-37

2.3. Summary 2-38

3. Theoretical Review of Micro-Electro-Mechanical Actuation 3-1

3.1. Theory of Electrostatic Actuation 3-1

3.2. Modeling of Electrostatic Cantilevers and Microbridges 3-5

3.3. Modeling of Electrostatic Comb-Drive Actuators 3-14

3.4. Modeling of the Thermally Activated Beam Flexure (Heat-Drive Actuator) 3-28

3.5. Summary 3-34

4. Experimental Procedure, Fabrication, and Design Descriptions 4-1

4.1. Design Submission Process 4-1

4.2. MUMPs Process 4-2

4.2.1. General Design Considerations 4-2

4.2.2. MUMPs Post Processing Procedures 4-5

4.2.3. Device Descriptions 4-7

4.3. LIGA Process 4-41

4.3.1. General Design Considerations 4-41

4.3.2. LIGA Post Processing Procedures 4-42

4.3.3. Device Descriptions 4-43

4.4. Test and Characterization Equipment 4-49

4.5. Switch Testing Procedures 4-51

4.6. Summary 4-57

5. Results and Discussion 5-1

5.1. General Process Results 5-1

5.2. Electrostatic Device Results 5-3

5.2.1. Microbridge Switch 5-4

5.2.2. Cantilever Beam Switch 5-10

5.2.3. Simple Comb-Drive Switch 5-15

5.2.4. Push Lock Switch 5-18

5.2.5. Clamp-Lock and Cantilever Lock Switches 5-19

5.2.6. Plate Switch 5-25

5.3. Heat-Actuated Devices 5-30

5.3.1. MUMPs 5 Version of the Push Lock Switch 5-31

5.3.2 Heat Spring Switch 5-31

5.3.3. MUMPs 6 Heat-Drive Actuator Test Array 5-32

5.3.4. MUMPs Heat Lock Switches 5-55

5.3.5. Hinge Switches and the Vertical Heat-Drive Actuator 5-61

5.3.6. Rotating Lever Switch 5-65

5.4. Summary 5-65

6. Conclusions and Recommendations 6-1

6.1 Conclusions 6-1

6.2 MEM Fabrication Processing 6-3

6.3 Recommendations 6-4

Appendix A: Layout Plots not Shown in Chapter 4 ..... A-1

Appendix B. Heat-Drive Actuator Test Array Graphs B-1

Bibliography BIB-1

Vita VITA-1

List of Figures

Figure Page

1.1 Basic MEM actuators and structures 1-9

2.1 Anisotropic etching of a masked silicon substrate 2-3

2.2 Cantilever fabrication 2-4

2.3 Layers used in the CMOS process available through MOSIS 2-5

2.4 Fabrication of a SiO_2 cantilever by bulk micromachining 2-7

2.5 Basic concept behind surface micromachining 2-9

2.6 Basic layers used in the MUMPs process 2-14

2.7 Micromotor fabricated in the MUMPs process 2-15

2.8 The LIGA process 2-17

2.9 The sacrificial LIGA process 2-19

2.10 Bimetallic actuator 2-22

2.11 Horizontal heat-drive actuator 2-24

2.12 Basic electrostatic cantilever 2-26

2.13 Resonant microbridge/switch 2-29

2.14 Resonating microswitch/voltage-frequency converter 2-31

2.15 Lateral comb-drive resonator 2-33

3.1 Three conductor system in equilibrium 3-2

3.2 Three conductor system with one electrode displaced 3-4

3.3 Geometry for modeling the behavior of the microbridge and cantilever 3-6

3.4 Geometry of the rectangular interdigital finger arrangement 3-15

3.5 Geometry of a trapezoidal-shaped finger and comb 3-18

3-6 Top-view schematic of the trapezoidal finger arrangement 3-18

3.7 Folded beam suspension truss 3-22

3.8 3-D and cross-sectional view of the horizontal heat-drive actuator 3-29

3.9 Conductor heated with an applied current 3-31

4.1 Depiction of the conformal effect of one polysilicon layer to another 4-4

4.2 MAGIC layout of four microbridge switches 4-9

4.3 SEM micrograph of the fabricated devices shown in Figure 4.2 4-9

4.4 MAGIC layout of two 165 μm long cantilever beam switches 4-11

4.5 SEM micrograph of two 165 μm long cantilever beam switches 4-12

4.6 MAGIC layout of the simple comb-drive switch 4-13

4.7 SEM micrograph of a fabricated simple comb-drive switch 4-14

4.8 MAGIC layout of the push lock switch 4-16

4.9 SEM micrograph of the fabricated comb-drive push switch 4-17

4.10 MAGIC layout of the heat spring switch 4-19

4.11 SEM micrograph of the fabricated heat spring switch 4-19

4.12 MAGIC layout of the clamp-lock switch 4-21

4.13 SEM micrograph of the fabricated clamp-lock switch 4-22

4.14 MAGIC layout of the electrostatic cantilever-lock switch 4-24

4.15 SEM micrograph of fabricated electrostatic cantilever-lock switch 4-25

4.16 CADENCE layout of the hinge switch 4-27

4.17 SEM micrograph of the fabricated hinge switch 4-27

4.18 CADENCE layout of the vertical heat-drive actuator 4-29

4.19 SEM micrograph of the fabricated vertical heat-drive actuator 4-29

4.20 CADENCE layout of the heat lock switch 4-32

4.21 SEM micrograph of fabricated heat lock switches 4-32

4.22 CADENCE layout of the rotating lever switch 4-34

4.23 SEM micrograph of the fabricated rotating lever switch 4-34

4.24 CADENCE layout of the plate switch 4-36

4.25 SEM micrograph of the plate switch 4-36

4.26 CADENCE layout of the back bending switch 4-37

4.27 CADENCE layout of the heat-rotate switch 4-39

4.28 CADENCE layout of the simple heat switch 4-40

4.29 CADENCE layout of the locking comb switch 4-45

4.30 CADENCE layout of the heat clamp switch 4-47

4.31 CADENCE layout of the heat lock switch 4-48

4.32 Schematic of the testing process for the "simple" switches 4-54

5.1 Comb-drive actuator characteristics for POLY1 actuators 5-23

5.2 Comb-drive actuator characteristics for POLY2 actuators 5-24

5.3 SEM micrograph of a plate switch after shorting out 5-27

5.4 Heat spring switch hanging problem 5-33

5.5 Heat-drive actuator dimensions 5-33

5.6 Deflection vs. current characteristics for a device in array # 2 5-37

5.7 ΔT vs. I data for a device in array # 10 5-40

5.8 ΔT vs. I data for a device in array # 10 with predicted curve 5-43

5.9 Deflection vs. increasing thick-section width for POLY1 heat-drive actuators for three different lengths of actuators..... 5-45

5.10 Deflection vs. increasing thick-section width for POLY2 heat-drive actuators for three different lengths of actuators..... 5-46

5.11 Deflection vs. increasing thick-section width for four different drive-section widths..... 5-47

5.12 Deflection vs. flexure length 5-48

5.13 Backbending deflection vs. increasing thick-section width for POLY1 heat-drive actuators for three different lengths of actuators. 5-49

5.14 Backbending deflection vs. increasing thick-section width for POLY2 heat-drive actuators for three different lengths of actuators. 5-50

5.15 Backbending deflection vs. increasing thick section width for different drive-section widths 5-51

5.16 Backbending deflection vs. flexure length 5-52

5.17 SEM of a rectangular electrode simple heat switch 5-57

5.18 SEM of a trapezoidal electrode simple heat switch 5-58

5.19 MUMPs 6 die after blasting with high velocity air for 2 minutes..... 5-62

List of Tables

Table		Page
2.1	Surface Micromachining Thin Film Layers	2-10
4.1	Etch Procedures for Die with Aluminum as the Metal Layer	4-6
4.2	Etch Procedures for Die with Copper or Gold as the Metal Layer	4-6
4.3	Microbridge Switch Dimensions	4-8
4.4	Cantilever Beam Switch Dimensions	4-11
4.5	Push Lock Switch Dimensions	4-15
4.6	Heat-Spring Switch Dimensions	4-18
4.7	Electrostatic Cantilever-Lock Switch Dimensions	4-24
4.8	Hinge Switch Dimensions	4-26
4.9	Heat Lock Switch Dimensions	4-31
4.10	Plate Switch Dimensions	4-35
4.11	Heat-Rotate Switch Dimensions	4-38
4.12	Locking Comb Switch Dimensions	4-44
4.13	Heat Clamp Switch Dimensions	4-46
4.14	Heat Lock Switch Dimensions	4-48
4.15	List of Switch Categories for Determining Proper Test Procedures	4-53
4.16	Testing Procedures for Switches in the "Simple" Switch Category	4-53
4.17	Testing Procedure for Switches in the "Locking" Category	4-56
5.1	Process Statistics for MUMPs 4, MUMPs 5, and MUMPs 6	5-2
5.2	Microbridge Switch Summary Data	5-7

5.3 Cantilever Beam Switch Summary Data 5-13

5.4 Plate Switch Summary Data 5-28

5.5 Variations of Arrays Used in the Heat-Drive Actuator Array 5-35

5.6 Fitting Constants and R^2 Values for Each Array 5-38

5.7 Figgting Constant "a" as Actually Fit and as Predicted 5-42

5.8 Simple Heat Switch Summary 5-60

5.9 Hinge Switches with Vertical Heat-Drive Actuator Summary Data 5-64

5.10 Hinge Switches with Added Force Summary Data 5-64

Abstract

Many different micro-electro-mechanical switches were designed in the Multi-User MEMS Processes (MUMPs) and deep x-ray lithography and electroforming (LIGA) processes. The switches were composed of actuators that operated based upon either electrostatic forces or thermal forces. Switches were designed to be either actuated and held in place by continuous input power, or they were designed to actuate into a locked position that required no input power to maintain the connection. A thermally activated beam flexure actuator that operated based upon differential heating was used extensively. This actuator, which was fabricated in the MUMPs process, was able to deflect up to 12 μm with a total input power of less than 25 mW. Equations were developed that allowed the deflection of the actuator to be predicted from the applied current with known dimensions and known thermal resistance between the actuator and the atmosphere. The thermal resistance was extracted from a material constant, 1.9 +/- 0.08 $m^{1.5}$-°C-W^{-1} for the POLY1 layer in MUMPs and 7.4 +/- 0.88 $m^{1.5}$-°C-W^{-1} for the POLY2 layer in MUMPs, which was determined from 1020 actuator test cases. A switch using a hinge mechanism that allowed metal-to-metal contacts to be formed was also developed in the MUMPs process. The contact resistance of these devices was determined to be 9.91 +/- 6.22 kΩ. An electrostatically deformable microbridge structure (2 μm thick, 40 μm wide, 332 μm long, and with a capacitive gap of 2 μm) was also employed as a switch. A voltage of 53.3 volts applied between the microbridge and two drive electrodes was able to force the center of the microbridge to touch a sense electrode. The observed contact resistance for this connection was 300 +/- 89.7 Ω. Many other switches based upon the thermally activated beam flexure and electrostatic forces were developed. Contact resistances of these switches varied from hundreds of ohms to the kilo-ohm range.

DESIGN AND DEVELOPMENT OF MICROSWITCHES FOR MICRO-ELECTRO-MECHANICAL RELAY MATRICES

1. Introduction

1.1. Background

Over the past few years, the design and fabrication of small micro-electro-mechanical (MEM) devices for a wide variety of applications has received considerable attention. MEM systems (MEMS) are miniature (anywhere from 1 μm to 1000 μm in size), movable devices and machines, many of which have macroscopic counterparts. With MEM devices, many functions that are performed at the macroscopic level may also be performed at the microscopic level. Miniature devices have the advantage of reduced size and weight, and the possibility of monolithic integration with electronic circuits to perform control, communication, and calibration functions [1].

Although MEMS technology is barely out of its infancy, it has been successfully used for several applications and is currently being proposed for many more. Automobile makers are currently fabricating tiny cantilevers fabricated alongside very large scale integrated circuits (VLSI) for use as trigger sensors for air bag deployment [2]. Other applications in the development stage include micromachined accelerometers as well as

micro-electro-mechanical resonators for use in aerospace navigation and control systems [3]. High definition television systems currently on the drawing boards are also exploring using vast arrays of miniature deformable mirrors developed using MEM technology [4]. This thesis focuses on another feasible application--the development of a miniature switching relay composed of arrays of tiny micro-electro-mechanical switching elements.

Currently, commercially available matrix switching systems are physically cumbersome, highly specialized, and very expensive. These systems usually consist of consoles into which large matrix switching cards can be inserted [5]. Each card is designed for a specific purpose and signal type and is usually limited in the number of matrix crosspoints. Because of this limited utility, many cards are required to accommodate applications involving large switching matrices and/or wide varieties of signals. As a result, current switching systems lack the ease of implementation, versatility, and small size that are desirable in many applications. Micro-electro-mechanical systems have the potential to overcome many of the limitations inherent in conventional switching systems.

Fabricating MEM devices requires a process that is able to create miniature devices with sufficient detail and size needed by the application. Conventional photolithography techniques used in commercial integrated circuit (IC) foundries are an excellent resource since such techniques can create well defined structures down to a very small feature size. With minimal modification of current IC fabrication techniques, the structural design of desired MEM devices can be accommodated. Coupling IC technology with an appropriate post-processing technique, it is possible to create movable structures suitable

for use in MEM systems (a full description of the fabrication techniques is given in Chapter 2). Advantages of such processes include not only the ease of creating MEM devices, but also the possibility of incorporating on-chip conventional solid-state electronics in a single processing run. A drawback of using conventional IC processes, however, is that metallic films used in these processes are too thin for use as a structural layer. On the other hand, processes specifically developed for MEMS, such as deep x-ray and deep ultraviolet lithography, are suitable for MEM applications requiring thick metallic films. These processes, however, are difficult to implement and do not allow easy integration of solid-state electronics [6].

The basic element in a micro-electro-mechanical switching matrix is the MEM switch. This switch involves moving two physically separated conductors, forming the "off" position, into contact, forming the "on" position. Because the switch involves physical contact, the signal carrying ability of the switch would be dictated by the properties of the materials used in fabrication. Theoretically any electrical signal, large or small, a.c. or d.c., digital or analog may be switched with the same MEM device. Additionally, because of the small size achievable using MEM technology and the simple nature of the MEM switch, it is feasible that many MEM switches could be located in a very small area, thus forming an N by N matrix relay. These factors show significant promise for a MEM switching matrix to improve upon many of the disadvantages of conventional matrix relay systems.

1.2. Problem Statement

As part of a continuing effort to realize utilization of micro-electro-mechanical devices in Air Force systems, this research focused on implementing a MEM relay assembly using commercial fabrication facilities. The objective was to design, fabricate, and evaluate the performance of the produced MEM switches.

The goal was to produce a micro-electro-mechanical switching matrix constructed as a monolithic element for advanced high-performance switching networks. The individual switching elements were desired to meet the following criteria: extremely high electrical isolation in the "off" position, very low series resistance in the "on" position, and uniform wide bandwidth performance with small and large signals. The MEM relay is intended for applications where low switching times are acceptable, but very high signal fidelity is required.

1.3. Scope

This project involved the design and fabrication of micro-electro-mechanical switches for the development of a first generation MEM switching relay. The design of the switches and the relay was based upon current literature in the MEM field and fabrication techniques available to the Air Force Institute of Technology (AFIT). The available fabrication techniques included bulk micromachining of silicon devices using a commercial complementary metal oxide semiconductor (CMOS) process through MOSIS; surface micromachining using a three level polysilicon process (MUMPs: Multi-User MEMs Processes) available through MCNC; and deep x-ray lithography (LIGA) nickel structures

available from the University of Wisconsin through MCNC. Details of the processing techniques are given in Chapter 2.

Characterization of the produced switches included several aspects of the MEM devices. The mechanical motion and the physical principles behind the motion were modeled and compared with experimental results and current literature. The quality of switching contacts was investigated for durability and contact resistance, as well as the signal carrying ability of the structural material in each fabrication process.

1.4. Assumptions

Due to the novelty of this research and the processes involved in the design of the MEM switches, much must be assumed about the structural and electrical properties associated with the materials used in each fabrication process. It is well documented that the structural and electrical properties (i.e. resistivity, stress, Young's modulus, etc.) of thin films depend on many process factors, and it must be assumed that these factors do not vary significantly from run to run in an individual fabrication facility. To this end, it must also be assumed that stated values for these structural and electrical parameters are accurate and do not vary significantly.

More specifically, the MUMPs process uses polycrystalline silicon (polysilicon) as the only structural material. As such, it becomes necessary for most designs to have a significant portion of signal lines, as well as contact electrodes, to be composed of polysilicon. Even at the high doping levels used in this process, polysilicon is only a marginally good conductor. For this research it is assumed that the conductivity of the

polysilicon is high enough to be treated as a conductor in the design and analysis of devices fabricated in the MUMPs process.

1.5. Approach

The basic devices used for creating the necessary motion to form a MEM switch included the cantilever beam, the microbridge, the comb-drive actuator, the heat-drive actuator, and the hinge (Figure 1.1). These devices were chosen because of their ease of fabrication and generally ubiquitous nature in the literature. Modifications to each device were made to allow two conductors to come into contact, thus forming a switch.

The basic principle behind each potential MEM switch was to bring the maximum amount of electrode surface area into contact while keeping the actuation distances minimal. This principle was adopted to reduce the switching contact resistance, as well as reducing the amount of contact force required to achieve a good connection. Additionally, it was desired that the switches require little or no power to hold the switch in either the open or closed positions. This allows the switch to operate with virtually any type of signal at the highest level of signal fidelity allowable by the structural material.

The next step was to use a high level computer aided design (CAD) tool to create the lithography masks used in the fabrication process. The tools used were MAGIC, a well-known, manhattan geometry layout editor, and CADENCE, a newer VLSI package that allows non-manhattan geometries (i.e. circles, ellipses, etc.). Many variations of the basic designs were created and arrayed to help determine optimum performance

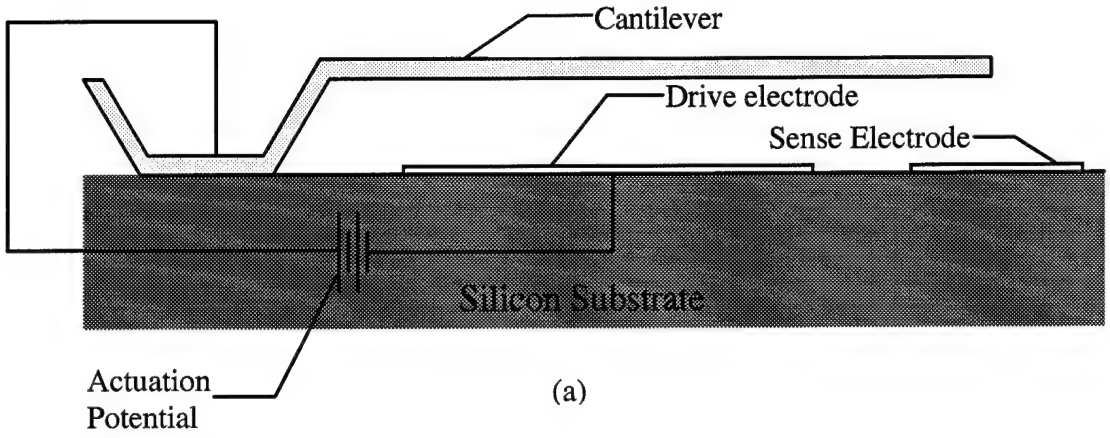
Cantilever
Drive electrode
Sense Electrode
Silicon Substrate
Actuation
Potential

(a)

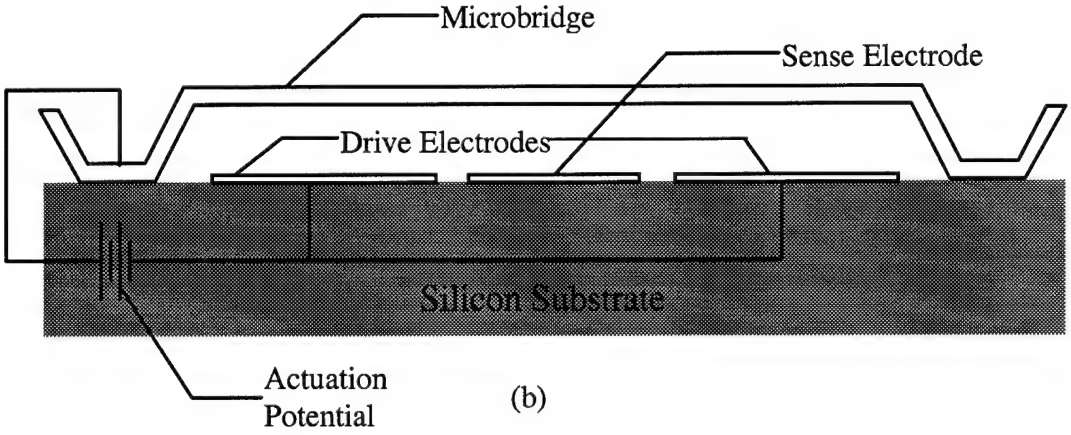
Microbridge
Sense Electrode
Drive Electrodes
Silicon Substrate
Actuation
Potential

(b)

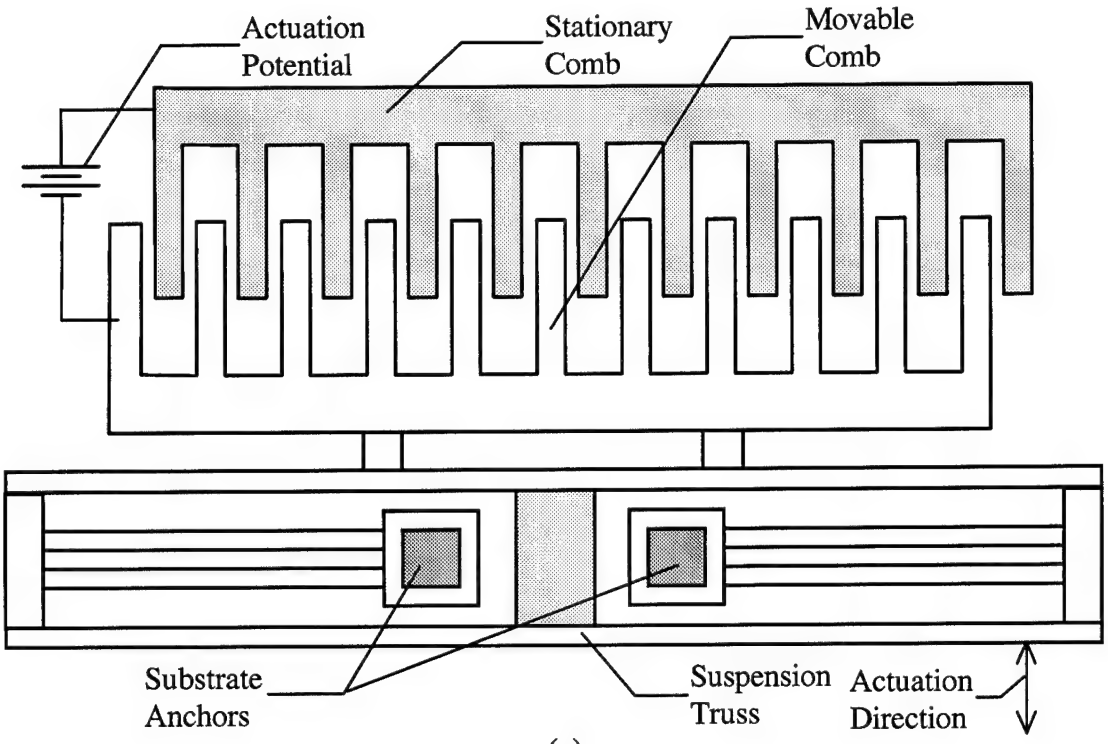
Actuation
Potential
Stationary
Comb
Movable
Comb
Substrate
Anchors
Suspension
Truss
Actuation
Direction

(c)

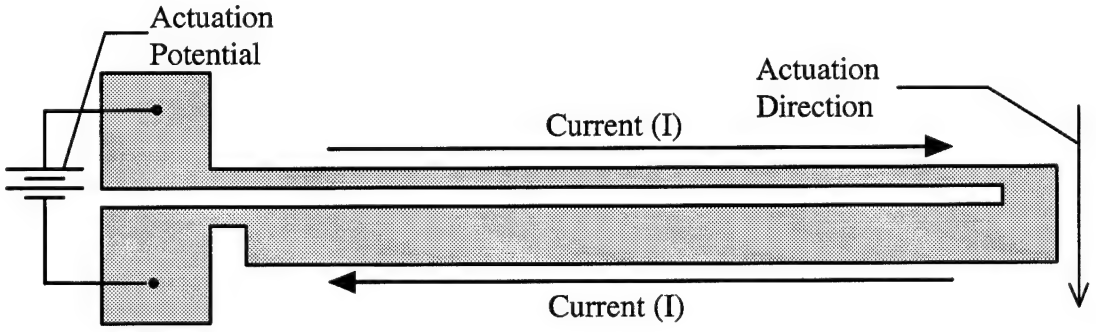
Actuation
Potential
Actuation
Direction
Current (I)
Current (I)

(d)

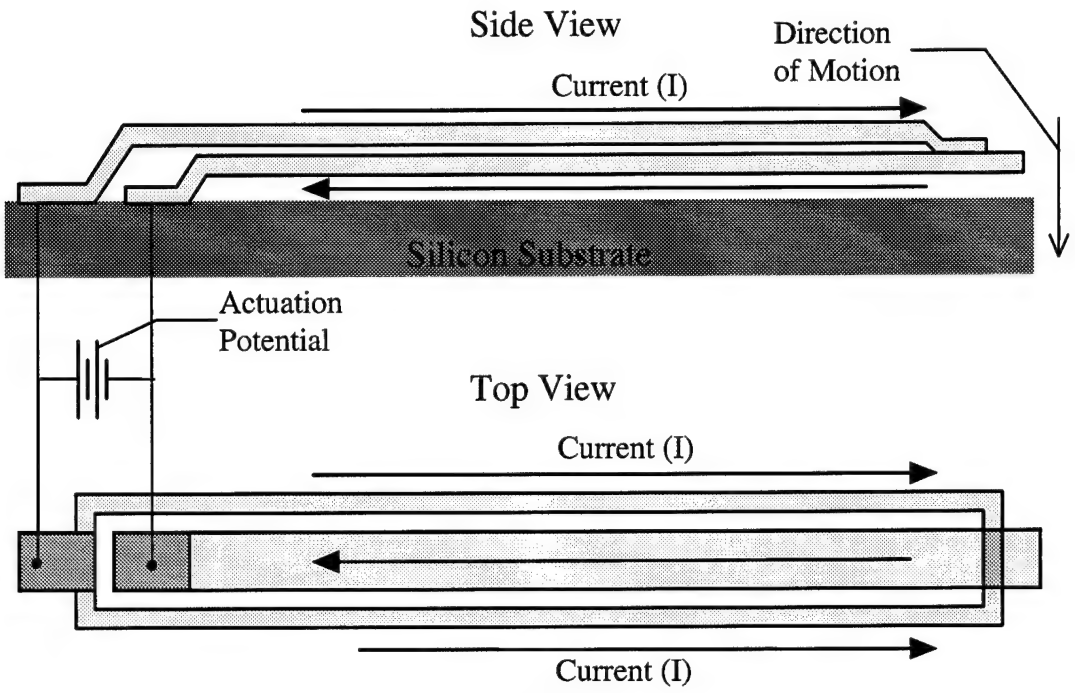

(e)

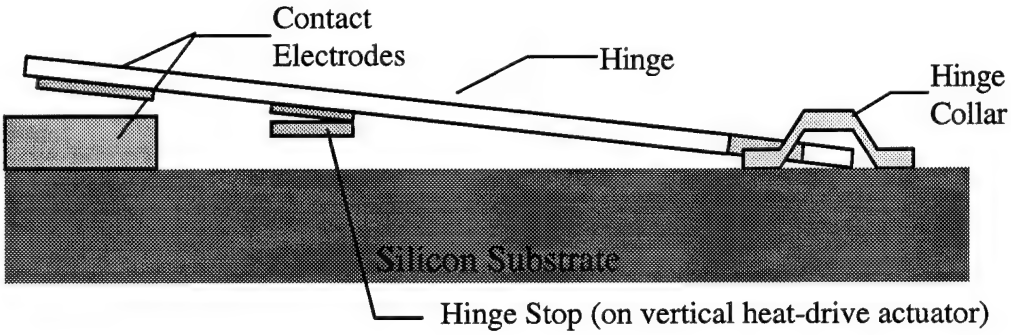

(f)

Figure 1.1. Basic MEM actuators and structures. (a) electrostatic cantilever actuator, (b) electrostatic microbridge actuator, (c) electrostatic comb-drive actuator, (d) horizontal heat-drive actuator, (e) vertical heat-drive actuator, (f) hinge structure.

specifications for each switch. Many of the devices were arrayed into small two by two relays for testing relay characteristics for each basic switch design.

The two most promising processes, MUMPs and LIGA, were used to fabricate the devices. Switches utilizing all the basic actuators of Figure 1.1 were fabricated in the MUMPs process, but only the comb and heat-drive actuators were used in the LIGA process (the high aspect ratio nature of the LIGA process made vertical motion devices infeasible). Three fabrication runs were sent through the MUMPs process and one run was sent through the LIGA process.

1.5.1. Cantilever and Microbridge Designs. The cantilever and microbridge switches were designed for the capability of passing small a.c. signals. The cantilever (microbridge) was actuated by the capacitive electrostatic force generated by a d.c. bias voltage applied between the cantilever (microbridge) and the drive electrode (Figure 1.1. (a) and (b)) The motion of this device was characterized by the amount of voltage required to bring the cantilever tip electrode (microbridge center electrode) into contact with the sense electrode with enough force to form a suitable contact.

1.5.2. Comb-Drive Actuator Design. These structures were used in designing switches for passing all signal types. The comb-drive actuators operated by placing a potential difference between the stationary comb and the suspended, movable comb (Figure 1.1. (c)). The actuation distance was determined by the magnitude of the applied voltage, the number of fingers on the comb, the amount of finger overlap, and the strength of the suspension spring. Some comb drive structures were designed to pull and hold two conductors in contact with a d.c. bias, thus allowing a small a.c. signal to be passed.

Other devices were designed to provide necessary motion in more complex interlocking switching systems. In either case, the actuators were primarily characterized by the amount of drive voltage required to perform the switching task.

1.5.3. Heat-Drive Actuator Design. The heat-drive actuator structures used for actuation in MEM switches operated by using d.c. current to cause differential heating between the two sides of the device, forcing it to bend (Figures 1.1. (d) and (e)). Because of the high conductivity of the structural materials in both the MUMPs and LIGA processes, these devices were designed to be operated with low voltages. The devices were characterized by the amount of applied power that was required to move the device a given distance. Additionally, switches implementing these structures were designed such that maximum actuation distances were not needed, thus avoiding critical breakdown.

1.5.4. Hinge Switch Design. Hinge switches were designed to allow metal to metal electrical contacts in the MUMPs process. After fabrication, the hinges can be flipped over 180 degrees such that the metal on the surface of the hinge can contact two metal pads on the substrate surface. A signal can then be passed between the two pads on the substrate. For use as a switch, a vertical heat-drive actuator was designed to operate with the hinge. When the hinge is rotated from its post-fabrication position, it will contact an extension from a vertical heat-drive actuator that holds it slightly above the two substrate contact pads. When the vertical heat-drive actuator is actuated downward, the hinge's weight allows the gap between the two substrate pads to be bridged by the metal pad on the hinge. The "off" position can be recovered by restoring the vertical heat-drive actuator to its initial position. The hinge switches were characterized by how easily the

devices of different sizes could be to flip-over into the operating position. Additionally, various sizes of vertical heat-drive actuators were used to determine the optimum contact design.

1.6. Switch and Relay Characterization Effort

After each design was fabricated and post processed at AFIT, the devices were characterized in two ways. First, each device was characterized with respect to its mechanical motion, either motion actually forming the switch contact, or motion necessary for the operation of a more complex MEM mechanism. Secondly, each mechanically operational switch was then characterized for its electrical switching ability both as an individual unit and as a member in a larger relay array.

The structural and electrical properties of the materials used in each fabrication process were determined. The results included the electrical properties such as resistivity, thermal resistance to air, and power dissipation, as well as the structural properties such as stress and strain in the released structure, Young's modulus, coefficient of thermal expansion, and effective spring constant.

The initial characterization of each device was performed by using a micromanipulator probe station to electrically probe up to four contacts at a time. Each of the four probes could be linked with a range of a.c. and d.c. currents and voltages as well as several monitoring devices. Properties such as actuation potential, electrical isolation, bandwidth performance, and ability of handling large and small signals were determined.

1.7. Plan of Development

The current level of knowledge in the field of MEMS fabrication and device performance is reviewed in Chapter 2. Chapter 3 contains the theoretical development of the operation of the cantilever beam, microbridge, comb-drive actuator, and heat-drive actuator. Chapter 4 describes in detail the many devices that were fabricated in the microswitch design effort, and the experimental procedure used to fabricate and characterize each of the individual devices, switches, and relays. Chapter 5 discusses the experimental data and Chapter 6 details the results of this project and proposes recommendations for further research.

2. *Literature Review of Micro-Electro-Mechanical Technology Applicable to Microswitch Development*

2.1. Fabrication Techniques

Three primary fabrication techniques are used to create MEM movable devices and mechanisms. The three techniques are bulk micromachining of crystalline silicon, surface micromachining, and deep x-ray lithography combined with electroforming and molding (LIGA).

2.1.1. Bulk Micromachining of Crystalline Silicon. Silicon is a crystalline material which can be anisotropically etched using wet chemical etchants. Anisotropic etching solutions etch silicon crystal planes at different rates. Examples of anisotropic etchants of silicon include hydrazine, tetramethylammonium hydroxide (TMAH), cesium hydroxide (CsOH), potassium hydroxide (KOH), and ethylenediamine-pyrocatechol-water (EDP). The most commonly used etchants are KOH and EDP. For silicon, the (111) crystal planes etch at a much slower rate than all the other crystallographic planes. Combining this property with appropriate masking techniques, dopant concentrations, and epitaxial layers, it is possible to create MEM devices [7].

A very effective and easily realizable mask for EDP and KOH is silicon dioxide (SiO_2). By depositing and lithographically patterning SiO_2 on a silicon substrate, it is possible to create regions of exposed silicon across the wafer. By orienting the mask such that the straight edges of the opening are aligned with the (110) plane, a (100) oriented

silicon wafer submerged in EDP or KOH would be anisotropically etched as shown in Figure 2.1. The pit would be bounded by the (111) planes because of the slower etch rate of the (111) plane relative to the other crystal directions. If the wafer is left in the etchant for a long period of time, the pit will be etched until a perfect inverted pyramid is formed. By leaving the wafer in the etchant for a shorter period of time, however, a shallower, flat-bottomed pit can be realized [7].

In order to ensure that the (111) planes are oriented correctly, it is necessary to align the mask with the (110) wafer flat. Undercutting of the SiO_2 mask can be achieved by correctly choosing proper geometries and orientations for the exposed regions. Openings created with convex corners will be undercut while those created with concave corners will not (Figure 2.2).

Timing plays an important role in the anisotropic etching of silicon. In order to achieve more control over the etching process, the etch rate dependence on dopant concentration can be exploited. By heavily doping silicon with boron concentrations greater than 2.5×10^{19} cm^{-3}, it is possible to slow the etch rate of silicon in all directions by three orders of magnitude [7]. Many novel structures can be created by appropriate doping of parts of a silicon wafer.

Using commercial integrated circuit CMOS processes followed by a wet anisotropic etch, many different MEM devices can be realized. The layers in CMOS processes available through MOSIS are shown in Figure 2.3. In addition, a special layer, known as "open", allows all layers from the top of the integrated circuit down to the silicon surface to be etched away. The MOSIS process also allows the patterning of a heavily

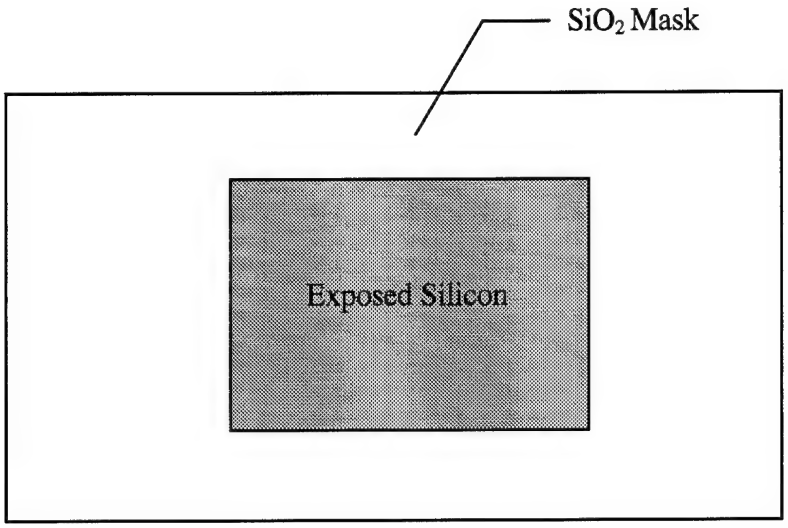

(a)

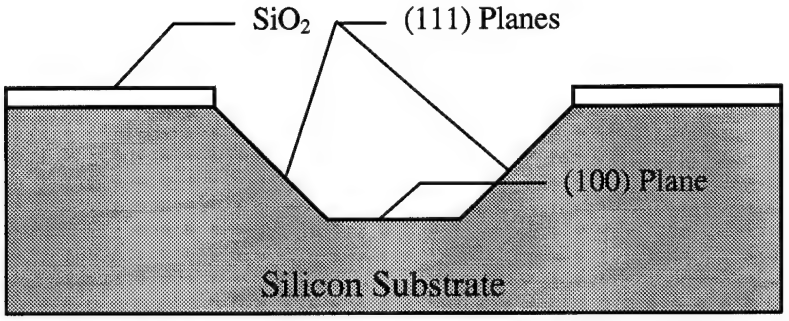

(b)

Figure 2.1. Anisotropic etching of a masked silicon substrate: (a) top view, (b) side view [7].

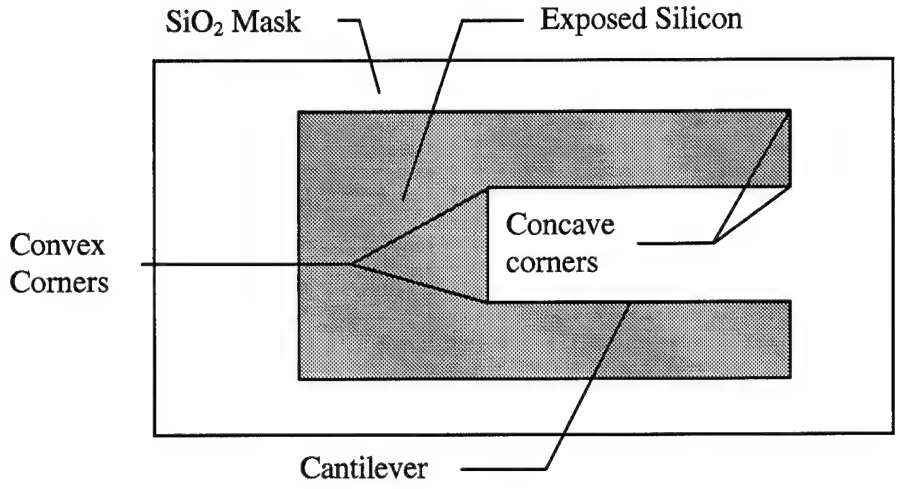

(a)

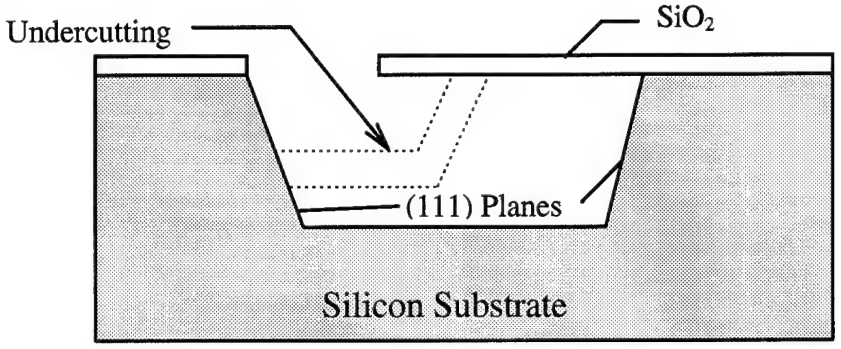

(b)

Figure 2.2. Cantilever fabrication--convex corners are undercut, concave corners are not: (a) top view, (b) side view [7].

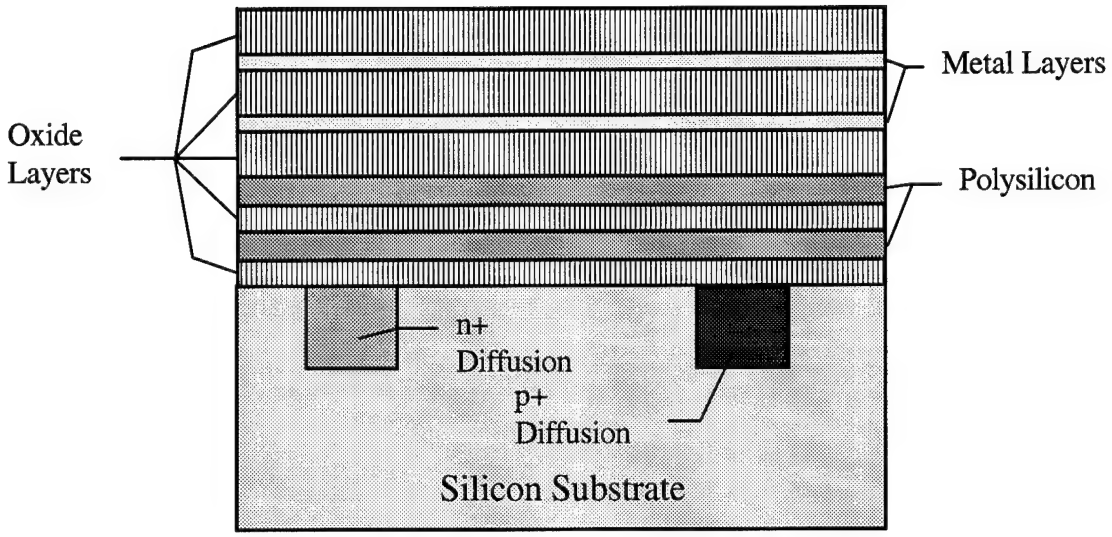

Figure 2.3. Layers used in CMOS processes available through MOSIS.

doped boron layer, known as the "p-stop" layer, which serves as an effective etch stop for anisotropically etched MEM devices. Because it is a standard procedure for commercial foundries to orient their masks with the (110) wafer flats, MEM devices can be fabricated in commercial foundries without any further modifications to the processing sequence. The devices can then be released in-house by immersing produced dies in baths of EDP or KOH solutions [8].

An example of a cantilever fabricated using bulk micromachining of a CMOS processed die is given in Figure 2.4. First, the wafer is implanted with a border ring of p+ dopants to act as an etch stop. Following this, a patterned layer of SiO_2 is deposited to act as a mask (Figure 2.4 (a) and (b)). The combination of the oxide mask and the p+ ring makes the border of the pit very well defined and controlled during the etching process. When the wafer is etched with EDP or KOH, the oxide cantilever is left suspended as shown in Figure 2.4. (c).

A major advantage of creating devices in this way is that the structures can be integrated with on chip circuitry [9]. Any standard electronics would be safely protected under layers of SiO_2 with the only exposed regions being the desired MEM structures. Despite this very strong plus, there are disadvantages as well. The most important is the fact that any structures created are necessarily encased in oxide. Therefore any structures for which access to the structural layers contained within the oxide is necessary are generally not possible. Additionally, the minimum size of realized MEM devices is relatively large. The smallest device size would be determined from a combination of all the structural layers contained within the oxide plus the thickness of the oxide, the open

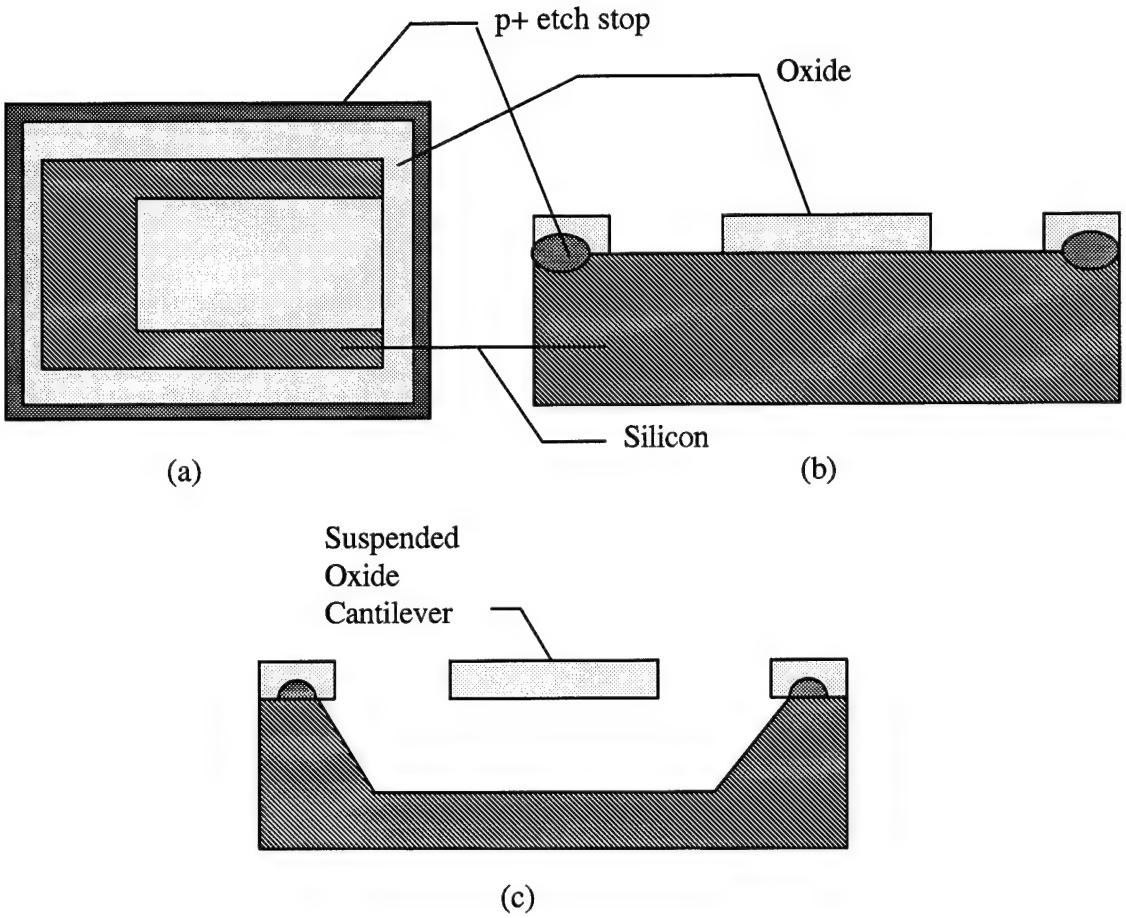

Figure 2.4. Fabrication of a SiO_2 cantilever by bulk micromachining: (a) top view, (b) front view (before etch), (c) front view (after etch) [9].

regions, and the large pits formed in the substrate. For applications requiring smaller overall dimensions, other processing techniques, such as surface micromachining, may be more useful.

2.1.2. Surface Micromachining. Another major method of producing MEM devices is through surface micromachining. Whereas devices created using bulk micromachining require etching of the silicon wafer, devices realized using surface micromachining are released by selective etching of sacrificial layers deposited on the substrate. Through such surface micromachining processes, multiple level, three dimensional structures can be created.

Figure 2.5 depicts the basic concept behind surface micromachining. Processing begins with a standard silicon substrate that is then passivated with a thin isolation layer--usually silicon nitride (Si_3N_4). On the isolation layer, a spacer layer, usually SiO_2, is deposited and lithographically patterned. This layer is usually referred to as a sacrificial layer because it is later etched away and sacrificed to release the MEM structures. Next a structural layer is deposited and patterned, afterwhich the sacrificial layer may be isotropically etched away, leaving a free standing device. In order to create multiple level, three dimensional structures, several sacrificial and structural layers are successively deposited and patterned atop one another. When the final isotropic etch is performed, all the sacrificial layers are removed releasing the multiple level MEM structure [10].

Structural materials used in surface micromachining processes vary widely depending on the application. The structural layer may be polysilicon, Si_3N_4, SiO_2, as well as other

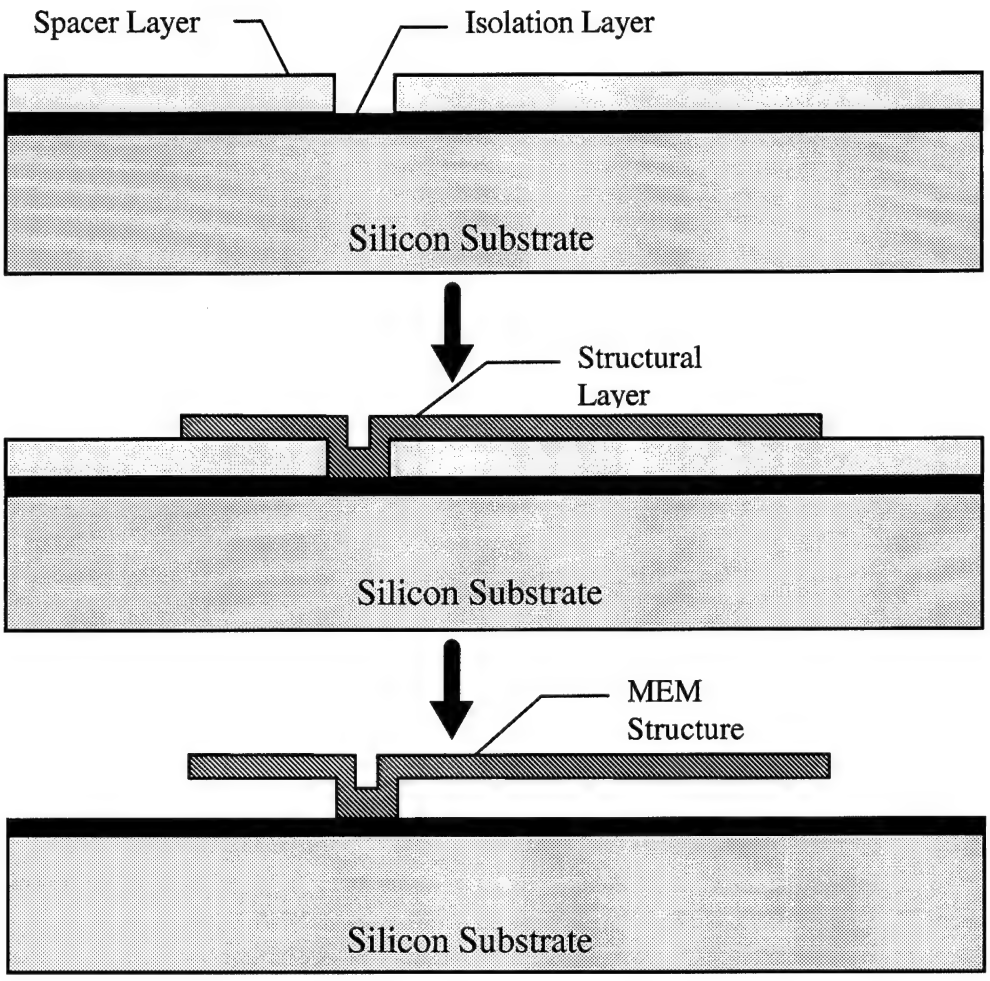

Figure 2.5. Basic concept behind surface micromachining [10].

materials. The sacrificial layer used depends on the structural layer chosen and the available etchants (the etchant must be able to etch the sacrificial layer quickly relative to the structural material). Table 2.1. contains a list of commonly used materials and their typical thicknesses. Because of its well studied electrical and mechanical properties, the most common structural material is polysilicon with silicon dioxide as a sacrificial layer.

Table 2.1. Surface Micromachining Thin Film Layers [10].

Structural Layer		***Sacrificial Layer***	
Material	***Typical Thickness (μm)***	***Material***	***Typical Thickness (μm)***
Polysilicon	1-4	PSG, SiO_2	1-7
Si_3N_4	0.2-2	PSG, SiO_2	2
SiO_2	1-3	Polysilicon	1-3
Polyimide	10	Al	1.5-3
W	2.5-4	SiO_2	8
Mo	0.5	Al	0.7
TiNi	1.5	Polyimide, Au	1.5
NiFe	8	Al, Cu	7

The polysilicon used in surface micromachining is usually deposited using low pressure chemical vapor deposition (LPCVD) at temperatures at or above 600 °C. The polysilicon film can be deposited as either a doped or undoped thin film. In either case, the properties of polysilicon and this deposition technique conspire to create a large amount of residual stress (greater than 175 MPa) in the polysilicon film [10]. If this stress is not relieved before sacrificial release, it will cause undesirable deformation of the polysilicon MEM structure. The primary way of reducing the residual stress is by thermal

annealing. Thermal annealing of undoped polysilicon at a temperatures greater than 1000 °C can reduce the residual stress to less than 50 MPa [10]. While this is a significant improvement, even better results are achieved for thermal annealing of doped polysilicon films [10].

The most common sacrificial layer used in surface micromachining is silicon dioxide (SiO_2). This is because a well-known etchant, hydrofluoric acid (HF), has a high degree of etch selectivity between SiO_2 and polysilicon. Often a phosphorous doped silicon dioxide, referred to as phosphosilicate glass (PSG), is used because this even further improves the etch selectivity. Additionally, the PSG can be used to aid in the reduction of the residual stress in polysilicon thin films. When heavily phosphorous doped PSG surrounds an undoped polysilicon layer, the phosphorous atoms will diffuse into the polysilicon during the thermal annealing phase of fabrication. This has the effect of reducing the residual stress as well as increasing the conductivity of the polysilicon film. Residual stresses low enough to avoid deformation are achieved as well as polysilicon sheet resistances of below 50 Ω/square [10]. The sacrificial release of MEM structures using polysilicon as a structural material and SiO_2 as a sacrificial layer is performed with an HF solution.

The surface micromachining process available to AFIT is the Multi-User-MEMs-Processes (MUMPs) through MCNC (loc: 3021 Cornwallis Road, research Triangle Park, North Carolina, 27709) [11]. The MUMPs process uses polysilicon for the structural material, deposited oxide (PSG) for the sacrificial layer, and silicon nitride (Si_3N_4) for an isolation layer. This process is different from many similar processes in that it is purposely

designed to be as general as possible in order to allow many different structures. Because the process is not optimized for any specific devices, the layer thicknesses, structural materials and design rules were chosen to suite many users and guarantee the highest possible yield.

The MUMPs process begins with a (100) oriented, n-type silicon wafer with a resistivity of 0.5 Ω-cm which is then heavily doped with phosphorous in a standard diffusion furnace. This helps prevent charge feed-through to the substrate from electrostatic devices located on the surface of the wafer. Next, the Si_3N_4 isolation layer is deposited using LPCVD to a thickness of 0.5 μm. Following this, a 0.5 μm layer of low stress polysilicon is deposited (poly 0) and lithographically patterned. The etch of the poly 0 layer is performed using a reactive ion etching (RIE) system. After this step, a 2.0 μm thick PSG sacrificial layer is deposited. Next, the entire PSG film is patterned and etched using RIE to form 0.75 μm deep "dimples" in the oxide. The wafers are then recoated with photoresist and the PSG film is etched to form via holes to the poly 0 film. Subsequently, the first structural layer is deposited to form a 2.0 μm thick polysilicon film (poly 1). On this layer, a thin layer of PSG is then deposited after which the wafer is annealed for one hour at 1050 °C. Because the poly 1 structural layer is surrounded by PSG films, it becomes heavily doped by the diffusion of phosphorus atoms from the PSG into the polysilicon film. The resulting polysilicon film is characterized by a fine grain size and very low internal stress. The thin PSG layer is then stripped and followed by RIE etch of the polysilicon layer below. Next, a 0.5 μm layer of PSG is deposited by LPCVD. This PSG layer is then lithographically patterned and etched two separate times. The first

pattern and etch are designed to provide a via between the poly 1 layer and another polysilicon layer, poly 2, that will be deposited on top of this PSG layer. The second pattern and etch are performed to allow a mechanical and electrical connection between the poly 2 and poly 0 layers (i.e. both the 0.5 μm PSG layer and the lower 2.0 μm PSG layer are etched). After the vias to poly 0 and poly1 are created, the second structural polysilicon layer, poly 2, is deposited (by LPCVD) to a thickness of 1.5 μm. Similar to the poly 1 layer, a thin PSG layer is deposited above the poly 2 layer and is then annealed at 1050 °C for one hour. As before, this produces an inherently low stress thin film polysilicon layer. The thin oxide is then stripped and the poly 2 layer is patterned and etched by RIE. Finally, 0.5 μm thick layer of metal is deposited and lithographically patterned on the poly 2 layer. Figure 2.6 depicts the structural and sacrificial layers associated with the MUMPs process.

The sacrificial release is performed by a wet etch in a bath of 49 wt% hydrofluoric acid (HF) for 2-3 minutes. The die is then rinsed in de-ionized water followed immediately by a bath in propanol. Because of the lower surface tension of the propanol (as opposed to water), the number of devices rendered unusable due to substrate sticking is reduced. The die is then dried in an oven at 110 °C for 5 minutes. Figure 2.7 shows a completed micromotor, both before and after sacrificial release, as designed in the MUMPs process.

2.1.3. Deep X-ray Lithography, Electroforming, and Molding. Deep x-ray lithography, electroforming, and molding (LIGA) is a process by which high precision,

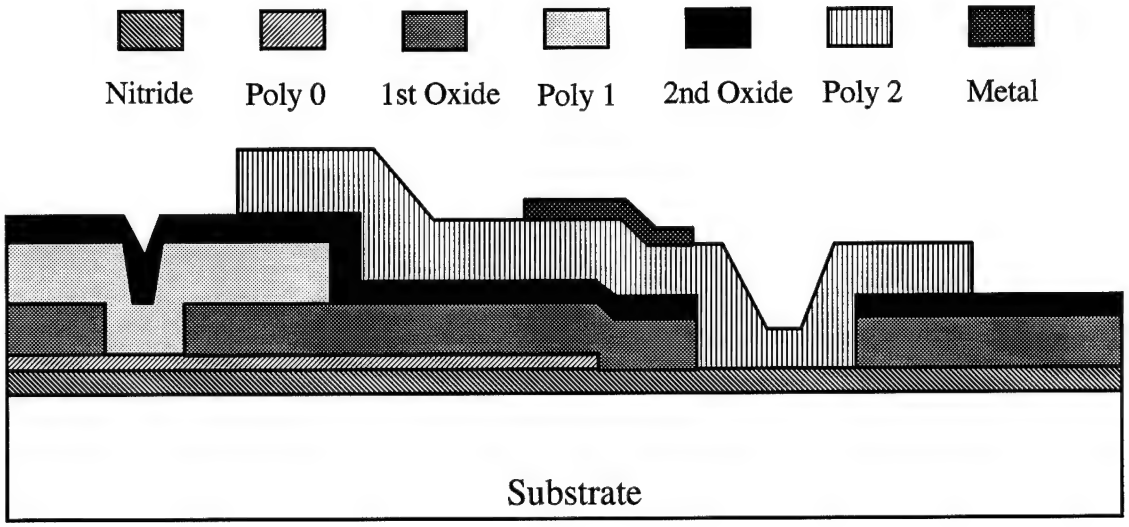

Figure 2.6. Basic layers used in the MUMPs process [11].

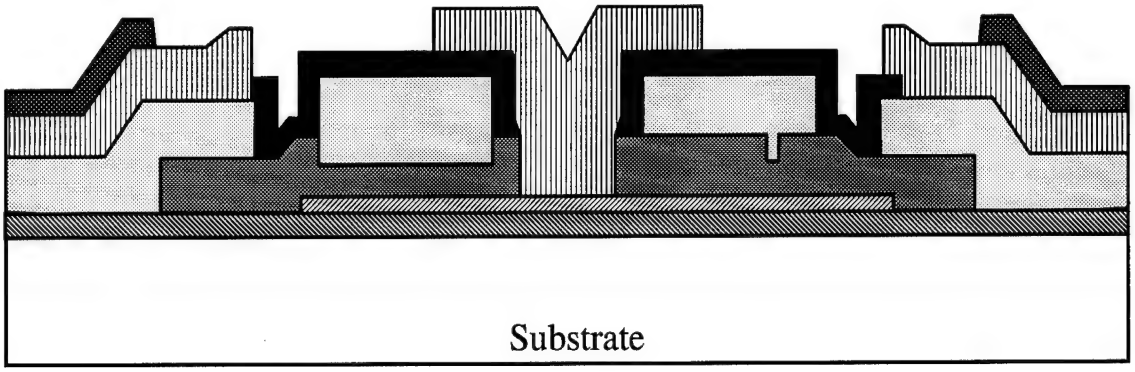

(a)

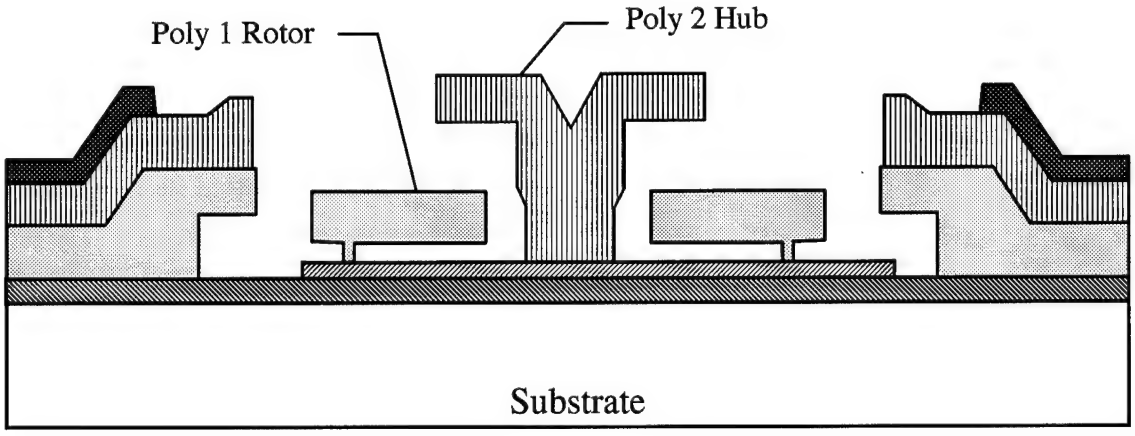

(b)

Figure 2.7. Micromotor fabricated in the MUMPs process: (a) before release, (b) after release [11].

high aspect ratio (very tall and thin) metal structures are formed. Characteristics of produced structures include structural heights of 20-500 μm, minimum dimensions of 2 μm with a minimum incremental feature size of 0.5 μm, a surface roughness of 0.03-0.05 μm (max. peak to valley), and a maximum dimension of 20 x 60 mm [12]. The details of the LIGA process are shown in Figure 2.8.

The process begins with a substrate, typically a glass plate or silicon wafer, which is coated with an adhesive layer and seed metal to ensure optimum electroforming results. On the substrate, a thick polymethylmethacrylate (PMMA) layer is then deposited. This polymer-like material is sensitive to x-ray illumination in the same manner that photoresist is sensitive to ultraviolet light in standard photolithography. Next, the wafer is masked with special x-ray masks consisting of a membrane and thick x-ray absorbing materials. The wafer is then exposed to synchrotron x-ray radiation followed by the development and dissolution of the exposed regions of the PMMA film. Because of the high energy associated with the synchrotron x-rays, very thick layers of PMMA can be properly exposed leaving behind a plastic mold with very high aspect ratios. Metal (such as nickel or copper) is then deposited into the resulting plastic mold by electroforming. With a chemical strip of the remaining PMMA resist, a final metal structure or a metal mold insert for mass replication is created [12], [13].

The realization of movable structures in the LIGA process can be achieved in two ways, both of which require slight modifications to the basic LIGA process described above. The simplest method involves coating the substrate with an *unpatterned*, metal layer which can be used as a sacrificial layer. The LIGA process is then performed as

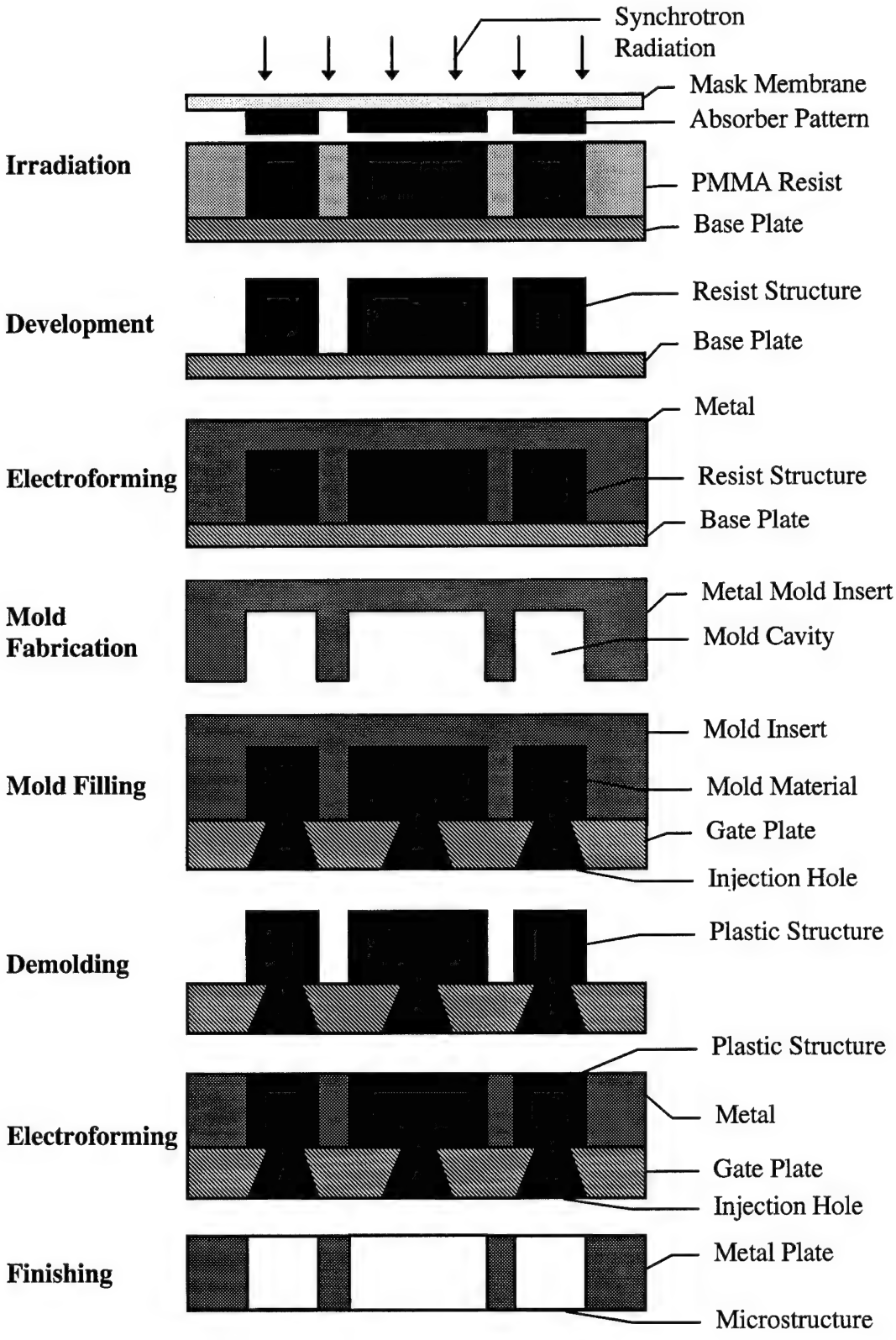

Figure 2.8. The LIGA process [12].

described above. After the PMMA strip, however, the entire wafer is then immersed in a selective isotropic etching solution. By appropriately timing the etch, structures smaller than a desired size can be undercut and released while larger structures will not be completely undercut and will remain attached to the substrate.

The second method used to create released movable structures in the LIGA process involves using a *patterned* sacrificial layer on the substrate (Figure 2.9). In this process, often referred to as SLIGA (Sacrificial LIGA), a sacrificial layer is deposited on the substrate which is then patterned and etched using a standard photolithography procedure. The thickness of the sacrificial layer can be on the order of several micrometers. The LIGA process is then performed normally except that during the x-ray masking step, very precise mask alignment is required to produce proper structures. This method has the advantage of producing movable devices with a large sacrificial layer, but has the disadvantage of requiring significantly different photolithography steps and exact mask alignment [13].

The LIGA process is advantageous for use in many MEM systems primarily because of its high aspect ratio advantages over other processes. The increased aspect ratio greatly improves the effectiveness of devices relying on electrostatic and thermal forces for actuation. Additionally, the high conductivity of the structural layer allows this process to be viable for structures needing high quality electrical performance. The primary disadvantage of the LIGA process is its lack of availability due to the limited number of synchrotron x-ray sources in the continental United States.

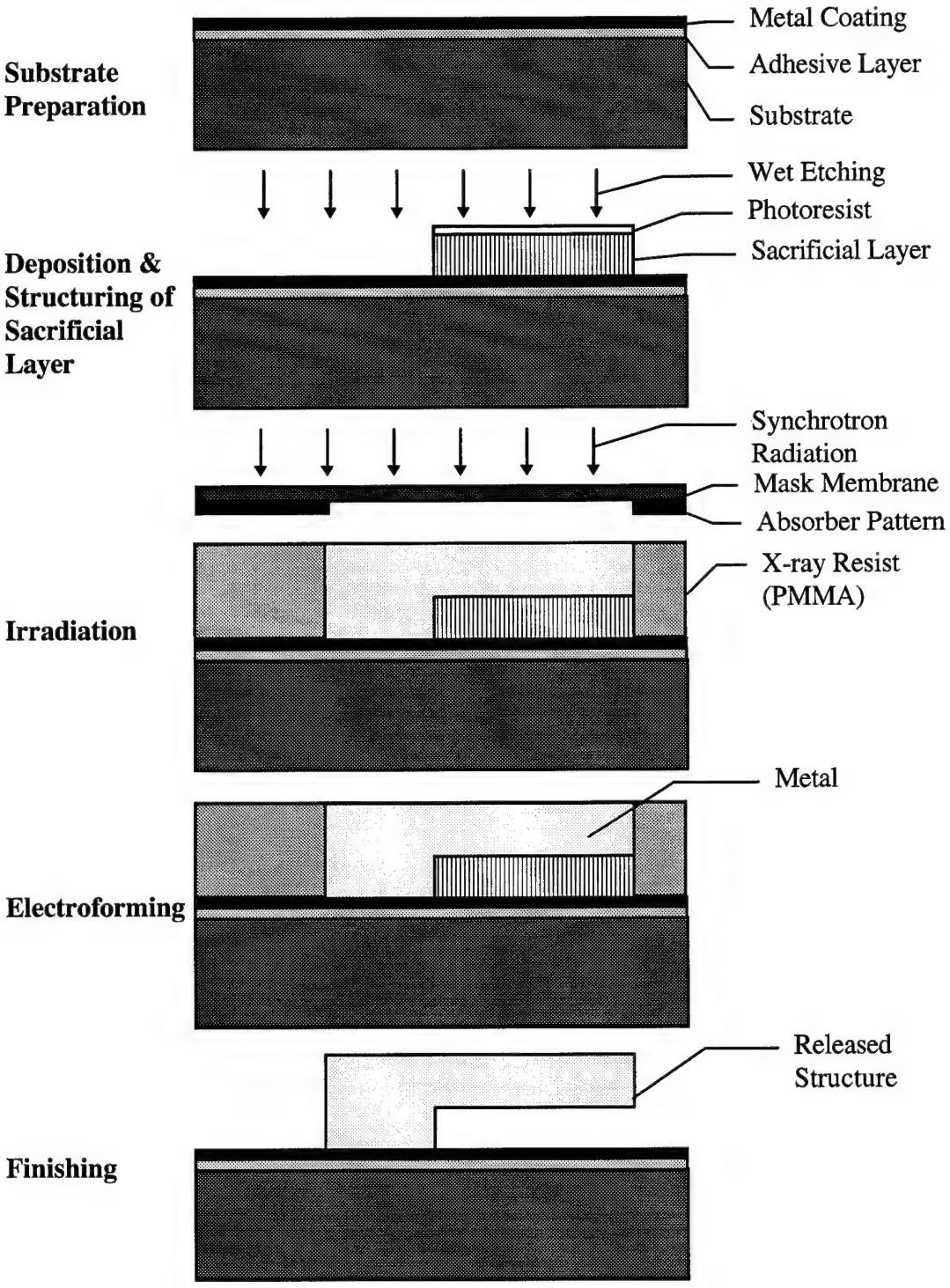

Figure 2.9. The sacrificial LIGA (SLIGA) process [13].

2.2. *Micro-Electro-Mechanical Actuation*

Because micro-electro-mechanical switching involves moving two electrodes into electrical contact, it is necessary to have a method of producing accurate, small-scale forces to move at least one of the conductors. In MEMS literature, the basic methods used for micromechanical actuation are electrostatic forces, forces due to thermal energy, magnetic, and piezoelectric forces. Numerous structures have been realized based on these actuation techniques, however, many of the devices have been made using very specific fabrication processes [14] [15]. Because this thesis research is based upon processing currently available to AFIT, only the most useful structures and techniques realizable in the MUMPs, CMOS, and LIGA processes are covered.

2.2.1. Thermal Actuation. Actuation based upon thermal energy has been achieved for many different micro-electro-mechanical applications. Reasons for the popularity of thermal actuators are many. First, the energy density achievable using thermal actuation is up to 10^7 J/m^3 for some devices [16]. This has allowed many applications to achieve large deflections (greater than 50 μm) with voltages comparable to those used in standard microelectronic circuits (less than 10 volts). However, thermal devices are usually characterized by high power consumption (up to 10's of milliwatts) and slow response times (up to 10's of milliseconds) [16]. Additionally, achieving precise motion requires thin films with well controlled material properties which may not be easily implemented in current processing techniques. However, thermal actuation remains useful for a number of applications requiring large forces and/or displacements.

*2.2.1.1. **Bimetallic Actuators**.* The most common method of implementing heat-driven devices is the bimetallic actuator. The bimetallic actuator consists of two or more materials with differing coefficients of thermal expansion. When the materials are uniformly heated, the thermal coefficient of expansion mismatch between the two materials forces a displacement directly related to the amount of applied thermal energy. The method used to heat the actuator depends on the application, but the most common method consists of using a winding thermal resistor. A simple device that uses the bimetallic actuator is the cantilever beam as shown in Figure 2.10. Deflection distances of up to 65 μm have been achieved using such cantilevers composed of a gold-silicon sandwich [17]. The device was heated by converting electrical energy into thermal energy with a polysilicon heater which was electrically isolated from the gold and silicon layers by CVD deposited SiO_2. Because such isolation layers are often required for bimetallic devices heated with electrical resistors, most devices operating under the bimetallic principle are fabricated using bulk micromachining in a CMOS-type process. In such a process, the SiO_2 layers interleaving all the conductive layers can be used for electrical isolation because the SiO_2 is not severely attacked by the etchants used in bulk micromachining.

*2.2.1.2. **Thermally Activated Beam Flexure**.* Another device utilizing thermal energy is the thermally activated beam flexure (heat-drive actuator). Rather than using a thermal expansion coefficient mismatch between materials to provide a thermally generated force, the heat-drive actuator uses differential heating of the same material created by running a d.c. current through a loop of conductive material of varying

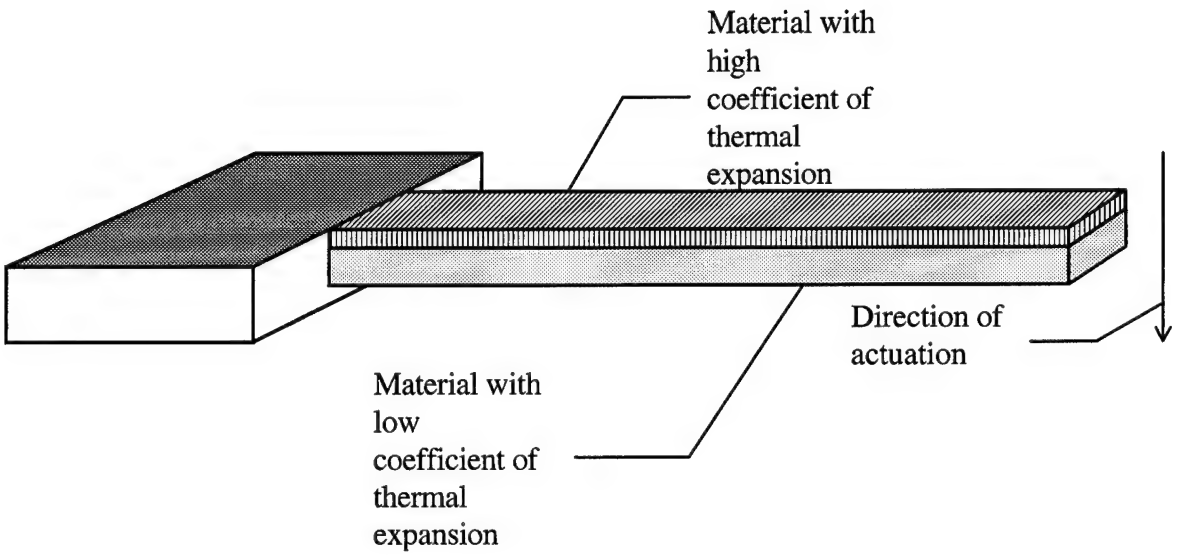

Figure 2.10. Bimetallic actuator [17].

thickness (Figure 2.11). Because the cross-sectional area of section C is larger than of sections A or B, section C has a lower resistance than the narrower sections. When current is run through the device, the difference in resistance causes a corresponding difference in temperature between the wide and narrow sections. As a result, section A thermally expands to a greater degree than sections B and C combined, forcing the tip to deflect [18].

Although the thermal effects dominate, magnetic forces also play a role in the operation of this device. Because the current driving the actuator is traveling in opposite directions on each side of the device, a repulsive magnetic force between the two sides is created. This effect is beneficial to the operation of the device in that it forces section A to move away from sections B and C, preventing a short circuit during large tip deflections. A thermally activated beam flexure (heat-drive actuator), formed from nickel, designed with a length (L) of 1000 μm, height (h) of 50 μm, section A and B thickness of 4 μm, section C thickness of 8 μm, and a center to center separation (g) between sections A and B of 10 μm has achieved a tip deflection of well over 100 μm with 100 mA of applied current [18].

2.2.2. Electrostatic Actuation. Actuation by using electrostatic forces has become popular because these forces can be implemented using static voltages requiring only insulative and conductive thin films which are available using conventional IC fabrication techniques. Additionally, for MEM devices designed with feature sizes achievable in current lithography techniques, the utility of electrostatic actuation increases due to the smaller capacitive gaps. The smaller gaps allow for much stronger electric fields than are

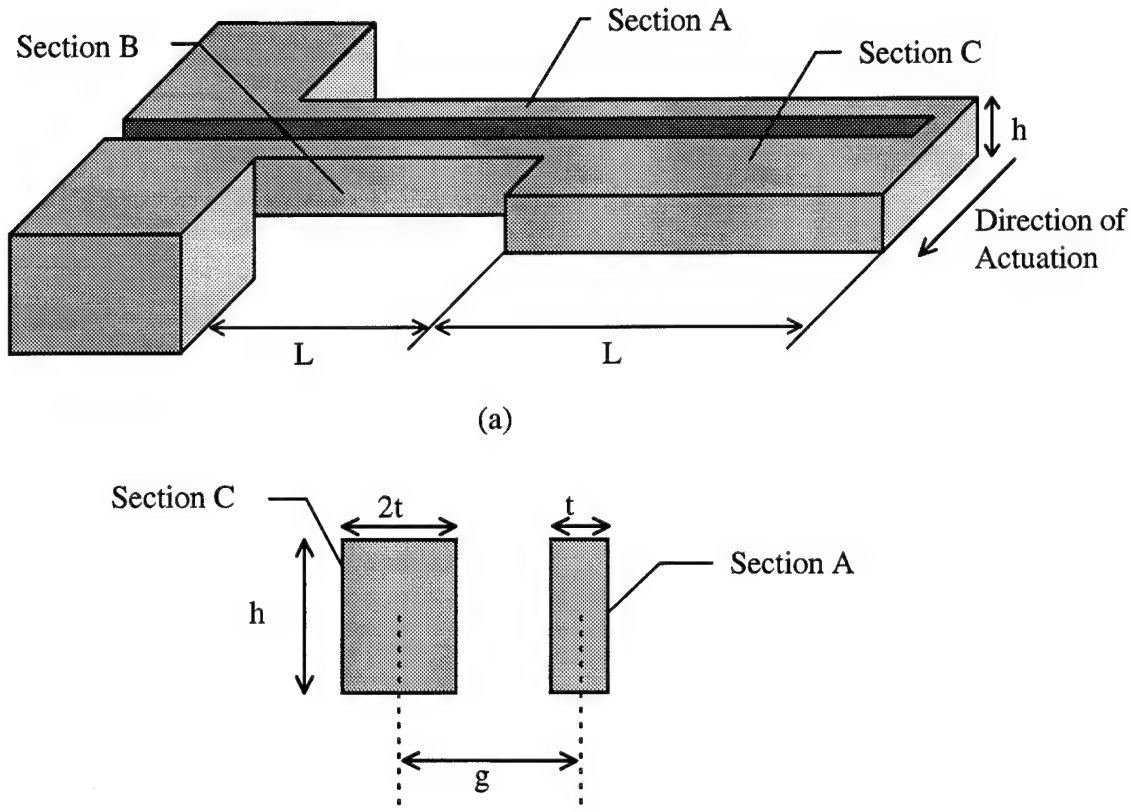

Figure 2.11. Horizontal heat-drive actuator (a) 3-D view, (b) cross-sectional view and dimensions [18].

normally achievable for a given voltage. These strong electric fields allow stored energy densities to reach levels up to 4 x 10^5 J/m^3 which is large enough to facilitate actuation [19]. Additionally, electrostatic forces can achieve precise control of the actuation force by fine tuning the applied actuation voltage, as well as being able to facilitate response times down into the microsecond range. Despite these advantages, however, electrostatic devices generally have lower maximum actuation distances than can be achieved with other actuation methods.

2.2.2.1. Electrostatic Cantilever Actuators. The simplest structure that can be achieved using electrostatic actuation is the cantilever actuator (Figure 1.1 (a)). Once a cantilever has been fabricated, the beam and the substrate drive electrode form a simple parallel plate capacitor. Therefore, any deflection in the beam approximately follows the parallel plate capacitor arrangement--assuming the slight deformations of the beams are negligible. Cantilever structures, while conceivably useful as actuators, have generally been used for resonant sensors. For such applications, the beam is acted upon by outside forces and any resulting deflection can be capacitively sensed. Using the same principle, however, it is also possible to force the cantilever to deflect by applying a voltage between the beam and the drive electrode.

The electrostatic deflection of a cantilever was demonstrated by Peterson (Figure 2.12) [20]. These cantilever devices were fabricated beginning with a (100) oriented, p-doped silicon substrate that was then implanted with boron to form a highly conductive p+ layer. Subsequently, a 12 μm thick epitaxial layer of p-doped silicon was grown followed by an unpatterned, 0.5 μm layer of SiO_2, as shown in Figure 2.12. Then, a very thin

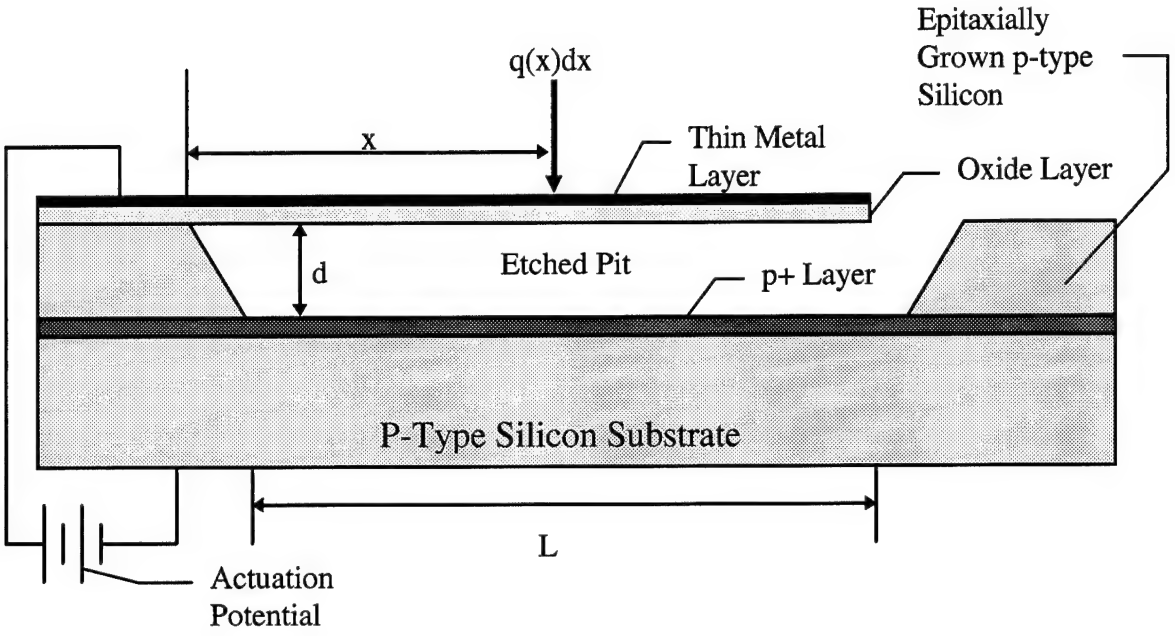

Figure 2.12. Basic electrostatic cantilever [20]. Here d is the capacitive gap between the cantilever and the p+ layer and q(x)dx is the magnitude of the capacitive force at any point, x, along the length of the cantilever.

coating of chromium-gold was deposited and patterned such that the cantilevers would be oriented square to the (110) plane. Next, the exposed regions of SiO_2 were etched to allow access to the silicon surface. Finally, the wafer was immersed in EDP, and water at 118 °C for 20 minutes, and was carefully rinsed and dried. The released cantilevers were 100 μm long and were suspended over a 12 μm pit [20].

By applying a voltage between the cantilever electrode and the p+ bottom electrode, a capacitive force was induced on the cantilever. The author modeled the beam as a simple, single-end supported beam actuated by a simple parallel plate capacitor consisting of one flat side, associated with the p+ pit bottom, and one curved side, associated with the curvature of the deflected cantilever beam. This method was very accurate for small deflections, but large deflections caused most of the electrostatic force to be concentrated at the tip of the beam, making the model less accurate for deflections greater than 4 μm. For deflections beyond this point, the device became unstable and instantly deflected to the substrate [20].

2.2.2.2. Electrostatic Microbridge Actuators. Electrostatic microbridges, which operate under the same principle as cantilevers, are also simple to design and fabricate. Most microbridges are fabricated in a surface micromachining process using polysilicon as the primary structural material. Beneath the bridge, several conductive regions are either deposited or diffused for use as drive and sense electrodes (Figure 1.1 (b)). For use as a sensor, an alternating voltage is applied between the microbridge and the drive electrodes. The resulting oscillation is sensitive to parameters such as ambient temperature and pressure. By capacitively sensing the oscillation of the bridge it is

possible to sense differences in ambient conditions. For use as a microswitch, a d.c. voltage of sufficient magnitude between the microbridge and drive electrodes can force the microbridge to touch the sense electrode, thus allowing a connection to be made.

The microbridge structures have been fabricated and tested primarily for use as resonant sensors and simple micromechanical switches (Figure 2.13) [21]. For the resonant device, the fabrication process begins by diffusing boron to form a thick p-type tub in the silicon substrate. Following this, the heavily doped n+ drive and sense electrodes are formed during a phosphorous diffusion. Next, a 0.25 μm thick isolation layer of Si_3N_4 is deposited uniformly across the wafer followed by a patterned 1 μm thick SiO_2 sacrificial layer. Subsequently, an undoped 1 μm thick polysilicon layer is deposited and patterned. Then, a sacrificial p-doped SiO_2 is deposited on the polysilicon film and annealed at 1050 °C. The annealing process serves to reduce any thin film stress present in the polysilicon layer and allows impurities in the SiO_2 layers to dope the polysilicon. Sacrificial etching using 49 wt.% hydrofluoric acid is performed to release the structures. Beam lengths of 120-1000 μm and beam widths of 15-60 μm formed from 1 μm thick p-doped polysilicon were tested as resonators. The maximum achievable resonant frequencies were in the 100 kHz range [22].

Additionally, tests of the devices as microbridge microswitches using beams 300 μm long, 25 μm wide, and 1 μm thick were also performed. Using d.c. voltages of 15 volts, deflection of the microbridge center to the sense electrode was achieved [22]. Such voltages are advantageous in that they are not far from the range of voltages compatible with microelectronic circuits. Further, the authors were able to accurately predict the

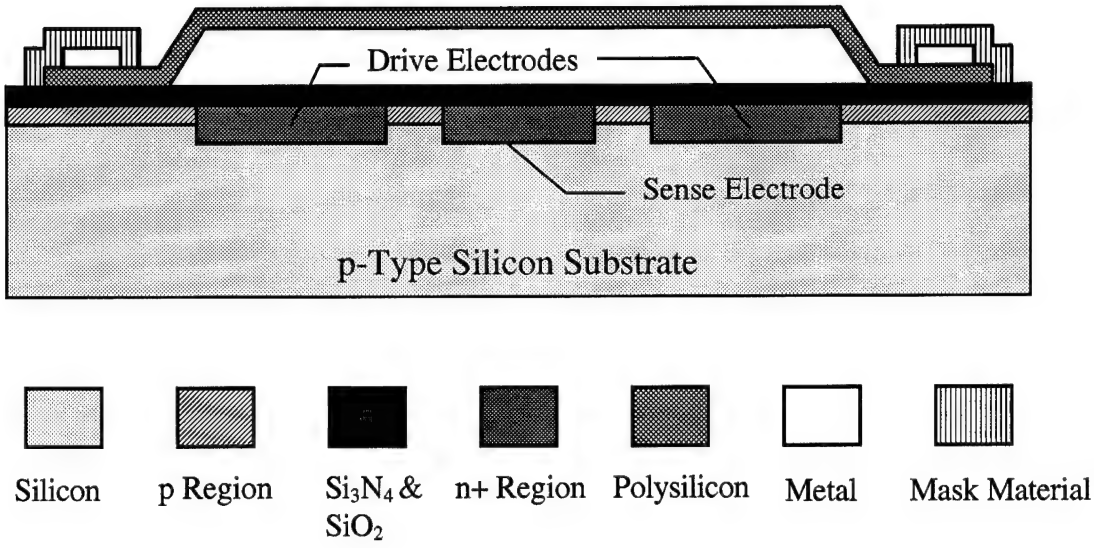

Figure 2.13. Resonant microbridge/switch microbridge [22].

closing voltage (13.5 volts was calculated) using simple parallel plate capacitor relations and simple beam mechanics.

Sun, et al were also able to fabricate and test a microbridge actuator for use as a resonating microswitch (Figure 2.14) [23]. Processing of this device began by depositing and patterning a 0.35 μm thick Si_3N_4 passivation layer on an n-type silicon substrate. Next, a 1.1 μm thick, heavily p-doped, sacrificial layer of SiO_2 was thermally grown and patterned. On the sacrificial layer, a 1.0 μm thick layer of p-doped polysilicon was deposited by LPCVD at 750 °C and thermally annealed at 1100 °C for 9 minutes to reduce any thin film mechanical stress. Next, aluminum was deposited and patterned and was then covered with a layer of negative photoresist to prevent aluminum degradation during the sacrificial release. Finally, the microbridges were released with a buffered hydrofluoric acid [23].

The switches were designed with lengths of 50-250 μm, widths of 25-100 μm, a thickness of 1 μm, and an air gap of 1.1 μm. The microswitch was operated by placing a voltage between the beam and the substrate which forced the beam to bend. At a certain critical voltage, the beam was bent such that the capacitive gap between the bridge and substrate was small enough that discharge could take place. When this point was reached, the beam snapped back into its original position and began the process over again. Thus, by keeping the applied potential above the critical voltage, continued oscillation and discharge were possible. The resulting output waveform, measured using an oscilliscope, was a sawtooth wave whose frequency varied linearly with applied voltage above the critical voltage. The voltage required for discharge of these structures ranged from 12.9

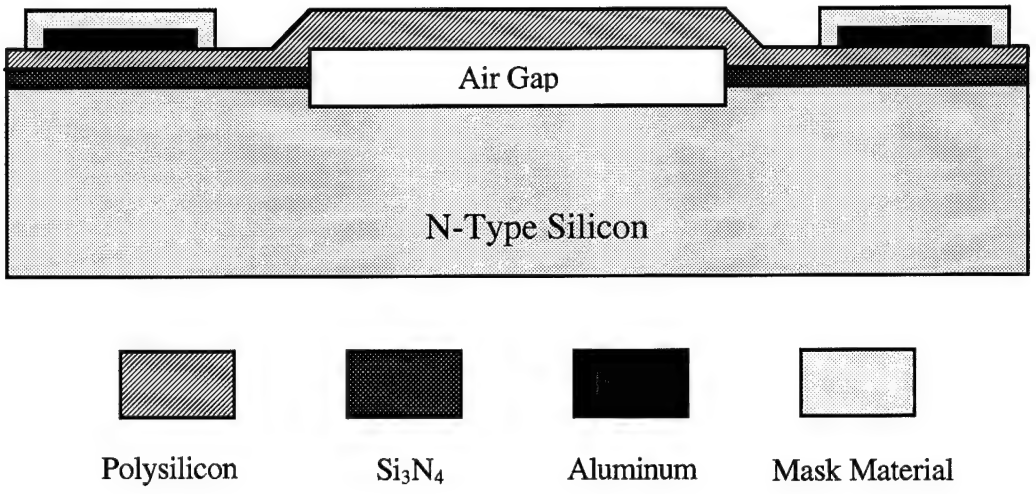

Figure 2.14. Resonating microswitch/voltage-frequency converter [23].

volts to 17.8 volts [23].

2.2.2.3. Electrostatic Comb-Drive Actuators. For applications involving movement in the plane of the substrate, the most common method of electrostatic actuation in MEM systems is the electrostatic comb-drive actuator (Figure 1.1 (c)). These actuators are composed of two arrays of fingers--one which is anchored to the substrate, and one which is suspended above the substrate by a folded suspension truss. The truss mechanism allows the movable array of fingers to move in the plane of the wafer, as shown in Figure 1.1 (c). By applying a potential difference between the two combs, an electrostatic force will cause the movable comb to be displaced toward the stationary comb. These devices have been used for creating very accurate, controlled linear displacements, and for resonators used in accelerometers and various types of sensors.

Laterally driven resonant microstructures have been designed by using two sets of comb-drive actuators in which the movable combs of both actuators share the same folded beam suspension truss (Figure 2.15). In a device developed by Tang, et al, a sacrificial surface micromachining process was used [24]. The process began by creating an n+ diffused surface layer on a silicon substrate. The wafer was then passivated with a 0.15 μm thick layer of LPCVD Si_3N_4 deposited atop a 0.5 μm thick layer of thermally grown SiO_2. Via holes for contact windows to the substrate were created with a combination of plasma and wet etching. Two polysilicon layers were then deposited by LPCVD and lithographically patterned. The first polysilicon layer, which was used as a ground plane, was deposited at 650 °C to a total thickness of 0.3 μm, while the second polysilicon layer, which was used as the structural layer, was deposited at 605 °C to a total thickness of 2.0

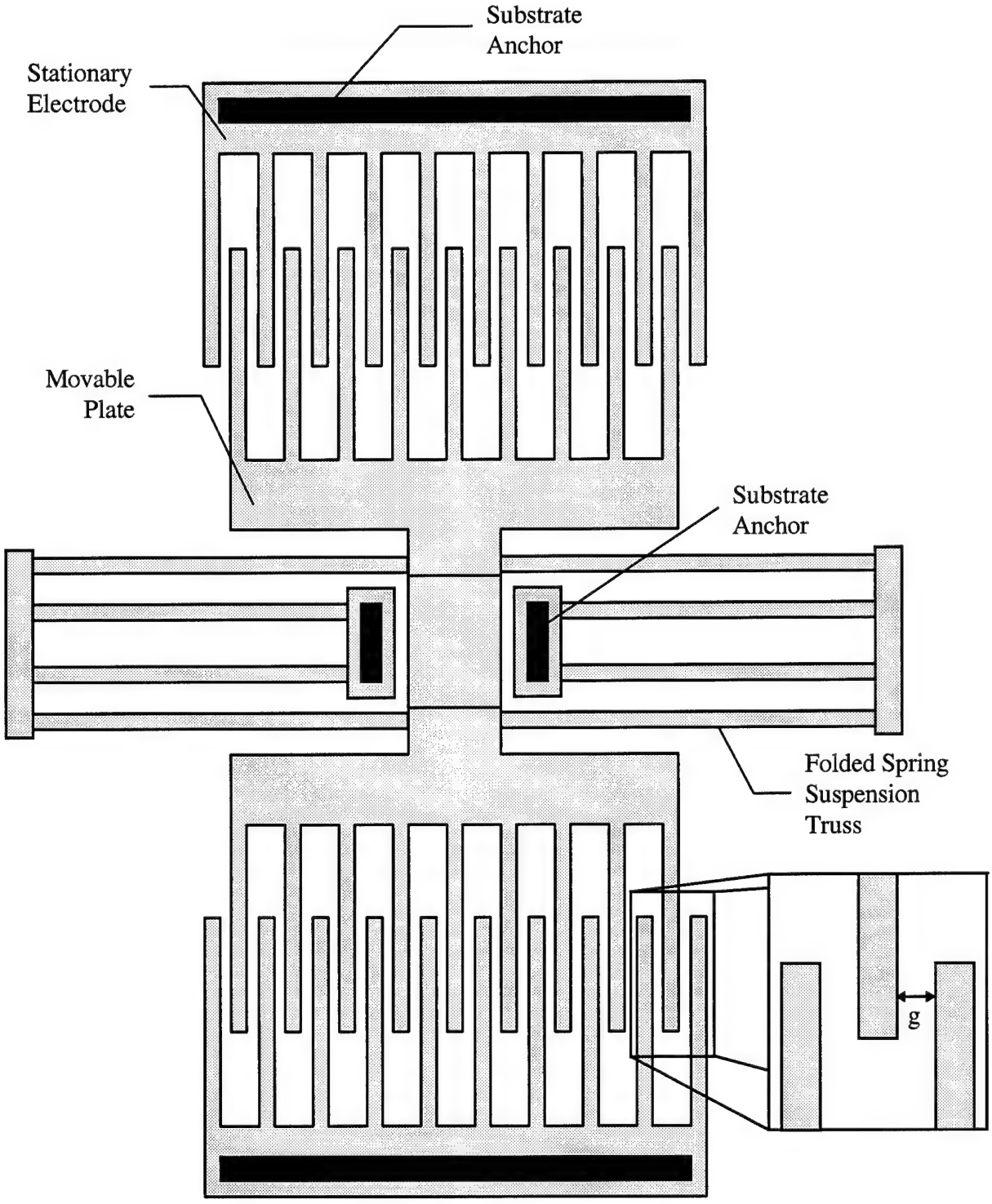

Figure 2.15. Lateral comb-drive resonator [24].

μm. The two polysilicon layers were separated by a 0.3 μm thick PSG layer which, when the polysilicon was annealed at 950 °C for one hour, created a heavy doping in the structural polysilicon. A final stress-relieving anneal step was performed at 1050 °C for 30 minutes in N_2. The release etch was performed using a buffered hydrofluoric solution [24].

The resonators were operated by placing a d.c. bias voltage between one set of combs and then superimposing a driving a.c. voltage. Bias voltages of up to 40 volts were used for large amplitude lateral motion with a.c. drive voltage amplitudes of up to 10 volts. The motion of the structure can be determined by capacitively sensing the movement with the other set of combs. Separate devices using 9 and 11, 50 μm long fingers were investigated with folded suspension beam lengths varying from 80 to 200 μm in length [24] [25].

The authors were able to predict the expected oscillation by using force relations based upon the capacitance of each interdigitated comb. This capacitance, which is formed from the overlap between adjacent comb fingers, is a function of the polysilicon thickness, the gap between fingers, and the amount of overlap. Because the suspension springs only allow motion in the actuation direction, the capacitance changes linearly with the amount of finger overlap. As a result, the attractive force is constant due to the fact that the force is directly proportional to the rate of change of the interdigital capacitance. This constant force makes precise actuation using electrostatic forces much more feasible than parallel plate capacitor arrangements that move in the direction of the capacitive gap. Theoretical results based upon the capacitive force model developed by the authors were

accurate to within 2% of experimental values [24], [25]. Specifics of this theoretical development are given in Chapter 3.

Comb-drive structures used for controlled linear displacement have also been fabricated. In devices developed by Jaecklin, et al, significant displacements with low driving voltages have been achieved (Figure 1.1 (c)) [26], [27]. The devices were fabricated in a three mask surface micromachining process with a feature size of 0.6 μm. First, a silicon substrate was passivated with a double SiO_2/Si_3N_4 layer which was then followed by a lithographically patterned and etched ground plane formed by 0.2 μm thick polysilicon film. Next, a 2 μm thick, phosphorous doped sacrificial CVD SiO_2 layer was deposited and patterned. A second 2 μm thick polysilicon film was then deposited by LPCVD at 600 °C. This was followed by the CVD deposition of a thin PSG layer such that the polysilicon layer was totally surrounded by oxide. The wafer was then thermally annealed at 1050 °C. The suspension beam truss was specifically fabricated with the 0.6 μm minimum dimension in order to reduce the restoring force of the spring (and thus the drive voltage required) [27].

The resulting devices were fabricated with 20 μm long 9 finger combs suspended with suspension beam lengths of 150-300 μm with a gap between opposing fingers (shown as g in Figure 2.15) of 3.4 μm. As in the resonant devices developed by Tang, the comb's motion was predicted using a model based upon the capacitance of the comb structures which is independent of the deflection distance. As expected, the voltage needed to achieve maximum actuation depended upon the flexibility of the spring. In tests performed by the authors at a constant voltage of 10 volts, 0.6 μm deflections were noted

for 150 μm long suspension beams while 3.3 μm deflections were observed for 300 μm long suspension beams. The best performance achieved was a displacement of 7.3 μm which at 14.5 volts with suspension springs 300 μm long. [27]. Such low driving voltages are a direct result of the submicrometer feature size used by the authors.

One of the limitations associated with comb-drive actuators is the critical voltage at which the device sticks. Depending on the design of the device, the fingers of the movable comb can become slightly displaced from the central position between the fingers of the stationary comb at which time the unbalanced capacitive force between the fingers will cause them to stick together (called side-sticking). Additionally, if the device is actuated too far, the electrostatic force between the front ends of the fingers and the base of the opposite comb becomes significant and forces the combs to clamp together (called front-sticking). The side sticking phenomena can be avoided by designing structures with very large spring constants in the non-actuation direction while having a very low spring constant in the actuation direction. The front sticking phenomena can be avoided by designing devices to actuate a distance much less than the space between the ends of the fingers and the base of the opposite combs [27].

Another non-ideal effect noted in the operation of the comb-drive actuators is the levitation phenomena. This effect is caused by the electrostatic repulsion between the movable comb and the ground plane. For the structures created by Jaeklin, et. al, the maximum displacement was approximately 1.2 μm [27]. Although not debilitating to the device operation, higher aspect ratio structures, such as those possible in the LIGA process could possibly avoid this phenomena.

2.2.3. Magnetic and Piezoelectric Actuation. The last methods of micromechanical actuation, magnetic and piezoelectric, are less popular, but have been achieved for very specific applications. The energy densities achievable with magnetic actuation are up to 10^6 J/m^3 which is slightly better than electrostatic actuation [16]. In order to implement magnetic actuation, a magnetic field on the MEM scale must be produced. This can be done by using super small permanent magnets or by developing a MEM sized electromagnet. The former has been performed [28], [29], but the size limitations and fabrication difficulties preclude the use of permanent magnets for most MEM systems. The latter is more feasible, but presents its own array of difficulties. Magnetic actuation involves persistent conduction losses due to the currents required for static excitation as well as hysterisis and eddy current losses at higher actuation speeds [19].

Piezoelectric actuation shares many similarities with electrostatic actuation. For example, the energy densities achievable with piezoelectric actuation are up to 10^5 J/m^3, which is approximately the same as in electrostatic actuation [16]. Piezoelectric actuators operate utilizing the property that when a voltage is applied across a piezoelectric material, a small deformation can be created. Because piezoelectric materials can be deposited and lithographically patterned, it is possible to create small-scale devices if large enough voltages to achieve the desired motion are employed. However, thin film piezoelectric actuation shares many of the disadvantages of magnetic actuation.

For both magnetic and piezoelectric devices, fabrication is due to required special modifications to current IC fabrication processes are required in order to accommodate the necessary magnetic or piezoelectric film materials. Whereas many devices could

conceivably use magnetic or piezoelectric properties to actuate [30], the processing limitations without having a specialized in-house facility are significant enough to discourage wide development. Electrostatic and thermal devices are preferable due to compatibility with commercial microelectronics fabrication processes [31].

2.3. Summary

In this chapter, fabrication techniques including bulk micromachining, surface micromachining, and LIGA processing were discussed and described. Additionally, thermal, electrostatic, magnetic, and piezolectric actuation methodes were discussed, compared, and contrasted. Many examples of actuators present in the current literature were also discussed. Chapter 3 details the theory behind the actuation methods most applicable to this thesis.

3. *Theoretical Review of Micro-Electro-Mechanical Systems*

3.1. Theory of Electrostatic Actuation.

Many of the structures in micro-electro-mechanical devices use electrostatic forces as a means of generating motion. If the nature of the electric fields in a particular device configuration is known, it is possible to determine how the resultant electrostatic forces will affect the system. However, solving Maxwell's equations to determine the necessary electric and magnetic fields associated with a specific geometry can be difficult--especially for the geometries often associated with MEM devices. In order to make the design and modeling of MEM structures less calculation intensive, another technique for determining electrostatic forces is used. This technique involves first calculating the capacitance between the charged conductors of a MEM device and then determining the forces on the structure from the calculated capacitance.

The force-capacitance relation can be derived by considering a simple example of several charged conductors in equilibrium as shown in Figure 3.1. This figure shows three conductive sheets. The two outer, fixed electrodes are each positively charged to a charge Q while the central conductor is oppositely charged to charge 2Q. Because the central electrode is placed exactly between the two fixed electrodes, so no net forces are induced in this arrangement. From this position, it takes an infinitesimal amount of energy, dE, to move the center electrode an infinitesimal distance in the x direction (dx).

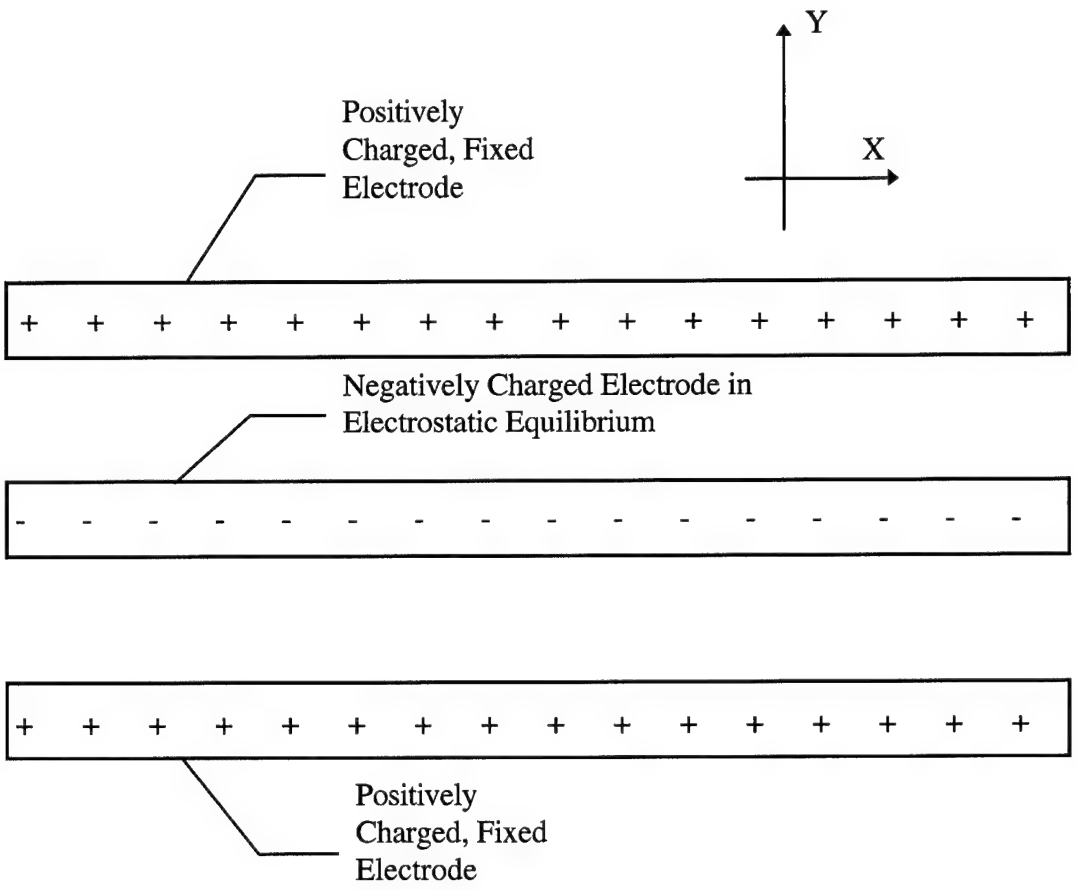

Figure 3.1. Three conductor electrostatic system in equilibrium.

The externally applied force, $\vec{F}_{ext}$, required to move the center conductor is related to dE and dx by the following equation:

$$dE = \vec{F}_{ext} \cdot dx \tag{3.1}$$

If $\vec{F}_{ext}$ is the force required to pull the conductor out of electrostatic equilibrium, the force attempting to draw the conductor back to its original position is equal to $-\vec{F}_{ext}$. This restoring force, denoted by F, can then be related to Eq. (3.1) as follows:

$$\vec{F} = -\frac{dE}{dx} \cdot \hat{x} \tag{3.2}$$

Additionally, the energy stored in any capacitor, E_{cap}, as a function of voltage or total charge, can be found from Eqs. (3.3) and (3.4), respectively:

$$E_{cap} = \frac{1}{2} C \cdot V^2 \tag{3.3}$$

$$E_{cap} = \frac{1}{2} \frac{Q_{tot}^{\ 2}}{C} \tag{3.4}$$

Where:

C = capacitance of the capacitor arrangement (farads);

V = applied potential on the capacitor arrangement (volts);

Q_{tot} = total charge on a conductor that forms the capacitor arrangement (coulombs).

Referring to Figure 3.1, the capacitance between the middle conductor and either of the fixed electrodes is a function of how far the center electrode is displaced (Figure 3.2).

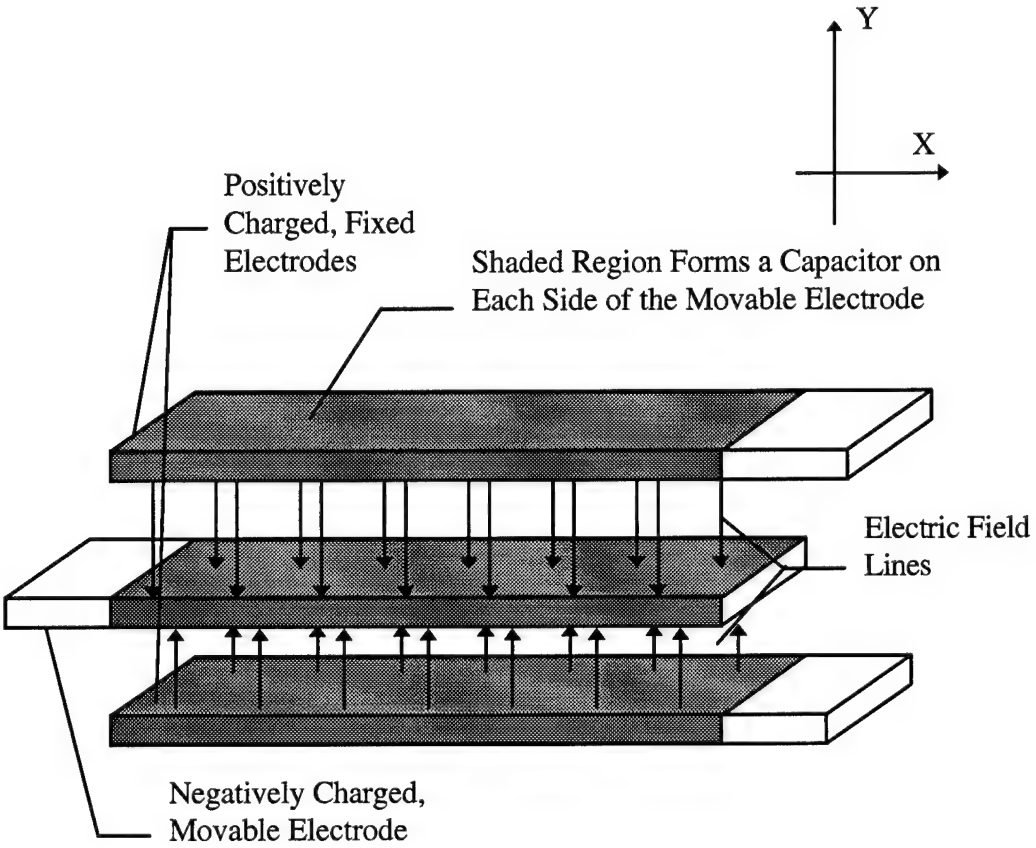

Figure 3.2. Three conductor system with one electrode displaced.

Substituting Eq. (3.3) into Eq. (3.2), gives a relationship between the capacitance and the magnitude of the restoring force.

$$\vec{F} = \frac{1}{2} V^2 \frac{dC}{dx} \cdot \hat{x} \tag{3.5}$$

where C is the total capacitance of the electrostatic arrangement. Although, Eq. (3.5) was derived based upon a simple one-dimensional model for ease of understanding, it is possible to derive a three-dimensional version of Eq. (3.5) using the same principles. The resulting formula, given by Eq. (3.6), is valid for all three dimensional electrostatic configurations [32].

$$\vec{F} = \frac{1}{2} V^2 \cdot \vec{\nabla} C \tag{3.6}$$

Once the capacitance for a given geometry is known, the electrostatic forces acting on the structures can be found using Eq. (3.6). Although calculating the capacitance can be difficult in some instances, it is usually less difficult than calculating electrostatic forces directly from Maxwell's equations.

3.2. Modeling of Electrostatic Cantilevers and Microbridges

Micromechanical electrostatic cantilevers and microbridges can be effectively modeled by combining beam theory and the force-capacitance relationship derived in Section 3.1. The basic geometry of the electrostatic cantilever is shown in Figures 1.1 (a) and 2.12, while the basic geometry of the electrostatic microbridge is shown in Figures 1.1 (b), 2.13, and 2.14. The diagrams used for the derivation of force relations and

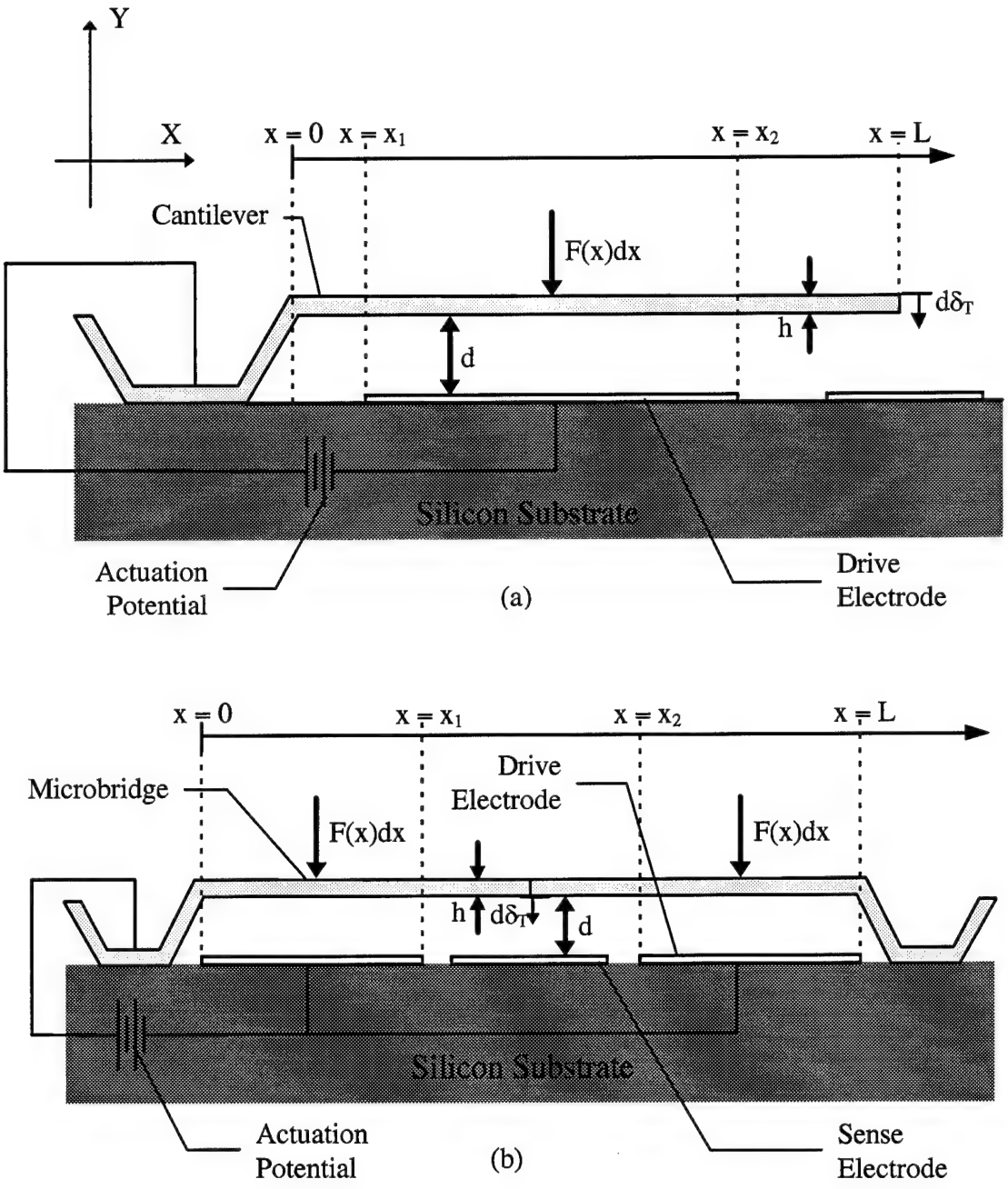

Figure 3.3. Geometry for modeling the behavior of the cantilever and microbridge: (a) electrostatic cantilever, (b) electrostatic microbridge. δ_T denotes the deflection at x = L for the cantilever and at x = L/2 for the microbridge, and F(x) denotes the capacitive force per unit area at any position, x, along the length of the beam.

modeling equations are given in Figure 3.3.

From beam theory, the differential deflection at the tip of a cantilever, $d\delta_T$, due to a distributed force along the length of the cantilever (x direction) can be found with the following equation:

$$d\delta_T = \frac{x^2}{6 \cdot E \cdot I} \cdot (3 \cdot L - x) \cdot b \cdot F(x) \cdot dx \tag{3.7}$$

$$I = \frac{1}{12} \cdot b \cdot h^3 \tag{3.8}$$

where:

F(x) = force per unit area acting on the cantilever at a point, x. Note: x in Eq. (3.7) is only the location of F(x), *not* the deflection of the beam at a point x (Newtons/meter^2);

L = length of the cantilever (meters);

b = width of the cantilever (into the page on Figure 3.3 (a)) (meters);

h = thickness of the cantilever (meters).

E = Young's modulus (pascals);

In order to predict the deflection of the cantilever using Eqs. (3.7) and (3.8), it is necessary to derive the force acting on the cantilever beam. This is done by calculating the capacitance between the drive electrode and the cantilever beam and then using Eq. (3.6) to determine the capacitive force. In this case, the area between the cantilever and the drive electrode forms a parallel plate capacitor. Thus, the capacitance per unit area, C, between the cantilever beam and the drive electrode can be determined from physical constants and the dimensions shown in Figure 3.3 (a).

$$C = \begin{Bmatrix} 0 & 0 < x < x_1 \\ \dfrac{\varepsilon \cdot \varepsilon_o}{d} & x_1 < x < x_2 \\ 0 & x_2 < x < L \end{Bmatrix} \tag{3.9}$$

where: x_1, x_2 = dimensions corresponding to the drive electrode (see Figure 3.3 (a)) (meters);

d = capacitive gap between the drive electrode and cantilever beam (meters);

ε = dielectric constant;

ε_o = permitivity of free space (farads/meter).

A problem with Eq. (3.9) is that it is only correct for situations in which the capacitance between the cantilever and the drive electrode forms a parallel plate capacitor. This assumption is not correct for situations in which the cantilever is deflected. As the cantilever is deflected, the beam becomes curved and the two "plates" of the capacitor formed between the cantilever and the drive electrode are no longer flat, parallel conductors. However, this inaccuracy can be corrected by assuming the deflection of the upper capacitor electrode (the cantilever beam) approximately follows a square-law relationship to the deflection at the cantilever tip. Eq. (3.10) shows the square-law relationship, $\Delta(x)$, of the beam curvature at any point, x, along the length of the cantilever.

$$\Delta(x) \cong \left(\frac{x}{L}\right)^2 \cdot \delta_T \tag{3.10}$$

where: δ_T = deflection of the cantilever at the cantilever tip (x = L) (meters);

L = length of the cantilever (meters).

Eq. (3.10) can now be used as a correction term in Eq. (3.9) to account for the curvature of the cantilever. The capacitance per unit area between the cantilever beam and the drive electrodes then becomes [20]:

$$C = \begin{Bmatrix} 0 & 0 < x < x_1 \\ \dfrac{\varepsilon \cdot \varepsilon_o}{d - \Delta(x)} & x_1 < x < x_2 \\ 0 & x_2 < x < L \end{Bmatrix} \tag{3.11}$$

With the capacitance of the device properly modeled, it is possible to calculate the electrostatic force per unit area, F(x), on the cantilever. This is done by substituting Eq. (3.11) into the capacitive force relation given in Eq. (3.6).

$$F(x) = \begin{Bmatrix} 0 & 0 < x < x_1 \\ \dfrac{\varepsilon \cdot \varepsilon_o}{2} \cdot \left(\dfrac{V}{(d - \Delta(x))} \right)^2 & x_1 < x < x_2 \\ 0 & x_2 < x < L \end{Bmatrix} \tag{3.12}$$

where V is the voltage applied between the cantilever and the drive electrode. Eq. (3.12) shows that as x is increased from $x = x_1$ to $x = x_2$, F(x) is increased due to the smaller capacitive gap. As expected, there is no contribution to F(x) outside the drive electrode area ($0 < x < x_1$ and $x_2 < x < L$).

Once the force per unit area has been defined, the total deflection at the tip of the cantilever, δ_T, can be calculated. This is performed by integrating both sides of Eq. (3.7) from x = 0 to x = L. However, because F(x) = 0 for $0 < x < x_1$ and $x_2 < x < L$, the limits of integration are simply x_1 and x_2.

$$\delta_T = \int_{x_1}^{x_2} \frac{x^2}{6 \cdot E \cdot I} (3 \cdot L - x) \cdot b \cdot F(x) \cdot dx \tag{3.13}$$

where δ_T is the total deflection at x = L. Solving Eq. (3.13) is difficult because the variable on the left side of the equation, δ_T, is also on the right side of the equation. δ_T is a parameter in $\Delta(x)$ which is used to calculate F(x). This type of transcendental equation, an equation that is a function of itself, cannot usually be solved analytically. The best method to solve this equation is to use a computer driven numerical iteration technique.

Electrostatic microbridge actuators are modeled in a manner similar to the electrostatic cantilevers. The primary differences are that the differential deflection equation is different and that there are two drive electrodes. With the dimensions shown in Figure 3.3. (b), the differential deflection at the center of a microbridge due to a distributed force along the microbridge length (x direction) is given by Eq. (3.14).

$$d\delta_T = \begin{cases} \frac{2}{3 \cdot E \cdot I} \cdot \left[\frac{x^2 \cdot (L-x)^3}{(3 \cdot L - 2 \cdot x)^3} \right] \cdot b \cdot F(x) \cdot dx & 0 < x < \frac{L}{2} \\ \frac{2}{3 \cdot E \cdot I} \cdot \left[\frac{x^3 \cdot (L-x)^2}{(2 \cdot x + L)^3} \right] \cdot b \cdot F(x) \cdot dx & \frac{L}{2} < x < L \end{cases} \tag{3.14}$$

$$I = \frac{1}{12} \cdot b \cdot h^3 \tag{3.15}$$

where:

F(x) = force per unit area acting on the microbridge at a point, x. Note: x in Eq. (3.14) is only the location of F(x), *not* the deflection of the beam at a point x (Newtons/meter^2);

L = length of the microbridge (meters);

b = width of the microbridge (into the page of Figure 3.3 (b)) (meters);

E = Young's modulus (pascals);

h = thickness of the microbridge (meters);

In order to predict the deflection of the microbridge using Eqs. (3.14) and (3.15), it is necessary to derive the force acting on the microbridge. Like the electrostatic cantilever, this is done by finding the capacitance between the drive electrodes and the microbridge and then using Eq. (3.6) to calculate the capacitive force. As before, the capacitance per unit area, C, between the microbridge and both the lower drive electrodes can be determined using a parallel plate capacitor model.

$$C = \begin{Bmatrix} \frac{\varepsilon \cdot \varepsilon_o}{d} & 0 < x < x_1 \\ 0 & x_1 < x < x_2 \\ \frac{\varepsilon \cdot \varepsilon_o}{d} & x_2 < x < L \end{Bmatrix} \tag{3.16}$$

where: x_1, x_2 = dimensions corresponding to the drive electrodes (see Figure 3.3 (b)) (meters);

d = capacitive gap between the drive electrodes and the microbridge (meters).

However, Eq. (3.16) is only correct for situations in which the capacitance between the microbridge and the drive electrodes form a parallel plate capacitor. As the microbridge is deflected, the beam becomes curved and the two "plates" of the capacitor formed between the microbridge and the drive electrodes are no longer parallel. As was done for the cantilever, this inaccuracy is corrected by assuming the deflection of the upper capacitor electrode, (the microbridge) approximately follows a square-law relationship to the

deflection at the center of the microbridge. Eq. (3.17) shows the square-law relationship, $\Delta(x)$, of the beam curvature at any point, x, along the length of the microbridge.

$$\Delta(x)=\begin{Bmatrix} \left(\frac{x}{L/2}\right)^2 \cdot \delta_T & 0<x<L/2 \\ \left(\frac{L-x}{L/2}\right)^2 \cdot \delta_T & L/2<x<L \end{Bmatrix} \tag{3.17}$$

where δ_T is the deflection at x = L/2 (center of the microbridge). This square-law relation can now be used to correct Eq. (3.16) for the deflected microbridge like Eq. (3.10) was used to correct Eq. (3.9).

$$C=\begin{Bmatrix} \frac{\varepsilon \cdot \varepsilon_o}{d-\Delta(x)} & 0<x<x_1 \\ 0 & x_1<x<x_2 \\ \frac{\varepsilon \cdot \varepsilon_o}{d-\Delta(x)} & x_2<x<L \end{Bmatrix} \tag{3.18}$$

Now that the capacitance for the microbridge has been properly modeled, the force per unit area, F(x), can be derived. This is done by substituting Eq. (3.18) into Eq. (3.6) [20].

$$F(x)=\begin{Bmatrix} \frac{\varepsilon \cdot \varepsilon_o}{2}\left(\frac{V}{d-\Delta(x)}\right)^2 & 0<x<x_1 \\ 0 & x_1<x<x_2 \\ \frac{\varepsilon \cdot \varepsilon_o}{2}\left(\frac{V}{d-\Delta(x)}\right)^2 & x_2<x<L \end{Bmatrix} \tag{3.19}$$

where V is the voltage applied between the microbridge and the drive electrodes. As expected, the force per unit area increases the closer x is to the center of the electrode for $0 < x < x_1$ and $x_2 < x < L$, while the force is 0 for $x_1 < x < x_2$.

Now that the force per unit area is known, the total deflection at the center of the microbridge, δ_T, can be calculated. This is performed by integrating Eq. (3.14) from x = 0 to x = L.

$$\delta_T = \int_0^{x_1} \frac{2}{3 \cdot E \cdot I} \cdot \left[\frac{x^2 \cdot (L-x)^3}{(3 \cdot L - 2 \cdot x)^3} \right] \cdot b \cdot F(x) \cdot dx \tag{3.20}$$

$$+ \int_{x_2}^{L} \frac{2}{3 \cdot E \cdot I} \cdot \left[\frac{x^3 \cdot (L-x)^2}{(2 \cdot x - L)^3} \right] \cdot b \cdot F(x) \cdot dx$$

where δ_T is the total microbridge deflection at x = L/2. Again, like the cantilever, the final deflection equation (Eq. (3.20)) is a transcendental equation. The maximum deflection, δ_T, is on the left side of the equation and on the right side (buried within F(x)). As a result, a numerical iteration technique is required to calculated the deflection at the center of the microbridge.

For both the cantilever and the microbridge, the deflection force is inversely proportional to the square of the capacitor gap formed between the beam and the drive electrodes. As a result, the capacitive force pulling the cantilever and microbridge increases rapidly as the beams deflect. At some critical deflection, the force is great enough to force the beam electrode to instantly deflect the remaining distance to the sense electrode. This critical distance is at 1/3 of the actuation distance between the open and closed positions [35]. For all intents and purposes, the voltage at which a deflection of 1/3 the capacitive gap is achieved is the closing voltage. Other electrostatic devices, such as the comb-drive actuators described in the next section, do not suffer as greatly from this problem.

3.3. Modeling of Electrostatic Comb-Drive Actuators

The force-capacitance relation defined in Section 3.1 can also be used to model the electrostatic forces created in the electrostatic comb-drive actuator. Figures 1.1 (c) and 2.15 show the basic designs of the comb-drive actuators. The capacitance relationship of interest in this actuator is the capacitance between the interdigitated fingers of the movable and stationary combs. A schematic of the interdigitated finger arrangement is shown in Figure 3.4.

Based upon the dimensions shown in this figure, the capacitance, C, between two adjacent interdigitated fingers is given by the following equation:

$$C = \varepsilon \varepsilon_o \frac{h \cdot L}{g} \tag{3.21}$$

where L = amount of finger overlap (meters);

h = height of the fingers (meters);

g = gap between adjacent fingers (meters).

The distance between the end of the movable comb finger and the stationary comb base, d, as shown in Figure 3.4, is assumed to be very large compared to g. Thus, the only significant capacitance in the comb is that given by Eq. (3.21). The force due to the

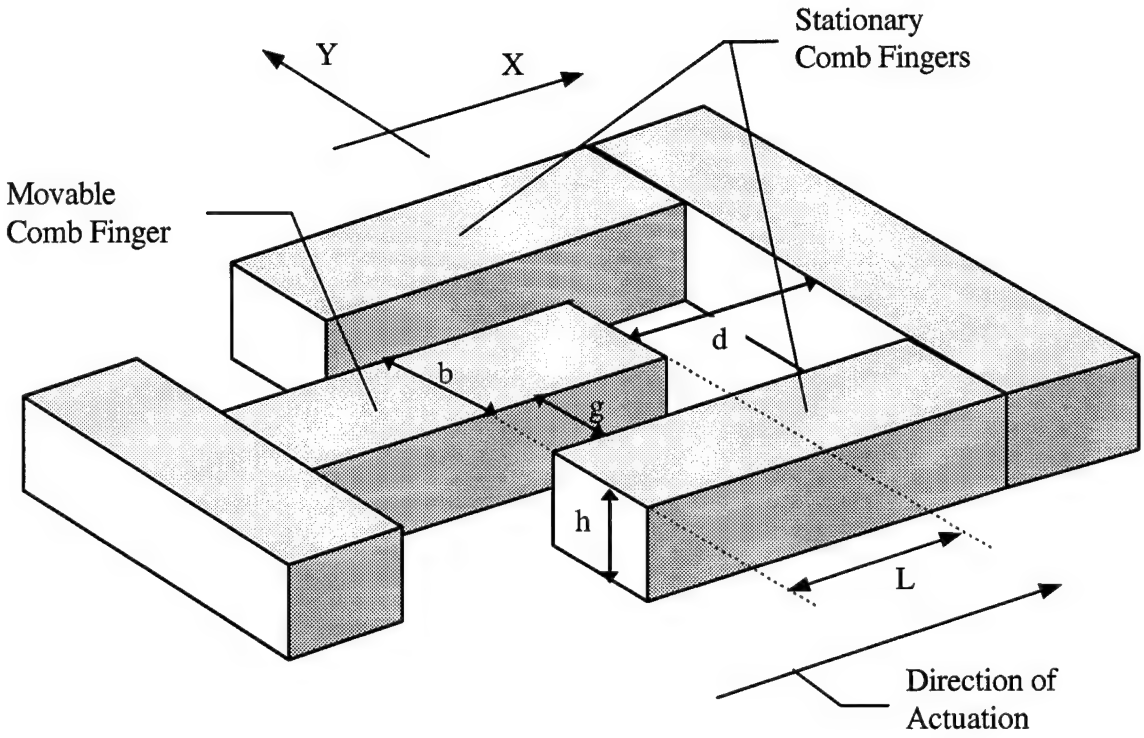

Figure 3.4. Geometry of the rectangular interdigital finger arrangement [26].

capacitance between each pair of adjacent oppositely charged fingers can be found by substituting Eq. (3.21) into Eq. (3.6).

$$\vec{F} = \frac{1}{2}\varepsilon\varepsilon_o V^2 \frac{h}{g} \cdot \hat{x} \tag{3.22}$$

where V is the voltage applied between the stationary and movable comb fingers. In this case, the capacitance changes directly with the amount of overlap as the movable finger moves in the direction of actuation. When Eq. (3.21) was substituted into Eq. (3.6), the amount of finger overlap, L, was differentiated out. As a result, the attractive force is independent of the amount of deflection (i.e. there is no x dependence in Eq. (3.21)). In contrast, the attractive force in the electrostatic cantilever and microbridge increased quadratically with deflection distance (see Eqs. (3.12) and (3.19)). As a result, the comb-drive actuator can be much more predictably deflected a specific distance as long as d, shown in Figure 3.4, remains much larger than g. Thus, the comb-drive actuator is advantageous for applications in which controlled actuation in precision MEM devices is required [26], [27], [36].

The force derived in Eq. (3.22) is due to the capacitance formed from one side of the movable comb finger depicted in Figure 3.4. However, there is an identical capacitance formed on the opposite side of the movable comb finger. Therefore, the total force between the movable comb finger and the two surrounding stationary comb fingers is double the force shown in Eq. (3.22). When many fingers are present in a comb-drive actuator, the total attractive force is given by:

$$\vec{F}_{total} = \varepsilon \cdot \varepsilon_o \frac{n}{2} \cdot \frac{V^2 \cdot h}{g} \cdot \hat{x} \tag{3.23}$$

where n is the total number of capacitive gaps in the entire comb. For example, n = 2 in Figure 3.4. and n = 18 for each comb in Figure 2.15.

The total force generated by a comb-drive actuator (for a given voltage) can be increased by adding more fingers to each comb. Additionally, because the comb height is directly proportional to the force (see Eq. (3.23)), it is also possible to increase the force by increasing the structural layer thickness (i.e. increasing *h*). Similarly, the force can be increased by reducing the capacitive gap, g, between the fingers of the movable and stationary combs. However, both options require changes in the fabrication process (to either thicken a layer or decrease the minimum feature size) which may not be possible.

A better option for improving the force generated by a comb-drive actuator is to use trapezoidally shaped fingers on each comb. By using this finger geometry, it is possible to improve the actuator performance without modifying the fabrication process. The basic design of a trapezoidal finger arrangement is shown in Figure 3.5. Initially, the gap between the fingers is designed to be the minimum feature size (the gap at this point is denoted as g_{open} in Figure 3.6) for the fabrication process. As the fingers are drawn together, the capacitor gap between the movable and stationary fingers is decreased. In this way, the gap between the fingers can be reduced below the minimum feature size of the fabrication process. The gap between the trapezoidal shaped fingers, g(x), can be linearly related to the actuation distance, x, by the following equation [36].

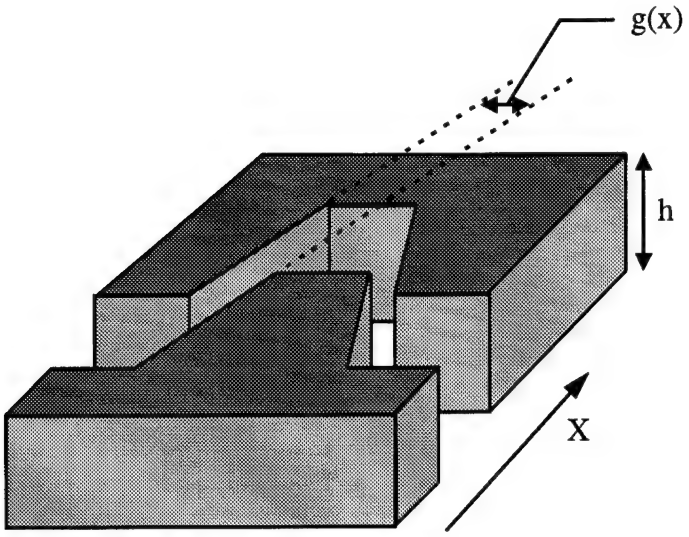

Figure 3.5. Geometry of a trapezoidal-shaped finger and comb [36].

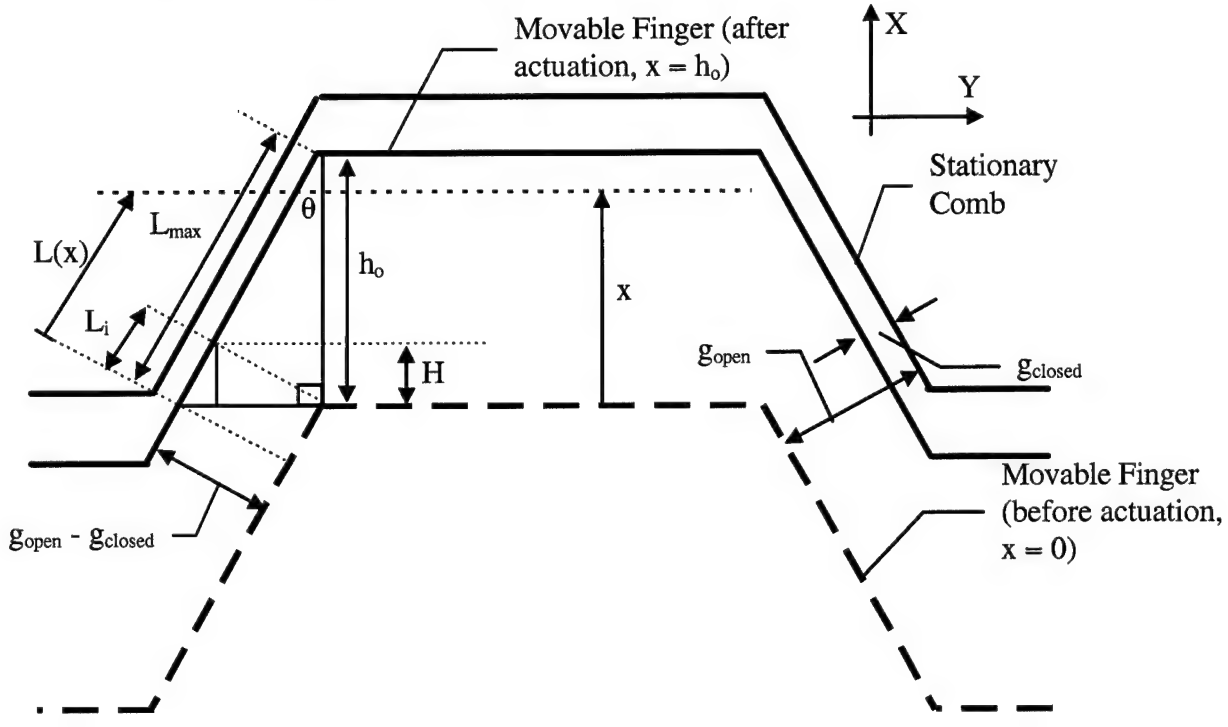

Figure 3.6. Top-view schematic of the trapezoidal finger arrangement.

$$g(x) = \frac{g_{closed} - g_{open}}{h_o} x + g_{open} \tag{3.24}$$

where: g_{closed} = capacitor gap after full actuation ($x = h_o$) (meters);

g_{open} = capacitor gap in the full-open position ($x = 0$) (meters);

h_o = maximum desired displacement in the x direction (meters).

Figure 3.6 shows a top-view schematic of a trapezoidal shaped finger arrangement depicting the movable finger in both the fully closed (solid line) and the fully open positions (dashed line). L(x) is the amount of overlap between the movable and stationary fingers at a specific actuation distance, x. As shown, $L(x = 0) = L_i$, and $L(x = ho) = L_{max}$ where H is the vertical component of the initial overlap, L_i, and h_o is the vertical component of the final overlap, L_{max} (h_o is also the maximum desired displacement in the x direction). The angle, θ, dictates the steepness of the sides of the trapezoidal fingers.

Based upon the dimensions shown in Figure 3.6, the initial amount of overlap is given by:

$$L_i = \frac{H}{\cos(\theta)} \tag{3.25}$$

In a similar manner, the amount of overlap, L(x), as a function of displacement, x, can be found:

$$L(x) = \frac{H + x}{\cos(\theta)} \tag{3.26}$$

Now, the capacitance, as a function of x, can be calculated for one side of the movable finger by substituting L(x) and g(x) into Eq. (3.21) (where L(x) is the same as L and g(x) is the same as g in Eq. (3.21) and Figure 3.4) [36].

$$C(x) = \varepsilon \cdot \varepsilon_o \frac{h \cdot \frac{(H+x)}{\cos(\theta)}}{\left(\frac{(g_{closed} - g_{open})}{h_o} \cdot x - g_{open} \right)} \tag{3.27}$$

Once the capacitance has been found, the attractive force generated by one side of the movable, trapezoidal shaped finger can be determined by substituting Eq. (3.27) into Eq. (3.6) [36].

$$\vec{F} = \frac{1}{2} \varepsilon \varepsilon_o V^2 \cdot h \frac{g_{open} - H \sin(\theta)}{\left(g_{open} - x \cdot \sin(\theta)\right)^2 \cdot \cos(\theta)} \cdot \hat{x} \tag{3.28}$$

where:

$$\sin(\theta) = \frac{g_{open} - g_{closed}}{h_o} \tag{3.29}$$

Unlike the rectangular finger comb-drive actuators, the force is not independent of the actuation distance. Thus, these designs may suffer from the same instability problems as the electrostatic cantilever and microbridge actuators. However, by comparing forces generated from the rectangular and trapezoidal fingers, a significant amount of improvement due to the finger shape is evident. For the same initial overlap, gap between fingers, and restoring forces (such as those supplied by suspension springs), combs with trapezoidal fingers can produce the same actuation distances at a voltages 2.34 times lower than for combs with rectangular fingers. Conversely, combs with trapezoidal

fingers can actuate 5.48 times the distance for the same actuation potential than for combs with rectangular fingers. Thus, it is evident that the trapezoidal finger geometry shows promise for better comb-drive actuator performance.

Once the driving elements of a comb-drive actuator have been designed, it is necessary to interconnect them using a suspension spring truss. These trusses are designed to allow the movable comb to move freely in the actuation direction with very little movement in the non-actuation direction. A diagram of an example suspension truss, also called a folded beam, is shown in Figure 3.7.

The folded beam suspension provides a restoring force that is designed to pull the movable comb back into its initial position after each actuation. The springs can be modeled with a simple, first order, Hooke's law relationship.

$$F_{spring} = -k_{spring} \cdot x \tag{3.30}$$

where k_{spring} is the spring constant in the actuation direction. However, based upon the specific geometry for a given suspension spring, it is possible to analytically determine the spring constant. The restoring beams, which are perpendicular to the direction of actuation, provide resistance to motion in the actuation direction while the cross beams, which are parallel to the direction of actuation, do not affect the spring constant (Figure 3.7 points out the restoring beams and the cross beams). In the example truss of Figure 3.7, the spring constant can be determined by applying a force, $F_{applied}$, to the suspension

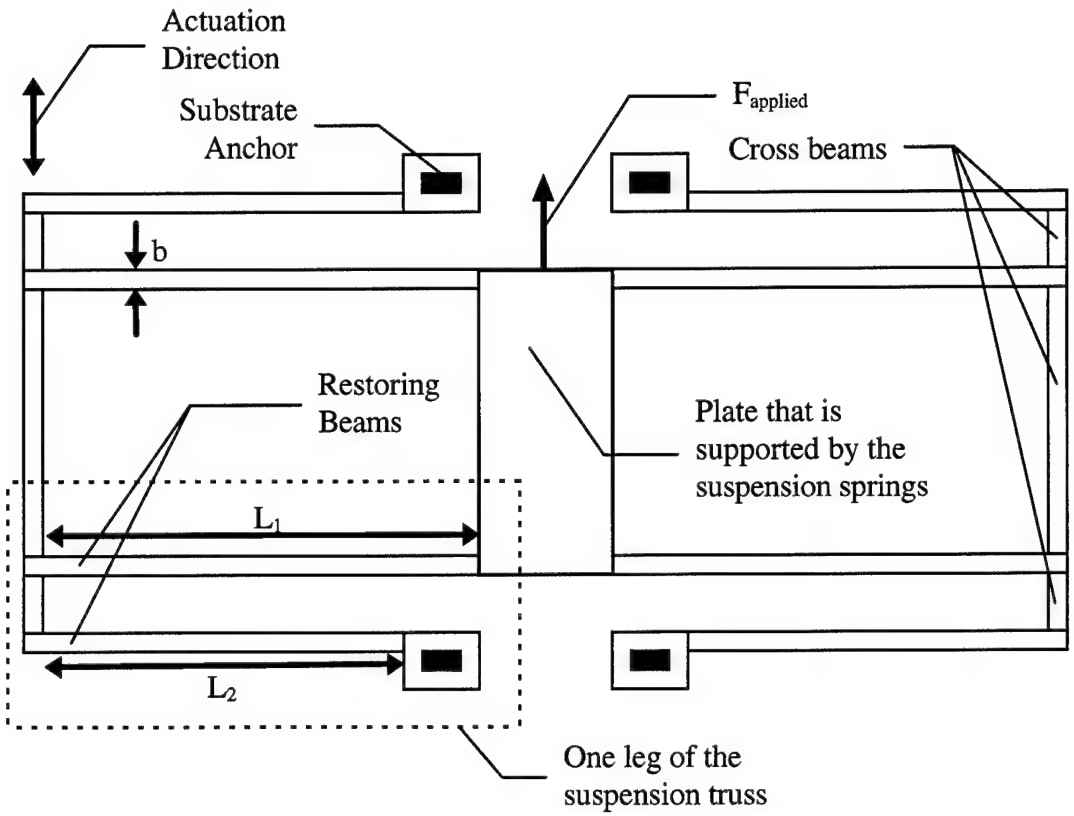

Figure 3.7. Folded beam suspension truss [27].

truss. The deflection of the L_1 long restoring beams, Eq. (3.31), and the L_2 long restoring beams, Eq. (3.32), can be found from beam theory [27].

$$x = \frac{L_1^{\,3} \cdot F_{applied}}{12 \cdot E \cdot I} \tag{3.31}$$

$$x = \frac{L_2^{\,3} \cdot F_{applied}}{12 \cdot E \cdot I} \tag{3.32}$$

$$I = \frac{1}{12} \cdot h \cdot b^3 \tag{3.33}$$

where: $F_{applied}$ = force applied to the suspension truss (see Figure 3.7) (newtons);

E = Young's modulus (pascals);

b = width of each beam (see Figure 3.7) (newtons);

h = height of each beam (out of the page in Figure 3.7) (meters).

The deflection of one leg of the suspension spring truss can be determined by summing the deflections of each of the restoring beams in that leg (One leg is boxed in Figure 3.7).

$$x = \frac{F_{applied}}{12 \cdot E \cdot I} \cdot \left[L_1^{\,3} + L_2^{\,3} \right] \tag{3.34}$$

Now, by solving the Hooke's law relationship of Eq. (3.30) for F_{spring} and substituting the result into Eq. (3.34), the spring constant for one leg of the suspension truss, k_{leg}, can be calculated.

$$k_{leg} = \frac{12 \cdot E \cdot I}{L_1^{\,3} + L_2^{\,3}} \tag{3.35}$$

There are a total of four legs on the suspension truss of Figure 3.7, so the total spring constant, k_{spring} is given by [27]:

$$k_{spring} = \frac{48 \cdot E \cdot I}{L_1^{\,3} + L_2^{\,3}} \tag{3.36}$$

Once the spring constant is known, the design of a MEM comb-drive actuator can be performed by setting the restoring force of the folded beam suspension spring (Eq. (3.30)) equal to the force generated by the comb-drive actuator. The actuation distance can then be solved for as a function of the spring constant, k_{spring}, and the force generated by the comb-drive actuator, F_{comb}.

$$x = \frac{F_{comb}}{k_{spring}} \tag{3.37}$$

Using a rectangular comb-drive actuator as described by Eq. (3.23) and the suspension truss of Figure 3.7, Eq. (3.37) becomes:

$$x = \frac{n \cdot \varepsilon \cdot \varepsilon_o \cdot h \cdot \left(L_1^{\,3} + L_2^{\,3}\right)}{96 \cdot g \cdot E \cdot I} \cdot V^2 \tag{3.38}$$

where: n = number of capacitive gaps in the comb-drive actuator (see discussion on Eq. (3.23) for a complete description);

h = height of the comb-drive structural layer (meters);

g = gap between fingers (meters);

V = voltage applied across the comb-drive actuator (volts).

Thus, it is possible to predict the deflection of a comb-drive actuator for a specific applied voltage.

Once a comb-drive actuator has been designed according to the equations in this section, it is important to take into account other factors that may limit performance. The most common limiting factors include front and side sticking--either of which can limit the maximum deflection of the actuator. Front sticking occurs if a comb-drive actuator is deflected far enough such that capacitive force between the tips of the fingers of the movable comb and the base of the stationary comb becomes significant. At this point, the additional capacitive force, F_{front}, acting in the direction of actuation, can cause the combs the tips of the fingers on the movable comb to stick to the base of the fixed comb. Assuming a rectangular finger comb-drive actuator and the dimensions of Figure 3.4, F_{front} is of the form [26]:

$$F_{front} = \frac{n\varepsilon\varepsilon_o}{2} \cdot \frac{h \cdot b \cdot V^2}{(d-x)^2} \tag{3.39}$$

where: x = actuation distance (meters);

n = total number of capacitive gaps in the comb;

b = width of each individual finger (see Figure 3.4) (meters);

d = initial distance between the finger tips of the movable comb to the base of the opposing comb when no potential is applied (see Figure 3.4) (meters);

h = height of the fingers in the comb-drive actuator (meters).

From Newton's second law, every force must be balanced with an equal and opposite force. Thus, all forces in the actuation direction, F_{comb} and F_{front}, must be exactly balanced by the restoring force of the suspension springs. Thus, the balance of pulling and restoring forces is given in Eq. (3.40) with F_{front} taken into account.

$$F_{spring} = F_{comb} + F_{front} \tag{3.40}$$

where: F_{spring} = restoring force of a suspension spring supporting the movable comb (newtons);

F_{comb} = pulling force of the comb-drive actuator (newtons).

The maximum actuation distance (x value) for which a stable equilibrium position can be maintained before front sticking occurs is found by substituting Eqs. (3.39) and (3.40) into with the following equation and solving for x [26]:

$$\frac{\partial F_{spring}}{\partial x} \geq \frac{\partial F_{front}}{\partial x} \tag{3.31}$$

Side sticking is another phenomena that occurs when a movable finger is moved slightly off center between two fixed electrodes. This causes an imbalance of the forces in the non-actuation direction, causing the sides of the fingers to stick together. Assuming a rectangular comb-drive actuator and the dimensions of Figure 3.4, a small displacement in the non-actuation direction results in a net force, F_{side}, in the y direction [26].

$$F_{side} = n\varepsilon\,\varepsilon_o \cdot \frac{h \cdot L \cdot V^2}{2}\left[\frac{1}{(g-y)^2} - \frac{1}{(g+y)^2}\right] \tag{3.41}$$

where: n = number of capacitor arrangements in the comb;

ε_o = permitivity of free space (farads/meter);

ε = dielectric constant;

h = height of the interdigitated fingers (meters);

L = length of overlap between the fingers (meters);

V = applied voltage (volts);

g = gap between the fingers of the movable and stationary combs (meters);

y = offset displacement in the non-actuation direction that can force side sticking (meters).

Based upon Eq. (3.41), there is some voltage at which the offset in the y direction will cause a large enough force to cause side sticking to occur. This voltage depends on magnitude of the spring constant of suspension springs in the non-actuation direction. The smaller the spring constant in the non-actuation direction, the lower the voltage at which side-sticking will occur. For a given voltage, the spring constant in the non-actuation direction at which side sticking occurs can be determined from Eq. (3.41) [26].

$$k_{critical} = \frac{\partial F_{side}}{\partial y}\Big|_{y=0} = \frac{2 \cdot n\varepsilon \varepsilon_o h \cdot L \cdot V^2}{g^3} \tag{3.42}$$

Thus, if it is determined that a specific voltage is needed to deflect the necessary distance, the spring constant in the non-actuation direction must be larger than that given by Eq. (3.42) to avoid side-sticking.

By using the modeling equations given in this section, it is possible to design comb-drive actuators to meet MEM specifications. Additional analysis using Eqs. (3.39) through (3.42) can also help designs overcome side and front sticking problems.

However, for these calculations to be accurate enough for comb-drive actuator design, accurate values for structural and process parameters are needed. Values such as Young's modulus vary greatly with a variety of processing factors including doping concentration, annealing temperature, and residual stress. This uncertainty requires that very controlled fabrication processes be used for consistent design results. Even under such conditions, the design of workable comb-drive actuators can still be a difficult task.

3.4. Modeling of the Thermally Activated Beam Flexure (Heat-Drive Actuator).

Thermally activated beam flexure devices, or heat-drive actuators, operate using differential heating of a loop of structural material. The basic schematic and geometry for the heat-drive actuator is shown in Figure 2.11 and repeated in Figure 3.8.

By running a constant current through the device, it is possible to heat sections A and B higher than section C. If ΔT is the temperature difference between sections B and C, the tip deflection, Δx, can be modeled with the following equation [18]:

$$\Delta x = \frac{\alpha\ \Delta T \cdot L^2}{g\left(0.7707 + 0.3812\frac{t^2}{g^2}\right)} \tag{3.43}$$

where:

α = thermal coefficient of expansion ($^{\circ}C^{-1}$);

g = center to center distance between sections A and C (meters);

L = length of sections B or C (meters);

t = thickness of sections A or B (meters).

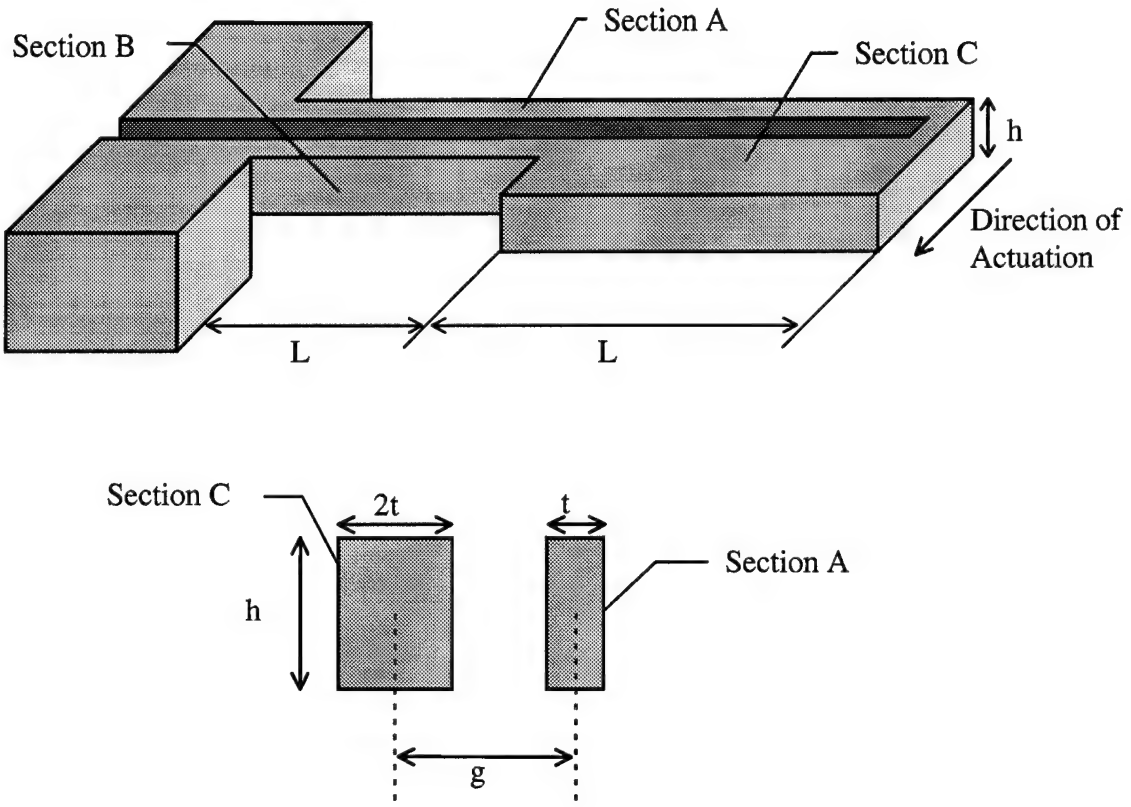

Figure 3.8. Horizontal heat-drive actuator: (a) 3-D view, (b) cross-sectional view and dimensions [18].

(Note: the deflection at the tip of the heat-drive actuator is independent of the structural layer height and Young's modulus). In order for Eq. (3.43) to be useful for designing heat-drive actuators for operation at a specific current, it is necessary to determine the relationship between ΔT and the applied current, I.

One major effect that must be modeled in order to determine ΔT as a function of I is the radiation of heat from a conductor into the atmosphere. This can be modeled by assuming the geometry of Figure 3.9 for a single conductive element that is heated by an applied current, I. For any conductor, the following relationship is true:

$$P_{DISS} = \frac{T - T_o}{\theta_{junct}} = I^2 \cdot R(T) \tag{3.44}$$

where: P_{DISS} = power dissipated in the conductor (watts);

T = temperature of the conductor (°C);

T_o = ambient atmosphere temperature (°C);

θ_{junct} = thermal resistance between the conductor and the ambient atmosphere (°C-W^{-1}).

I = applied current (amps);

$R(T)$ = resistance of the conductor as a function of temperature (ohms).

For the specific geometry defined in Figure 3.9, the resistance of the conductor is given by Eq. (3.45).

$$R(T) = \rho_o \cdot \frac{L}{t \cdot h} \cdot \exp\left(\alpha_R \cdot (T - T_o)\right) \cong \rho_o \cdot \frac{L}{t \cdot h} \cdot \left(1 + \alpha_R \cdot (T - T_o)\right) \tag{3.45}$$

where: ρ_o = conductor resistivity (ohm-cm);

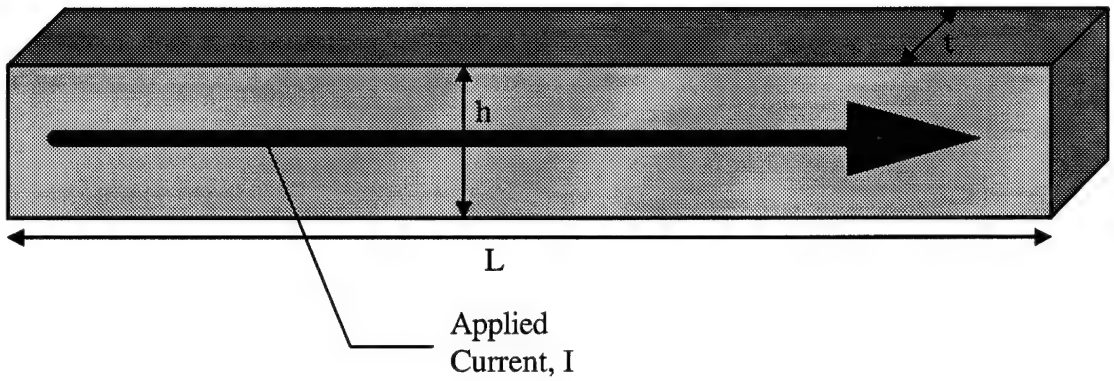

Figure 3.9. Conductor heated with an applied current, I.

α_R = thermal coefficient of resistance for the conductor ($^oC^{-1}$).

Because α_R is small (approx. 10^{-3}), the approximation in Eq. (3.45) is generally accurate for the temperature ranges of interest. By substituting Eq. (3.45) into Eq. (3.44), the temperature of the conductor relative to the ambient atmosphere temperature ($T - T_o$) can be determined.

$$T - T_o = \frac{I^2 \cdot \rho_o \cdot L \cdot \theta_{junct}}{h \cdot t - I^2 \cdot \rho_o \cdot L \cdot \alpha_R \cdot \theta_{junct}} \tag{3.46}$$

Using Eq. (3.46) it is possible to find the difference in temperature between sections A and C (Figure 3.8) due to the same applied current.

$$\Delta T = I^2 \cdot \rho_o \cdot L \cdot \left[\frac{\theta_A}{h \cdot t - I^2 \cdot \rho_o \cdot L \cdot \alpha_R \theta_A} - \frac{\theta_C}{2 \cdot h \cdot t - I^2 \cdot \rho_o \cdot L \cdot \alpha_R \theta_C} \right] \tag{3.47}$$

where: ΔT = temperature difference between section A and section C (^oC);

θ_A = thermal resistance between section A and the atmosphere (^oC-watt^{-1});

θ_C = thermal resistance between section C and the atmosphere atmosphere (^oC-watt^{-1});

The unkowns in Eq. (3.47) are the thermal resistances (θ_A and θ_C) of each section of the heat-drive actuator. Because these parameters model the radiation of the conductors heat into the atmosphere, they can be assumed to be proportional to the conductor surface area.

$$\theta_A = a \cdot 2 \cdot L \cdot (h + t) \tag{3.48 (a)}$$

$$\theta_C = a \cdot 2 \cdot L \cdot (h + 2 \cdot t) \qquad (3.48\ (b))$$

where a is the proportionality constant between relating the surface area of each conductor to the thermal resistance. These relations can then be substituted into Eq. (3.47):

$$\Delta T = I^2 \cdot \rho_o \cdot L \cdot \left[\frac{a \cdot 2 \cdot L \cdot (h + t)}{h \cdot t - 2 \cdot I^2 \cdot \rho_o \cdot L^2 \cdot \alpha_R \cdot a \cdot (h + t)} - \right.$$

$$\left. \frac{a \cdot 2 \cdot L \cdot (h + 2 \cdot t)}{2 \cdot h \cdot t - 2 \cdot I^2 \cdot \rho_o \cdot L^2 \cdot \alpha_R \cdot a \cdot (h + 2 \cdot t)} \right] \qquad (3.49)$$

The only unknown now is "a" and this should be constant for both sections of the heat-drive actuator. Once this constant is known (or determined empirically from the data), ΔT can be determined directly from the applied current which will then induce a given deflection (Eq. (3.43)).

Besides deflection due to thermal effects, a magnetic repulsive force between the two sides of the flexure is developed due to current running in opposite directions. This force is beneficial in that it keeps the two sides from coming into contact and it also helps increase the amount of tip deflection. The amount of tip deflection due to the magnetic force can be modeled with the following equation [18]:

$$\Delta x = \frac{p \cdot L^4}{27 \cdot E \cdot I} \qquad (3.50)$$

$$I = \frac{1}{12} t \cdot h^3 \qquad (3.51)$$

where: p = magnetic pressure in force/length between each side of the heat-drive actuator (newtons/m^2).;

t = thickness of sections A and B (meters);

E = Young's modulus (pascals).

These equations can be used to design and test heat-drive actuators as a means for actuation in MEM devices. As with the electrostatic devices, the modeling equations require detailed knowledge of the structural and process parameters of the thin films used for fabrication. As is the case with many MEM devices, many of these parameters can vary greatly during processing which can make precise design difficult.

3.5. Summary

In this chapter, the basic theory of calculating electrostatic forces from the capacitance of devices was developed. This method was used to calculate the electrostatic forces in some simple MEM devices. These devices included the electrostatic cantilever, the electrostatic microbridge, and the electrostatic comb-drive actuator. Additionally, the modeling of the folded beam suspension springs associated with comb-drive actuators was discussed as well as the commonly encountered sticking problems. The displacement of the thermally activated beam flexure, or heat-drive actuator, was also modeled as a function of temperature and specific beam parameters.

Chapter 4 details the processing considerations used for this thesis research and also describes many of the devices that were fabricated in the microswitch design effort. Additionally, all the laboratory equipment used and all the testing procedures employed are described in detail.

4. Experimental Procedure, Fabrication, and Design Descriptions

This chapter describes the MEMS design submission process, general design considerations, post processing procedures, device descriptions, testing procedures, and test equipment used in the testing of the micromechanical switches fabricated in the MUMPs and LIGA processes. This chapter should give a complete picture of what devices were fabricated, their intended operational characteristics, and how the devices were tested.

4.1. Design Submission Process

The submission procedures for the MUMPs and LIGA processes are similar to the processes used for submitting designs for fabrication of electronic IC's through commercial foundries. First, each mask layer used in a design must be digitized for transfer to the fabrication facility. Various computer aided design (CAD) tools allow the user to draw and manipulate desired designs in the form of shaded and colored polygons. The CAD tool can then translate the designs into the required mask layers and output the design in a standardized format. Once the design is in such a format, it can be transferred to the commercial fabrication facility by electronic mail (email) or file transfer protocol (FTP).

The CAD tools available to AFIT are MAGIC and CADENCE. Both MAGIC and CADENCE are layout editors that were designed primarily for the development of CMOS and BiCMOS integrated circuits. MAGIC is an older tool that allows designs to be digitized only in manhattan geometries (all rectangular shapes), while CADENCE allows

the user to create layers in many different shapes (circles, angles, etc.). By writing customized technology files for each editor, suitable masks can be digitized specifically for both the MUMPs and LIGA processes. Once a design is complete, both editors can output digitized masks in the form of Caltech Intermediate Files (CIF). These CIF files are a standard format accepted by most commercial fabrication facilities.

Once the CIF file has been created and is at the fabrication facility, there will generally be some feedback at various stages of the fabrication process. For the MUMPs process, fabrication usually takes approximately 10 to 11 weeks. Due to the lack of synchrotron x-ray radiation sources in the United States, however, the LIGA process can take significantly longer. The designs submitted to MCNC for the LIGA fabrication, are actually fabricated at the University of Wisconsin - Madison, so MCNC has limited control over the turn-around time.

4.2. MUMPs Process

4.2.1. General Design Considerations. Before AFIT obtained the CADENCE design package, designs submitted in the MUMPs process were developed in the MAGIC layout editor. This required that all devices be designed in manhattan geometries. However, some non-manhattan shapes could be created by "stair-stepping" curves and angles. Because the minimum feature size was only 2.0 μm and MAGIC could create 1.0 μm "stair-steps", some of the jagged nature of such shapes was smoothed during fabrication. Regardless, creating shapes in this manner was tedious and was not very precise. When CADENCE was obtained, such shapes could be easily drawn and this limitation was removed.

The most important design consideration in the MUMPs process is the placement of etch holes. In order to ensure that large polysilicon structures are released, it is necessary that etch holes be placed such that the etchant can dissolve the sacrificial oxide beneath the structures (See section 4.2.2.). According to the MUMPs Design Rules [11], etch holes should be placed at least every 30 μm from device edges or from other etch holes. If etch holes are not present or are too far apart, devices will require longer times in the etchant solution which can harm the functionality of some devices.

Another major consideration in the design of MUMPs devices is the conformal nature of material layers to the topography immediately below them. Figures 2.6 and 2.7 show this effect to some degree. The effect is most pronounced when the second polysilicon layer (POLY2) is crossed directly over the first polysilicon layer (POLY1). Because the separating oxide is only 0.5 μm thick, the upper layer conforms very closely to the lower layer and can severely inhibit device operation if this is not taken into account (Figure 4.1 (a)). Conversely, this effect can be used to the designer's advantage for the creation of specific devices (Figure 4.1 (b)).

Consideration must also be given to many of the design rules specified in the MUMPs design rules package [11]. Many of the design rules are in place so that the fabrication facility can guarantee that exactly what is drawn in the layout editor is what will be produced. For example, the design rules state that POLY1 must be 4.0 μm away from any POLY0 edges. This is to ensure that the POLY1 edge will be approximately

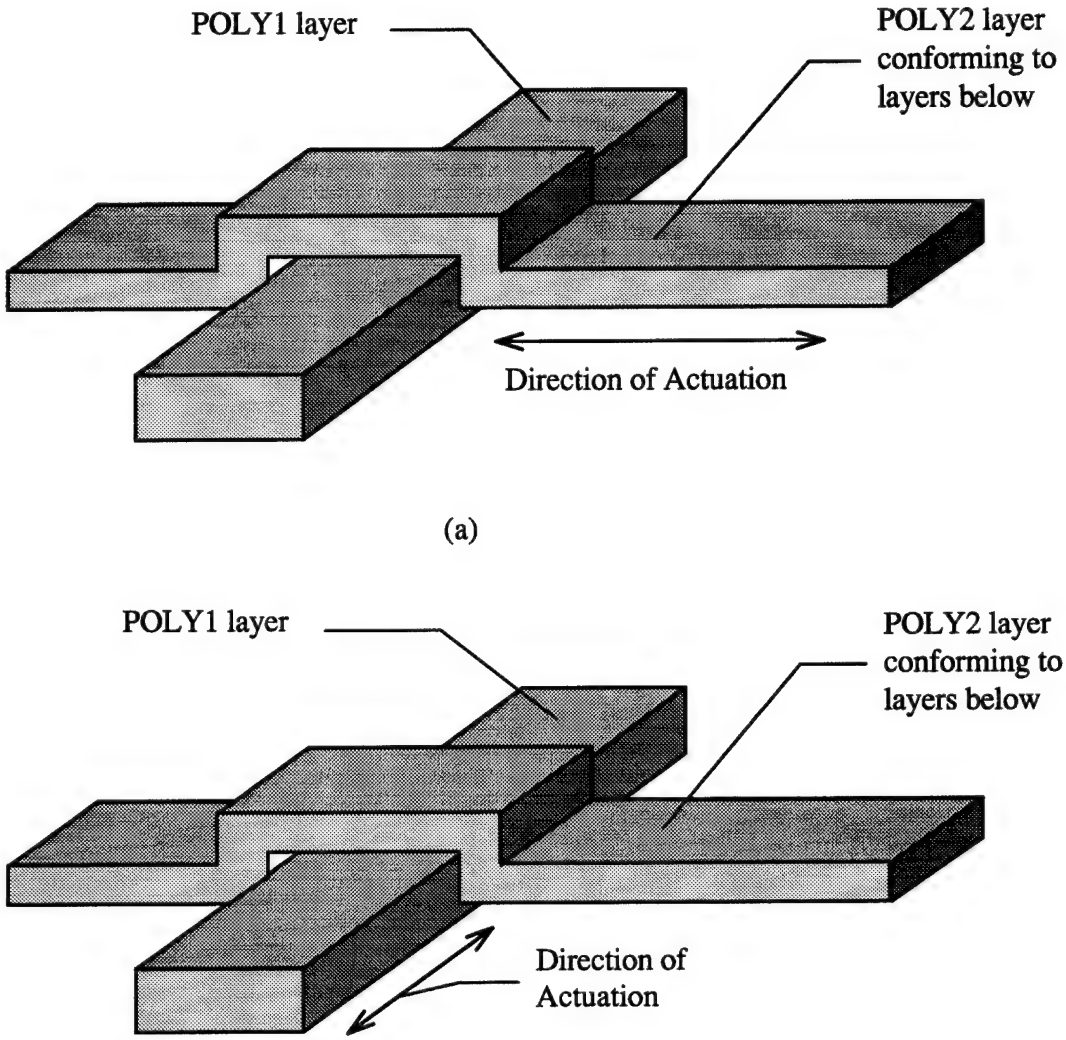

Figure 4.1. Depiction of the conformal effect of one polysilicon layer to another in the MUMPs process: as shown in (a), neither polysilicon layer can move in the indicated direction of actuation, however, the upper polysilicon layer can form an excellent guide for movement in the direction shown in (b).

where it was drawn. If termination of the POLY1 is required but the position of the POLY1 edge relative to the POLY0 edge does not matter, then the design rule can be safely disregarded. However, it is important to fully understand the implications of changes to specific design rules. Failure to do so could result in inoperational devices, therefore, it is best to design conservatively and avoid such situations as often as possible.

4.2.2. MUMPs Post Processing Procedures. Once MUMPs devices have been fabricated and returned to the end user, it is necessary to post process the die to release the MEM structures. The individual die are shipped unreleased (i.e. all SiO_2 layers are intact) and coated with a thick layer of photoresist to protect them during shipping. To release the MEM structures, first the photoresist must be removed and then the sacrificial SiO_2 must be etched. The release procedures are summarized in Tables 4.1 and 4.2.

Removal of the protective photoresist is performed, according to the MCNC instructions, by a 20 minute submersion with mild agitation in acetone (CH_3COCH_3). This is followed by a one minute immersion in 2-propanol (C_3H_7OH) and a thorough, five minute rinse in deionized (DI) water. The die can then be dried with a steady nitrogen (N_2) flow and viewed before sacrificial release. Viewing at this stage can help to gauge oxide and metal film quality.

Next, the sacrificial release is performed. Depending on which metal is used, the release procedures differ slightly. (Some of the MUMPs fabrication runs used different materials for the METAL layer. MUMPs 3 and earlier fabrications used aluminum, MUMPs 4 used copper, and MUMPs 5 and later used gold). For devices with aluminum as a metal layer, the etchant solution is a 4:2:1 mixture of ammonium fluoride (NH_4F):

Table 4.1. Etch Procedures for Die with Aluminum as the Metal Layer.

Step	Solution	Time	Notes
1	Acetone	20 min.	removes photoresist
2	Isopropal Alcohol	1 min.	rinses off acetone
3	Deionized Water	5 min.	rinses off isopropal alcohol
4	4:2:1 NH_4F:Glycerine:HF	15 min.	etches oxide layer
5	Deionized Water	2 min.	rinses off the etchant solution
6	Methanol Bath	2 min.	displaces water
7	Dry at 100 °C	5 min.	evaporates methanol

Table 4.2. Etch Procedures for Die with Copper or Gold Metal Layers.

Step	Solution	Time	Notes
1	Acetone	20 min.	removes photoresist
2	Isopropal Alcohol	1 min.	rinses off acetone
3	Deionized Water	5 min.	rinses off isopropal alcohol
4	49 wt% HF	2 min.	etches oxide
5	Deionized Water	2 min.	rinses off the etchant off
6	Nitric Acid	15 sec	
7	2-Propanol Bath	2 min.	displaces water
8	Dry at 100 °C	5 min.	evaporates 2-propanol

glycerine:49 wt% hydrofluoric acid (HF). With a theoretical SiO_2 etch rate of 18 nm/sec, an etch time of approximately 15 minutes is required to release structures with 30 μm between etch holes. The glycerin in the mixture is intended to help keep the solution from destroying the aluminum film. After sacrificial release in the etchant solution, the die is placed in vat of DI water and swirled very gently for at least 2 minutes. The die is then removed and bathed in methanol (CH_3OH) for 2 minutes and dried in an oven at 100 °C for 5 minutes. The methanol is used prior to the drying process to reduce sticking and breakage of polysilicon structures from the high surface tension of water.

For devices with copper as the metal layer, the etchant solution used is 49 wt% HF. The die is immersed in the etchant for 2 minutes followed immediately by immersion in DI water. The die is gently swirled in the DI water for 2 minutes after which it is removed and dipped into nitric acid (HNO_3) for 15 seconds. The die is then submerged in 2-propanol for 2 minutes and baked at 100 °C for 5 minutes. The same procedures are used for the designs with gold metal layers, except that the dip in nitric acid is omitted.

An etch gauge was used to judge the etch process. The etch gauge was a set of POLY2 and POLY1 squares varying in size from 2 μm to 50 μm on a side which were unattached to the substrate. As each square was underetched, the square washed away thus showing the progress of the etch.

4.2.3. Device Descriptions. Following is a detailed list of all the devices that were designed and fabricated in the MUMPs process. The operation of each device is described in detail and is accompanied by layout plots from either CADENCE or MAGIC (as appropriate) and a scanning electron microscope (SEM) micrograph of at least one

version of the device. Layout plots and SEM micrographs of other switch versions are shown in Appendix A.

Device Name: **Microbridge Switch**
Fabrication Runs: **MUMPs 4 (ver. 1-4), MUMPs 7 (ver. 5, 6)**
Actuation Method: **Electrostatic Forces**

The microbridge switch is operated by applying a d.c. potential between the bridge and the drive electrodes. The switch is closed when the center of the bridge comes into contact with the sense electrode. A small a.c. signal, relative to the d.c. actuating potential, can then be passed through the connection between the bridge and sense electrode. The switch can be restored to the "off" position by removing the d.c. potential. The variations of the dimensions between the versions of this switch are summarized in Table 4.3.

Table 4.3. Microbridge Switch Dimensions.

Version #	Length (μm)	Width (μm)	Drive Elec. Area (μm) *	Sense Electrode Area (μm^2)	Hinge Size (μm)
1	332	40	40 x 80	32 x 30	4 x 30
2	332	40	40 x 80	32 x 30	8 x 12
3	242	30	30 x 50	22 x 38	3 x 29
4	242	30	30 x 50	22 x 38	6 x 12
5	290	30	90 x 90	25 x 20	6 x 20
6	340	30	90 x 115	25 x 20	6 x 20

* Drive area for one drive electrode in the microbridge.

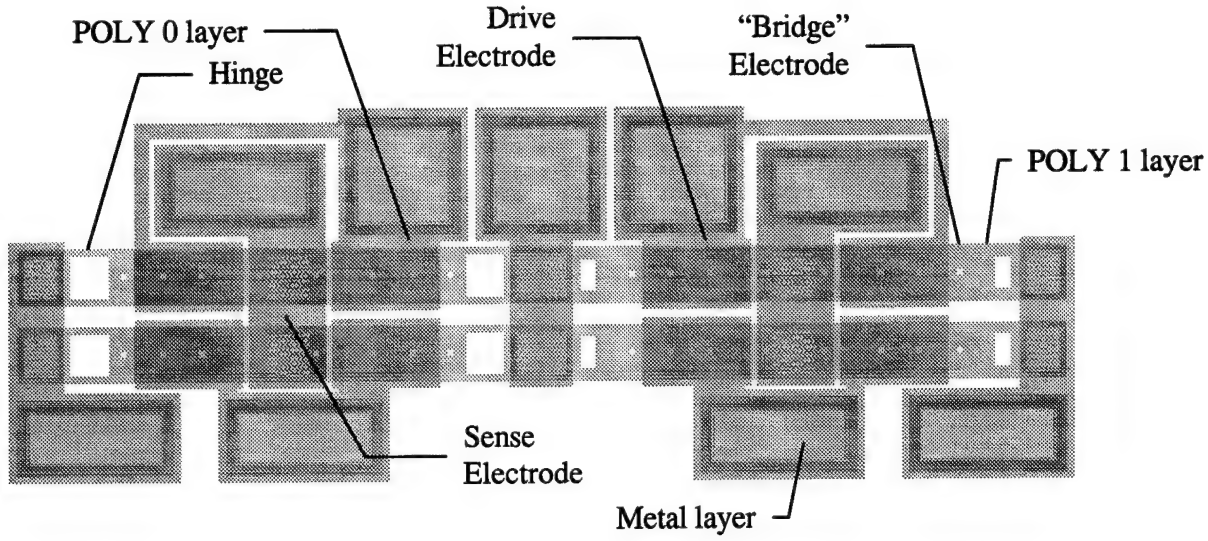

Figure 4.2. MAGIC layout of four microbridge switches. Shown here: two version 1 switches (left two bridges) and two version 2 switches (right two bridges) fabricated in MUMPs 4.

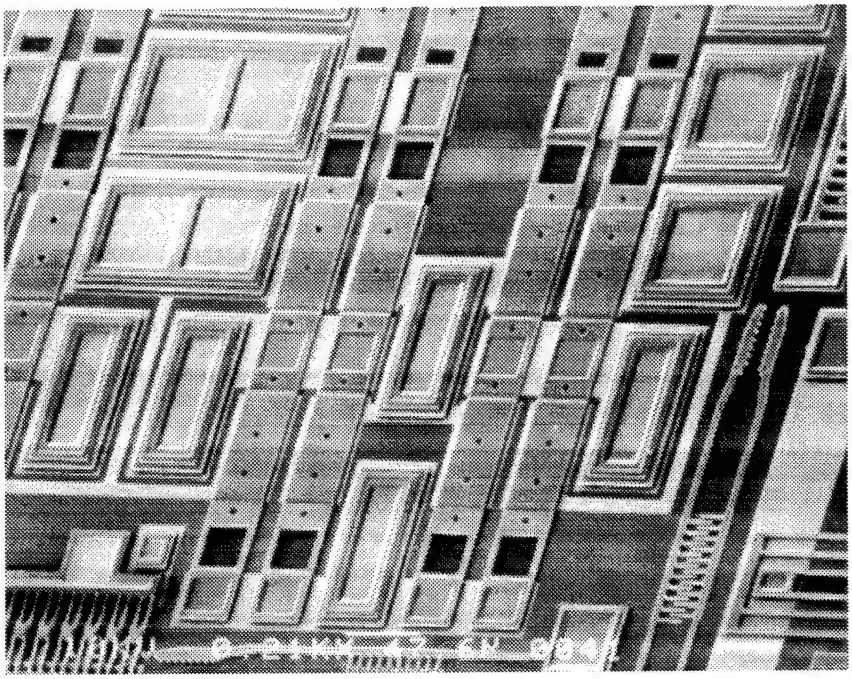

Figure 4.3. SEM micrograph of the fabricated device shown in Figure 4.2. Shown here: version 1 fabricated in MUMPs 4.

Device Name: **Cantilever Beam Switch**
Fabrication Runs: **MUMPs 4 (ver. 1-5), MUMPs 5 (ver. 6-9)**
Actuation Method: **Electrostatic Forces**

The cantilever beam switch is intended to close by applying a d.c. potential between the cantilever and the drive electrode. If the actuating potential is large enough, the end of the beam will contact the sense electrode thus allowing a small a.c. signal, relative to the actuating potential, to be passed. Releasing the actuating d.c. potential returns the cantilever to its original "off" position. Versions 6 and 7 differ from versions 1 and 2 in that the DIMPLE layer on the tip of the cantilever is "checkered". This is intended to improve the "on" contact resistance by increasing the amount of force per area between the tip of the cantilever and the sense electrode. Version 8 is intended to decrease the actuation potential needed by using the thinner POLY2 layer as the primary structural layer. The conductivity of cantilever is also improved by a gold layer on top of the POLY2 structural layer. Additionally, a layer of POLY1 is attached to the POLY2 cantilever (with POLY1_POLY2_VIA) to reduce the capacitive gap between the cantilever and the drive electrode. The dimensional variations between the versions of this device are summarized in Table 4.4.

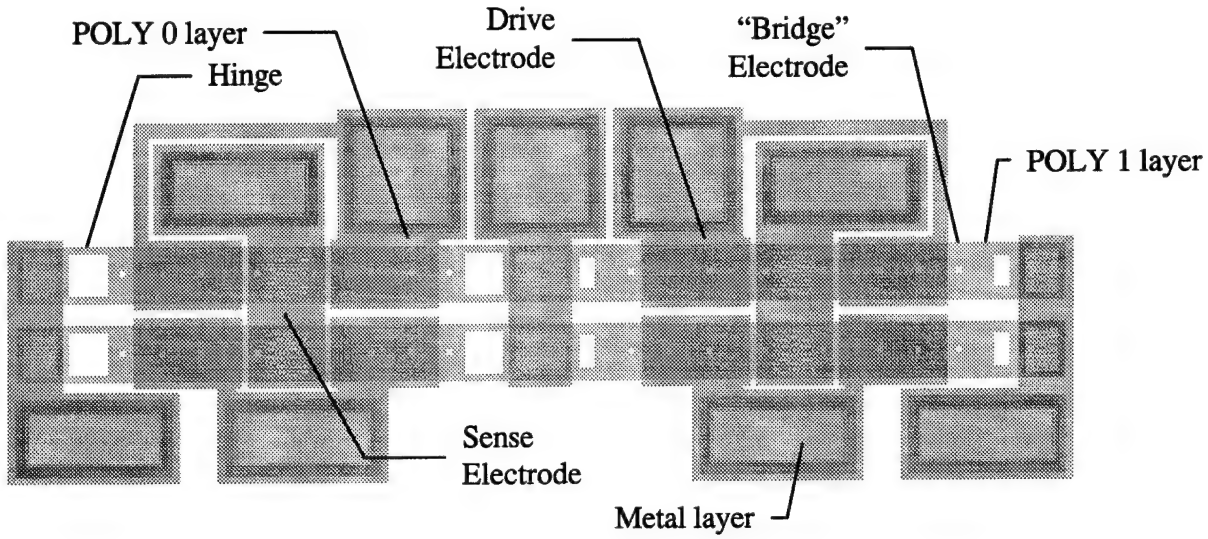

Figure 4.2. MAGIC layout of four microbridge switches. Shown here: two version 1 switches (left two bridges) and two version 2 switches (right two bridges) fabricated in MUMPs 4.

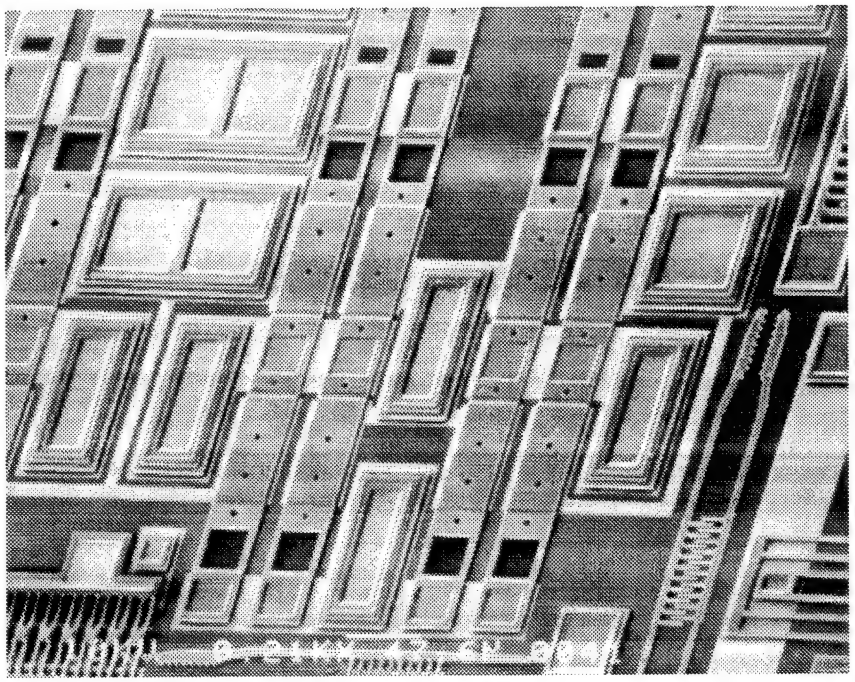

Figure 4.3. SEM micrograph of the fabricated device shown in Figure 4.2. Shown here: version 1 fabricated in MUMPs 4.

Table 4.4. Cantilever Beam Switch Dimensions.

Version #	Length (μm)	Width (μm)	Drive Elec. Area (μm)	Sense Electrode Area (μm^2)	Hinge Size (μm)
1	108	30	30 x 50	20 x 22	2 x 20
2	108	30	30 x 50	20 x 22	4 x 25
3	108	30	30 x 50	20 x 22	6 x 37
4,6	165	40	40 x 75	32 x 25	3 x 34
5,7	165	40	40 x 75	32 x 25	8 x 12
8	220	20	94 x 131	27 x 14	3 x 16
9	270	20	94 x170	27 x 14	3 x 16

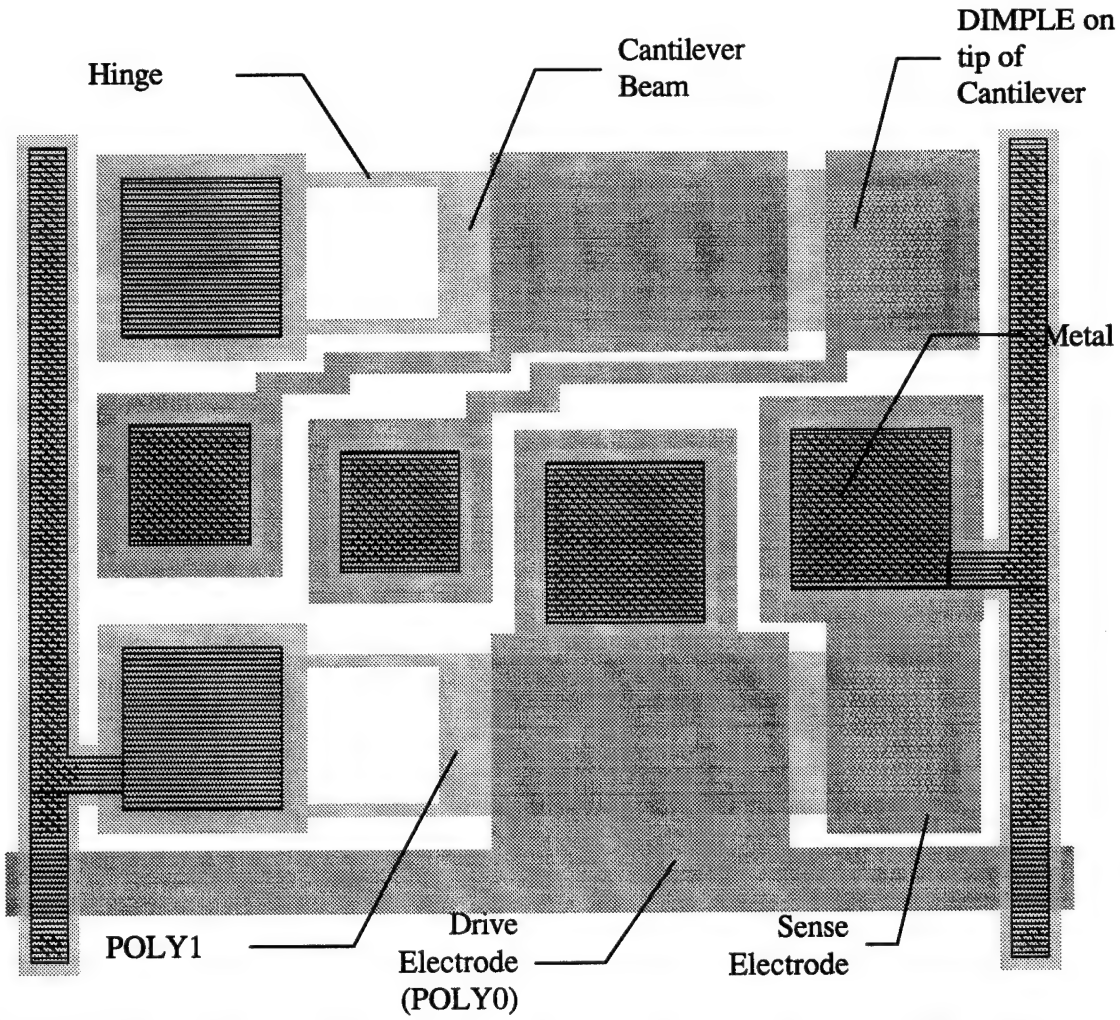

Figure 4.4. MAGIC layout of two 165 μm long cantilever beam switches. Shown here: two version 6 switches fabricated in MUMPs 4.

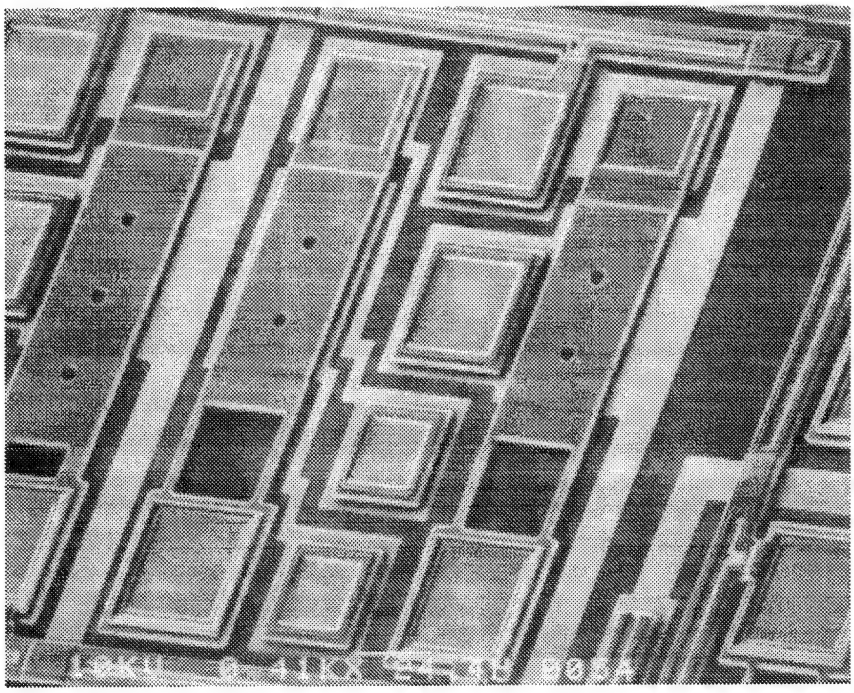

Figure 4.5. SEM micrograph of two fabricated 165 μm long cantilever switches. Shown here: two version 6 switches fabricated in MUMPs 4.

Device Name:	**Simple Comb-Drive Switch**
Fabrication Runs:	**MUMPs 4 (ver. 1, 2)**
Actuation Method:	**Electrostatic Forces**

The movable and fixed combs are drawn together by applying a d.c. potential between them. As the combs draw together, the contact electrodes attached to the movable comb will touch the contact electrodes attached to the fixed comb. At this point, a small a.c. signal, relative to the d.c. actuation potential, can be passed through the contact. Version 1 of this switch uses POLY1 beams for the contact electrodes. Version 2 of this switch, however, has a POLY2 layer added to the contact electrodes. As noted in Figure 4.1, the POLY2 layer conforms closely to the layers beneath it. In this case, the POLY2 layer will conform into the gap between the contact electrodes. This reduces the

effective gap between the contact electrodes to 0.5 μm. Additionally, the overlapping POLY2 layer helps ensure that the contact electrodes do not slip off one another when in contact.

All dimensions for this switch are identical. There are a total number of 15 fingers on the fixed comb and 14 fingers on the movable comb. The finger dimensions are 4 μm x 24 μm for the movable comb and 5 μm x 28 μm for the fixed comb. The springs are 300 μm long and are composed of 2 μm thick POLY1 beams. The total contact area is 61 μm x 2 μm.

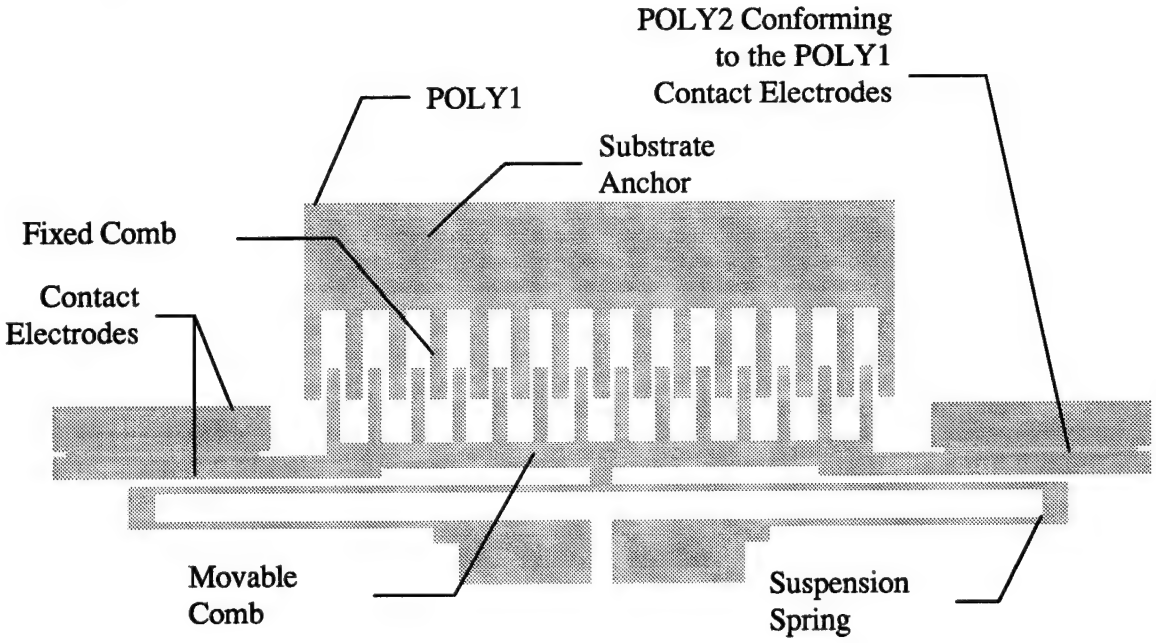

Figure 4.6. MAGIC layout of the simple comb-drive switch. Shown here: version 2 fabricated in MUMPs 4. The POLY2 conforming to the POLY1 contact electrodes can be more easily seen in Figure 4.7.

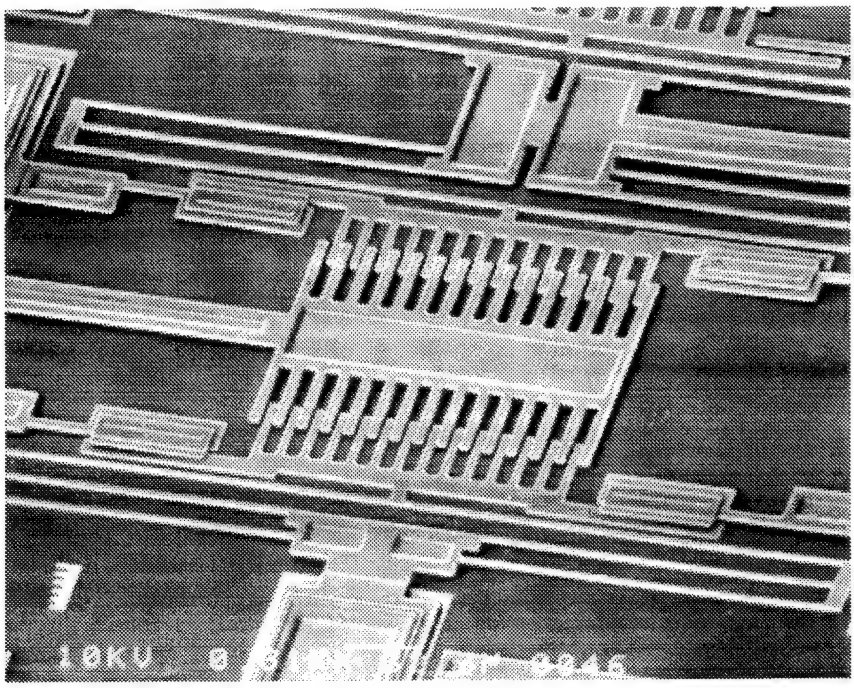

Figure 4.7. SEM micrograph of a fabricated simple comb-drive switch. Shown here: version 2 fabricated in MUMPs 4.

Device Name:	**Push Lock Switch**
Fabrication Runs:	**MUMPs 4 (ver. 1, 2), MUMPs 5 (ver. 3, 4)**
Actuation Method:	**Electrostatic Forces (ver. 1,2)**
	Differential Heating (ver. 3, 4)

This device utilizes three comb-drive actuators to lock two conductors into contact. First, the two smaller comb-drive actuators pull the signal electrodes out from behind the contact pusher. Then, the main comb-drive actuator pulls until the contact pusher is behind the signal electrodes which were moved out of the way by the small comb-drive actuators. At this point, the potential holding the small comb-drive actuators is released, followed by the release of the potential holding the main comb-drive actuator. Then, the signal electrodes snap back into place and are bent by the restoring force from the springs holding the contact pusher. This bending forces the signal electrodes into

contact with the conductors near them. Now, the device is locked into place without any input power needed to hold it in place. Both a.c. and d.c. signals may be passed from the signal electrodes and into the conductors they are in contact with. The switch can be returned to the "off" position by actuating the comb drives in the exact reverse order that brought them into contact. Version 2 of this device uses conformal POLY2 on the contact electrodes to keep the contacts from slipping past each other when locked into place. Version 3 and 4 of this device uses the same concept as versions 1 and 2 except that the comb-drive actuators are replaced with heat-drive actuators. Two heat-drive actuators work together in place of the main comb-drive actuator and one heat-drive actuator replaces each of the smaller comb-drive actuators. The necessary movement is provided by running current through the heat-drive actuators. The dimensions for each version of this switch are summarized in Table 4.5 (a) and (b). Note: a layout and SEM micrograph of version 3 can be found in Appendix A.

Table 4.5 (a). Push Lock Switch (Electrostatic) Dimensions.

Version/ /Type	Movable Finger Size (μm)	Fixed Finger Size (μm)	Initial Overlap/ Finger Gap (μm)	Spring Width/ Length (μm)
1,2 main	4 x 26	5 x 33	12/2	2/320
1,2 small	4 x 24	5 x 29	8/2	2/380

Table 4.5 (b). Push Lock Switch (Heat-drive Actuator) Dimensions*.

Version/ Type	Length (μm)	Thin-Side Width (μm)	Thick-Side Width (μm)	Flexure Length
3/main	250	4	10	9
3/small	148	4	10	6
4/main	200	4	10	9
4/small	148	4	10	6

*The gap between the thin and thick sides of the heat-drive actuators was 4 μm. This is the same as a value of 11 μm for "g" defined in Figure 3.8.

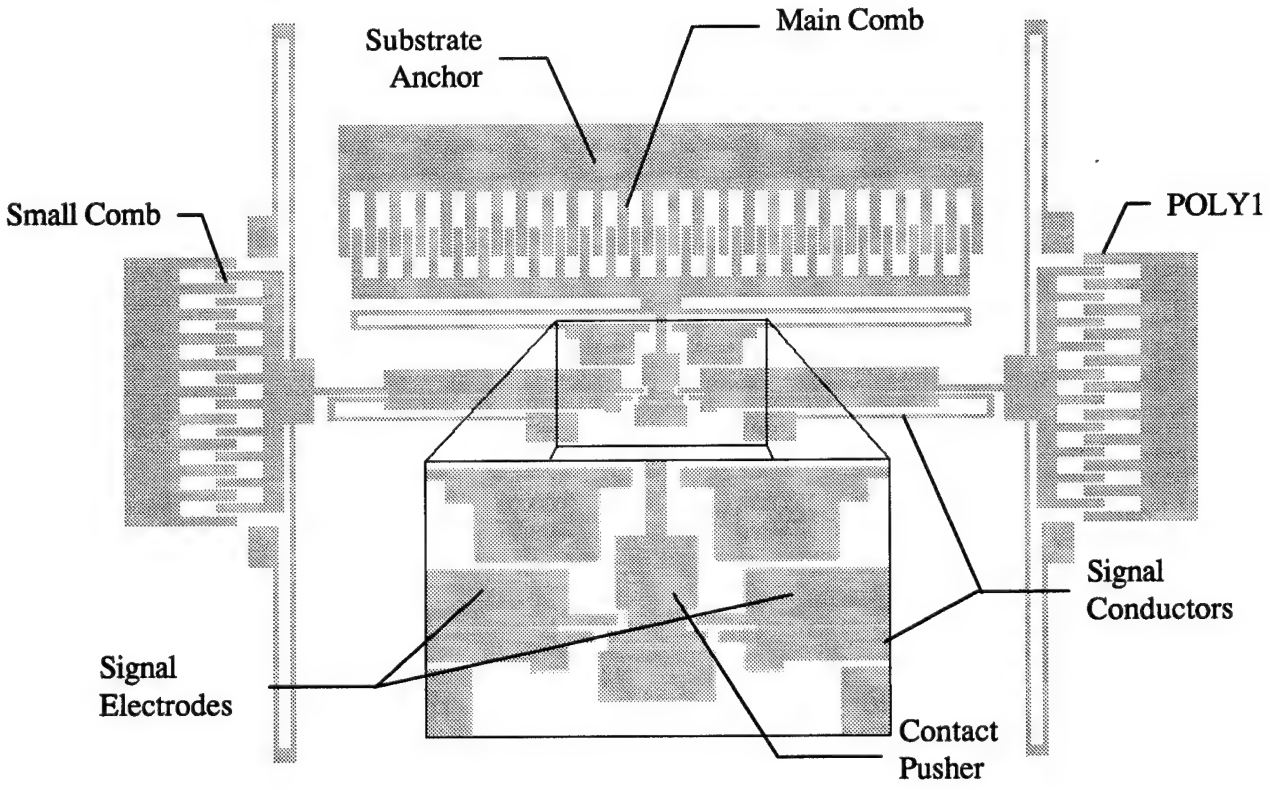

Figure 4.8. MAGIC layout of the comb-drive push lock switch. Shown here: version 2 fabricated in MUMPs 4.

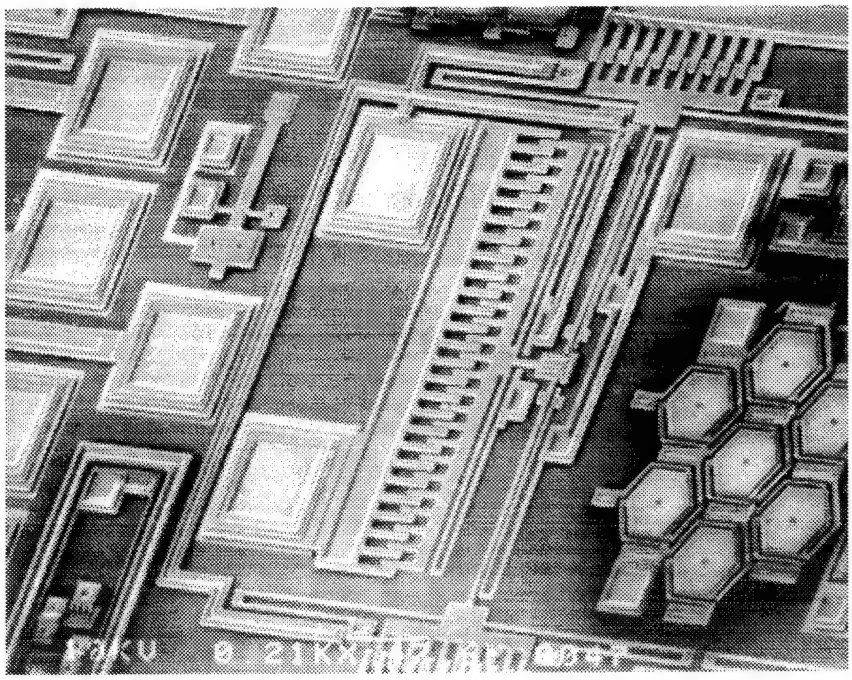

Figure 4.9. SEM micrograph of the fabricated comb-drive push switch. Shown here: version 2 fabricated in MUMPs 4.

Device Name:	**Heat-Spring Switch**
Fabrication Runs:	**MUMPs 5 (ver. 1, 2), MUMPs 6 (ver. 3)**
Actuation Method:	**Differential Heating**

In order to operate this device, first, the clamp into which the contact electrode will be inserted is opened by running equal amounts of current through the heat-drive actuators which form the clamp. While maintaining the drive current on the clamp, the main heat-drive actuators attached to the restoring springs are actuated in a similar manner. This will push the contact electrode into the clamp. By releasing the current to the clamp actuators, the contact electrode will be securely locked into place. No sustained actuation current is required to keep the switch locked into place, thus, any signal, a.c. or d.c., may be passed along the clamp and into the contact electrode. Version 2 of this

device is the same as version 1 except that it uses larger heat-drive actuators. The device can be restored to the "off" position by opening the clamp and allowing the contact electrode to spring back into place. Version 3 works similarly to versions 1 and 2 except that it has two heat-drive actuator clamp sections and two contact electrodes. When the contact electrodes are locked into their respective clamp sections, the switch is closed and either a.c. or d.c. signals can be passed from one clamp section to the other. This version is restored to the "off" position by opening the clamp sections and allowing the contact electrodes to snap back into their original positions.

The contact area for versions 1 and 2 of this switch is 24 μm^2 and the suspension spring length is 360 μm. Version 3 has a contact area of 52 μm^2 and a suspension spring length of 380 μm. Table 4.6 summarizes the dimensions specific to individual versions of this switch. All the suspension springs were composed of 2 μm wide beam elements.

Table 4.6. Heat-Spring Switch Dimensions*.

Version/ Type	Length (μm)	Thin-Side Width (μm)	Thick-Side Width (μm)	Flexure Length (μm)
1/main	200	4	10	11
1/clamp	166	4	10	6
2/main	250	4	10	11
2/clamp	166	4	10	6
3/main	300	4	8	9
3/clamp	200	4	8	8

*The gap between the thin-sections and thick sections of the heat-drive actuators was 4 μm. This corresponds to a "g" dimension of 11 μm for version 1 and 2 and a "g" dimension of 10 μm for version 3 (g is defined in Figure 3.8).

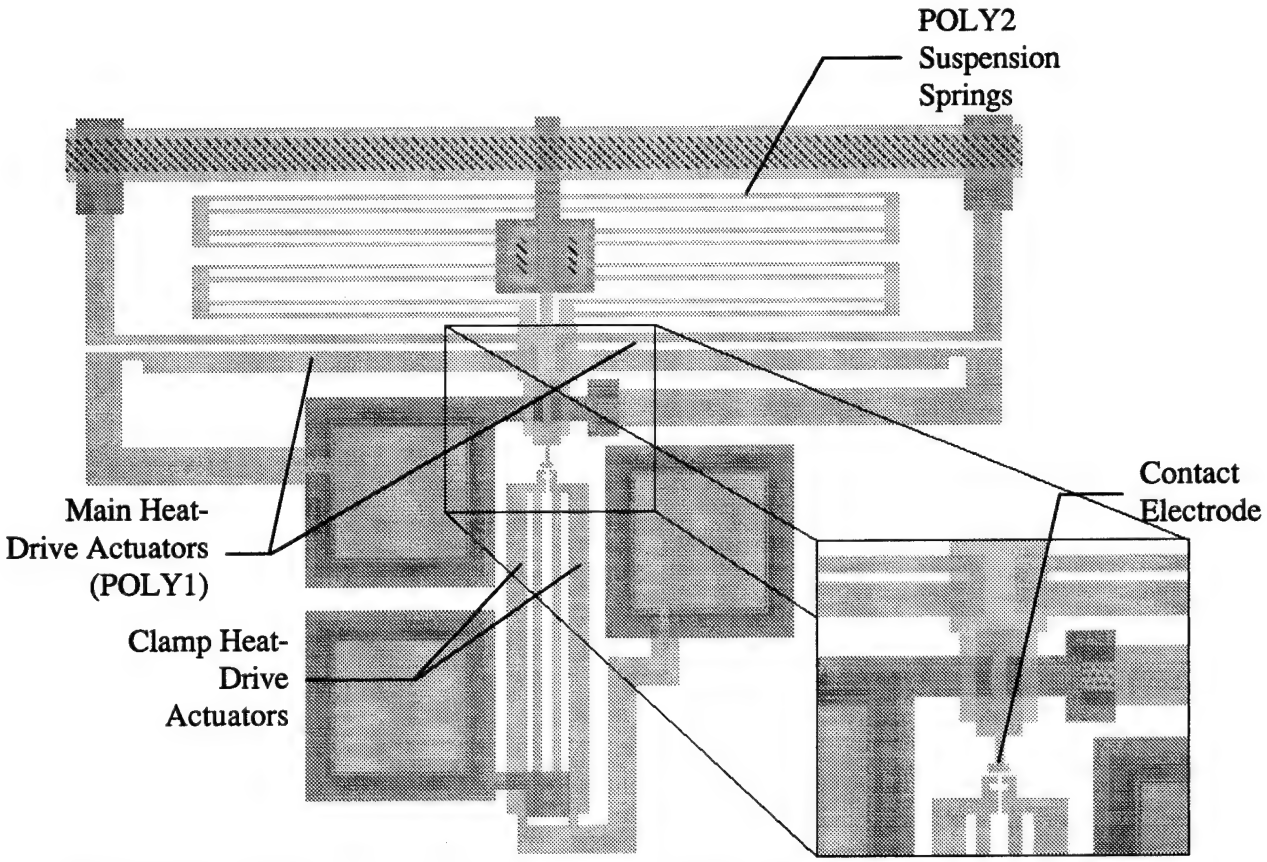

Figure 4.10. MAGIC layout of the heat-spring switch. Shown here: version 1 fabricated in MUMPs 5.

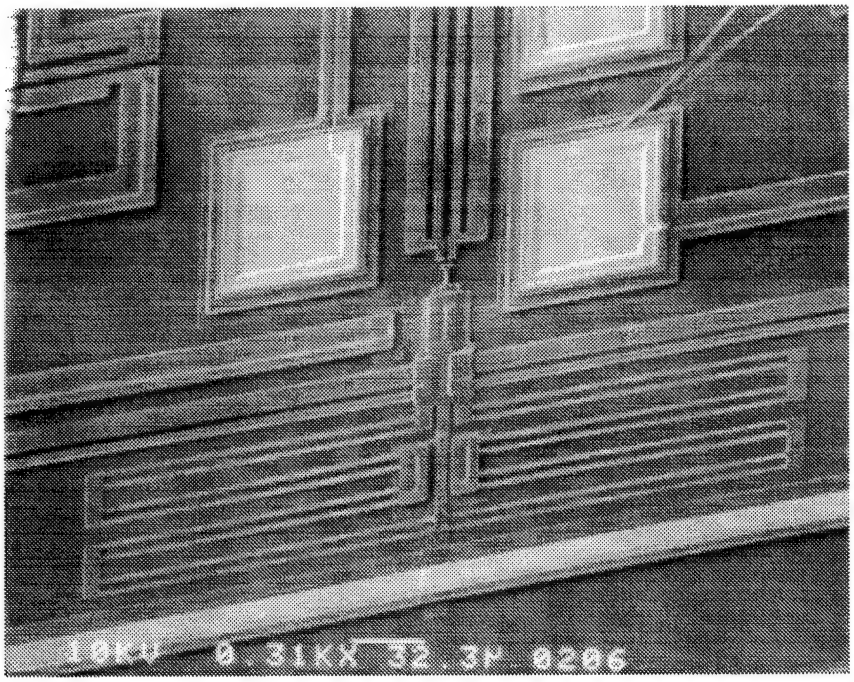

Figure 4.11. SEM micrograph of the fabricated heat-spring switch. Shown here: version 1 fabricated in MUMPs 5.

Device Name: **Clamp-Lock Switch**
Fabrication Runs: **MUMPs 5 (ver. 1, 2)**
Actuation Method: **Electrostatic Forces**

For version 1, the clamping device is opened by applying the same potential to each side of the clamp structure, forcing them to repel each other. This opens the clamp. For version 2, the clamping device is opened by applying a current to the heat-drive actuator forming one side of the clamp. Once the clamp is open, the contact electrode is drawn into position by applying a d.c. potential between the two large sets of comb-drive actuators. As the contact electrode moves into position, the clamp can be released to lock the electrode into place. At this point, either a.c. and d.c. signals can be passed from the clamp section into the contact electrode. The switch is returned to the "off" position by reopening the clamp and allowing the contact electrode to return to its original position.

For version 1, there are 9 fingers on the electrostatic clamping mechanism and the finger dimensions are 14 μm x 2 μm with an initial overlap of 12 μm. The spring length is 87 μm composed of beams with a width of 2 μm and the capacitive gap between opposing fingers is 2 μm. For version 2, the heat-drive actuator length is 190 μm, the flexure length is 9 μm, the thin-side width is 4 μm, and the thick-side width is 10 μm. The thin and thick sections are separated by a gap of 4 μm which corresponds to a "g"dimension, as described in Figure 3.8, of 11 μm. For both cases the electrode contact area is 24 μm^2. For both versions, the main electrostatic comb drives have the same dimensions. The movable comb fingers are 3 μm x 43 μm in size and the fixed comb fingers are 4 μm x 43 μm in size. The initial finger overlap is 22 μm and there are a total of 38 fingers on the

movable combs (36 on the fixed combs). The suspension spring length is 360 μm and is composed of 2 μm wide beam elements.

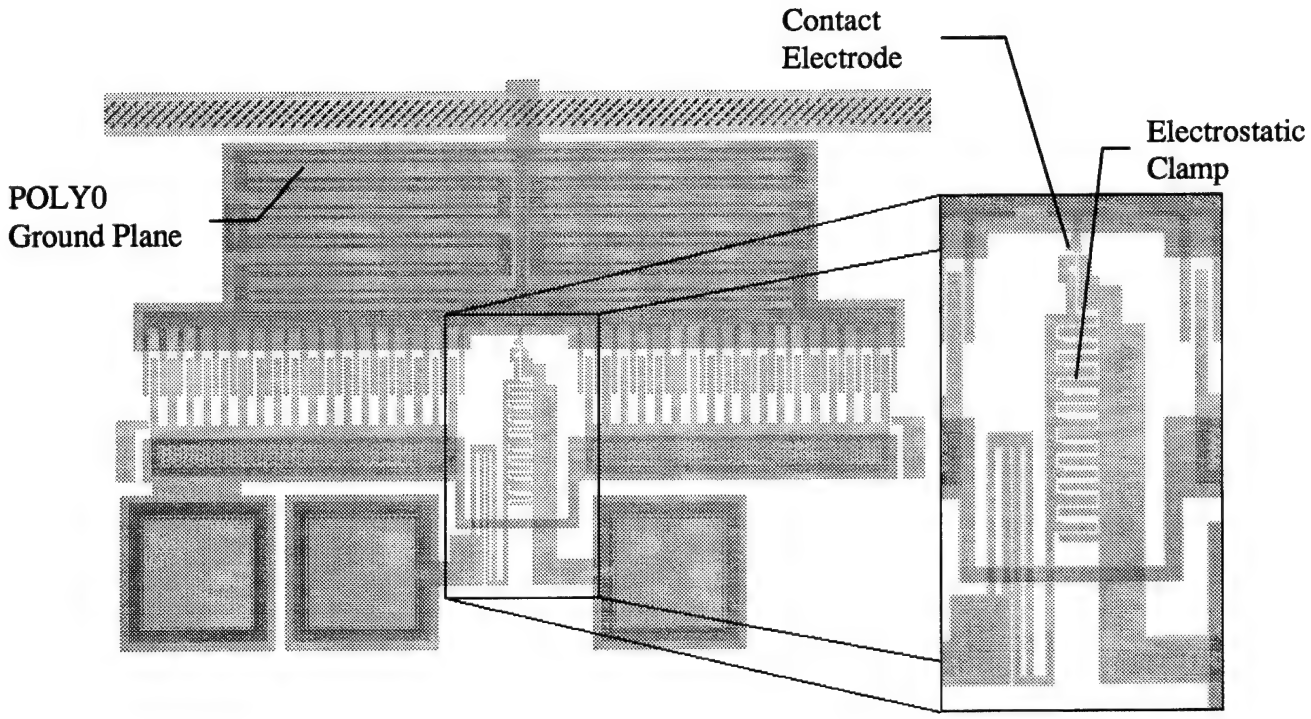

Figure 4.12. MAGIC layout of the electrostatic clamp-lock switch. Shown here: version 1 fabricated in MUMPs 5.

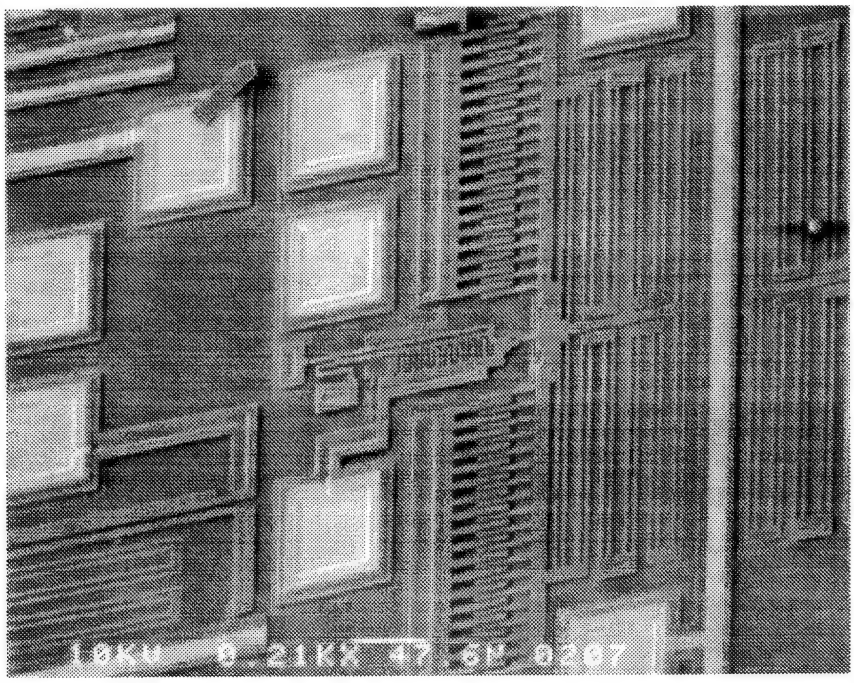

Figure 4.13. SEM micrograph of the fabricated electrostatic clamp-lock switch. Shown here: version 1 fabricated in MUMPs 5.

Device Name:	**Electrostatic Cantilever-Lock Switch**
Fabrication Runs:	**MUMPs 5 (ver. 1-5)**
Actuation Method:	**Electrostatic Forces**

Versions 1 and 2: The switch is operated by first applying a d.c. potential between the two cantilevers and the drive electrodes beneath them. Next, a d.c. potential is applied between the comb-drive actuators to pull the contact bar into position above the tips of the cantilevers. Once in position, the potential on the cantilevers can be released allowing them to rise up and touch the contact bar. In version 1, the holes in the tips of the cantilevers surround the dips in the contact bar (formed from DIMPLEs) and lock the structure in place. In version 2, the bumps in the cantilevers (formed from the POLY1 formers beneath them) slip into the openings in the contact bar and lock the structure in

place. For both cases, either a.c. or d.c. signals can be passed from one cantilever, through the contact bar, and into the other cantilever. The switch can be turned "off" by reversing the actuating process.

Versions 3, 4 and 5: First, a d.c. potential between the cantilevers at the edges of the movable comb-drive actuators and the drive electrodes beneath them is applied. Next, a d.c. potential is applied between the fixed and movable comb-drive actuators. This moves the entire structure (including cantilevers) forward and shoves the cantilever tips underneath the small bridges immediately in front of them. Once in position, the actuating potential on the cantilevers can be released. For versions 3 and 4, the hole in the cantilever tips surround the dips in the small bridges (formed from DIMPLEs) and lock the structure in place. For version 5, the bumps in the cantilever tips (formed from the POLY1 formers beneath them) slip into the openings in the small bridges and lock the structure in place. Once versions 3, 4 and 5 are locked in place, either an a.c. or d.c. signal can be passed from one bridge (via the cantilevers) to the other. The critical dimensions for all versions of the electrostatic cantilever-lock switch are summarized in Table 4.7.

Table 4.7. Electrostatic Cantilever-Lock Switch Dimensions.

Version	Cant. Hinge Size (μm)	Cant. Drive Area (μm)	Number of Fingers*	Spring** Length (μm)	Contact Area (μm^2)
1	3 x 20	102 x 104	38	360	58 x 8
2	10 x 25	102 x 100	44	360	74 x 10
3	4 x 4	50 x 48	20	360	20 x 8
4	4 x 4	50 x 48	20	360	38 x 8
5	4 x 4	50 x 48	26	360	28 x 8

*The finger dimensions and initial finger overlaps are the same as for the clamp-lock switch that was previously described.

**The thickness of the beams that compose the suspension springs are 2 μm wide.

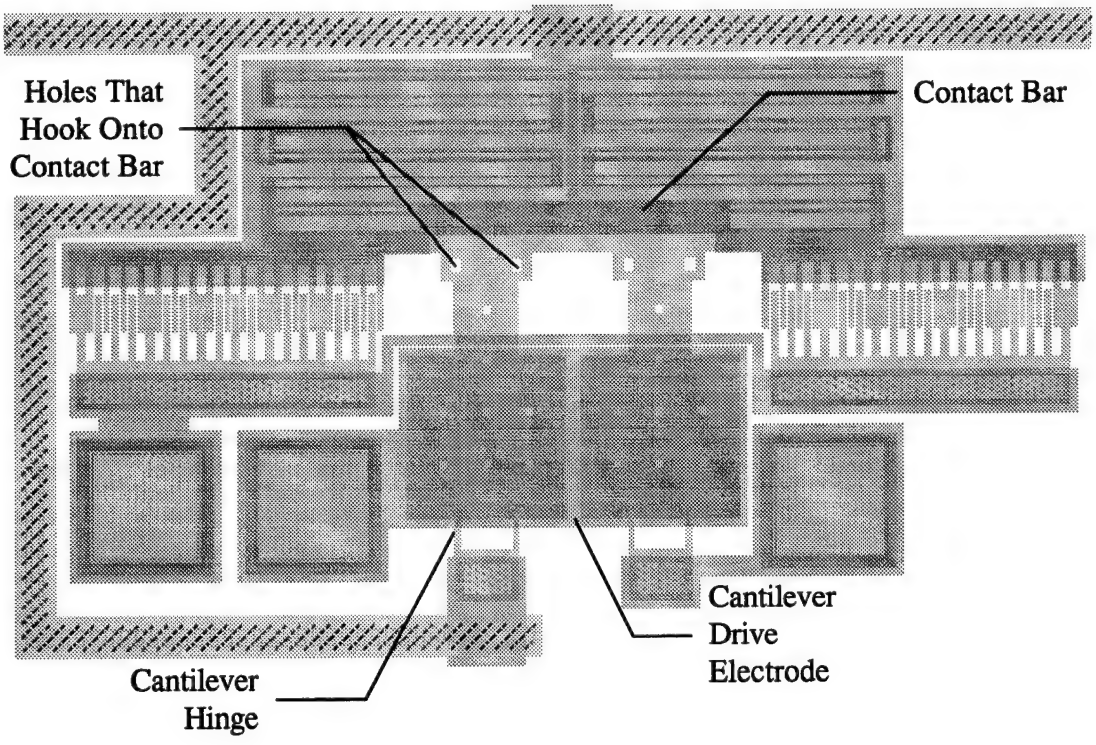

Figure 4.14. MAGIC layout of the electrostatic cantilever-lock switch. Shown here: version 1 fabricated in MUMPs 5.

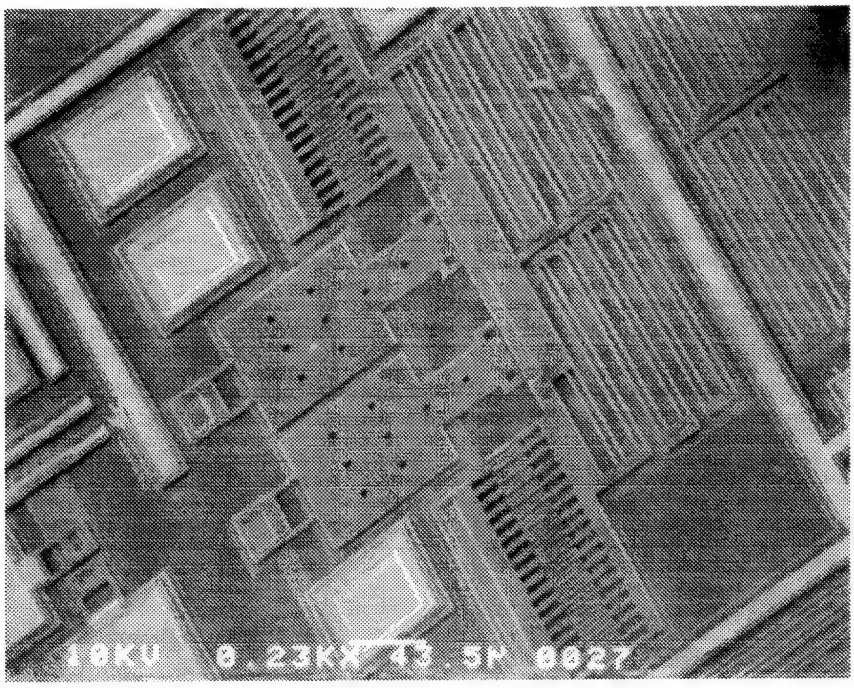

Figure 4.15. SEM micrograph of fabricated electrostatic cantilever-lock switch. Shown here: version 1 fabricated in MUMPs 5.

Device Name: **Hinge Switch**
Fabrication Runs: **MUMPs 6 (ver. 1, 2), MUMPs 7 (ver. 3)**
Actuation Method: **Mechanical/Differential Heating**

This device is designed such that metal to metal contacts can be formed. After fabrication, the hinge is laying flat with metal on its upper surface. The hinge is then flipped over until the metal on the end of the hinge is facing towards the substrate. For version 1, the metal covered tip of the hinge is allowed to contact two electrically separated metal covered pads on the substrate. At this time, either an a.c. or d.c. signal can be passed between the two pads on the substrate through the contact formed by the metal on the hinge. For versions 2 and 3, the hinge is initially not allowed to contact with the two metal covered pads on the substrate. Rather, the hinge is held above the substrate

pads by a lever located about 2/3 the way along the hinge length. This lever is attached to a vertical heat-drive actuator (see the following device description). If the current is applied to the heat-drive actuator, the lever moves down and allows the hinge to sink into contact with the two substrate pads. When the current is removed from the heat-drive actuator, the lever is returned to its initial position and the contact is broken.

All versions of the hinge switch have 2 μm pivots about which they rotate. These pivots are held to the substrate by a collar formed by two POLY2 bridges that cross over the pivots. Due to the conformal nature of the POLY2 to the POLY1, the POLY2 collars hold the pivot closely. Other critical dimensions for each of the versions are detailed in Table 4.8. (Note: the heat actuator column simply refers to what different vertical heat-drive actuators were attempted with each hinge version).

Table 4.8. Hinge Switch Dimensions.

Version	Hinge Length (μm)	Hinge Width (μm)	Contact Electrode Area (μm^2)	Heat Actuator Versions
1	90	46	22 x 14	1, 2, 3
2	110	46	22 x 14	1, 2, 3
3	130	46	22 x 14	1, 2, 3
4	150	46	22 x 14	1, 2, 3
5	170	46	22 x 14	1, 2, 3

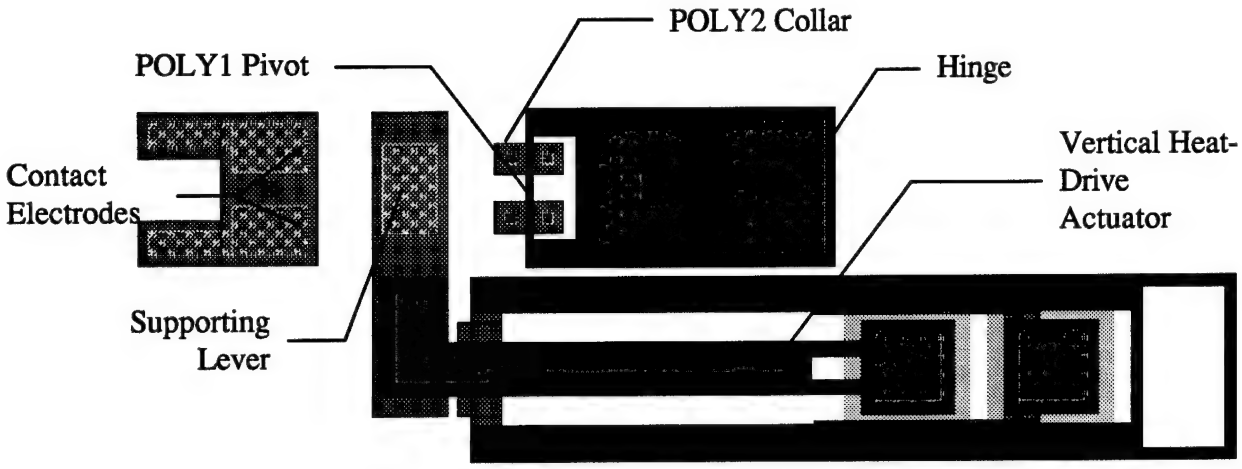

Figure 4.16. CADENCE layout of the hinge switch. Shown here: version 2 fabricated in MUMPs 6.

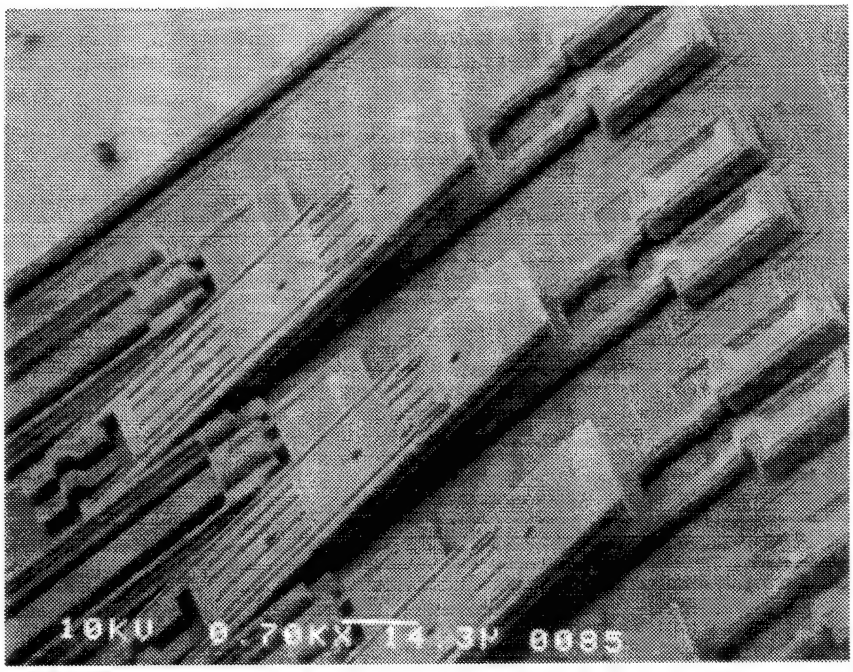

Figure 4.17. SEM micrograph of the fabricated hinge switch. Shown here: version 2 fabricated in MUMPs 6.

Device Name: **Vertical Heat-Drive Actuator**
Fabrication Runs: **MUMPs 6 (ver. 1-8), MUMPs 7 (ver. 9-16)**
Actuation Method: **Differential Heating**

For this device to operate, the POLY1 slider must be removed using a micromanipulator probe. After this is performed, the structure is actuated by running a d.c. current through the device. As a result, the thin POLY2 sections will be heated more than the thick POLY1 section due to the higher resistance of the POLY2 sections. Since the thin POLY2 sections are located above the thick POLY1 section, the greater thermal expansion of the POLY2 will cause the tip of the structure to deflect downward. (Note: these devices are not used as switches, rather, they are an important actuator that is used in the hinge switches).

The lengths of the POLY1 sections increase by 20 μm for each consecutive version of the device beginning with version 1 at 92 μm. All versions have POLY2 sections that are 4 μm wide and POLY1 sections that are 15 μm wide. Versions 9-16 are essentially the same as versions 1-8 except they have POLY2 sections that are 8 μm wide and POLY1 sections that are 32 μm wide. The lengths of versions 9 through 16 begin with POLY1 lengths of 151 μm and increase by 25 μm intervals. The POLY2 lengths are exactly 45 μm longer than the POLY1 sections for all versions 1-8 of this device and are exactly 65 μm longer than the POLY1 sections for versions 9-16 of this device.

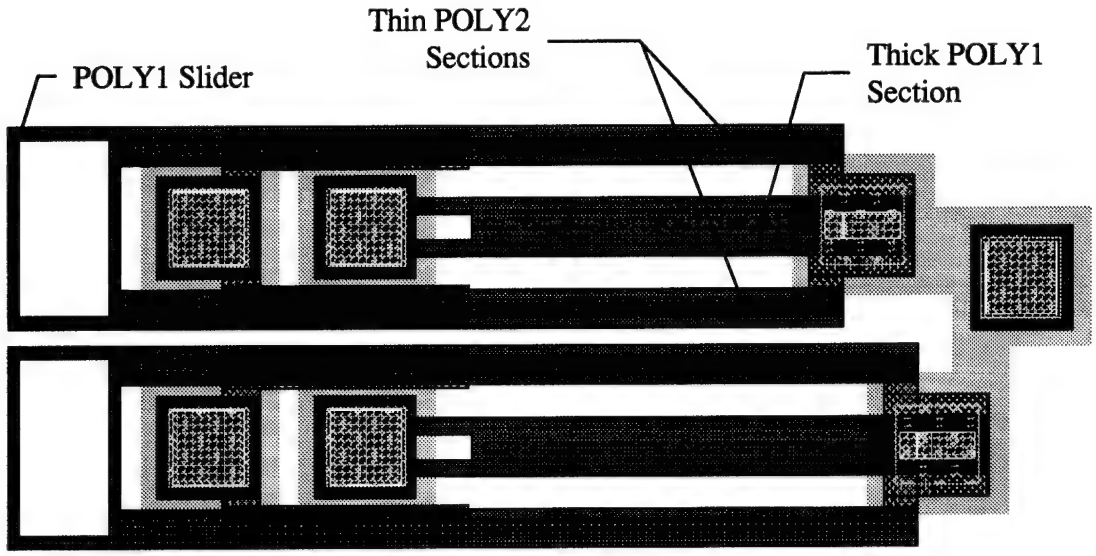

Figure 4.18. CADENCE layout of the vertical heat-drive actuator. Shown here: version 1 fabricated in MUMPs 6.

Figure 4.19. SEM micrograph of the fabricated vertical heat-drive actuator. Shown here: version 1 fabricated in MUMPs 6.

Device Name: **MUMPs Heat Lock Switches**
Fabrication Runs: **MUMPs 6 (ver. 1-6)**
Actuation Method: **Differential Heating**

These devices are operated by first actuating the heat-drive actuators that form the clamps. Once the clamp is open, the main heat-drive actuator attached to the contact electrode can be actuated into position. By releasing the current which holds the clamp open, the contact electrode is locked into place. The main heat-drive actuator is then turned off. At this time, either an a.c. or d.c. signal can be passed from the clamp section, through the contact electrode, and into the main heat-drive actuator. The switch can be turned "off" by opening the clamp and allowing the contact electrode to snap back to its original position.

Versions 1, 2, and 3 use POLY1 as a structural layer, while versions 4, 5, and 6 use POLY2 as a structural layer. Versions 1 and 4 use a rectangular shaped contact electrode, versions 2 and 5 use a trapezoidal shaped contact electrode, and version 3 and 6 use a round contact electrode. The POLY2 versions are intended to be more efficient because the METAL on the thick sections of the heat-drive actuators should act as a heat-sink, thus improving the temperature difference between the thin and thick sides of the device. The dimensions for each version of this switch are summarized in Table 4.9.

Table 4.9 Heat Lock Switch Dimensions*.

Version/ Type	Length** (μm)	Thin-Side Width (μm)	Thick-Side Width (μm)	Flexure Length (μm)	Contact Elec. Area (μm^2)
1/main	300	4	10	8	16
1/clamp	230	4	10	8	16
2/main	300	4	10	8	52
2/clamp	230	4	10	8	52
3/main	300	4	10	8	17
3/clamp	230	4	10	8	17
4/main	300	4	10	8	12
4/clamp	230	4	10	8	12
5/main	300	4	10	8	39
5/clamp	230	4	10	8	39
6/main	300	4	10	8	17
6/clamp	230	4	10	8	17

*The gap between the thin and thick sections of these heat-drive actuators is 4 μm. this corresponds to a "g" dimensions (see Figure 3.8) of 11 μm.

**This length is the total length including the length of the flexure.

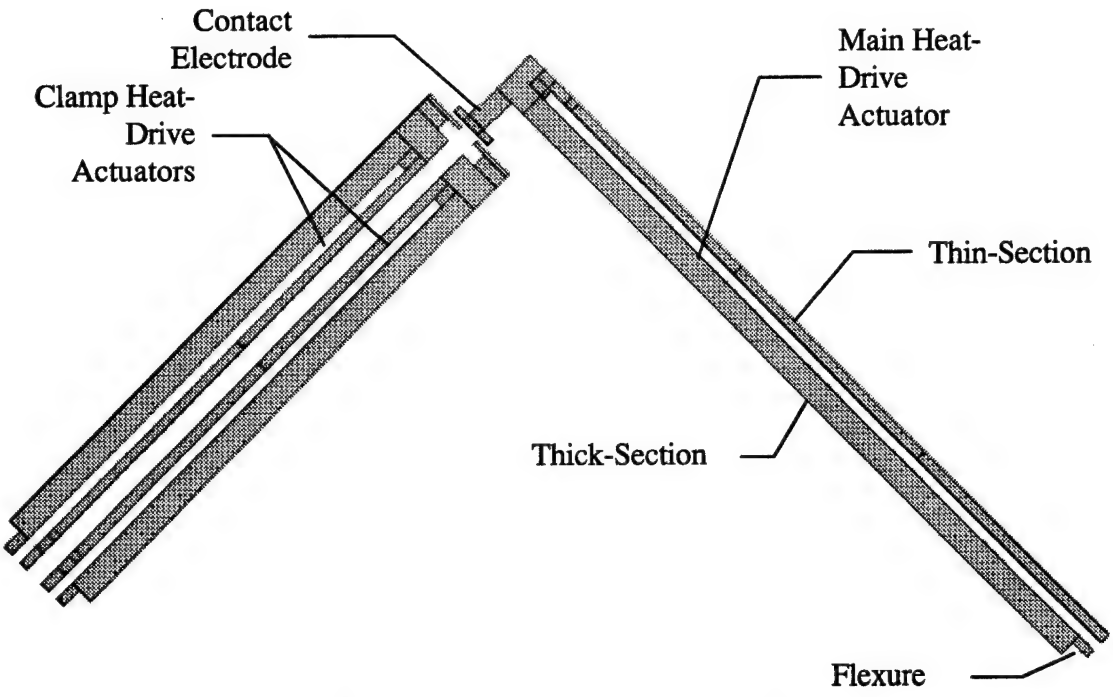

Figure 4.20. CADENCE layout of the heat lock switch. Shown here: version 1 fabricated in MUMPs 6

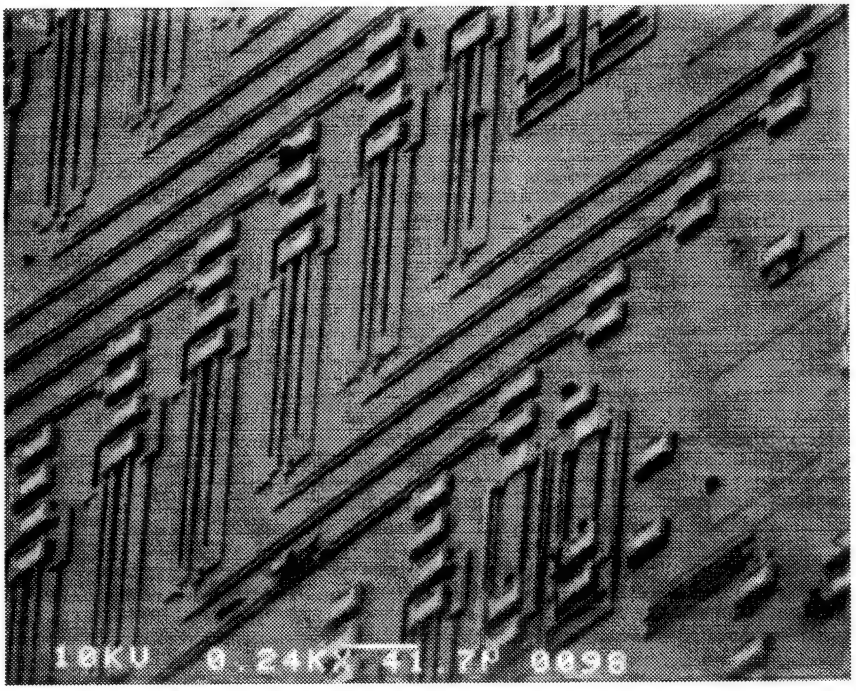

Figure 4.21. SEM micrograph of fabricated heat lock switches. Shown here: version 1 fabricated in MUMPs 6.

Device Name: **Rotating Lever Switch**
Fabrication Runs: **MUMPs 6 (ver. 1)**
Actuation Method: **Mechanical/Differential Heating**

This device is operated by applying current to one of the heat-drive actuators. The resulting deflection pushes on the short end of the lever arm and causes a large deflection at the opposite end of the lever arm. This large deflection rotates the contact tip far enough such that it is in contact with only one of the POLY0 signal pads. This forms the "off" position. By applying current to the other heat-drive actuator, the contact tip can be moved back into contact with both POLY0 signal pads. In this position, a signal, either a.c. or d.c., can be passed between the POLY0 signal pads. This forms the "on" position. Additionally, once the contact tip is in the "on" position, the contact resistance can be improved by applying additional pressure with a vertical heat-drive actuator.

The heat-drive actuators in the rotating lever switch have a length of 250 μm (including the flexure), a thick-side width of 10 μm, a thin-side width of 4 μm, and a flexure length of 8 μm. The gap between the thick and thin sections of the heat-drive actuator is 4 μm which corresponds to a "g" dimension (Figure 3.8) of 11 μm. The short arm of the lever is 42 μm long and the long arm of the lever is 127 μm in length. The vertical heat-drive actuator has a POLY1 section length of 92 μm, POLY2 section length of 137 mm, and a total contact area is 54 μm^2. The total contact area is defined as the total amount of area on the tip of the lever that contacts both signal pads.

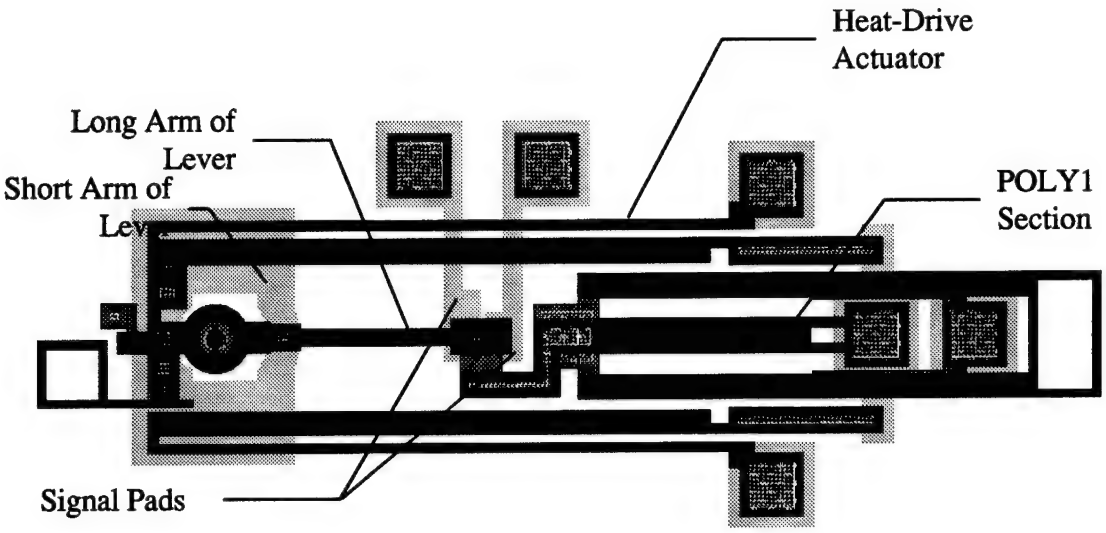

Figure 4.22. CADENCE layout of the rotating lever switch. Shown here: version 1 fabricated in MUMPs 6.

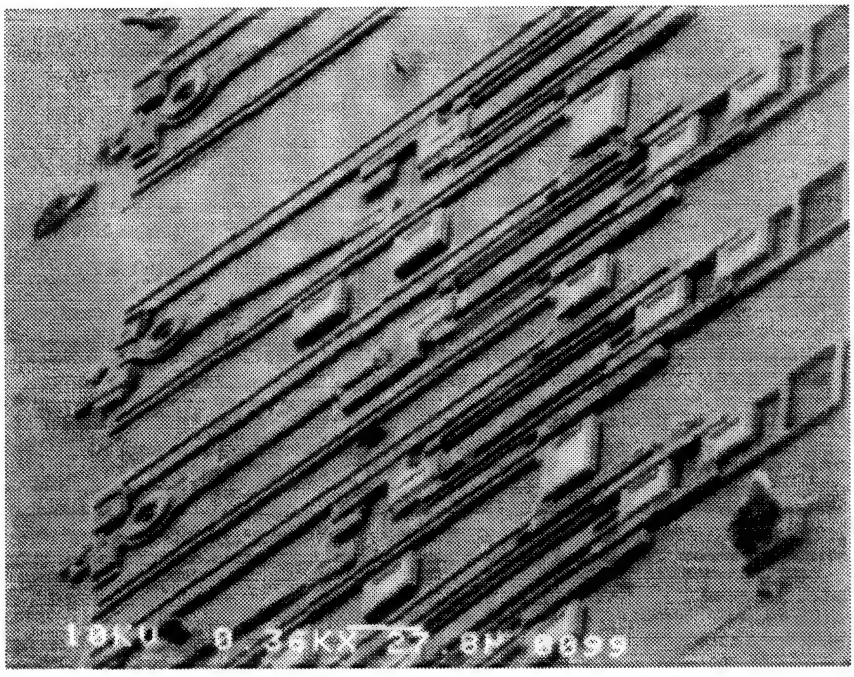

Figure 4.23. SEM micrograph of the fabricated rotating lever switch. Shown here: version 1 fabricated in MUMPs 6.

Device Name: **Plate Switches**
Fabrication Runs: **MUMPs 6 (ver. 1, 2)**
Actuation Method: **Electrostatic Forces**

These devices are operated by applying a d.c potential between the plate and the POLY0 drive electrode beneath it. When the plate is deflected downward, the DIMPLE contacts at each end of the plate come into contact with POLY0 signal pads. In this position, a small a.c. signal (relative to the d.c. actuating potential) can be passed from one POLY0 signal pad, through the plate, and to the other POLY0 signal pad. Releasing the d.c. actuating potential returns the device to its initial "off" position. Version 2 of this device is intended to reduce the necessary drive potential by using a longer plate with a larger drive electrode. The dimensions of both versions of this switch are summarized in Table 4.10.

Table 4.10. Plate Switch Dimensions.

Version	Drive Electrode Area (μm)	Signal Pad Contact Area (μm^2)	Spring "a" Length*	Spring "b" Length*
1	116 x 80	2736	86	43
2	166 x 80	2736	86	43

* These dimensions are labeled in Figure 4.24. The line width of the springs is 3 μm.

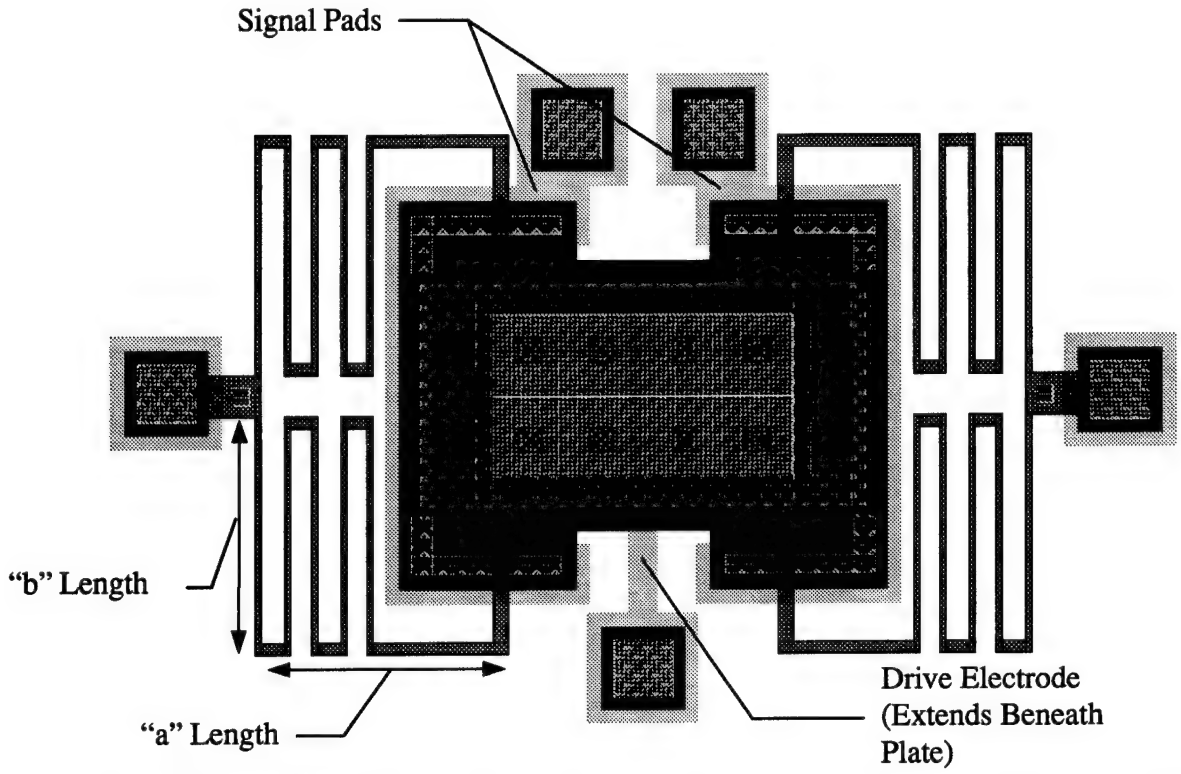

Figure 4.24. CADENCE layout of the plate switch. Shown here: version 1 fabricated in MUMPs 6.

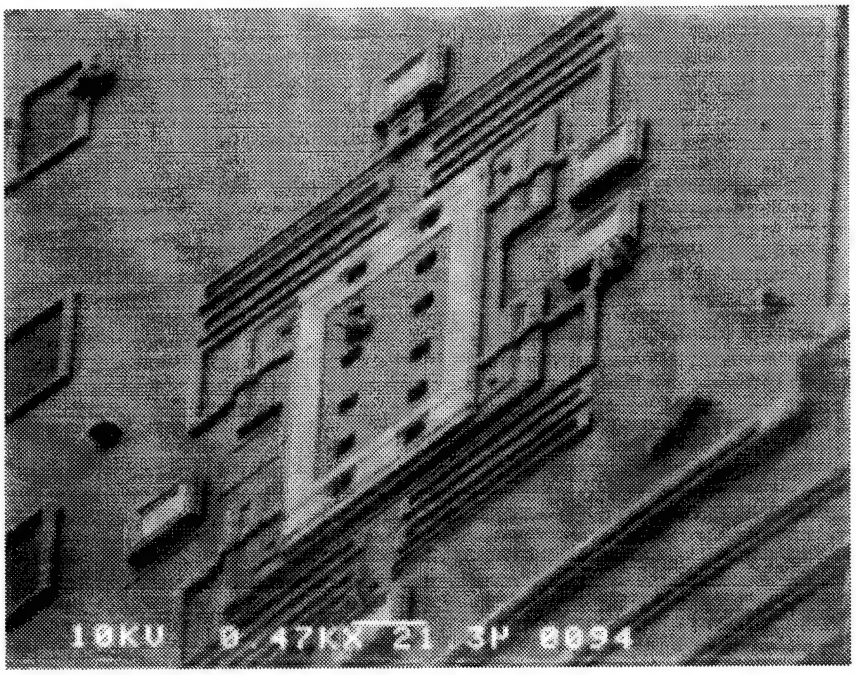

Figure 4.25. SEM micrograph of the plate switch. Shown here: version 1 fabricated in MUMPs 6.

Device Name: **Back Bending Switch**
Fabrication Runs: **MUMPs 7 (ver. 1)**
Actuation Method: **Differential Overheating**

This device is set up by using a micromanipulator probe to push the POLY1 contact block in between the two heat-drive actuators. Current is then applied to these two actuators until they just begin to overheat. This slight overheating makes the heat-drive actuators back-bend severely. When back-bent, they will contact the contact block at which time the actuating current is turned off and either an a.c. or d.c. signal can be passed from one heat-drive actuator to the other. The switch can be turned "off" by reactuating the heat-drive actuators. The length of the heat-drive actuators is 270 μm, with a thin-section width of 4 μm, a thick-section width of 15 μm, a flexure length of 11 μm, and a contact area of 32 μm^2. The gap between the thin and thick sections is 4 μm which corresponds to a "g" dimension (Figure 3.8) of 13.5 μm.

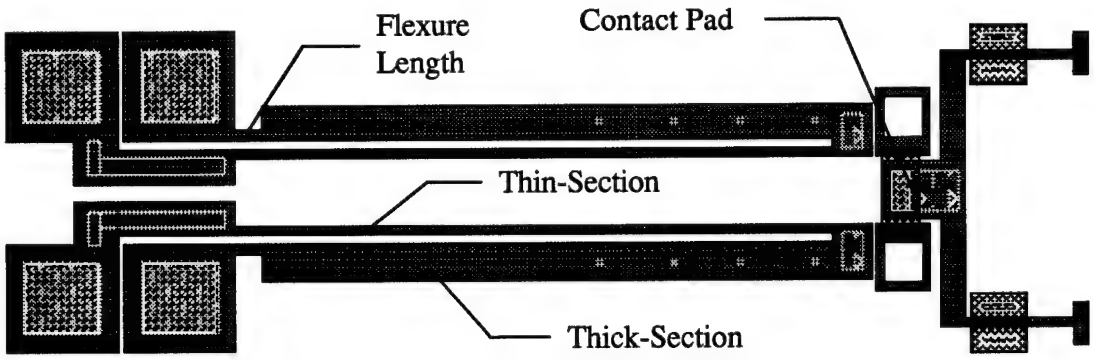

Figure 4.26. CADENCE layout of back bending switch. Shown here: version 1 fabricated in MUMPs 7.

Device Name: **Heat-Rotate Switch**
Fabrication Runs: **MUMPs 7 (ver. 1, 2)**
Actuation Method: **Differential Overheating**

This switch is operated by first opening and overheating the clamps in a similar manner to Back Bending Switch, above. The contact pad is brought into position by actuating one of the heat-drive actuators next to the lever arm. This forces the contact pad to rotate in between the two clamp heat-drive actuators. Because the clamp devices have been overheated, they will back-bend and contact the contact pad. At this point, either an a.c. or d.c. signal can be passed from one side of the clamp to the other. The switch can be turned "off" by opening the clamp and then actuating the other heat-drive actuator by the lever arm. This rotates the contact pad out from inside the clamp. Version 2 of the switch differs from version 1 only in the length of heat-drive actuators used. The signal contact area for both versions of this switch is 52 μm^2. The length of the short end of the lever is 105 μm and the length of the long end of the lever is 230 μm. The dimensions particular to both versions of this switch are summarized in Table 4.11. The gap between the thin and thick sections of the heat-drive actuators is 4 mm which corresponds to a "g" dimension (Figure 3.8) of 13.5 μm.

Table 4.11. Heat-Rotate Switch Dimensions.

Version/ Type	Length (μm)	Thin-Side Width (μm)	Thick-Side Width (μm)	Flexure Length (μm)
1/lever	250	4	15	11
1/signal	275	4	15	11
2/lever	325	4	15	11
2/signal	275	4	15	11

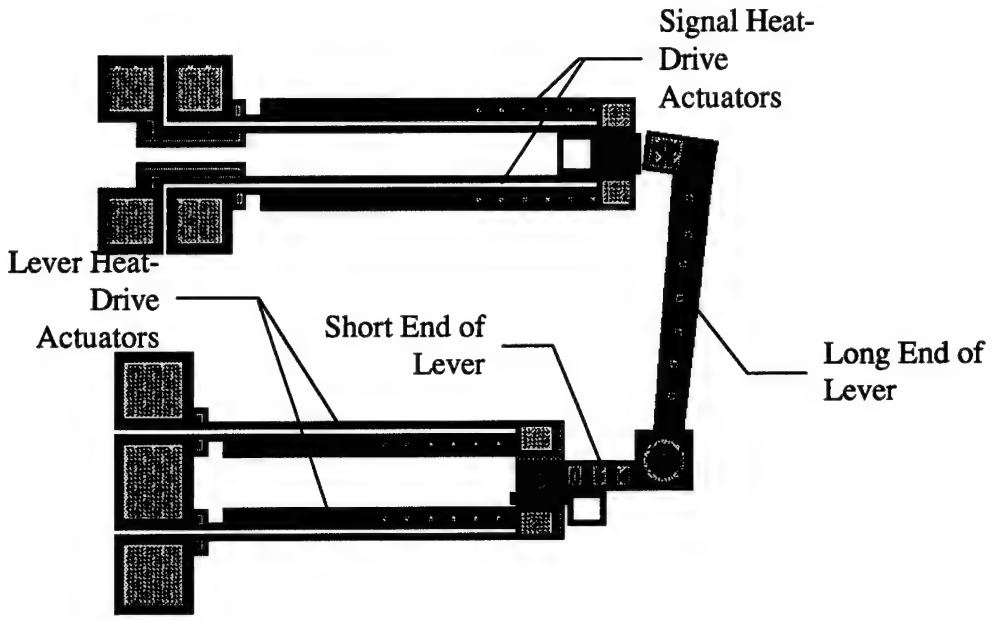

Figure 4.27. CADENCE layout of heat-rotate switch. Shown here: version 1 fabricated MUMPs 7.

Device Name:	**Basic Heat Switch**
Fabrication Runs:	**MUMPs 7 (ver. 1, 2)**
Actuation Method:	**Differential Heating**

This device is operated by first actuating the heat-drive actuator that can move freely without contacting the other actuator. Once fully actuated, the other heat-drive actuator is moved past the first actuators initial position. Then, the first actuator is released followed immediately by the second. The "hooks" on the ends of the actuators lock into place forming the electrical connection. Either an a.c. or d.c. signal can then be passed from one device to the other. The switch can be turned "off" by reversing the actuation process. Version 2 differs from version 1 only in the length of heat-drive actuators used. Both heat-drive actuators have a thin-section width of 5 μm, a thick-section width of 15 μm, and a flexure length of 12 μm. The gap between the thin and thick sections is 4 μm

which corresponds to a "g" dimension (Figure 3.8) of 14 μm. The total contact area for both versions of this switch is 12 μm^2. The length of the heat-drive actuator is 270 μm for version 1 and 340 μm for version 2.

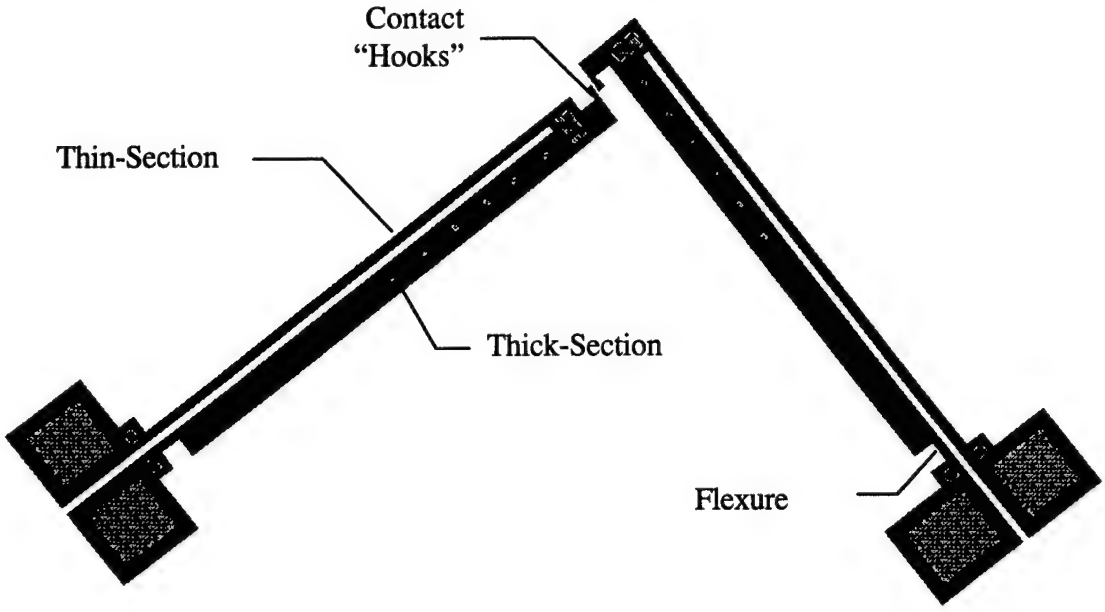

Figure 4.28. CADENCE layout of simple heat switch. Shown here: version 1 fabricated in MUMPs 7.

4.3. LIGA Process

4.3.1. General Design Considerations. The two LIGA processes available through MCNC are single layer processes allowing either 30 μm (thin process) or 150 μm (thick process) tall nickel structures to be fabricated with a minimum feature size of 5 μm. Because this LIGA process consists of only one structural layer, many of the resulting designs are very simple. However, there are several design considerations that must be taken into account.

The minimum feature size for both the thin and thick processes is 5 μm. This means that devices created in the LIGA process will necessarily be much larger than in the MUMPs process. However, because of the thickness of the structural layers, very high aspect ratio (height-to-width) devices can be created. Although this poses no major difficulties on the 30 μm process, it does force a special design rule for the 150 μm process. For devices fabricated with the thick nickel layer, the maximum length-to-width aspect ratio is 10 to 1. This is to avoid long thin runs of PMMA x-ray resist which may not allow proper fabrication of metal structures. This rule may significantly alter some designs and may cause some devices to be infeasible with the 150 μm process.

The major consideration for designing devices in either LIGA process is that there is no patterning of the sacrificial layer. This means that creating movable structures that are attached to the substrate is very difficult. In order to make a structure attached to the substrate, it must be made very large. If it is made large enough, the sacrificial release can be timed such that the etchant does not have enough time to eat underneath the large section. In this way, the device will remain attached to part of the sacrificial layer which is

in turn attached to the substrate. Without access to a truly sacrificial LIGA process, this is the only way to make movable, attached structures in the available process.

The next consideration in using either LIGA process is to note that the high aspect ratio of the LIGA structural layers will limit actuation to motion in the plane of the wafer. Thus, it is necessary to design all devices such that their intended motion is strictly parallel to the plane of the wafer. Additionally, the high aspect ratio will ensure that there will be very little bending out of the plane of the wafer. This can be beneficial because the high aspect ratio will disallow any sagging in long runs of the structural material. This is an immediate cure from some problems that occur in the MUMPs process where the maximum aspect ratio is 1.5 to 1.

4.3.2. LIGA Post Processing Procedures. Post processing of the LIGA devices involves etching the sacrificial layer to release the MEM devices. This is performed by using a solution of 1 part ammonium hydroxide (NH_4OH), 1 part hydrogen peroxide (H_2O_2), and 6 parts deionized water at room temperature. In order to correctly time the etch such that portions desired to be anchored to the substrate are not released, it is necessary to use an etch gauge similar to the one used in the MUMPs process (see page 4-7). At the time of this writing, the devices designed in the LIGA process have not been returned to AFIT for testing. Regardless, device descriptions are given in the following section.

4.3.3. Device Descriptions.

Device Name: **Locking Comb Switch**
Fabrication Runs: **LIGA 2 (ver. 1-7)**
Actuation Method: **Electrostatic Forces/Differential Heating**

This switch uses both comb-drive and heat-drive actuators to form a locking switch. First, the current is run through the heat-drive actuators to open both clamping mechanisms. Then, a d.c. potential is applied between the fixed and movable combs in order to draw the contact electrodes into the clamps. While held in place by the comb-drive, the clamps are then closed, locking the contact electrodes into place. At this point, the potential holding the comb-drive can be released and the device is locked into place. Either an a.c. or d.c signal can then be passed from one clamp to the other. The switch can be turned "off" by again opening the clamps which should allow the comb-drive suspension springs to pull the contact electrode back into its original position.

Versions 1, 2, and 3 are identical except for different numbers of fingers on the comb-drive actuators. Versions 4 and 5 are the same as versions 1 and 2 except that the fingers are shaped trapezoidally rather than rectangular. This is intended to increase the comb-drive actuation force and thereby decrease the necessary actuation voltage. Versions 1 through 5 of this device are all intended for the 30 μm LIGA process. Versions 6 and 7 are the same as versions 1 and 4 except that they were designed for the 150 μm LIGA process. For all versions the lengths of the heat-drive actuators are 200 μm, the thick-section widths are 13 μm, the thin-section widths are 5 μm, and the flexure lengths are 10 μm. The gaps between the thin and thick sections are 5 μm which

corresponds to a "g" dimension (Figure 3.8) of 14 μm. A summary of the dimensions of the different versions of the locking comb switch is given in Table 4.12.

All the heat-drive actuators have a tooth shape applied to the thick-section. This is an attempt to increase the surface are of the thick section, which should allow it cool more efficiently. Since the total deflection is directly proportional to ΔT (see Chapter 3), this should allow the heat-drive actuator to deflect farther.

Table 4.12. Locking Comb Switch Dimensions*.

Version	Number of Fingers	Finger Size (μm)	Spring Length (μm)	Contact Area (μm^2)
1	10	5 x 70	850	5 x 30
2	14	5 x 70	850	5 x 30
3	19	5 x 70	850	5 x 30
4	14	5-15 x 55	850	5 x 30
5	19	5-15 x 55	850	5 x 30
6	14	5 x 70	850	5 x 150
7	14	5-15 x 55	850	5 x 150

*The number of fingers is for the fixed comb. The spring line width size is 5 μm. The contact area is for each lock mechanism individually.

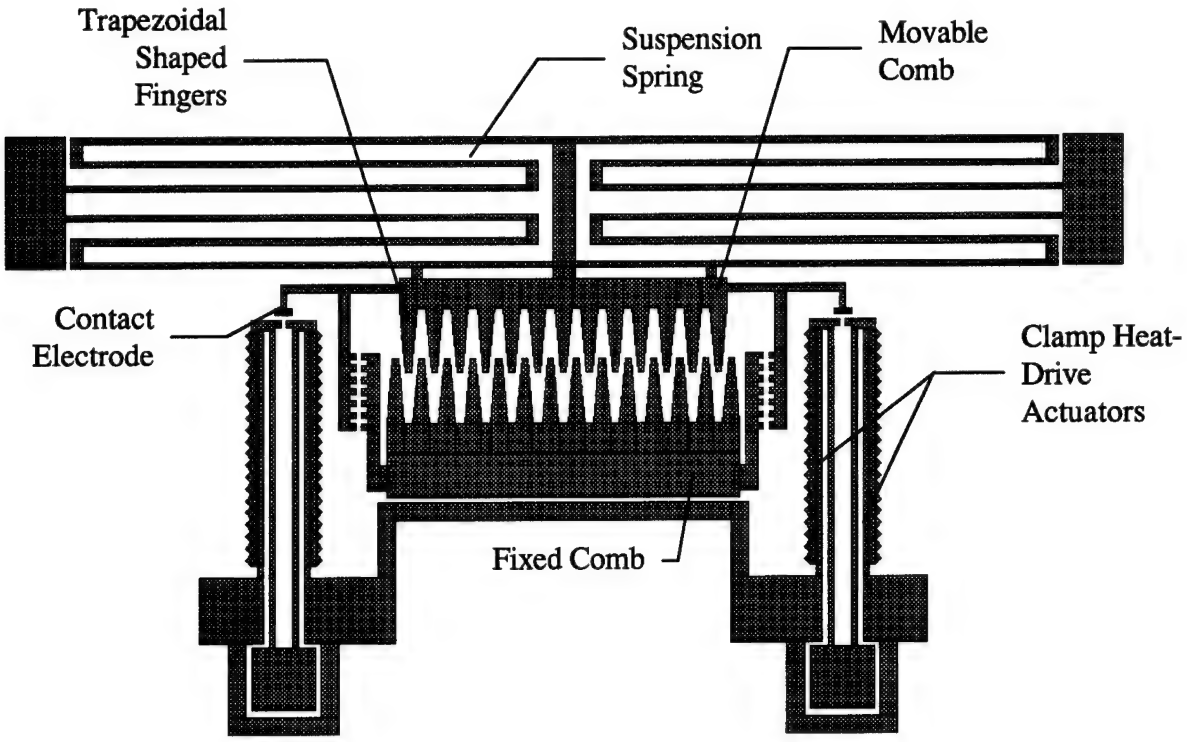

Figure 4.29. CADENCE layout of the locking comb switch. Shown here: version 4 fabricated in LIGA2 30 μm process.

Device Name: **Heat Clamp Switch**
Fabrication Runs: **LIGA 2 (ver. 1-3)**
Actuation Method: **Differential Heating**

The heat clamp switch is operated by first applying current to the heat-drive actuator forming one side of the clamp. This will open the clamp far enough for the contact electrode to be inserted. Once the clamp is open, the other heat-drive actuator is actuated which will force the contact electrode into position. At this time, the clamp can be closed followed by the release of the heat-drive actuator attached to the contact electrode. Now, either an a.c. or d.c. signal can be passed from the contact electrode and into the clamp. The device can be turned "off" by reopening the clamp and allowing the contact electrode to snap back to its original position.

Versions 1 and 2 differ only in the lengths of heat-drive actuators used in the device. Version 3, however, uses a curved heat drive actuator to provide actuation in a non-ninety degree angle. Version 1, 2, and 3 were submitted to the LIGA 30 μm process. A summary of the dimensions for the versions of this switch is given in Table 4.13.

Table 4.13. Heat Clamp Switch Dimensions*.

Version/ Type	Length (μm)	Thin-Side Width (μm)	Thick-Side Width (μm)	Flexure Length (μm)	Contact Area (μm^2)
1/main	200	5	13	10	780
1/clamp	100	5	13	12	780
2/main	400	5	13	10	780
2/clamp	100	5	13	12	780
3/main	125	5	10	10	780
3/clamp	150	5	10	10	780

*The gap between the thick and thin sections of the heat-drive actuators is 5 μm which corresponds to a "g" dimension of 13 μm for versions 1 and 2 and a "g" dimension of 12.5 μm for version 3.

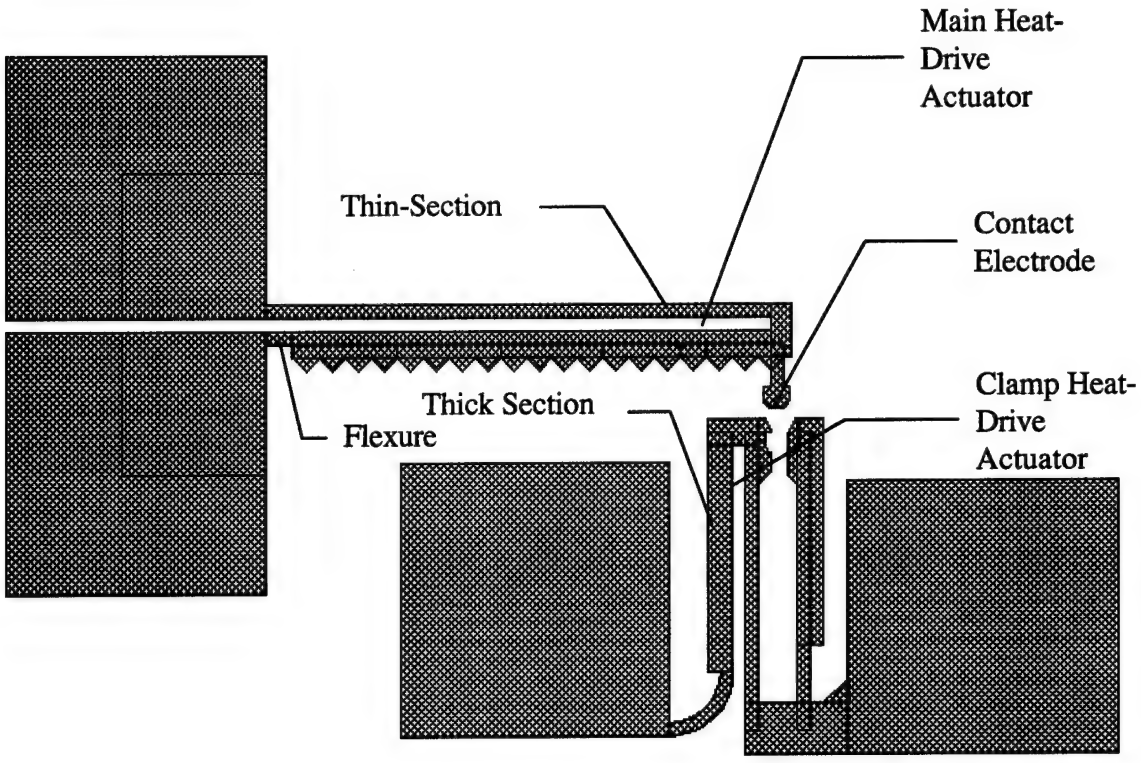

Figure 4.30. CADENCE layout of the heat clamp switch. Shown here: version 1 fabricated in LIGA2 in the 30 μm process.

Device Name: **LIGA Heat Lock Switch**
Fabrication Runs: **LIGA 2 (ver. 1-4)**
Actuation Method: **Differential Heating**

This device is operated by first actuating the heat-drive actuator that can move freely without contacting the other actuator. Once fully actuated, the other heat-drive actuator is moved past the first actuator's initial position. Then, the first actuator is released followed immediately by release of the second actuator. The "hooks" on the end of the actuators lock into place forming the electrical connection. Either an a.c. or d.c. signal can then be passed from one device to the other. The switch can be turned "off" by reversing the actuation process. Version 2 differs from version 1 only in the length of heat-drive actuators used. Versions 3 is the same as versions 1 except that it was designed

for the 150 μm LIGA process. A summary of the dimensions used in all versions of the heat lock switch is given in Table 4.14.

Table 4.14. Heat Lock Switch Dimensions*.

Version/ Type	Length (μm)	Thin-Side Width (μm)	Thick-Side Width (μm)	Flexure Length (μm)	Contact Area (μm^2)
1	200	5	13	10	9 x 30
2	400	5	13	10	9 x 30
3	400	5	13	10	9 x 150

*The gap between the thick and thin sections is 5 μm which corresponds to a "g" dimension of 14 μm.

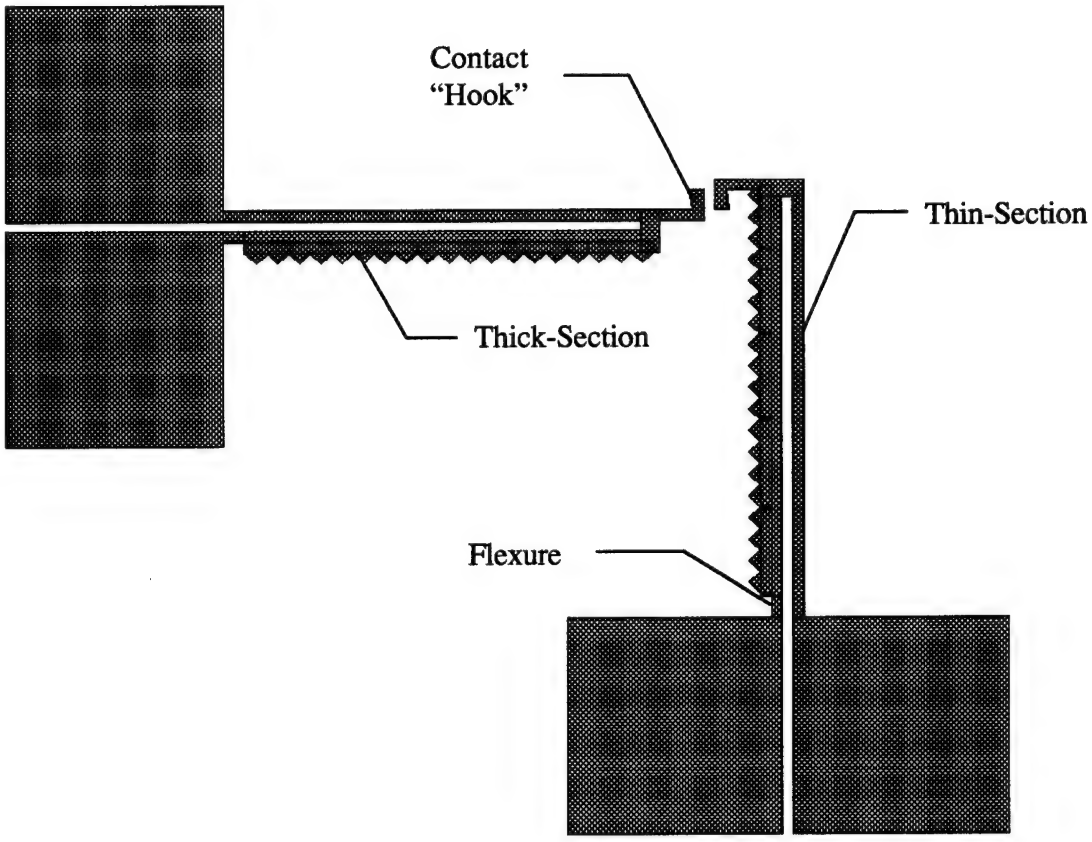

Figure 4.31. CADENCE layout of heat lock switch. Shown here: version 1 fabricated in LIGA2 in the 30 μm process

4.4. Testing and Characterization Equipment

Once devices have been fabricated and released in either the MUMPs or LIGA processes, they must be tested and characterized. The AFIT Cooperative Microelectronics Laboratory has an area designated for the testing of either packaged or unpackaged microelectronic circuits. The following list details the equipment available in this area for device testing, characterization, and post-processing.

Micromanipulator table--The Micromanipulator Company--Model # 6200

The micromanipulator is a device onto which individual die can be held in place by a vacuum chuck and probed with up to four different voltages and currents at a time. The size of probe tips ranges typically between 10 to 20 μm in diameter, but can be smaller. The probes used in this thesis were 15 μm in diameter for probing device pads ranging in size from 20 to 50 μm square. Many different voltage and current supplies and measurement instruments can be routed to the probes on the micromanipulator for testing of MEM devices. These include the electrometer, the high voltage source, the dual power supplies, the multimeters, the function generator, and the digital oscilloscope.

Electrometer--Kiethley Instruments--Model # 617

This device is a digitally controlled voltage source capable of delivering voltages up to +/- 120 volts while allowing very little current to flow. The electrometer is particularly useful for avoiding destruction of electrostatic MEM devices that might short out at high voltages.

Dual Power Supplies (2)--Hewlett Packard--Model # HP 6236B

These supplies are two analog controlled voltage/current sources capable of operating in several modes. The first mode allows either source to supply a maximum of +/- 6 volts or +/- 0.5 amps while the second model allows either source to supply a maximum of +/- 20 volts or +/- 2.5 amps. In addition, the sources may be wired together in series to get up to +/- 40 volts or +/- 2.5 amps.

High Voltage Source--Kikusui Electronics Corp.--Model # PAD 160-1L

The high voltage source is an analog controlled voltage/current source capable of +150 volts. This source is useful for applications in which high voltages are required and current is needed to flow through the circuit.

Multimeters (2)--1. Hewlett Packard--Model # 3478A 2. Fluke--Model # 8600A

The multimeters are the primary voltage, current, and resistance measurement tools available for use with the micromanipulator. The Hewlett Packard meter is capable of resolving voltages from 0 to +/- 300 volts and currents from 0 to +/- 3 amps. The Fluke meter is capable of resolving voltages from 0 to +/- 1200 volts and currents from 0 to +/- 2 amps. Both meters can read resistances of up to 30 MΩ.

Function Generator--Hewlett Packard--Model # 54100A

The function generator is capable of producing square-wave, sinusoidal and sawtooth waveforms at frequencies from 10 Hz to 20 MHz. The peak-to-peak voltage can be varied from 0.1 to 10 volts with a d.c. bias of up to +/- 10 volts.

Digital Oscilloscope--Hewlett Packard--Model # 54100A

The digital oscilloscope is capable of representing any voltage waveforms which do not exceed the input peak voltage limitation of 2.0 volts. It is also capable of displaying two different signals with independent scales. Scaling can be set manually or can be calibrated automatically.

Ball Bonder--Kulicke and Soffa Industries

This device uses a combination of temperature, pressure, and ultrasound to bond 25 μm thick gold strands to header packages for testing of devices requiring more than four contacts at one time. Pads of at least 100 μm on a side are required to be effectively bonded without damaging the die. The bonder can only be operated manually.

Scanning Electron Microscope--International Scientific Instruments--Model # WB-6

The scanning electron microscope is the most effective method for viewing micromechanical devices after release. It is capable of easily resolving the minimum feature sizes capable in either the MUMPs or LIGA processes. It is especially useful for viewing the three dimensional nature of fabricated MEM devices. However, in order to improve the focus to high resolutions, it is necessary to sputter a thin (300 angstroms) layer of gold onto the characterized die. This helps eliminate charging of polysilicon layers which can interfere with the electron beam and degrade the image.

4.5. Switch Testing Procedures

All the switches discussed in sections 4.2 and 4.3 can be broken down into two basic categories. The first category includes those switches that require constant voltage or current inputs in order to keep the switch closed. This necessarily limits the switchable

signal types to a.c. signals with the actuating potential as a d.c. bias. For the purposes of this section, switches in this category will be referred to as "simple" switches. The other category includes all the switches that can be locked into either the "on" or "off" positions without continuously applied drive inputs. These devices are more flexible because they can switch any type of signal, either a.c. or d.c. Switches in this category will be referred to as "locking" switches. Table 4.15. lists all the devices described in sections 4.2 and 4.3 and their corresponding category.

All the "simple" switches described in sections 4.2 and 4.3 operate using electrostatic forces, and, as a result, are tested in the same manner. The general procedures for testing these devices are given in Table 4.16, but in order to better illustrate this process, an example of the testing of a microbridge switch is given in Figure 4.32. First, the electrometer is set up such that it has a common ground with the function generator and the oscilloscope. Then, the positive lead from the electrometer is put into contact with the microbridge's drive electrodes while the ground lead is put into contact with the bridge. The function generator is then set at a conservative, sinusoidal frequency (1 kHz), low peak-to-peak voltage (0.5 volts), and a zero d.c. bias. The signal lead of the function generator is then connected to input 1 of the oscilloscope and to the bridge's sense electrode. Finally, input 2 of the oscilloscope is connected to the bridge portion of the microbridge.

Before the microbridge is actuated, the oscilloscope should be reading the input sinusoidal signal on input 1 and nothing on input 2 (meaning the switch is in the "off"

Table 4.15. List of Switch Categories for Determining Proper Test Procedures.

"Simple" Switches	"Locking" Switches
Microbridge Switch	Push Lock Switch
Cantilever Beam Switch	Heat-Spring Switch
Simple Comb-Drive Switch	Clamp-Lock Switch
MUMPs Heat Lock Switch	Electrostatic Cantilever-Lock Switch
Plate Switches	Hinge Switch
	Rotating Lever Switch
	Back Bending Switch
	Heat-Rotate Switch
	Basic Heat Switch
	Locking Comb-Drive Switch
	Heat Clamp Switch
	LIGA Heat Lock Switch

Table 4.16. General Testing Procedures for Switches in the "Simple" Category.

Step	Procedure
1	Connect electrometer, function generator, and oscilloscope to common ground.
2	Connect positive electrometer lead to the drive electrode and connect the ground lead to the appropriate electrode opposite the drive electrode.
3	Set the function generator to a sinusoidal signal at 1 kHz, 0 volts d.c. bias, and 0.5 volts peak-to-peak.
4	Connect function generator to sense electrode and to input 1 of the oscilloscope.
5	Connect input 2 of the oscilloscope to the switch electrode on the opposite side of the switch from input 1 (connected in step 4).
6	Check that input sinusoidal signal is displayed on input 1 of oscilloscope and nothing is displayed on input 2 (no short circuits).
7	Test a.c. isolation by scanning the input frequency from 10 Hz to 10 MHz. Any coupled signal on input 2 of the oscilloscope indicates a frequency limitation of the device.
8	Reset frequency to 1 kHz.
9	Slowly increase electrometer voltage until the signal on input 2 of the oscilloscope is the same as the signal on input 1. The switch is "on".
10	Scan the input frequency from 10 Hz to 10 MHz to determine the upper and lower 3 dB frequencies.
11	Return switch to "off" position by turning down electrometer voltage.

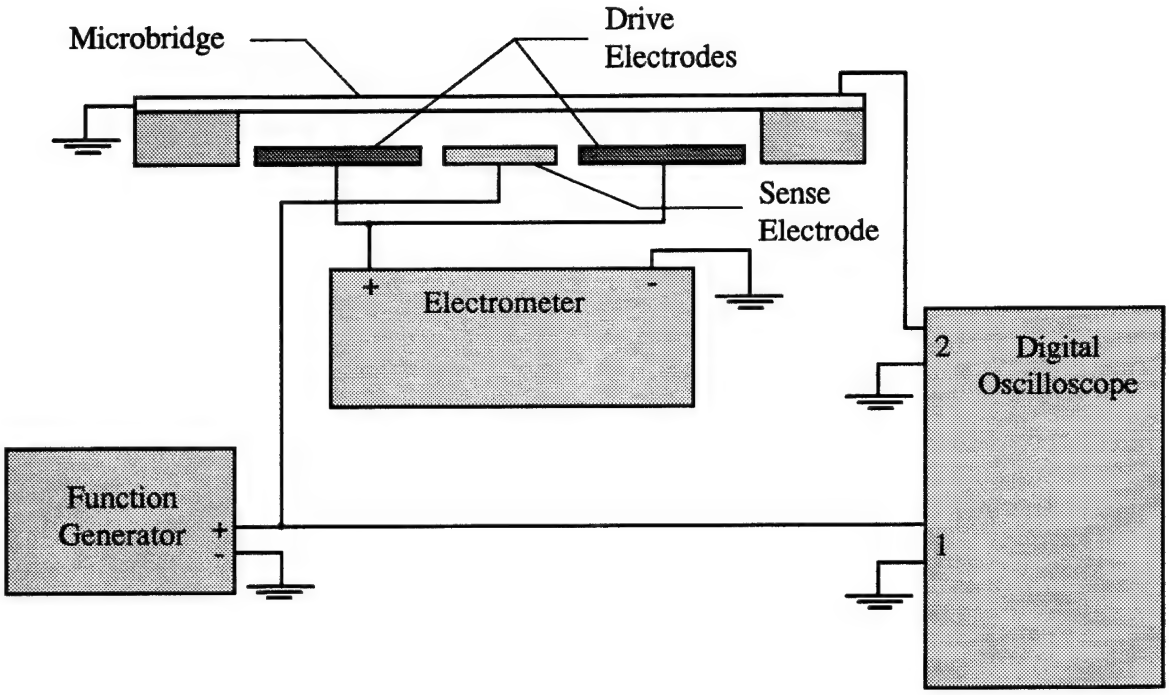

Figure 4.32. Schematic example of the testing process for the "simple" switches using a microbridge switch.

position). At this point, a.c. isolation ranges can be checked. This is performed by scanning the frequency between 10 Hz and 10 MHz. Any coupling of the input signal to the output signal up to this frequency would indicate the limit for a.c. isolation in this device. Next, the frequency is returned to 1 kHz and the d.c. bias from the electrometer is applied. The d.c. bias should be slowly increased until the a.c. signal on input 2 of the oscilloscope is equal to the a.c. signal on input 1. When this occurs, the switch is closed. While held closed, the frequency can be scanned again (from 10 Hz to 10 MHz) to determine the upper and lower 3 dB frequencies. To restore the switch to the "off" position, the bias voltage from the electrometer is turned off.

Like the "simple" switches, the testing of devices in the "locking" category also follows a general procedure (Table 4.17). Because these devices lock into place in both the "on" and "off" positions, the equipment set-up procedures are more straightforward than for the "simple" switches. The first step characterizing these devices is to test the a.c. isolation in the same manner as in the "simple" switches. After that has been performed, the switch is then locked in place using the appropriate power supplies afterwhich they can be disconnected from the MEM switch. Next, the upper and lower 3 dB frequencies can be determined by using the function generator and the oscilloscope in a manner similar to that for the "simple" switches. Subsequently, the contact resistance can be estimated by connecting a multimeter to probe pads on either side of the switch connection. Lastly, the switch can be returned to the "off" position performing the appropriate actuation process for each particular device.

Table 4.17. Testing Procedures for Switches in the "Locking" Category.

Step	Procedure
1	Start with the MEM switch in the "off" position.
2	Set oscilloscope and function generator to have common grounds.
3	Attach function generator lead to one side of the switch and to input 1 of the oscilloscope. Connect input 2 of oscilloscope to the opposite switch electrode than input 1 is attached.
4	Scan input frequency from 10 Hz to 10 MHz. Any coupling of the signal on input 1 to input 2 indicates a frequency limitation of the switch in the "off" position.
5	Disconnect the function generator and oscilloscope from the switch.
6	Use the appropriate voltage/current sources as needed to lock the switch in place.
7	Once locked, disconnect all sources from the switch.
8	Reattach function generator and oscilloscope as done in step 3.
9	Scan input frequency from 10 Hz to 10 MHz to determine the upper and lower 3 dB frequencies.
10	Disconnect function generator and oscilloscope. Attach multimeter leads to each side of the switch.
11	Test contact resistance of the "on" switch.
12	Test maximum current/voltage capacity of the switch by closing the switch (step 6) and then slowly increasing the d.c. signal through the switch until it fails.

4.6. Summary

In this chapter, many topics were discussed. The first of these was the design submission process for taking computer drawn layouts and having them fabricated in a commercial foundry. Additionally, general design considerations, post-processing procedures and device descriptions were given for switches created in both the MUMPs and LIGA processes. The last section dealt exclusively with the testing procedures associated with the two categories of switches that were developed, the "simple" switches and the "locking" switches. Chapter 5 introduces and discusses the results achieved after testing the MEM devices that have been received from the commercial foundries.

5. Results and Discussion

This chapter describes the results of the fabrication and testing procedures for each of the major devices and switches discussed in Chapter 4. First, the general results of each of the fabrication process (MUMPs 4, MUMPs 5, and MUMPs 6) are discussed, followed by device performance results. Device and switch performance results are broken down into the categories of electrostatic actuated switches and heat-drive actuated devices.

5.1. General Process Results

Only designs submitted to the MUMPs fabrication process were completed during this thesis research. Although designs were submitted to the LIGA process, the fabrication cycle is not yet complete so devices designed in the LIGA process could not be tested. For the three MUMPs runs (MUMPs 4, MUMPs 5, and MUMPs 6) which have been fabricated and returned to AFIT, the fabrication quality has generally been very good. Statistics for each of these MUMPs runs are given in Table 5.1. Designs were also submitted for the MUMPs 7 fabrication run, however, the devices have not yet been returned to AFIT for testing.

The only *major* processing difficulty with the MUMPs fabrication process was the use of copper for the metal layer in the MUMPs 4 run. Copper was chosen by the foundry because it would survive the sacrificial release process better than the aluminum which was used prior to MUMPs 4. However, the copper tended to corrode over time such that after a few weeks of exposure to the ambient atmosphere, all metal surfaces

Table 5.1. Process Statistics for MUMPs 4, MUMPs 5, and MUMPs 6.

Film	Thickness (A)	Stress (MPa)	Resistivity(Ω-cm)
MUMPs 4			
POLY0	5207	14 (C)	1.74E-3
POLY1	18755	4 (C)	2.95E-3
POLY2	14800	9 (C)	2.74E-3
Cu	5200	73 (T)	2.08E-6
Si_3N_4	5169	63 (T)	---
OXIDE1	Not Given	---	---
OXIDE2	Not Given	---	---
MUMPs 5			
POLY0	5450	10 (C)	2.34E-3
POLY1	20175	3 (C)	3.33E-3
POLY2	14800	8 (C)	4.00E-3
Cr/Au	5200	29 (T)	2.96E-6
Si_3N_4	4940	113 (T)	---
OXIDE1	20800	---	---
OXIDE2	5150	---	---
MUMPs 6			
POLY0	5200	19.7 (C)	1.84E-3
POLY1	20220	5.1 (C)	2.58E-3
POLY2	15650	5.1 (C)	2.72E-3
Cf/Au	5540	30 (T)	3.39E-6
Si_3N_4	6213	19.2 (T)	---
OXIDE1	20151	---	---
OXIDE2	5230	---	---

were coated with a reddish-blue film. This film could be scraped away for probe contacts, but this left unwanted debris on the wafer surface. The copper also proved

troublesome for wirebonding. As the die was brought up to temperature for bonding, the rate of corrosion dramatically increased. After five to ten minutes at elevated temperature (100 °C), the corrosion was prevalent enough to keep the bonding wires from adhering to the bonding pads on the die. For all subsequent fabrication runs, the MUMPs foundry used Cr/Au as the metal layer. The gold adequately survived the sacrificial release and did not have any wirebonding or corrosion problems.

5.2. Electrostatic Device Results.

Many of the devices fabricated on the MUMPs 4, 5, and 6 fabrication runs operated based upon electrostatic forces. These included the microbridge switch, the cantilever switch, the plate switch, and the numerous switches which employed comb-drive actuators. Although many of the devices worked to some degree, there were some general problems with the electrostatic based devices.

The primary problem was a direct result of the thickness of the polysilicon layers and the minimum feature sizes available in the MUMPs process. All movable structures were required to be designed with a minimum feature size of 2.0 μm with a thickness of either 2.0 μm or 1.5 μm depending on whether POLY1 or POLY2 was used. Because of these limitations, the minimum thickness of device structural layers was 2.0 μm or 1.5 μm (depending on whether POLY1 or POLY2 was used) and the minimum horizontal dimension was 2.0 μm (minimum feature size). This limited all suspension beams and springs to these minimum dimensions and consequently made them very stiff. In order to move devices supported with such stiff beams and suspension springs, large electrostatic

forces were necessary. Because the minimum electrostatic gap achievable was 1.5 μm in the vertical direction and 2.0 μm in the horizontal direction, very large voltages were required to achieve significant deflection.

As a result of the sacrificial release process and the die's exposure to the atmosphere, significant amounts of dust and debris were scattered across the wafer surface. The dust and debris became particularly troublesome as voltages were increased to achieve significant deflection. At high voltages, nearby dust and debris were often pulled into the electrostatic gap and shorted the connection. Even with current limiting equipment such as the electrometer, some current would flow through the short and usually destroy the device.

5.2.1. Microbridge Switch. The microbridge switch was intended to operate as a switch that could couple an a.c. signal superimposed over a d.c. actuation potential. The switch was closed by applying a d.c. potential between the drive electrodes and the microbridge beam (see Chapter 4 for complete device description and test procedures). However, because the microbridge elements were fabricated from the 2.0 μm thick POLY1 layer, they were extremely stiff and large voltages were required to force the microbridge center to touch the sense electrode. Once closed, however, the switch could not usually be reopened by releasing the drive potential. The microbridge center would stick to the sense electrode requiring vigorous agitation with the micromanipulator probe to release the switch. This release technique did not work in all cases, though. Approximately 50% of the switches were destroyed during attempts to release them in this manner.

While stuck in the closed position, though, the microbridge switch was able to pass d.c. as well as a.c. signals. This allowed the d.c. switching quality of the microbridge to be investigated along with the a.c. quality. The switching characteristics tested included the necessary drive voltage to close the switch (closing voltage), the d.c. contact resistance while in the stuck-down position, maximum signal amplitude (voltage and current), and upper and lower 3 dB frequencies.

The closing voltage was determined to be the potential needed to switch an a.c. signal such that the output signal was not distinguishable from the input signal when viewed on the oscilloscope. The first column in Table 5.2 shows the mean and standard deviation for the closing voltages for each of the microbridge versions that were tested. The relatively low standard deviation (< 10% of the mean value) indicates that the structural quality of the POLY1 structural layer was consistent for the devices that were tested. However, the mean values did deviate somewhat from the predicted values (all the predicted values are given in column three of Table 5.2). This deviation can be accounted for in the way the predicted voltage was calculated. The predicted closing voltage was calculated by iteratively solving Eq. (3.20). The gap between the center of the microbridges and the sense electrode, 2 μm, was substituted into Eq. (3.20) as δ_T and all other physical dimensions needed were taken from Table 4.3. A value of 200 GPa was assumed for Young's modulus (E in Eq. (3.20)). Thus, the only unknown left was the applied voltage. This was iteratively solved for using a MathCAD solve block.

For example, for a version one microbridge, the length, L, was 332 μm, the bridge width, b, was 40 μm, the thickness of the POLY1 layer, h, was 2 μm, and the gap between

the center electrode and the sense electrode, d, was 2 μm. Referring to Figure 3.3 (b), the first drive electrode for the version one microbridge began at x = 45 μm and ended at x = 125 μm. The other drive electrode began at x = 207 μm and ended at x = 287 μm. Substituting the known parameters into Eq. (3.20), the following relation was specified for the version one microbridges:

$$2\mu m = \int_{45\mu m}^{125\mu m} \frac{4\varepsilon_o}{E \cdot h^3}\left[\frac{x^2 \cdot (L-x)^3}{(3L-2x)^3}\right] \cdot \frac{V^2}{\left(d - \left(\frac{x}{1/2}\right)^2 \cdot 2\mu m\right)^2} dx + \int_{207\mu m}^{287\mu m} \frac{4\varepsilon_o}{E \cdot h^3}\left[\frac{x^3 \cdot (L-x)^2}{(2x-L)^3}\right] \cdot \frac{V^2}{\left(d - \left(\frac{L-x}{1/2}\right)^2 \cdot 2\mu m\right)^2} dx \qquad (5.1)$$

where E is 200 GPa, ε_o is 8.85 x 10^{-12} F/m and all other parameters were given above. The only unknown was V which was the voltage applied between the microbridge and the drive electrodes. By placing Eq. (5.1), as shown, directly into MathCAD between a GIVEN and a FIND statement and supplying a guess value (V = 50 volts), the applied voltage necessary to close the microbridge was calculated. In this example, V was determined to be 62.3 volts.

The predicted values actually give what should be an upper limit for the expected value for the closing voltage. This is because Eq. (3.20) (and Eq. (5.1)) assumes that the beam is one solid structure without any holes or deformations in the beam. However, each beam has a hinge section that should serve to reduce the closing voltage needed to

Table 5.2. Microbridge Switch Summary Data.*

Parameter	Mean Value	Std. Dev.	Predicted Value	# of Test Cases
Version 1				
Closing Voltage	53.3 volts	0.70 volts	62.3 volts	23
Contact Resistance	300 ohms	89.7 ohms	288 ohms	23
Failure Voltage	7.5 volts	0.41 volts	---	8
Failure Current	39.8 mA	2.6 mA	---	8
Upper 3 dB Freq.	> 16 MHz	---	see text	23
Lower 3 dB Freq.	< 10 Hz	---	see text	23
Version 2				
Closing Voltage	57.8 volts	3.8	62.3 volts	35
Contact Resistance	215 ohms	148 ohms	158 ohms	35
Failure Voltage	7.4 volts	0.4 volts	---	8
Failure Current	41.4 mA	2.3 mA	---	8
Upper 3 dB Freq.	> 16 MHz	---	see text	35
Lower 3 dB Freq.	< 10 Hz	---	see text	35
Version 4				
Closing Voltage	59.3 volts	8 volts	67.5 volts	14
Contact Resistance	642 ohms	593 ohms	536 ohms	14
Failure Voltage	4.975 volts	0.05 volts	---	8
Failure Current	24 mA	1.4 mA	---	8
Upper 3 dB Freq.	> 16 MHz	---	see text	14
Lower 3 dB Freq.	< 10 Hz	---	see text	14

*Version 3 is not tabulated because the devices were not able to operate as switches and none of the above parameters could be measured.

fully deflect the microbridge. Thus, it is expected that the closing voltage is lower than the predicted value.

The d.c. contact resistance was determined by measuring the d.c. resistance between the input signal pad and the sense electrode and then subtracting out the resistance of the microbridge. The d.c. resistance between the input signal pad and the sense electrode pad was measured by placing micromanipulator probes on the two pads and using a multimeter to measure the resistance between them. The microbridge resistance was determined by measuring the resistance from the probe pad at one end of the bridge to the probe pad at the other end. Because the signal only passes through one half this length, the measured resistance was halved. A total of 12 microbridges for each version were tested in this manner. The mean bridge resistance was 136 +/- 20 ohms (the error is taken as the first standard deviation from the mean) for version 1, 134 +/- 3.9 ohms for version 2, and 206 +/- 25 ohms for version 3, and 185 +/- 4.2 ohms for version 4. These values can be compared to the predicted resistances which were calculated from the dimensions of the microbridge and the resistivity of the POLY1 structural layer found in Table 5.1. For example, in version one of the microbridges, the bridge was 40 μm wide, had a length of 332 μm, and had hinges that were 4 μm by 30 μm. By assuming that the resistance R, equals (ρ x length)/Area, the resistance of each hinge was (0.00295 ohm-cm x 0.0030 cm)/(0.00018755 cm x 0.0004 cm) which equals 117.9 ohms. The hinges actually formed resistors in parallel, thus the total resistance contribution due to both hinges was 58.9 ohms. The resistance between the hinges and the sense electrode was (0.00295 ohm-cm x 0.0166 cm)/(0.00018755 cm x 0.0040 cm) which equals 65.3 ohms. Thus, the microbridge resistance for version one of the microbridges was 58.9 ohms + 65.3 ohms or 124 ohms. Calculations for the other versions resulted in resistances of 77.1 ohms for

version 2, 139.5 ohms for version 3, and 79.2 ohms for version 4. In general, the measured values were not that close to the predicted values. These differences are most likely due to slight variations in the dimensions of the microbridge after fabrication.

The contact resistance was determined by subtracting the measured microbridge resistance from the resistance measured between the input signal pad and the sense electrode pad. The results are tabulated in Figure 5.2. For the versions tabulated, the contact resistance was in the hundreds of ohms with large standard deviations. The large contact resistance and standard deviation was due to the fact that it takes a very large force to make a good connection between two separate polysilicon conductors. The drive electrodes on the microbridge were unable to generate a large enough force to get a good connection.

The maximum signal amplitude was determined to be the voltage and current at which the switch began to physically deform. At this point, the current density was high enough such that the polysilicon bridge began to overheat. This caused the bridge to thermally expand which caused the microbridge to deform. This point could be very accurately detected by viewing the microbridge under a microscope. As the current was increased, the most highly resistive portions of the microbridge would begin to glow slightly. This point was where the bridge began to deform and the failure current and voltage were annotated. A total of eight microbridges for each version were tested for failure voltage and current. The results are tabulated for each version tested in Table 5.2. As indicated by the low standard deviation of the failure voltage and current for all the microbridge versions, the failure point was very predictable for a given device.

The upper and lower 3 dB frequencies were determined by scanning the input a.c. signal from 10 Hz to 16 MHz with the oscilloscope. For all the microbridges tested, no upper or lower 3 dB frequencies were noted in the testable frequency range. Since the microbridges stick in the closed position and are capable of passing a d.c. signal, it is expected that the lower 3 dB frequency is zero. The upper 3 dB frequency, however, should exist. This frequency can be determined by calculating the RC time-constant for the switch connection, taking the inverse, and then dividing by 2π. R is given as the contact resistance in Table 5.2, but C, the parasitic capacitance of the contact, is unknown. Despite this, a lower limit can be put on the value of C because it is known that the upper 3 dB frequency is at least 16 MHz (from Table 5.2). This limit is found by taking 16 MHz, multiplying by 2π, taking the inverse of that, and then dividing by the contact resistance. C was determined to be less than or equal to 33 pF for version 1, 46 pF for version 2, and 16 pF for version 4.

5.2.2. Cantilever Beam Switches. Essentially, these devices operated and were tested in the same manner as the microbridge switches. They were intended to pass an a.c. signal using a d.c. bias as an actuation potential (see Chapter 4 for a complete description of switch operation). However, because the cantilevers were fabricated from the 2.0 μm thick POLY1 layer, the beams were very stiff and required high actuation voltages. This was especially true in this case because there was only one drive electrode on the cantilever beam switch as opposed to two drive electrodes on the microbridge switch. Like the microbridge switches, the cantilever beams would usually remain in the closed position after the actuation potential was removed. However, the cantilevers were

not as easy to release with the micromanipulator probe. Approximately 85% of the cantilevers released with the probe were destroyed.

The same characteristics were tested for the cantilever beam switches as were for the microbridge switches. They were tested for required actuation potential to couple the a.c. input signal, the d.c. contact resistance while in the stuck-down position, the maximum signal amplitude (voltage and current), and the upper and lower 3 dB frequencies.

Like the microbridge, the closing voltage of the cantilever was determined to be the potential needed to switch an a.c. signal such that the output signal was not distinguishable from the input signal when viewed on the oscilloscope. Table 5.3 shows the observed closing voltages for the versions of cantilevers that were tested. Versions 1, 2, and 3 of this switch were not able to close in the voltage range of the electrometer (up to 120 volts) so they are not tabulated in Table 5.3. These switch versions were usually destroyed by short circuits caused by dust and debris that was electrostatically attracted into the drive electrode area. For the switch versions that were able to operate as a switch, relatively low standard deviations from the closing voltage mean were observed. This low standard deviation indicates that the POLY1 layer used to form the cantilever was structurally consistent from device to device. Additionally, the closing voltage for the cantilever beams switches was higher than for the microbridge switches. This points out that it was more advantageous to have two drive electrodes, as in the microbridge, than to have the beam fixed at only one end, as in the cantilever beam.

As was done for the microbridge, the predicted closing voltages for the cantilever beam switches were determined as upper limits for the expected closing voltage. The predicted closing voltage was calculated by substituting all known parameters into Eq. (3.13) and iteratively solving using MathCAD. Two micrometers was used for δ_T, and all other parameters were taken from Table 4.4. A value of 200 GPa was used for Young's modulus. For a version four cantilever, the length, L, was 165 μm, the bridge width, b, was 40 μm, the thickness of the POLY1 layer, h, was 2 μm, and the gap between the cantilever tip and the sense electrode, d, was 2 μm. Referring to Figure 3.3 (a), the drive electrode for the version four cantilever began at x = 45 μm and ended at x = 120 μm. Substituting the known parameters into Eq. (3.13), the following relation was specified for the version four cantilevers:

$$2\mu m = \int_{45\mu m}^{120\mu m} \frac{\varepsilon_o}{E \cdot h^3}[3L - x] \cdot \frac{V^2}{\left(d - \left(\frac{x}{L}\right)^2 \cdot 2\mu m\right)^2} dx \qquad (5.2)$$

where E is 200 GPa, ε_o is 8.85 x 10^{-12} F/m and all other parameters are given above. The only unknown was V which was the voltage applied between the cantilever and the drive electrode. By placing Eq. (5.2) as shown directly into MathCAD between a GIVEN and a FIND statement and supplying a guess value (V = 50 volts), the applied voltage necessary to close the cantilever was calculated. For this example, V was determined to be 64 volts.

As expected, the predicted, upper limit closing voltage was larger than the measured closing voltages. Thus, the use of a hinge at the base of the cantilever can be used to reduce the closing voltage.

Table 5.3. Cantilever Beam Switch Summary Data.

Parameter	Mean Value	Std. Dev.	Predicted Value	# of Test Cases
Version 4, 6				
Closing Voltage	59.3 volts	3.2 volts	64 volts	20
Contact Resistance	1649 ohms	481 ohms	1649 ohms	20
Failure Voltage	4.1 volts	0.06 volts	---	8
Failure Current	25 mA	0.8 mA	---	8
Upper 3 dB Freq.	> 16 MHz	---	see text	20
Lower 3 dB Freq.	< 10 Hz	---	see text	20
Version 5, 7				
Closing Voltage	62.5 volts	3.0 volts	64 volts	24
Contact Resistance	2098 ohms	1208 ohms	2098 ohms	24
Failure Voltage	5.75 volts	0.40 volts	---	8
Failure Current	58.8 mA	1.9 mA	---	8
Upper 3 dB Freq.	> 16 MHz	---	see text	24
Lower 3 dB Freq.	< 10 Hz	---	see text	24

The contact resistance of the cantilever beam switches was determined by measuring the resistance between the input signal pad and the sense electrode pad (while in the stuck down position) and subtracting out the resistance of the cantilever beam. Because it was impossible to make resistance measurements for the cantilever beam switch as was done for the microbridge switch (there is a probe pad at only one end of the cantilever), the predicted values for the resistance of the cantilevers was used. The predicted values for the resistance of the cantilevers was calculated by using the cantilever dimensions (found in Table 4.4) and the resistivity of the POLY1 layer (found

in Table 5.1). For example, in version 4 of the cantilever beam switches, the hinge dimensions were 3 μm x 34 μm, the beam was 165 μm long, and the beam width was 40 μm. Assuming the resistance, R, is equal to (ρ x length)/Area, the hinge resistance was calculated to be (0.00295 ohm-cm x 0.0034 cm)/(0.00018755 cm x 0.0003 cm) or 178.3 ohms. Because the hinges essentially form resistors in parallel, the total contribution due to the hinges was 89.1 ohms. The resistance of the remaining length of the cantilever was (0.00295 ohm-cm x 0.0165 cm)/(0.00018755 cm x 0.0040 cm) or 64.9 ohms. Thus, the total cantilever resistance was 64.9 ohms + 89.1 ohms which is 154 ohms. For the other versions, the predicted cantilever resistance was 154 ohms for version 6, and 76.7 ohms for versions 5 and 7. Versions 1, 2, and 3 were not calculated because they were unable to exhibit switch operation. These calculated resistances were then subtracted from the resistance between the input signal pad and the sense electrode pad to get the contact resistance. The mean values, standard deviations, and the predicted values for the contact resistance of the cantilever beam switches are tabulated in Table 5.3. The contact resistance for the cantilever beam switches was in the kilo-ohm range with a large standard deviation. The large contact resistance and standard deviation was due to the poor electrical quality of polysilicon contacts. The contact quality was poor because of the electrical quality of the polysilicon and because the cantilever was unable to generate a large enough force, with only one drive electrode, to get a good connection.

The maximum signal amplitude (voltage and current) was determined to be the point at which the cantilevers were seen, through the probe station microscope, to physically deform. The maximum voltage and current statistics are tabulated in Table

5.3. As evidenced by the low standard deviations in the failure current and voltage, the point at which the devices failed was very consistent. Like the microbridges, the deformations occurred in the regions of the cantilever with the highest resistance (i.e. the hinges).

The upper and lower 3 dB frequencies were determined in the same manner as the microbridges. Like the microbridges, no 3 dB frequencies were observed in the testable frequency range. Because the cantilever is able to pass a d.c. signal in the stuck-down position, it is expected that there is no lower 3 dB frequency. However, the upper 3 dB frequency should exist. Using the same RC time-constant method as described in section 5.2.1 (Microbridge Switch), the lower limit on C can be determined for the cantilever beam switches. C was determined to be 6 pF for versions 4 and 6, and 5 pF for versions 5 and 7.

5.2.3. Simple Comb-Drive Switch. The simple comb-drive switch was intended to operate as an a.c. switch. An a.c. signal was to be passed between two electrodes that are brought into contact by applying a d.c. potential between the interdigitated comb structures (for complete device description see Chapter 4). While held in this position, the a.c. signal was coupled between the two electrodes.

There were several problems with this device. First, the POLY1 suspension spring was very stiff (because of the 2.0 μm minimum feature size) and very large voltages (100 + volts) were required for actuation. When such large voltages were applied, the movable comb either stuck to the substrate, or it tilted slightly such that the fingers on the movable comb stuck onto the sides of the fingers on the fixed comb. When stuck to the substrate,

the device was unharmed, but was unable to move due to friction. This problem was alleviated to a small degree by biasing the substrate to the same potential as the movable comb. This caused a repulsion effect which helped levitate the movable comb and keep it from sticking to the substrate. When the fingers of the two combs were stuck together, a severe short circuit was developed which destroyed the fingers that were in contact. This problem was caused by the central placement of the attachment between the suspension springs and the movable comb. Because it was only secured at one point, the comb could rotate too easily.

Because of these problems, very few of these structures were operable. Of those, only those with the POLY2 sheaths on the contact electrodes (version 2 of this switch--see descriptions in Chapter 4) were able to operate as a switch. This was because the presence of the POLY2 between the contact electrodes decreased the necessary actuation distance to 0.5 μm (instead of the 2 μm distance of version 1). Much like the microbridge and cantilever beam switches, when the switch was actuated to the closed position, the polysilicon contact electrodes often stuck together and held the switch in the closed position even after the drive potential was released. Thus, these switches were tested for their d.c. switching capabilities as well.

Because so few devices were operational (only version 2), only a few parameters were testable. The closing voltages for version 2 of this switch was observed to be 37.5 +/- 9.6 volts (the error is one standard deviation) which was determined from four simple comb-drive switches. This can be compared to the theoretical closing voltage by calculating the spring constant and the deflection force for this comb-drive actuator using

the theory developed in Chapter 3. The spring for this switch had two 2 μm wide restoring beams--one 150 μm long and the other 120 μm long (All other dimensions were taken from the device description in Chapter 4)--on each leg and there were two legs. By substituting 150 μm for L_1, 120 μm for L_2, 2 μm for b, 2 μm for h, and 200 GPa for E into Eq. (3.34) and then solving Eq. (3.30) for x and substituting the result into Eq. (3.34), the spring constant, k_{spring} for each leg can be calculated. The total spring constant (twice the value calculated for each leg) for the suspension spring of this switch was calculated to be 1.254 N/m. This spring constant can then be substituted into Eq. (3.37) along with the force generated by the comb-drive actuator (which can calculated using Eq. (3.23) and the dimensions taken from the device description in Chapter 4). Next, the closing voltage can be solved for by substituting the deflection needed to close the switch (0.5 μm) into Eq. (3.37) and solving for the voltage. Performing this calculation, the necessary voltage was determined to be 71 volts. This is so far off the actual closing voltage because the springs, although designed to have 2 μm wide restoring beams, actually had restoring beams of around 1.5 μm to 1.6 μm wide. This was caused by lithography limitations in the fabrication process when near the minimum feature size. This reduction in the restoring beam size had the effect of reducing the spring constant by a factor of 2.37. This decrease in the spring constant reduces the predicted actuation voltage to 46 volts. This is much closer to the observed value and is within one standard deviation.

The contact resistances were determined by measuring the resistance between the input signal electrode and the output signal electrode and then subtracting out the resistance of the polysilicon in-between. Using the statistics in Table 5.1 and the

dimensions given in Chapter 4, the resistance of the polysilicon was determined (in exactly the same manner as described for the microbridges and cantilever beams) to be (0.00295 ohm-cm x 0.035 cm)/(0.00018755 cm x 0.001 cm) or 550 ohms. Subtracting this from the resistance between the input signal electrode and the output signal electrode, which was 1410 +/- 321 ohms (the error is one standard deviation), the contact resistance was determined to be 968 +/- 321 ohms. These values were determined from the same four simple comb-drive switches that were tested for closing voltage. The large contact resistance and standard deviation was a direct result of the limited electrical capabilities of the polysilicon and the lack of sufficient force to make a good connection.

No upper or lower 3 dB frequencies were noted for the comb-drive switches that were tested. Like the cantilever and microbridge switches, no lower 3 dB frequency is expected since the switch is able to pass a d.c. signal in the stuck-closed position. However, the upper 3 dB frequency should exist. Using the same RC time constant method that was used for the cantilever beam switches and the microbridge switches, the upper limit on the parasitic capacitance of the contact, C, was determined to be 10 pF.

5.2.4. Push Lock Switch. This switch, which used a combination of comb-drive actuators, suffered from the same problems as the simple comb-drive switch. Extremely large actuation voltages (100 + volts) were necessary to observe the faintest movement in the comb-drive actuators. For all versions of this device, no significant deflection was observed (< 0.5 μm). The spring constants and comb forces of the comb-drive actuators in the switch can be calculated as was done in section 5.2.3. Assuming a Young's modulus of 200 GPa and using the dimensions described in the Chapter 4 description of

this switch, the spring constant for the main comb was calculated to be 0.00935 N/cm for the main comb suspension springs (which were 320 μm long with a 2 μm line width) and 0.00666 N/m for the small comb suspension springs (which were 380 mm long with a 2 μm line width). Using these spring constant values with Eq. (3.37), the voltage required to achieve the necessary deflection for both combs can be predicted (F_{comb} in Eq. (3.37) can be found using the dimensions given in Chapter 4 and Eq. (3.23)). The voltage required to move the signal conductors the required distance was determined to be 57 volts and the voltage required to move the contact pusher the required distance was calculated to be 78 volts. However, because the devices kept sticking to the substrate, this could not be verified. Because no devices were operational, no additional data and observations were recorded for these switches.

5.2.5. Clamp-Lock and Cantilever Lock Switches. Both of these switches attempted to improve upon the disadvantages of the comb-drive actuators fabricated in the MUMPs 4 fabrication run (sections 5.2.3 and 5.2.4). The performance of the comb-drive actuators used in these switches was improved over the MUMPs 4 comb-drive actuators, but they were still unable to actuate the necessary distance. The improvements in these actuators were due to the presence of a POLY0 ground plane beneath the movable comb, multiple attachments between the suspensions springs and the movable comb, and longer suspensions springs. The POLY0 ground plane could be charged the same as the movable comb to force electrostatic repulsion between them. This helped reduce substrate sticking more efficiently than just biasing the substrate. The multiple attachments between the suspension springs and the movable comb helped eliminate the

ability of the movable comb to rotate independent of the suspensions springs. This greatly reduced the tendency for the interdigitated comb fingers to stick together. The last improvement, the larger suspension springs, reduced the spring constant in the direction of actuation in an attempt to lower the necessary actuation potential.

Although unable to actuate the necessary distance required to lock into position, the voltage-deflection characteristics of the comb-drive actuators were determined. Figures 5.1 and 5.2 show the comb-drive actuator characteristics for the three major comb-drive actuators used in these switches--26 finger POLY2 combs, 38 finger POLY1 combs, and 20 finger POLY1 combs (see Chapter 4 for comb dimensions and version numbers). For each voltage data point, four different comb-drive actuators were tested to determine the deflection at that voltage. Each of these deflection data points was then averaged to determine the mean deflection at a given voltage. Finally, the mean deflection data points were plotted versus voltage. The error bars for each point represent one standard deviation about the deflection mean for the four test cases. This process was repeated for each comb-drive actuator.

After plotting the data, a theoretical curve was fitted to the data points. The first step in doing this was to calculate the force generated by each comb-drive actuator. This force is given by Eq. (3.23). This force was then substituted into Eq. (3.37). Thus, the deflection was a function of the parameters in Eq. (3.23), which were all known, and the suspension spring constant. For the POLY1 combs, the gap between fingers, g, was 2 μm, the height of the combs, h, was 2 μm, the permitivity of free space, ε_o, was 8.85 x 10^{12} F/m, and the dielectric constant, ε, was equal to 1. Now, the only unknown in Eq.

(3.37) was the spring constant, k_{spring}. This equation was fit to the voltage versus deflection data using k_{spring} as the fitting constant.

$$x = \frac{n \cdot \varepsilon \cdot V^2 \cdot h}{2 \cdot g \cdot k_{spring}} \tag{5.3}$$

where n is the number of capacitive gaps in the comb, h is the structural layer height (2μm for POLY1 and 1.5 μm for POLY2), g is the gap between fingers (2 μm) and the other values are given above. Using a least-squares fitting algorithm, k_{spring} was determined to be 0.541 N/cm for the 38 finger POLY1 comb, 0.556 N/cm for the 20 finger POLY1 comb, and 0.299 N/cm for the 26 finger POLY2 comb.

These spring constant values can be compared to the theoretical spring constant that can be derived from the beam theory of Chapter 3. For the POLY1 combs, there are a total of 12 pairs of restoring beams (Refer to Figure 3.7 for the definition of restoring beams) that consist of two 2 μm wide and 180 μm long beams. Using a similar development as was used for the example suspension truss of Figure 3.7, the spring constant for these combs can be calculated. In the case of the POLY1 combs, the spring constant for each leg is given by:

$$k_{spring} = \frac{12 \cdot E \cdot \frac{1}{12} h \cdot (2b)^3}{3 \cdot L^3} \tag{5.4}$$

for each pair of restoring beams in the spring. This equation was formed directly from Eq. (3.35) with L as the length of the pair of beams, (1/12) x (beam height, h) x (beam width, b)^3 as the beam moment of inertia, I, and 200 GPa for Young's modulus, E. A

value of 2 b was used for the beam width because there are two beams in each beam pair--thus acting like a single beam with twice the thickness. The three in the denominator is present because each spring leg is formed from three beam pairs. Because there are a total of four legs in each spring, the total spring constant is four times the value in Eq. (5.4). The spring constant for the POLY1 suspension springs was calculated to be 0.059 N/cm. A similar procedure was performed for the suspension springs that support the 26 finger POLY2 combs. The predicted spring constant for the POLY2 combs was calculated to be 0.044 N/cm.

The predicted values for the spring constants are significantly different than the values that were experimentally determined from the least-squares fitting algorithm. This was because the mass that was supported by the suspension springs was so great that the springs sagged to the substrate. As a result, a frictional force was also acting against the actuation of the comb-drive actuators making the effective spring constant much larger.

Of the two versions of the clamp-lock switches, only the clamp using a heat-drive actuator opened enough to admit the contact electrode (see Chapter 4 for operational descriptions and device dimensions of the clamp-lock switch). The heat-drive actuator clamp was able to open 3 μm in order to admit the contact electrode with the application of 4.5 mA. The electrostatic version of the clamp required around 50 volts before any noticeable deflection (approximately 0.5 μm) was observed. When voltages of up to 100 volts were applied to the electrostatic clamp, however, no increase in deflection was observed. Because the comb-drive actuators could not close the device, contact resistance measurements were attempted by pushing the contact electrode into the clamp

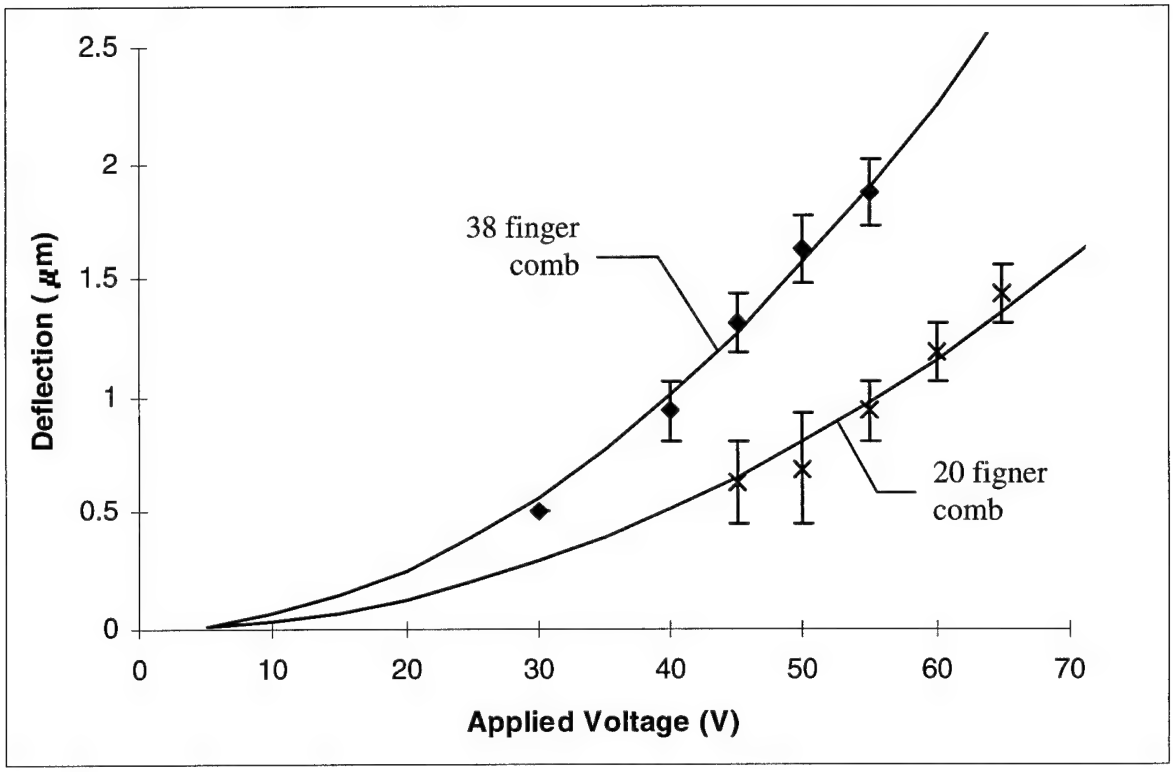

Figure 5.1. Comb-drive actuator characteristics for POLY1 actuators with 38 fingers on the movable comb (37 on the stationary comb) and 20 fingers on the movable comb (19 on the stationary comb). For both combs, the structural layer height is 2 μm, the movable fingers are 3 μm wide by 43 μm long, the stationary fingers are 4 μm wide by 43 μm long, the gap between the movable and stationary fingers is 2 μm, and the initial finger overlap is 22 μm. The suspension springs are 360 μm long and are formed from 2 μm wide beams. The data symbols represent the mean value of the deflection at a specific voltage for 4 test cases. The error bars represent one standard deviation of the deflection at a specific voltage for the same 4 test cases. The line is a least-squares fit to the data based upon comb-drive actuator theory.

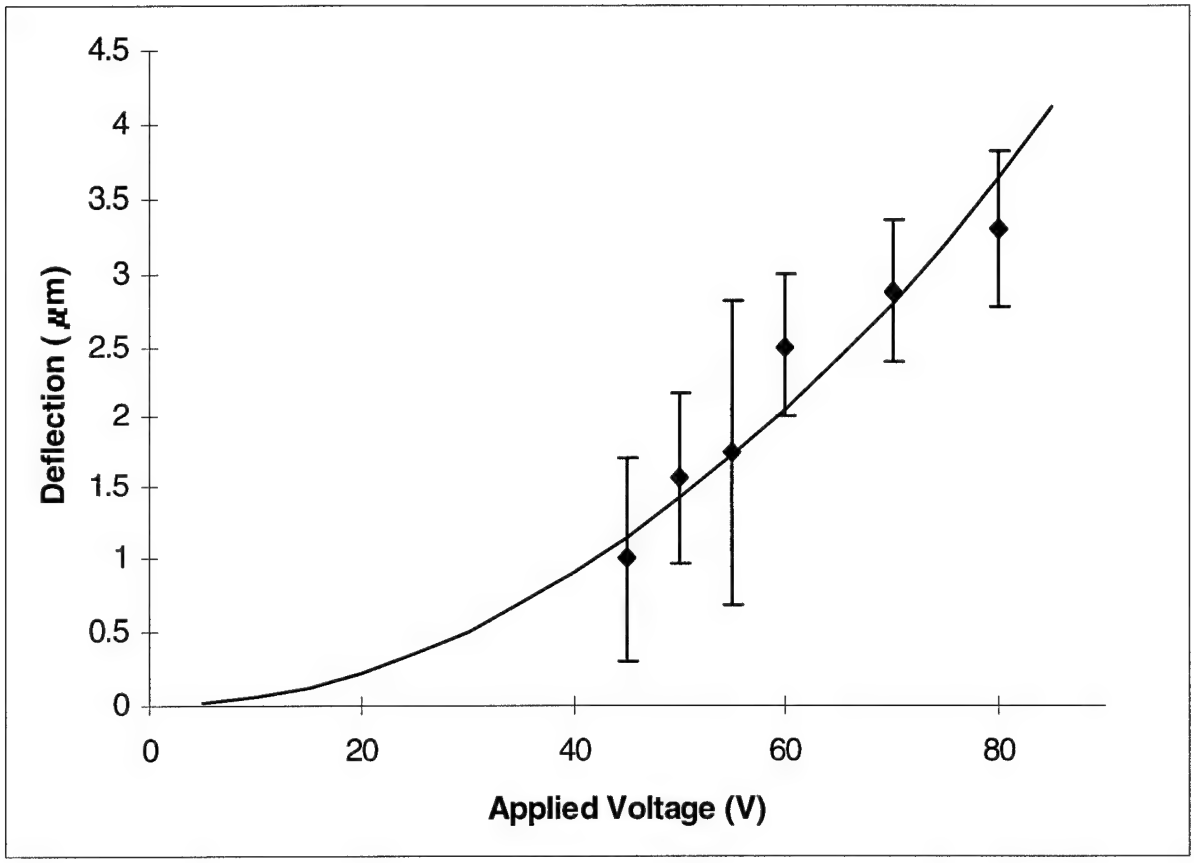

Figure 5.2. Comb-drive actuator characteristics for a POLY2 actuator with 36 fingers on the movable comb and 25 fingers on the stationary comb. The structural layer height is 1.5 μm, the movable fingers are 3 μm wide by 43 μm long, the stationary fingers are 4 μm wide by 43 μm long, the gap between the movable and stationary fingers is 2 μm, and the initial finger overlap is 22 μm. The suspension springs are 360 μm long and are formed from 2 μm wide beams. The data symbols represent the mean value of the deflection at a specific voltage for 4 test cases. The error bars represent one standard deviation of the deflection at a specific voltage for the same 4 test cases. The line is a least-squares fit to the data based upon comb-drive actuator theory.

with a micromanipulator probe. However, this did not work because the clamp was not able to hold the contact electrode tightly enough to keep the suspension springs from pulling the contact electrode out of the clamp.

The electrostatic cantilever-lock switches were designed to make electrical contact by hooking a cantilever to another electrode in some fashion (see Chapter 4 for operational descriptions of these devices). Like the clamp lock switches, the comb-drive actuators for these switches were unable to pull the cantilevers far enough to allow them to lock into place. Additionally, these switches were plagued with other problems. For versions 3, 4, and 5, the cantilevers were suspended from the suspension springs of the movable comb. When a d.c. potential was applied between the cantilevers and the drive electrodes beneath them, the entire suspension spring structure would move downward. This allowed the cantilevers to touch the drive pads and caused a short-circuit (and the destruction of the device). For versions 1 and 2, the cantilevers were required to deflect farther than designed which caused the cantilevers to short out when they were deflected far enough for proper operation. The extra deflection was required because the contact bar between the two sets of combs was suspended too low by the weight of the movable comb. Resistance tests were attempted for all versions of the cantilever lock switches by locking them in place with micromanipulator probes. However, only version 1 was able to be consistently locked in place. The contact resistance for these connections was greater than readable by the multimeters ($> 30\ M\Omega$).

5.2.6 Plate Switch. The plate switch was intended to operate in a manner similar to the microbridge switch and the cantilever beam switch, with the advantage that the

springs on the plate switches were longer and narrower (and thus less stiff) than the hinges on the cantilevers and microbridges (see Chapter 4 for operational descriptions of this device). By applying a d.c. potential between the plate and the drive electrode, the ends of the plate were drawn into contact with two separate signal pads, allowing an a.c. signal to be coupled.

These switches were noted to have a sticking effect similar to that of the cantilever beam switches and the microbridge switches. When the d.c. actuating potential was above a critical value (closing voltage), the switch would slam closed and would short out 90% of the time. Once stuck down, the plate switch was able to pass d.c. as well as a.c. signals. Releasing these switches was even more difficult than the cantilever beam switches and the microbridge switches. Less than 5% of the switches were released with a micromanipulator probe without destroying the switch. (Figure 5.3 shows a plate switch after sticking down). This Figure shows clear evidence of an electrostatic short. The POLY0 path to the drive electrode is melted completely away.

Both versions of this switch were tested for closing voltage, contact resistance, and upper and lower 3 dB frequencies. The data is summarized in Table 5.5. As expected, version 2 of this switch required a lower closing voltage because of the larger drive pad area. The low standard deviation of the closing voltage indicates that the structural quality of the POLY2 suspension springs was uniform form device to device. The predicted values for the closing voltages was calculated by first determining an effective spring constant for the POLY2 suspension springs. Although formed into the shape of an s, these springs act like one long beam that is supporting the plate. The total length of the

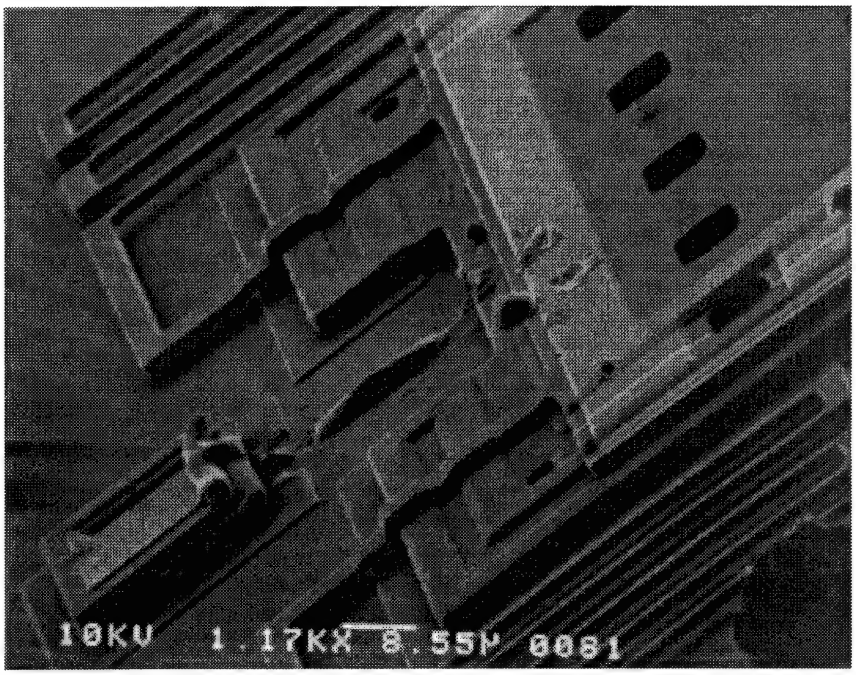

Figure 5.3. SEM micrograph of a plate switch after it has been actuated into the closed position. The melting between the drive electrode pad and the plate switch are evidence of a short-circuit. The springs are formed from the POLY2 structural layer and have a total length of 323 μm and a width of 3 μm. The plate is composed of the POLY1, POLY2, and metal layers. This device was fabricated in the MUMPs 6 fabrication run.

Table 5.4 Plate Switch Summary Data

Parameter	Mean Value	Range	Predicted Vals.	# of Test Cases
Small Plate Switches				
Closing Voltage	62.3 volts	+/- 9.0 volts	6.8 volts	18
Contact Resistance	465 ohms	+/- 363 Ω	464 ohms	18
Upper 3 dB Freq.	779 kHz	+/- 382 kHz	see text	18
Lower 3 dB Freq.	< 10 Hz	---	see text	18
Large Plate Switches				
Closing Voltage	53.6 volts	+/- 4.5 volts	5.7 volts	18
Contact Resistance	511 ohms	+/- 212 Ω	510 ohms	18
Upper 3 dB Freq.	726 kHz	*	see text	18
Lower 3 dB Freq.	< 10 Hz	---	see text	18

*Value ranged from 58 kHz up to 1.44 MHz.

springs for both plate switch versions was 323 μm with a line width of 3 μm. By combining Eqs. (3.30), (3.31), and (3.33), it is possible to solve for the spring constant of a beam element in terms of known parameters. In this case, L was 323 μm, b was 3 μm, h was 1.5 μm and Young's modulus, E, was assumed to be 200 GPa. The resulting spring constant relation becomes:

$$k_{spring} = \frac{12 \cdot E \cdot \frac{1}{12} b \cdot h^3}{L^3} \tag{5.5}$$

For both versions of the plate switch, the spring constant was 0.06 N/m. However, there were four such beams attached to the plate. Thus, the total spring constant was 0.24 N/m. Now, the capacitive force of the plate switch was calculated by simply substituting the equation for a parallel plate capacitor ($C = \varepsilon A/d$) into Eq. (3.6). This was set equal to the

Hooke's law force of the suspension springs, and the only unknowns were d, the capacitive gap, and the applied voltage.

$$V = \left[\frac{2 \cdot k_{spring} \cdot d^3}{\varepsilon_o \cdot Area} \right]^{\frac{1}{2}} \tag{5.6}$$

where the capacitive area, A, is is 116 μm x 80 μm for version 1 of the plate switch and 166 μm x 80 μm for version 2. By substituting 2 μm for the capacitive gap, d, the predicted closing voltage was determined. The closing force was calculated to be 6.8 volts for the smaller plate switch (version 1), and 5.7 volts for the larger plate switch (version 2).

The predicted closing voltage was much smaller than the closing voltage that was observed in Table 5.4. This is because the polysilicon plate was unable to make good contacts with the polysilicon signal electrodes. As the voltage was increased, the plate would deflect, however, it required much more voltage to increase the force enough to allow an a.c. signal to be coupled between the signal pads.

The contact resistance was calculated by measuring the d.c. resistance between the signal pads with the plate switch stuck down and then subtracting out the resistance of the plate. The resistance of the plate was determined (in exactly the same manner as the cantilever beams and microbridges) by using the known dimensions of the plate (as given in Chapter 4) and the statistics of Table 5.1. For the smaller plate, the conductive region of the plate (the gold on top of the plate) was 116 μm long, 0.5 μm thick, 80 μm wide. Assuming that the resistance, R, is equal to (ρ x Length)/Area, the resistance of version one was calculated to be (3.39 x 10^{-6} ohm-cm x 0.0116 cm)/(0.00005 cm x 0.008 cm) or

0.098 ohms. A similar calculation was performed for version 2 of the plate switch and the resistance was determined to be 0.14 ohms. These values were much lower than for other switches because the signal is primarily carried by the low resistance Cr/Au rather than the polysilicon. These values were subtracted from the resistance measured between the signal pads, which was 474.8 +/- 363 ohms for the small plate and 525.1 +/- 212 ohms for the larger plate (the errors on these figures are one standard deviation). The results are tabulated in Table 5.4. The contact resistance was in the hundreds of ohms with a large standard deviation. This contact characteristic is attributed to the poor electrical contact quality of the polysilicon and the inability of the plate switch to generate enough force to get a good connection.

Because the plate can pass a d.c. signal in the stuck-down position, a lower 3 dB frequency is not expected. However, the upper 3 dB frequency should exist. According to Table 5.4, the upper 3 dB frequency of the smaller plate switch was 779 kHz while the upper 3 dB frequency of the larger plate switch was 726 kHz. Using the simple RC time-constant modeling described in the microbridge switch section, the parasitic capacitance, C, can be extracted for each case. C was determined to be 440 pF for the small plate switch and 430 pF for the large plate switch.

5.3. Heat-Drive Actuated Devices.

Many of the switches that were designed to lock in place used heat-drive actuators for the necessary deflection. These devices were chosen because of their ability to work with low power and the fact that they seemed to have the most potential in the MUMPs

process. The only MUMPs 5 switches designed with these actuators were the MUMPs 5 version of the push lock switch and the heat spring switch. As the heat-drive actuators became more well understood, they were incorporated into more switches (especially in MUMPs 6 and MUMPs 7).

5.3.1. MUMPs 5 Version of the Push Lock Switch. This switch was designed to operate just like the comb-drive push lock switch except that it employed heat-drive actuators instead of comb-drive actuators (see Chapter 4 for operation description of these devices). The heat-drive actuators deflected much more than the comb-drive actuators, but were still unable to lock the switch in place. The problem was that the heat-drive actuators attached to the signal electrodes did not pull the signal electrodes straight out as was intended. Rather, because the heat-drive actuator curved as it deflected, the signal electrodes swung in an arc. Due to its arcing motion, the pusher could not get behind the signal electrodes to operate correctly. Unfortunately, this limitation did not allow any useful data regarding the switching characteristics to be taken.

5.3.2. Heat Spring Switch. This switch was intended to operate by using two heat-drive actuators to pull a contact electrode, which was attached to a suspension spring, into a clamp that was also driven by heat-driveactuators (see Chapter 4 for the operational description of this switch). Although the heat-drive actuators that formed the clamp section of the switch opened wide enough to admit the contact electrode, the two heat-drive actuators attached to the contact electrode had some problems. First, the springs were too stiff to allow a full 6 μm deflection that was needed to fully close the device. Added to this, the heat-drive actuators were so long (250 μm) that they hung down

approximately 1.5 μm towards the substrate. This caused the contact electrode to be blocked when it needed to cross a POLY0 wire directly beneath it (Figure 5.4).

A more far-reaching problem was evident in this device that could cause problems in other heat-drive actuator designs. Because they were intended to operate together, the two heat-drive actuators attached to the contact electrode were powered from the same two sets of probe pads. However, the polysilicon wires used to route to each heat-drive actuator were different lengths. This caused enough of a difference in resistance between the two paths that it caused one heat-drive actuator to get most of the current. Thus, one heat-drive actuator was providing most of the force, while the other was barely being actuated. This caused a great deal of inefficiency in the device and may have been ultimately why it was not able to fully close.

Although this switch was unable to lock on its own, contact resistance measurements were still attempted by using the micromanipulator probe to force the contact electrode into position. The probe was able to force the contact electrode into place, but the measured contact resistance was too high for the multimeters to measure.

5.3.3. MUMPs 6 Heat-Drive Actuator Test Array. After the problems found in the heat-drive actuator based devices in the MUMPs 5 fabrication run, it became evident that more study of the heat-drive actuators was necessary for proper design. For this purpose, a large set of 17 unique versions of heat-drive actuators was fabricated to help determine optimum design characteristics. The devices were fabricated to determine the effect of various heat-drive actuator dimensions on the overall performance. Figure 5.5 shows a basic figure labeling the various dimensions of the heat-drive actuator.

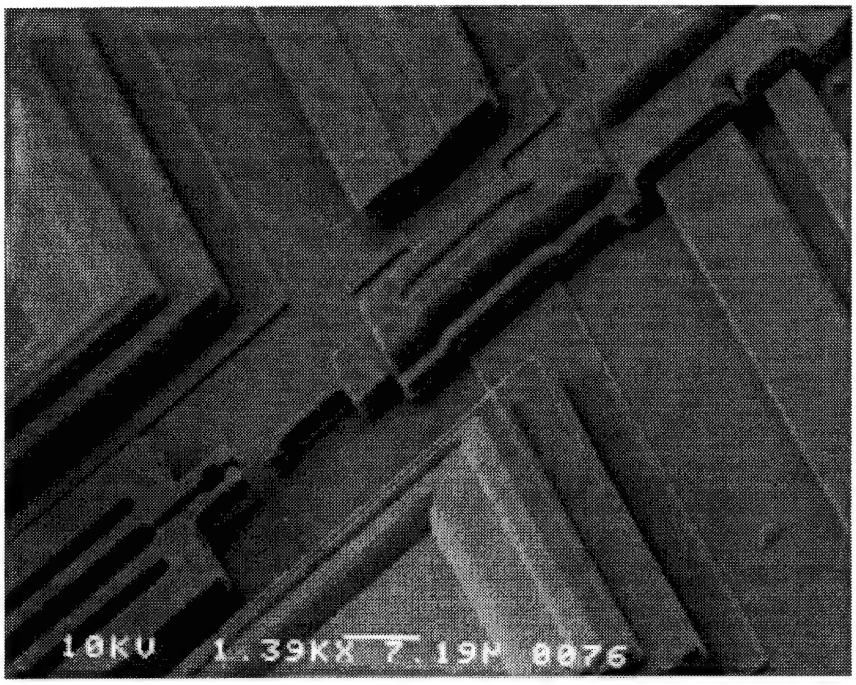

Figure 5.4. Heat Spring Switch hanging problem. The contact electrode seen in this SEM micrograph is hanging low enough that it becomes stuck on the POLY0 wire beneath it. The contact tip itself is fabricated from POLY1, but it is attached to the POLY2 layer that is conforming over the tips of the two heat-drive actuators. This combined weight is causing the sagging problem.

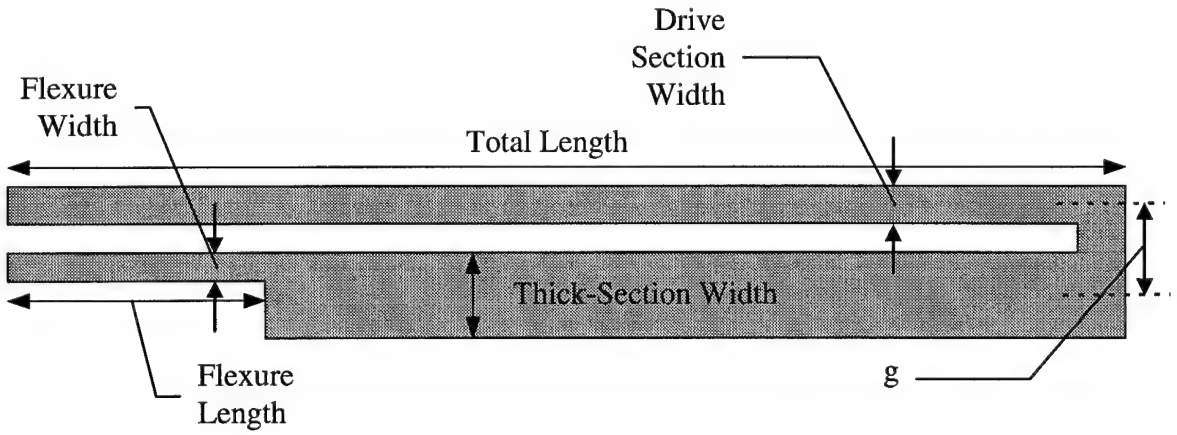

Figure 5.5. Heat-Drive Actuator. This figure shows some of the dimensions and labels some of parts of the heat-actuator. The dimension labeled g is measured from 1/2 the midsection of the drive section to the midsection of the thick section.

Each of the 17 arrays in the test set contained five sets of 12 heat-drive actuators. Each of the twelve heat-drive actuators was varied in its thick-section width by 1 μm increments. Thus, a total of twelve different thick-section widths were tested in each array. The five sets in each array were exact copies of one another so that there was a total of five copies for each of the 12 heat-drive actuators in a set. Each array was designed to test a specific dimensional characteristic of the heat-drive actuator. The characteristics tested include (as shown in Figure 5.5), the total length, the flexure length, the flexure width, and the drive section width. Table 5.5 lists each of the arrays (numbered 1 through 17) and the corresponding dimensions for the heat-drive actuators. The last column in Table 5.5 shows the range of thick section width in each array. In other words, the 3-14 for array 1 means that the thick section width varies from 3 μm on device number one of the twelve, to 14 μm on device number twelve of the twelve (with 1 μm increments for each device in-between).

The purpose of this data is to take a first-cut look at the heat-drive actuator characteristics for various dimensional variations. Regardless of dimensional variation, however, a basic current versus deflection characteristic is exhibited in all heat-drive actuators. Figure 5.6 shows the general current versus deflection characteristics for the heat-drive actuator. Each point on the graph indicates the mean value of the current required to achieve a given deflection for five separate heat-drive actuators with the same dimensions. The horizontal error bars were calculated as one standard deviation from the mean for the same five data points used to calculated the mean. The deflection of the heat-drive actuators was measured using a calibrated reticule inserted into the eyepiece of

Table 5.5. Variations of Arrays used in the Heat-Drive Actuator Array.

Array	Total Length*	Flexure Length*	Flex. Width*	Drive-Sec. Width*	Thick-Sec. Width*	Thick-Sec. Range
1	100	15	2	2	2	3-14 μm
2	150	15	2	2	2	3-14 μm
3	200	15	2	2	2	3-14 μm
4	200	20	2	2	2	3-14 μm
5	200	25	2	2	2	3-14 μm
6	200	30	2	2	2	3-14 μm
7	200	35	2	2	2	3-14 μm
8	200	40	2	2	3	3-14 μm
9	200	30	3	3	2	6-17 μm
10	200	30	4	4	2	6-17 μm
11	200	30	5	5	2	6-17 μm
12	200	20	3	3	2	6-17 μm
13	200	20	3	4	2	6-17 μm
14	200	20	3	5	2	6-17 μm
15	100	15	2	2	2	3-14 μm
16	150	15	2	2	2	3-14 μm
17	200	15	2	2	2	3-14 μm

*Dimensions are in μm.

the micromanipulator microscope. Based on the spacing of the markings on the reticule, the deflection error was determined to be +/- 0.5 μm. This error is plotted as the vertical error bars in Figure 5.6.

Once the data has been plotted, a definite pattern between the current and deflection is apparent. Thus, it was possible to fit the data to an empirical equation. The empirical equation with the best R^2 value (R2 = 1 is a perfect fit) was an exponential fit. The exponential fitting equation is given in Eq. (5.7).

$$\Delta x = A \cdot \exp(B \cdot I) \tag{5.7}$$

where Δx = deflection of the heat-drive actuator at the tip (meters);

I = current applied (amps);

A,B = fitting constants.

Similar deflection versus current plots for the best performing heat-drive actuators, complete with least-squares fits, were calculated for all 17 heat-drive actuator arrays. The plots are shown individually in Appendix B. The results of the least squares empirical fits of Eq. (5.7) to each of the 17 arrays is tabulated in Table 5.6. Based upon the R^2 values listed in Table 5.6, an exponential fit to the data is justified. The mean R^2 value was 0.9888 +/- 0.0084 (the error is one standard deviation from the mean) which means that the exponential fits were very good (an R^2 value of 1 is a perfect fit to the data).

Referring back to Eq. (3.43), the predicted deflection Δx is directly proportionaly to the difference in temperature between the drive section and the thick section, ΔT, of the heat-drive actuator. However, the derivation of Eq. (3.43) is for devices in which the

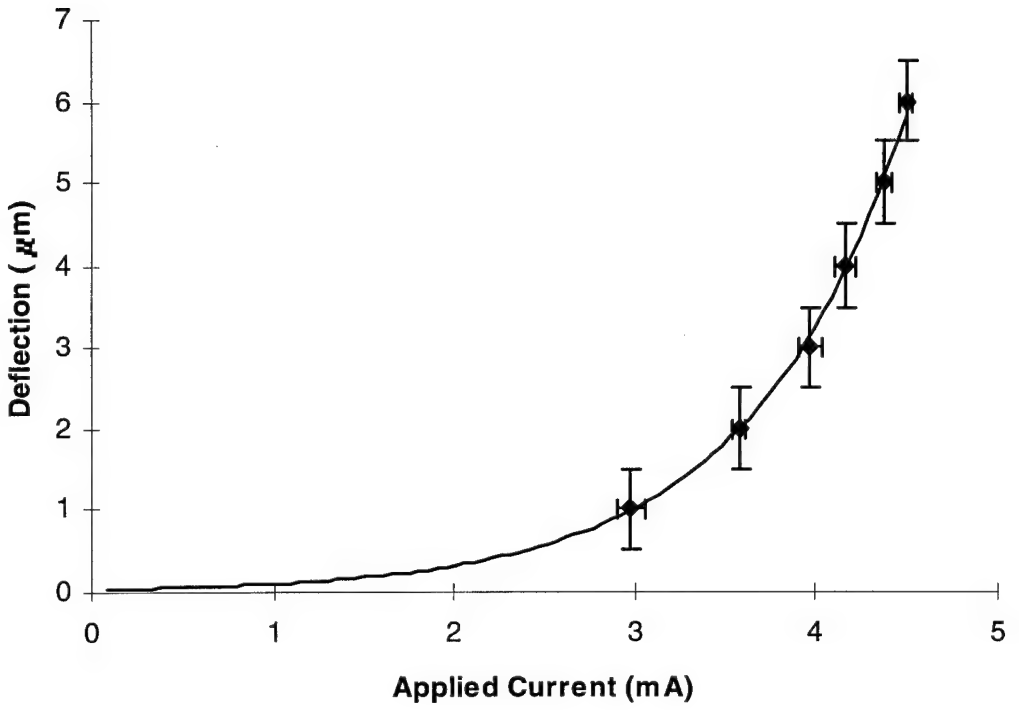

Figure 5.6. Deflection versus applied current for a POLY1 heat-drive actuator from array 2. Here the total length is 150 μm, the flexure length is 15 μm, the drive-section and flexure widths are 2 μm, the thick-section is 14 μm wide and g is 10 μm. The symbols indicated the mean value of the applied current at a specific deflection for five test cases. The horizontal error bars indicate the first standard deviation of the applied current at a specific deflection for the same five test cases. The vertical error bars indicate the uncertainty of the deflection measurement with a reticule under a microscope (+/- 0.5 μm). Here the data is fit very closely with the exponential fit of Eq. (5.1). The applied voltage range was 0 to 6 volts.

Table 5.6. Fitting Constants and R^2 Values for Each Array.

Array Number	A const ($^oC^{-1}$)	B const (mA^{-1})	R^2
1	0.186	0.7721	0.9852
2	0.0306	1.669	0.9984
3	0.1318	1.0121	0.9989
4	0.0977	1.0944	0.9922
5	0.134	0.9972	0.9858
6	0.1001	1.0912	0.9927
7	0.1063	1.0838	0.9938
8	0.1076	1.0833	0.9950
9	0.0483	0.9674	0.9853
10	0.0436	0.7902	0.9692
11	0.0325	0.6835	0.9925
12	0.0696	0.8872	0.9784
13	0.0625	0.7472	0.9800
14	0.0412	0.6825	0.9778
15	0.0268	1.9174	0.9961
16	0.0986	1.8967	0.9959
17	0.173	1.9732	0.9929

the thick section is twice as wide as the drive section. For the devices in the test array for which this condition was true, it was possible to determine ΔT based upon the observed deflection. This was done by substituting the observed deflection into Δx along with the length, L, the drive section thickness, t, and g and then solving for ΔT. Therefore, the applied current, I, that forced a deflection Δx also corresponded to a specific ΔT. In this way, ΔT verus applied current data was determined by substituing multiple Δx values into Eq. (3.43), solving for ΔT and noting the applied current for that data point. This ΔT versus I data was then fit with Eq. (3.49) using the material constant, a, as the fitting

parameter. This procedure was performed for POLY1 heat-drive actuators using arrays 1 through 11 and for POLY2 heat-drive actuators using arrays 15, 16 and 17. An example of the ΔT versus I data along with the least squares fit of Eq. (3.49) is shown in Figure 5.7.

If Eq. (3.49), which describes the relationship between ΔT and I, took every factor into account, the fitting constant, a, should not change for devices with different dimensions. However, Eq. (3.49) assumes that all the heat in the thick and drive sections of the heat-drive actuators is dissipated into the air. In actuality, though, much heat also escapes into the probe pads where the heat-drive actuators are attached to the substrate (which distorts the fitting constant in Eq. (3.49)). This effect cools the regions the drive and thick sections of the heat-drive actuator that are near the pads. If the heat-drive actuator was short enough, the entire lenght of the drive and thick sections could be cooled to a significant degree by heat escaping into the pads. For longer devices, however, there are regions of drive and thick sections that are far away from the probe pads such that little heat escapes to the probe pads. These regions must dissipate heat solely to the atmosphere. For this reason, it is expected that heat escaping into the probe pads is in some way be related to the length, L, of the heat-drive actuator. Additionally, it is expected that the cross-sectional area of the drive and thick sections are related to this effect because that is the area through which the heat must travel in order to excape into the probe pads.

After performing a least-squares fit to each of the arrays (plots of which are given in Appendix B) to determine the constant, a, it was empirically determined that *a* varies with

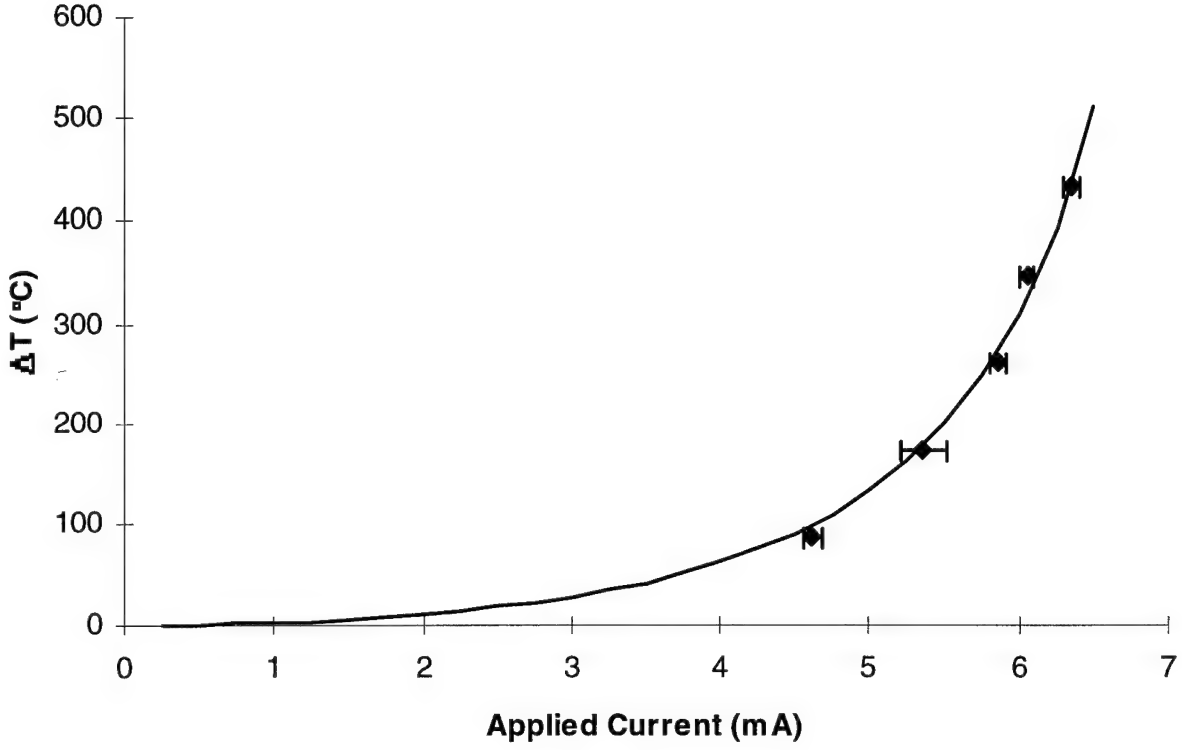

Figure 5.7. ΔT vs I data plotted for a heat-drive actuator that has a length of 200 μm, a drive section width of 4 μm, a thick section width of 8 μm, a flexure length of 30 μm, a flexure width of 4 μm, and a g dimension of 8 μm. The symbols represent the mean ΔT points at specific applied currents as derived from Δx using Eq. (3.43) for five test cases. The error bars represent one standard deviation from the mean for the same five test cases. The solid line is the least squares fit to the data using Eq. (3.49) with a as a fitting parameter

respect to length and cross-sectional area of the thick and drive sections according to the following relation:

$$a = A_{poly} \cdot \frac{10^5}{L^{\frac{3}{2}} \cdot (3 \cdot h \cdot t)^{0.2}} \tag{5.8}$$

where a = fitting constant as given in Eq. (3.49);

A_{poly} = constant not affected by dimensions of the heat-drive actuators;

L = length of the heat-drive actuator (meters);

t = drive section width. Note: the thick section is twice the width of the drive section or 2t (meters).

This relation introduces a new constant, A_{poly}, which is a constant for all the heat-drive actuators. For the POLY1 devices, A_{poly} was determined to be 1.9 +/- 0.08 ($m^{1.5}$-^oC-W^{-1}) while A_{poly} was determined to be 7.4 +/- 0.88 ($m^{1.5}$-^oC-W^{-1}) for POLY2 devices. Therefore, using Apoly, *a* can be determined by substituting L and t into Eq. (5.8). By substituting *a* back into Eq. (3.49), all the physical parameters are known and ΔT can be found as a function of I. ΔT can then be put into Eq. (3.43) such that Δx is simply a function of applied current. Table 5.7 shows a list of the heat-drive actuator arrays tested for this data, the value of *a* that was fit from Eq. (3.49), and the predicted value of *a* from the empirical formula of Eq. (5.8). Figure 5.8 shows the same plot as was shown in Figure 5.7 but includes an additional curve plotted with Eq. (3.49) using the *a* determined from Eq. (5.8). Plots like Figure 5.8 are given for each array in Appendix B.

The results in Table 5.7 and the plots in Figure 5.8 and in Appendix B show that the empirical relation of Eq. (5.8) can be used to design heat-drive actuators in which the

Table 5.7. Fitting Constant "a" as Actually Fit and as Predicted.

Array	"a" Fit from Eq. (3.49) ($^{o}C\text{-}W^{-1}\text{-}m^{-2}$)	"a" Calc from Eq. (5.8) ($^{o}C\text{-}W^{-1}\text{-}m^{-2}$)
1	3.041×10^{13}	2.939×10^{13}
2	1.535×10^{13}	1.6×10^{13}
3	1.011×10^{13}	1.039×10^{13}
4	1.017×10^{13}	1.039×10^{13}
5	1.025×10^{13}	1.039×10^{13}
6	1.036×10^{13}	1.039×10^{13}
7	1.052×10^{13}	1.039×10^{13}
8	1.038×10^{13}	1.039×10^{13}
9	1.046×10^{13}	1.039×10^{13}
10	0.9281×10^{13}	0.9485×10^{13}
11	0.8017×10^{13}	0.8954×10^{13}
15	12.96×10^{13}	12.0×10^{13}
16	5.66×10^{13}	6.534×10^{13}
17	3.863×10^{13}	4.244×10^{13}

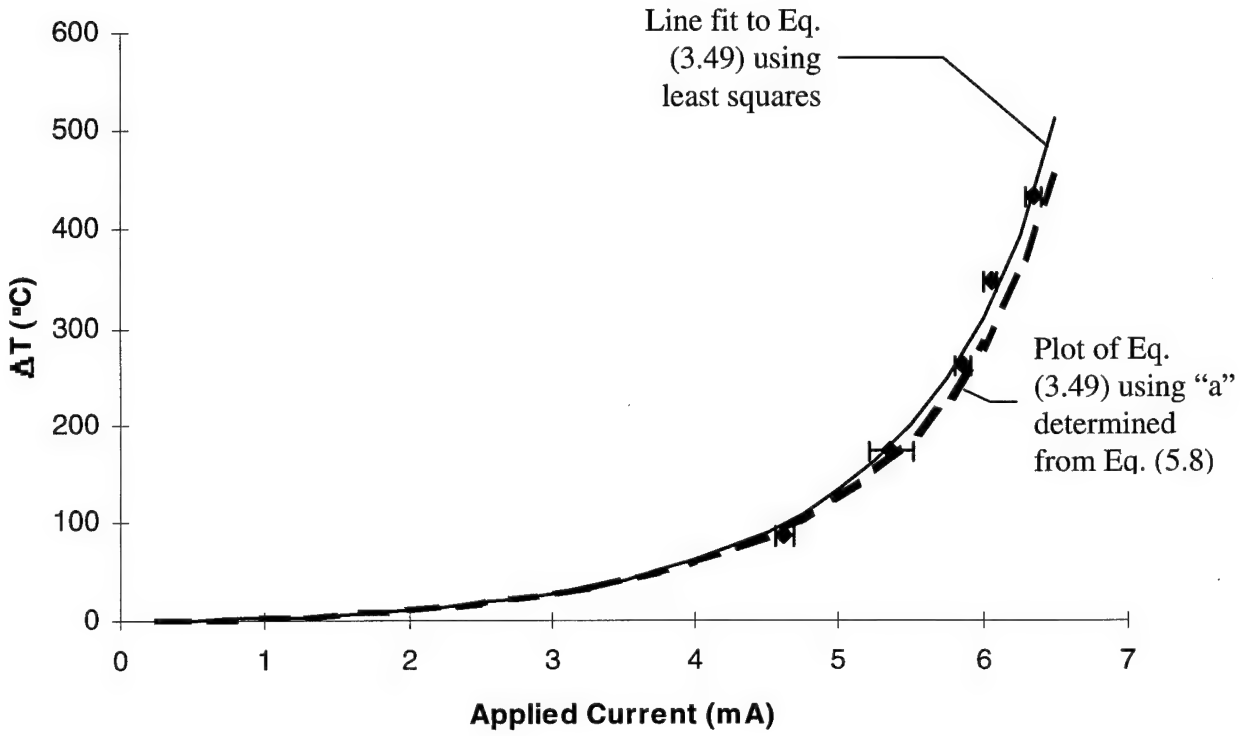

Figure 5.8. ΔT vs I data plotted for a heat-drive actuator that has a length of 200 μm, a drive section width of 4 μm, a thick section width of 8 μm, a flexure length of 30 μm, a flexure width of 4 μm, and a g dimension of 8 μm. The symbols represent the mean ΔT points at specific applied currents as derived from Δx using Eq. (3.43) for five test cases. The error bars represent one standard deviation from the mean for the same five test cases. The solid line is the least squares fit to the data using Eq. (3.49) with a as a fitting parameter. The dashed line is a plot of Eq. (3.49) using an *a* value calculated using Eq. (5.8).

thick section is twice the width of the drive section. Most of the predicted *a* vlaues were close to those that were fit directly using a least-squares algorithm. Additionally, Figure 5.8 shows that the predicted ΔT vs I curve closely matches the curve that was fit directly. The only disadvantage is that this data only includes heat-drive actuators in which the thick section is twice the width of the drive section. In order to get results that are valid for all possible heat-drive actuator dimensions, a more general equation than Eq. (3.43) is required.

Broader summaries of the data analyzed in the heat-drive actuator array are shown in Figures 5.9 through 5.16. Many of these figures plot deflection versus a parameter labeled thick-section/drive-section ratio. This parameter is the ratio of the thick section width to the drive section width. This allows, for example, devices from array 2 and array 11 to be plotted on the same x axis. In effect, it is a way of normalizing the variance of the width of the thick section in relation to the width of the drive section. Figure 5.9 (arrays 1, 2, and 3) shows plots of the maximum deflection achieved versus increasing thick-section width for three lengths of POLY1 heat-drive actuators with all other parameters held constant. It can clearly be seen that the 200 μm long devices were able to achieve more deflection than the others. The same general trend is shown in Figure 5.10 (arrays 15, 16, and 17) for POLY2 heat-drive actuators with the same dimensions as in Figure 5.9. Here the maximum deflection achieved is plotted versus increasing thick section width for 100 μm, 150 μm, and 200 μm long heat-drive actuators. Figure 5.11 (arrays 6, 9, 10, and 11) depicts the maximum achievable deflection versus increasing thick-section width for four different drive-section widths (the flexure width is

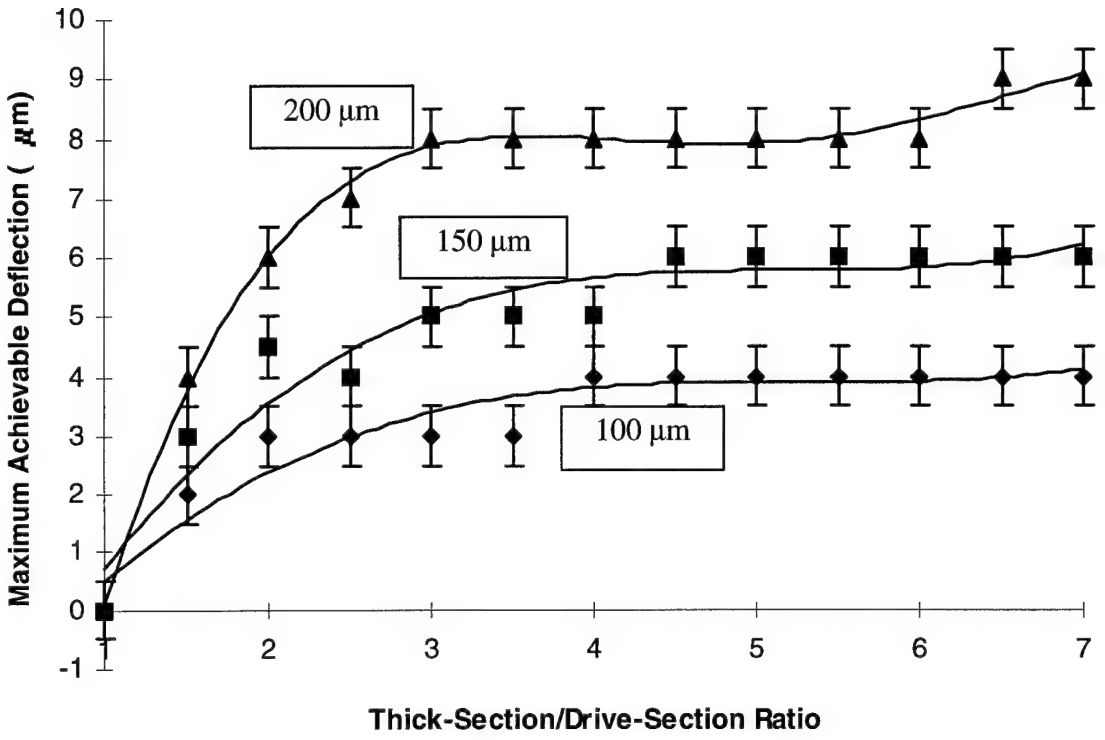

Figure 5.9. Maximum achievable deflection versus increasing thick-section width for 100 μm long, 150 μm long, and 200 μm long POLY1 heat-drive actuators. The flexure length is 15 μm, the flexure width and thin section width are 2 μm, and g varies with the thick-section width. The symbols indicate the mean value of the maximum achieved deflection for five test cases. The error bars are the errors (+/- 0.5 μm) associated with measuring the actuator deflection through a microscope. The lines fit to each data set are 4th order least-squares polynomial fits to the data to show the general trend. As the thick section gets wider relative to the drive section (as indicated by the thick-section/drive-section ration), the maximum deflection generally increases. Additionally, more deflection is achieved for the longer actuators.

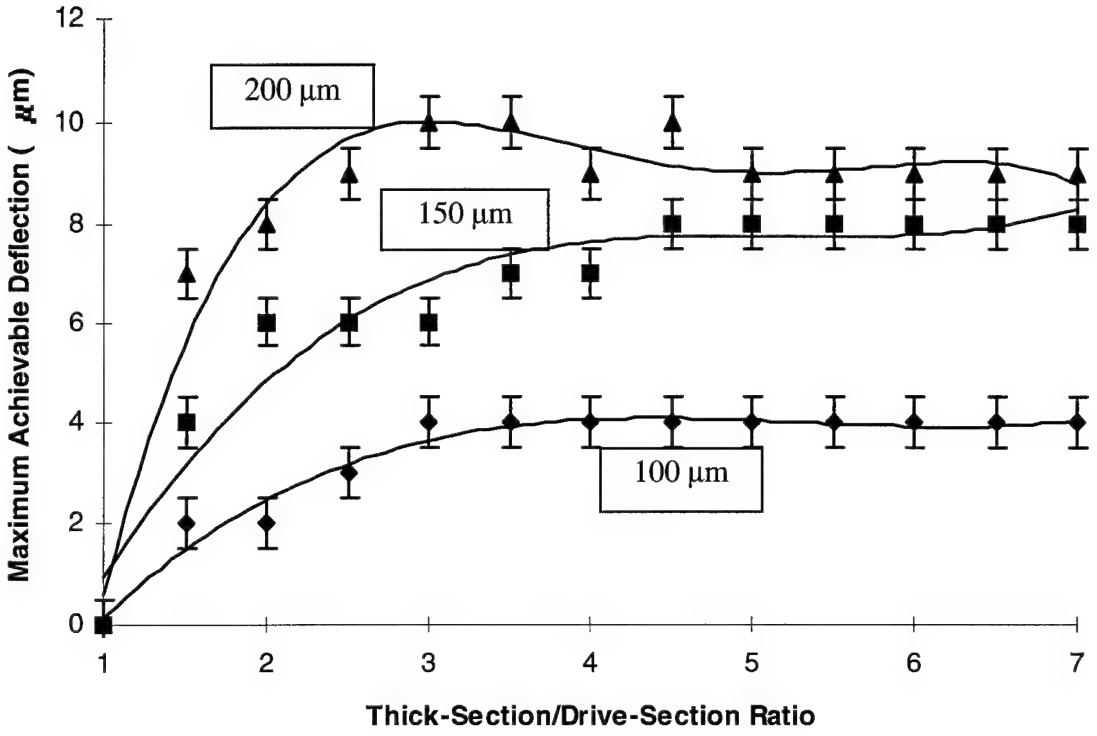

Figure 5.10. Maximum achievable deflection versus increasing thick-section width for 100 μm long, 150 μm long, and 200 μm long POLY2 heat-drive actuators. The flexure length is 15 μm, the flexure width and thin section width are 2 μm, and g varies with the thick-section width. The symbols indicate the mean value of the maximum achieved deflection for five test cases. The error bars are the errors (+/- 0.5 μm) associated with measuring the actuator deflection through a microscope. The lines fit to each data set are 4th order least-squares polynomial fits to the data to show the general trend. As the thick section gets wider relative to the drive section (as indicated by the thick-section/drive-section ration), the maximum deflection generally increases. Additionally, more deflection is achieved for the longer actuators.

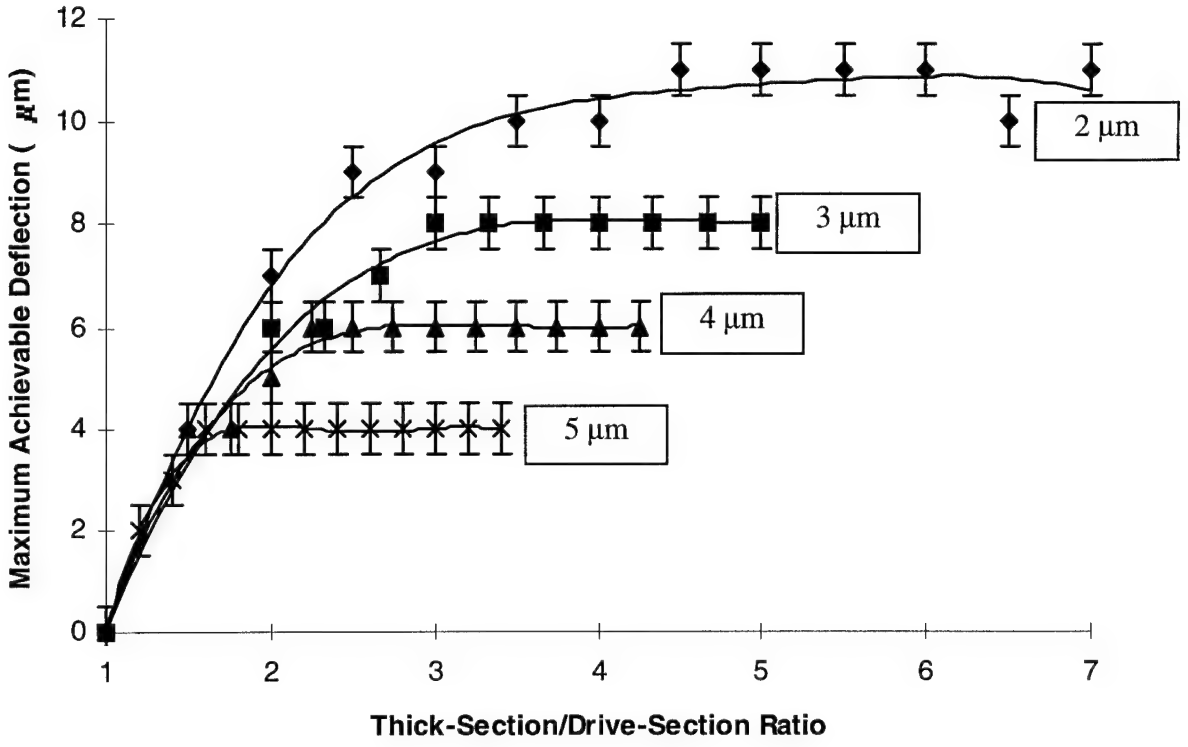

Figure 5.11. Maximum achievable deflection versus increasing thick-section width for 2 μm, 3 μm, 4 μm, and 5 μm wide drive-sections of a POLY1 heat-drive actuator. The flexure width is the same as the drive section width for all four cases. The heat-drive actuator length is 200 μm, the flexure length is 30 μm, and g varies with drive-section width and thick-section width. The symbols indicate the mean value of the maximum achieved deflection for five test cases. The error bars are the errors (+/- 0.5 μm) associated with measuring the actuator deflection through a microscope. The lines fit to each data set are 4th order least-squares polynomial fits to the data to show the general trend. For all cases, as the thick section gets wider, the maximum deflection generally increases. Additionally, this chart shows that maximum deflection is increased for thinner drive-section widths.

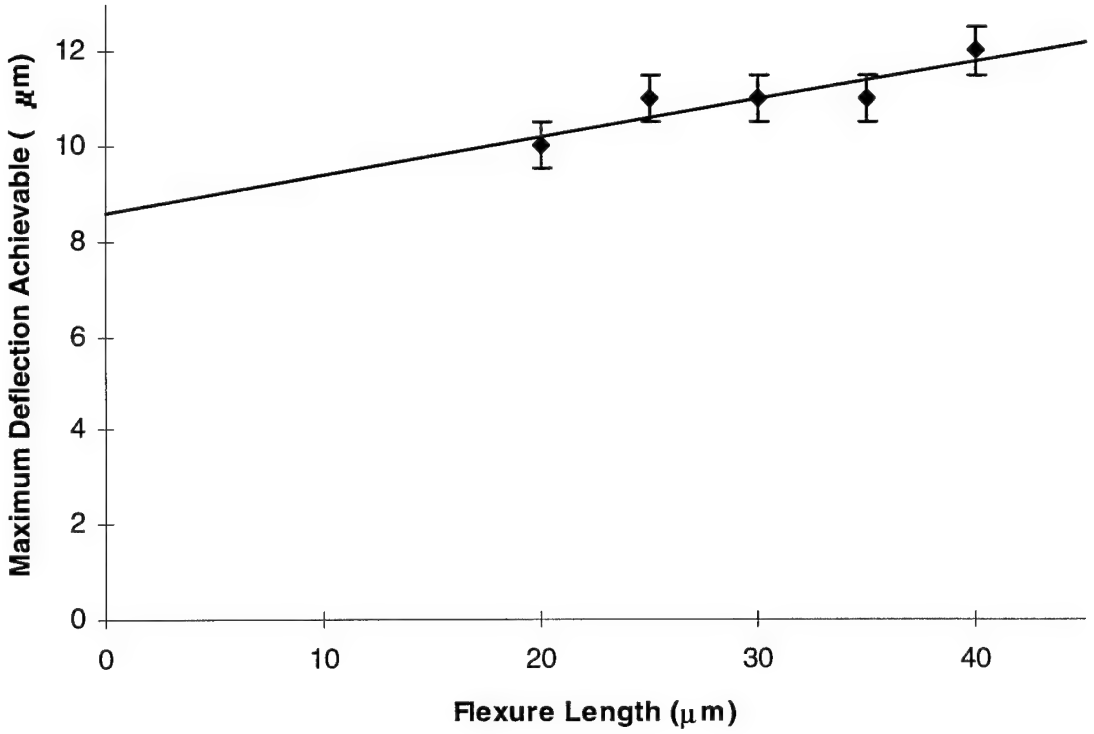

Figure 5.12. Maximum achievable deflection versus flexure length. For the heat-drive actuators used for these observations, the total length is 200 μm, the drive-section and flexure widths are 2 μm, the thick section width is 14 μm, and g is 10 μm. The symbols indicate the mean value of the maximum achieved deflection for five test cases. The error bars are the errors (+/- 0.5 μm) associated with measuring the actuator deflection through a microscope. The line fit to this data is a linear least-squares fit to show the general trend. This chart shows that the maximum deflection is slightly affected by flexure length.

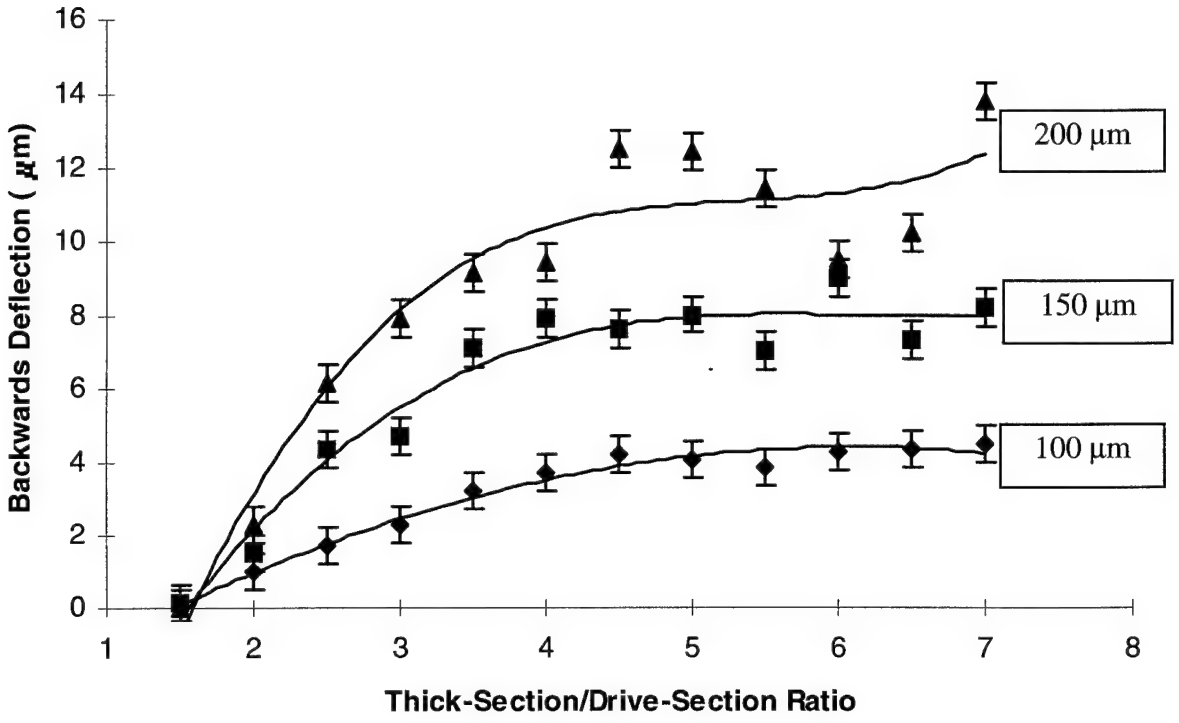

Figure 5.13. Maximum achievable backbending versus increasing thick-section width for 100 μm long, 150 μm long, and 200 μm long POLY1 heat-drive actuators. The flexure length is 15 μm, the flexure width and thin section width are 2 μm, and g varies with the thick-section width. The symbols indicate the mean value of the maximum achieved backbending for five test cases. The error bars are the errors (+/- 0.5 μm) associated with measuring the actuator deflection through a microscope. The lines fit to each data set are 4th order least-squares polynomial fits to the data to show the general trend. As the thick section gets wider relative to the drive section (as indicated by the thick-section/drive-section ration), the maximum backbending generally increases. Additionally, more backbending is achieved for the longer actuators.

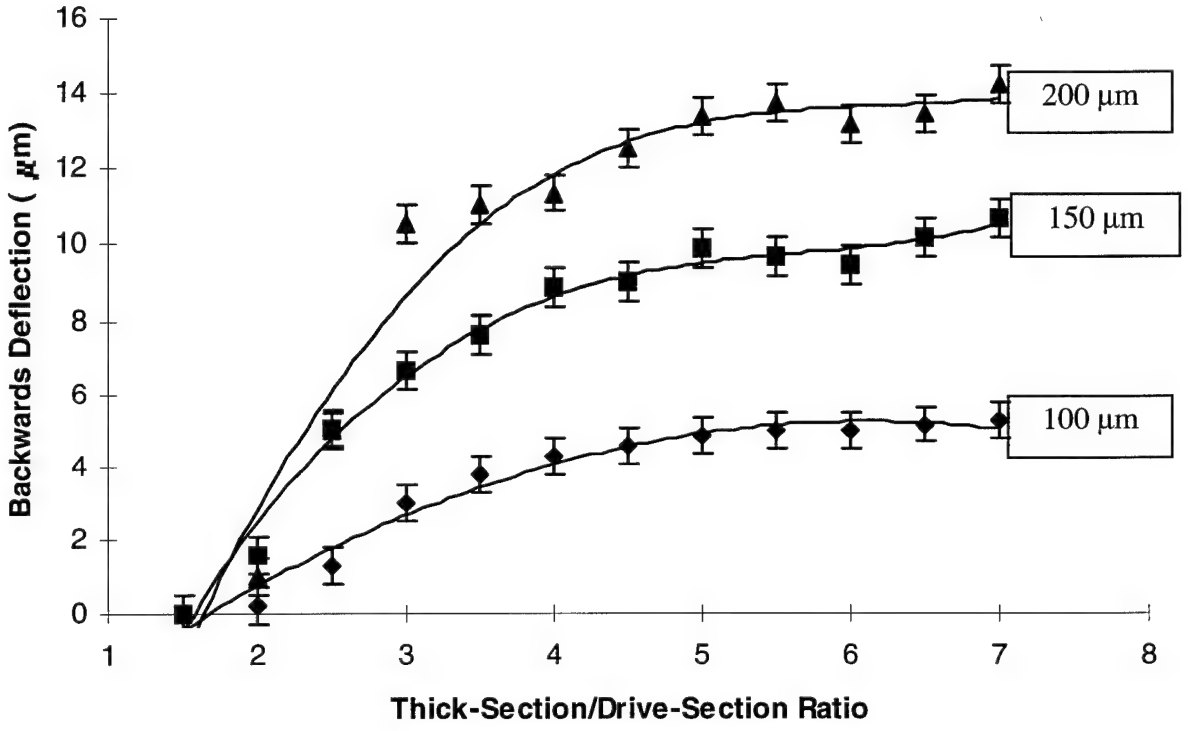

Figure 5.14. Maximum achievable backbending versus increasing thick-section width for 100 μm long, 150 μm long, and 200 μm long POLY2 heat-drive actuators. The flexure length is 15 μm, the flexure width and thin section width are 2 μm, and g varies with the thick-section width. The symbols indicate the mean value of the maximum achieved backbending for five test cases. The error bars are the errors (+/- 0.5 μm) associated with measuring the actuator deflection through a microscope. The lines fit to each data set are 4th order least-squares polynomial fits to the data to show the general trend. As the thick section gets wider relative to the drive section (as indicated by the thick-section/drive-section ration), the maximum backbending generally increases. Additionally, more backbending is achieved for the longer actuators.

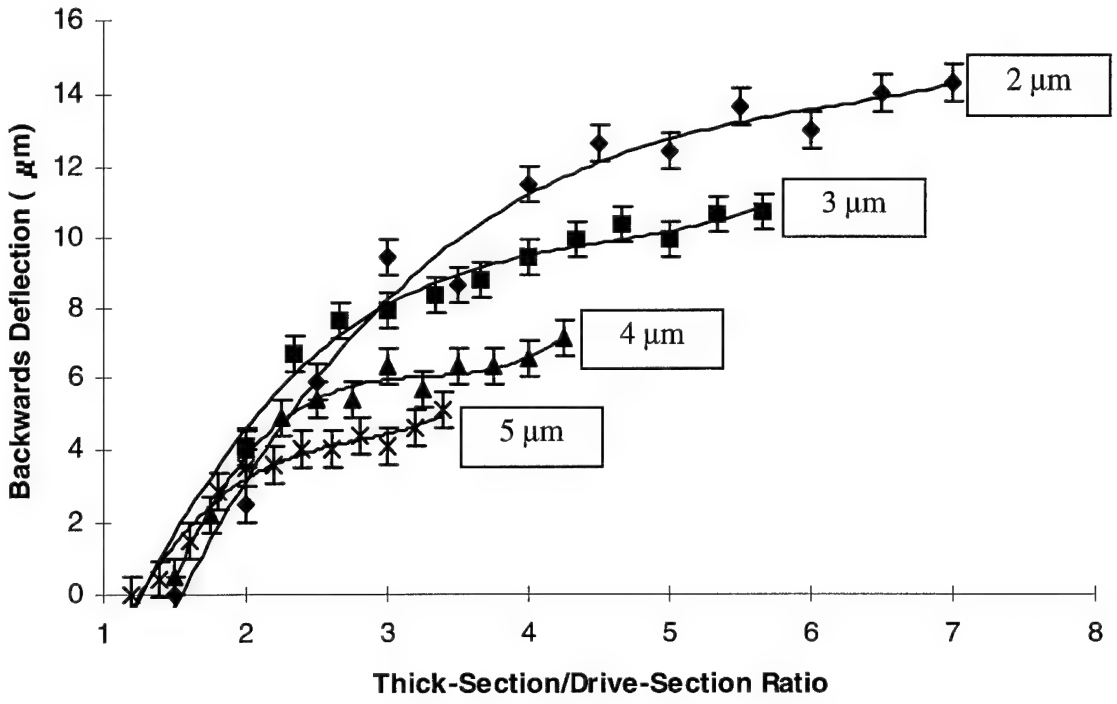

Figure 5.15. Maximum achievable backbending versus increasing thick-section width for 2 μm, 3 μm, 4 μm, and 5 μm wide drive-sections of a POLY1 heat-drive actuator. The flexure width is the same as the drive section width for all four cases. The heat-drive actuator length is 200 μm, the flexure length is 30 μm, and g varies with drive-section width and thick-section width. The symbols indicate the mean value of the maximum achieved backbending for five test cases. The error bars are the errors (+/- 0.5 μm) associated with measuring the actuator deflection through a microscope. The lines fit to each data set are 4th order least-squares polynomial fits to the data to show the general trend. For all cases, as the thick section gets wider, the maximum backbending generally increases. Additionally, this chart shows that maximum backbending is increased for thinner drive-section widths.

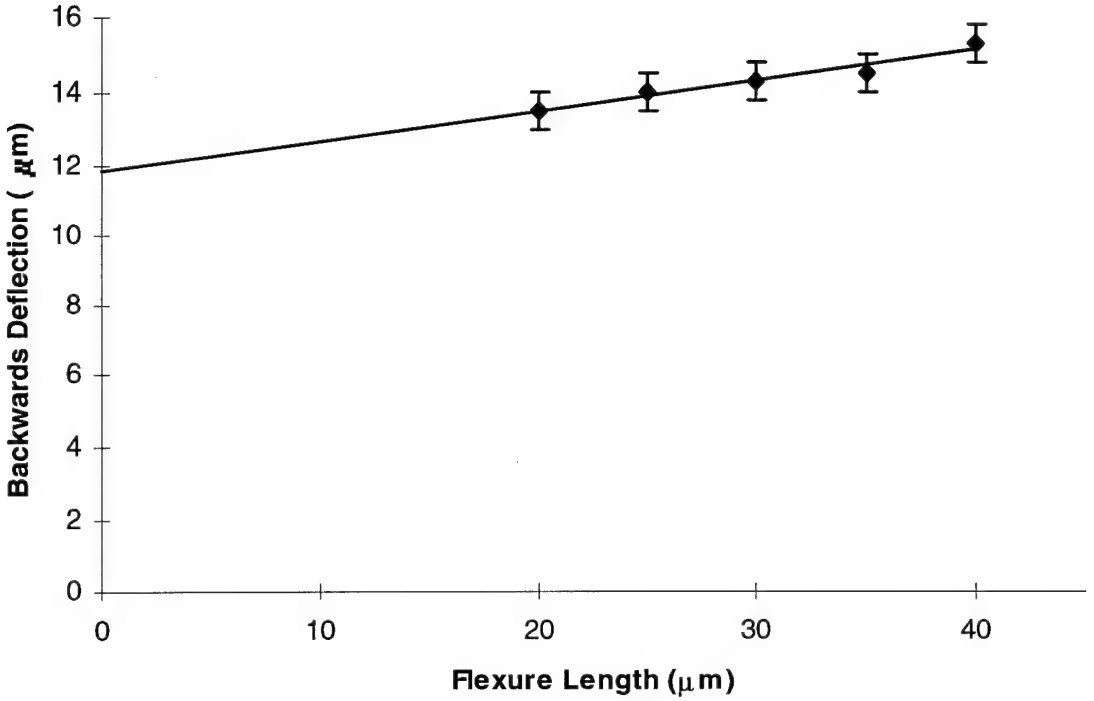

Figure 5.16. Maximum achievable backbending versus flexure length. For the heat-drive actuators used for these observations, the total length is 200 μm, the drive-section and flexure widths are 2 μm, the thick section width is 14 μm, and g is 10 μm. The symbols indicate the mean value of the maximum achieved backbending for five test cases. The error bars are the errors (+/- 0.5 μm) associated with measuring the actuator deflection through a microscope. The line fit to this data is a linear least-squares fit to show the general trend. This chart shows that the maximum backbending is slightly affected by flexure length.

the same as the drive-section for these arrays) with all other dimensions held constant. From this graph, it is clearly shown that the thinner drive-section widths (and flexure width) are able to achieve more total deflection. Figure 5.12 (arrays 4 through 8) shows the maximum deflection as a function of flexure length. The flexure length varies from 20 μm to 40 μm in 5 μm increments. All other dimensions are the same as shown in Table 5.5. This graph shows that slightly larger deflections can be achieved with longer flexures.

Figures 5.13 through 5.16 depict the back-bending characteristic of the heat-drive actuator. When the heat-drive actuators are subjected to too much current, the drive-section begins to overheat. When this occurs, the polysilicon in the drive-section begins to compress while the polysilicon in the thick section is not affected because it is at a slightly lower temperature. When the current is turned off, the drive section of the heat-drive actuator is shorter than the thick section (due to the compression) and the entire device bends backwards. Figure 5.13 (arrays 1, 2, and 3) shows the maximum backward deflection versus increasing thick-side width for three different POLY1 heat-drive actuator lengths with all other parameters held constant. Figure 5.14 (arrays 15, 16, and 17) shows the same data as Figure 5.13, but for heat-drive actuators formed from the POLY2 layer. These two figures clearly show that significantly more back bending occurs for longer heat-drive actuators. Figure 5.15 (arrays 6, 9, 10, and 11) depicts the maximum back bending versus increasing thick-section width for four different drive-section widths. Although less distinct than for the forward deflection case (Figure 5.11), this graph shows that the back bending gets greater as the drive-section gets thinner.

Figure 5.16 (arrays 4 through 8) shows the maximum backwards deflection due to overheating as a function of increasing flexure length. This plot shows a minimal amount of dependence of back bending on flexure length.

As a general result, the maximum deflection was achieved using heat-drive actuators that were 200 μm in total length, had a drive-section width and flexure width of 2 μm, a thick-section width of 14 μm, and a flexure length of 40 μm. Additionally, the heat-drive actuators with these dimensions also exhibited the largest amounts of back bending when overheated.

Using Figures 5.9 through 5.16, a designer should be able to estimate the achievable deflection for heat-drive actuators developed in the MUMPs process in both the forwards and backwards directions. It is often tempting for the designer to make the heat-actuators longer in order to get more actuation, however, this only works to a point. For heat-actuators much longer than 200 μm, the high polysilicon resistance does not allow current to easily flow (without very high voltages) and actuation becomes very difficult. Additionally, if maximum deflection is not needed, it may be useful to use a larger drive-section width when designing heat-drive actuators. Although this limits the maximum deflection achievable, it was noted during this study that the actuation is much smoother for wider drive-sections. Although actuators with 2 μm wide drive sections were able to achieve a large deflection, the deflection was unstable and the actuator could "jump" around. By using drive-section widths of 3 μm or 4 μm, the actuation is much smoother and more predictable.

5.3.4. MUMPs Heat Lock Switches. The MUMPs heat lock switches were intended to operate by using heat-drive actuators to move a contact electrode into a conductive clamp (see Chapter 4 for operational descriptions). These switches were designed with both POLY1 and POLY2 as the structural layer with several different shapes of contact electrodes. Once locked in position, the switches were able to pass both a.c. and d.c. signals.

There were three shapes of contact electrodes used on these switches. The rectangular shaped electrode was the simplest and required 6 μm of deflection for it to lock into place. The trapezoidal shaped electrode and the round electrode both required 10 μm of deflection to be locked into place. Because these designs were submitted before the heat-drive actuator study (above) was completed, no design criteria for these devices existed. As a result, the heat-drive actuators to which the contact electrodes were attached and the heat-drive actuators forming the clamps were not optimally designed. The heat-drive actuator attached to the contact electrodes was too long (300 μm) to be efficient in its operation (it was only able to move about 5 μm), had too thick of a drive section width and flexure width (4 μm), and had too short of a flexure length (8 μm). However, the heat-drive actuators forming the clamp section were able to actuate a sufficient distance for correct operation. These actuators were 230 μm long, had a drive section and flexure width of 4 μm and a flexure length of 8 μm.

Although these switches were unable to lock into position on their own, the signal contact quality of the POLY1 switches could be tested by forcing connection with the micromanipulator probes. Because of the low vertical aspect ratio in the MUMPs process

(layer thickness relative to the achievable horizontal dimension) and the tendency for the actuators to move up or down slightly, the initial contacts were not very good. Figures 5.17 and 5.18 show this effect. This poor mechanical connection also turned out to be a poor electrical connection as well. However, the connection resistance could be dramatically improved by "burning-in" the contact by running 2 mA of current through the contact for 30 seconds. The POLY2 versions of these switches could not be closed with the micromanipulator probe because the contact electrode kept slipping out of the clamp. This was because the low vertical aspect ratio of the POLY2 switches (which is even lower than the POLY1 switches) allowed the tips of the heat-drive actuators to move too much in the vertical direction (both up and down). Thus, the contact electrode usually totally missed the clamping mechanism. Additionally, the POLY1 heat switch with the round contact electrode was also not able to be locked into position. This is because the round electrodes were not held tightly enough by the clamp heat-drive actuators and they tended to slip out of the clamp.

The contact resistance was calculated by measuring the resistance from the input signal pad to the output signal pad and then subtracting out the resistance of the polysilicon in-between. The polysilicon resistance of the clamp was determined by first calculating the resistance of each heat-drive actuator in the clamp. This was done by treating the thick section and the drive section of each heat-drive actuator as parallel resistors. For the POLY1 clamps, the drive section resistance was (0.00258 ohm-cm x 0.023 cm)/(0.0004 cm x 0.0002022 cm) or 734 ohms and the thick section resistance was (0.00258 ohm-cm x 0.023 cm)/(0.0010 cm x 0.0002022 cm) or 294 ohms. Assuming

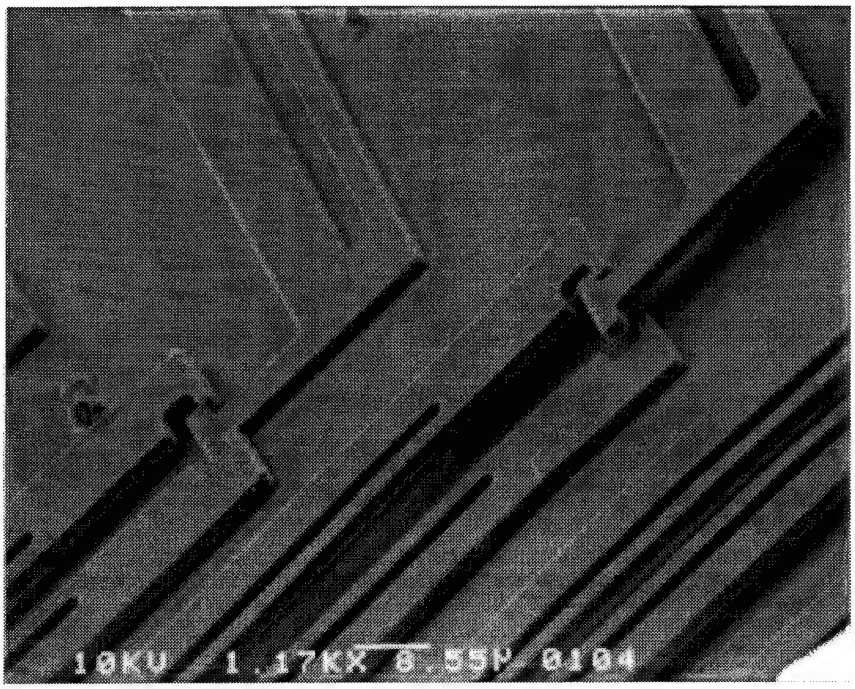

Figure 5.17. SEM micrograph of a Rectangular Electrode Simple Heat Switch. This is an example of the poor mechanical connection made with these switches. The heat-drive actuators are fabricated from POLY1 (2 μm thick). For these devices, the drive section and flexure widths are 4 μm, the thick section width is 10 μm, the flexure length is 8 μm, and g is 11 μm. The actuator connected to the contact electrode is 300 μm long and the actuators forming the clamp are 230 μm long. This device was fabricated in MUMPs 6 (ver. 1).

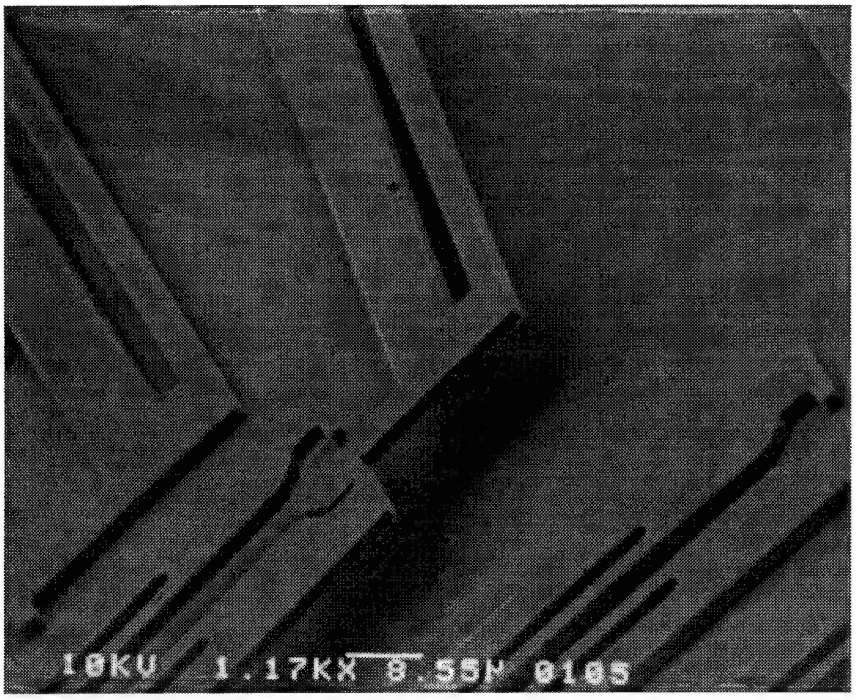

Figure 5.18. SEM micrograph of a Trapezoidal Electrode Simple Heat Switch. This is an example of the poor mechanical connection made with these switches. The heat-drive actuators are fabricated from POLY1 (2 μm thick). For these devices, the drive section and flexure widths are 4 μm, the thick section width is 10 μm, the flexure length is 8 μm, and g is 11 μm. The actuator connected to the contact electrode is 300 μm long and the actuators forming the clamp are 230 μm long. This device was fabricated in MUMPs 6 (ver. 2).

parallel resistors, the resistance of each heat-drive actuator in the clamp was 209 ohms. Then, the total resistance of the clamp is determined by assuming parallel resistors for each clamp heat-drive actuator--105 ohms. The resistance of the heat-drive actuator attached to the contact electrode was determined in the same manner as was done for the clamp heat-drive actuators--(0.00258 ohm-cm x 0.03 cm)/(0.0002022 cm x 0.0004 cm) in parallel with (0.00258 ohm-cm x 0.03 cm)/(0.0002022 cm x 0.001 cm) which was 274 ohms. Thus, the total resistance of the polysilicon between the input to the switch and the

output was 274 ohms + 105 ohms or 378 ohms. For the POLY1 versions of this switch (versions 1, 2, and 3), the resistance of the polysilicon was determined to be 378 ohms. Before "burning-in" the contact, the resistance measured between the input and output signal pads was 9.17 +/- 12.5 mega-ohms for the rectangular shaped electrode and 9.03 +/- 11.600 mega-ohms for the trapezoidal shaped electrode. Subtracting this value from the previously determined resistance of the polysilicon, the contact resistance before "burn-in" was found--9.17 +/- 12.5 mega-ohms for the rectangular shaped electrode and 9.03 +/- 11.600 mega-ohms for the trapezoidal shaped electrode. After "burn-in", the resistance measured between the input and output signal pads was 3552 +/- 2870 ohms for the rectangular electrode and 4570 +/- 3900 ohms for the trapezoidal electrode. Subtracting this resistance from the polysilicon resistance resulted in the following contact resistances after "burn-in": 3173 +/- 2870 ohms for the rectangular electrode and 4192 +/- 3900 ohms for the trapezoidal electrode.

The 3 dB frequencies of the simple heat switches was determined by varying an input a.c. signal from 10 Hz to 16 MHz and noting the amplitude changes. Because this switch was able to pass a d.c. signal, no lower 3 dB frequency was expected. However, an upper 3 dB frequency did exist. The upper 3 dB frequency was 82 kHz for the POLY1 version with the rectangular shaped contact electrode and 82 kHz for the POLY1 version with the trapezoidal shaped contact electrode. Based on these values and assuming a simple RC time-constant model for the upper 3 dB frequency, the parasitic contact capacitance can be estimated for each case. C was 472 pF for the trapezoidal shaped contact electrode and 627 pF for the rectangular shaped contact electrode.

Table 5.8. Simple Heat Switch Summary Data.*

Parameter	Mean Value	Range	# of Test Cases
Trapezoidal Electrode **			
R contact w/o burn-in	9.03 MΩ	1.4 kΩ to 30 MΩ	14
R contact w/ burn-in	4.19 kΩ	+/- 3.9 kΩ	14
% Improvement	89.8%	---	---
Upper 3 dB Freq.	82 kHz	9 to 210 kHz	13
Lower 3 dB Freq.	< 10 Hz	---	13
Rectangular Electrode ***			
R contact w/o burn-in	9.17 MΩ	13 kΩ to 30 MΩ	10
R contact w/ burn-in	3.17 kΩ	+/- 2.87 kΩ	10
% Improvement	86.1%	---	---
Upper 3 dB Freq.	82 kHz	9 to 210 kHz	13
Lower 3 dB Freq.	< 10 Hz	---	13

*Data shown here is for the POLY1 heat-drive actuators only. These are the only versions that were able to be locked in place.

**Contact area is 52 μm^2.

***Contact area is 16 μm^2.

Listed in Table 5.8. are the results of switch parameter testing on the MUMPs heat lock switches. The contact resistance is shown both before and after "burning in" the contacts as well as the percent improvement in the contact resistance after "burn in". Even after the 80%+ improvement of the contact resistance by "burning-in" with 2mA of current, the contact resistance for both the rectangular and trapezoidal contact electrodes was still in the 10s of kilo-ohms with a very large standard deviation. This is mostly due

to the bad physical connection achieved with these devices (Figures 5.17 and 5.18), but is also due to the limited electrical capabilities of the polysilicon. The upper 3 dB frequencies for these switches were also very low. This is because the large series contact resistance was causing a large RC time constant to be formed which was in turn limiting the frequency response of the switch.

5.3.5. Hinge Switches and the Vertical Heat-Drive Actuator. Because these switches actually form metal-to-metal contacts, they have the most promise for working as high-fidelity switches with low series resistances. The operation of the hinge switch depended on two critical factors. First, being able to effectively flip over the hinges from the fabricated position, and second, having a working vertical actuator.

Several methods were attempted to flip over the hinges. The first method attempted was to strongly agitate the entire MUMPs die during the final rinse of the sacrificial release. It was found that very few of the hinges were flipped over using this method. The second method attempted was to use an eyebrow hair attached to the end of a micromanipulator probe held beneath a microscope. The idea was to get underneath the hinge with the hair and flip the hinge over. Unfortunately, the hair was too large and too clumsy for this purpose. The final method involved blasting the area of the die containing the hinges with high velocity air. The high velocity air was provided with a simple aero-duster can used to dust electronics equipment. By keeping the die under the air stream for 1 to 2 minutes, approximately 90% of the hinges oriented properly (pointed so that the air will catch underneath the hinge and flip it over) under the stream would be flipped over (Figure 5.19). Although effective for flipping over a large area of hinges (in

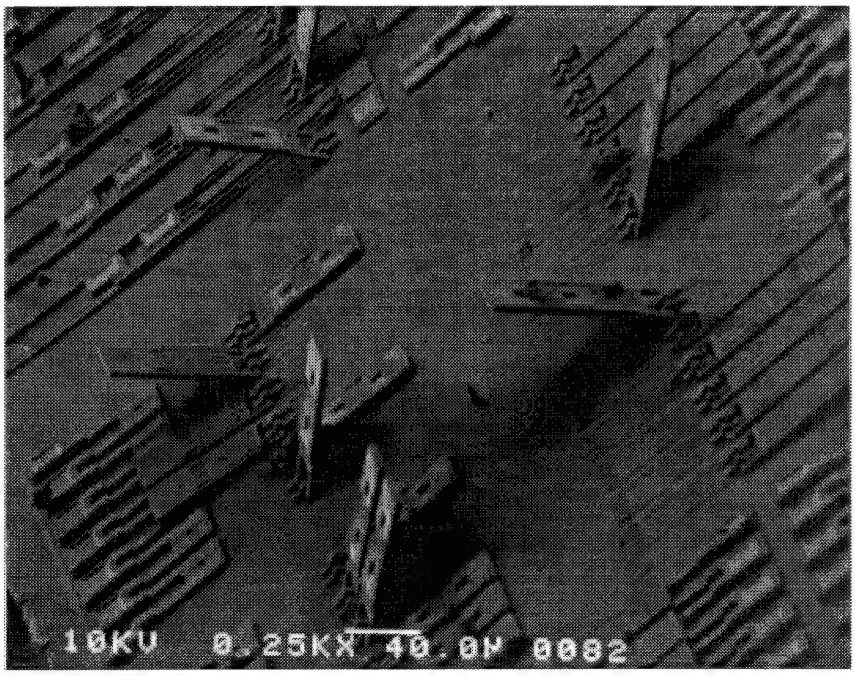

Figure 5.19. SEM micrograph of a MUMPs 6 die after blasting with high velocity air for 2 minutes. Most of the hinges are flipped over or can be easily flipped over with a micromanipulator probe. The hinges are formed from POLY1 and POLY2 anchored together. Metal is placed atop the POLY2 layer. The pivot is formed from a 2 μm wide POLY1 beam and is anchored to the substrate with a POLY2 collar. The hinges vary in length from 90 μm to 170 μm and are 46 μm wide.

this case, 1/4 of the die was covered with hinges), this method completely destroyed other regions of the chip containing delicate devices with beams smaller than 3 μm wide.

The hinge switches with vertical heat-drive actuators operated well mechanically. The hinges could be seen to be moving into and out of contact with the signal pads according to the deflection in the vertical heat-drive actuator. The long hinges (150 μm or 170 μm long) with medium (112 μm long POLY1 sections) or short (92 μm long POLY1 sections) length vertical heat-drive actuators operated the best. The long hinges were better because they were at less of an angle when contacting the signal pads than the

shorter (< 150 μm long) hinges. Because of this, the metal on the tip of the long hinges laid flatter on the signal pads, thus improving the contact area. The long vertical heat-drive actuators (132 mm or longer POLY1 sections) did not work well because the thin (4 μm wide) POLY2 sections sagged in the middle and did not allow the tip of the actuator to deflect properly.

Although the hinge switches operated well mechanically, they had difficulty making good electrical contact. The main problem was that the entire force of contact was delivered by the hinge's own weight. However, the mass of the hinges was so small that good contacts were never achieved. As a result, the contact resistance of these switches was held to the kilo-ohm range even though the switch used metal-on-metal contacts. Also, the poor contact quality resulted in widely varying contact resistances between test cases. As a result, the standard deviations between for some versions of the hinge switches were very large. Table 5.9 shows the contact resistances of the various types of hinge switches. Table 5.10 illustrates how increasing the force on the contact can decrease the contact resistance. The data in Table 5.10 shows the contact resistance of the versions of the hinge switches with additional force applied to the contact.. The additional force was applied using a micromanipulator probe pressed directly on the back of the contact area of the hinge switch. This resulted in the contact resistances being reduced by a factor of 100.

For all hinge switches tested, no upper or lower 3 dB frequencies were observed in the testable range between 10 Hz and 16 MHz. Because the hinge switch can pass a d.c. signal, no lower 3 dB frequency is expected, however, an upper 3 dB frequency should

Table 5.9. Hinge Switches With Vertical Heat-Drive Actuator Summary Data.

Parameter	Mean Value	Std. Deviation	# of Test Cases
All Hinge Switches			
Contact Resistance	9.91 kΩ	6.22 kΩ	37
90 μm Long Hinges			
Contact Resistance	16.95 kΩ	11.71 kΩ	6
110 μm Long Hinges			
Contact Resistance	8.5 kΩ	3.93 kΩ	8
130 μm Long Hinges			
Contact Resistance	8.96 kΩ	2.49 kΩ	8
150 μm Long Hinges			
Contact Resistance	6.36 kΩ	1.6 kΩ	6
170 μm Long Hinges			
Contact Resistance	11.47 kΩ	5.85 kΩ	9

*Devices were created in the MUMPs 6 fabrication run.

Table 5.10. Hinge Switches with Added Force Summary Data.*

Parameter	Mean Value	Range	# of Test Cases
All Hinge Switches			
Contact Resistance	75.02 Ω	17 Ω to 192 Ω	54
90 μm Long Hinges			
Contact Resistance	20.45 Ω	+/- 3.82 Ω	9
110 μm Long Hinges			
Contact Resistance	40.34 Ω	+/- 27.04 Ω	12
130 μm Long Hinges			
Contact Resistance	17.04 Ω	+/- 8.97 Ω	11
150 μm Long Hinges			
Contact Resistance	192.34 Ω	15.7 Ω to 1600 Ω	11
170 μm Long Hinges			
Contact Resistance	98.85 Ω	19.3 Ω to 673 Ω	11

exist. A limit can be put on the parasitic contact resistance by bounding it with the largest contact resistance in Table 5.9, which is 16.95 kilo-ohms, and the fact that the upper 3 dB frequency is greater than 16 MHz. This is done by taking the frequency, 16 MHz, multiplying by 2π, taking the inverse, and then dividing by the maximum contact resistance, 16.95 kΩ. By this method C must be less than 0.586 pF.

5.3.6. Rotating Lever Switch. This switch was another attempt to combine mechanical motion with heat-drive actuators. This switch operated by pushing on the short end of the lever with a heat-drive actuator and moving the contact pad either into or out of contact with the signal pads (see Chapter 4 for operational description of this switch).

This switch did not operate correctly mechanically or electrically. The heat-drive actuators used for this device had 4 μm wide drive sections and flexure widths and were therefore not able to actuate a great distance. Additionally, there was a large amount of friction and/or polysilicon sticking on the lever arm. The lever could be moved with a micromanipulator probe, but not by the heat-drive actuator. Additionally, the polysilicon contact electrode was unable to make a good contact with the signal pads.

5.4. Summary

In this chapter, the general results of the MUMPs fabrication runs were discussed. In addition, each of the devices fabricated and tested during this thesis research was discussed in detail and was supported by SEM micrographs, data tables and plots as necessary. Chapter 6 summarizes this thesis research, points out the major conclusions of this thesis, and makes suggestions for further research.

6. Conclusions and Recommendations

This chapter summarizes the main points of this thesis research, highlights the main conclusions, and gives suggestions for further research.

6.1. Conclusions.

Many different MEM switches were fabricated and tested during this research. The switches used electrostatic forces, mechanical forces, and differential heating to provide actuation. The switches ranged in complexity from single-actuator switches up to three or four actuators for a single switch. All switches were characterized for their ability to actuate correctly, and their ability to switch both a.c. and d.c. signals.

The heat-drive actuator is the most promising actuator used in this thesis research. It operated the most predictably, and it required very little less than 25 mW of input power to operate. It is possible to design heat-drive actuators that operate at 5 volts and less than 5 mA. Thus, heat-drive actuators are compatible with conventional electronics voltage and current standards which may lend itself to a great many applications in the future. The only disadvantage of the heat-drive actuator is the motion is limited to around 12 μm of deflection.

In order to more fully understand the operation of the heat-drive actuator, a significant portion of this research went into characterizing the deflection versus current relationships for the heat-drive actuator. Many different dimensions were tested and gauged to determine the optimum characteristics for maximum deflection. It was determined that heat-drive actuators 200 μm in length with a flexure length of 40 μm, a

drive-section and flexure width of 2 μm, a thick-section width of 14 μm, and a corresponding g value of 10 μm actuate the farthest distance (up to 12 μm) with the least amount of current (approx. 5 mA). It was also found that the difference in temperature, ΔT, between the drive and thick sections of the heat-drive actuator could be predicted using a single constant related to the thermal resistance of polysilicon to air, A_{poly}. This constant, 1.9 +/- 0.08 ($m^{1.5}$-°C-W^{-1}) for POLY1 devices and 7.4 +/- 0.88 ($m^{1.5}$-°C-W^{-1}) for POLY2 devices, could be applied to an empirical formula to determine the thermal resistance constant, a, for a specific device geometry. With *a* known, it was then possible to predict ΔT from the applied current. As a result, it was found that the deflection of the heat-drive actuator could be predicted from the applied current.

The next most promising actuator usable for MEM switching in the MUMPs process is the hinge-actuator. This device is attractive because of its ability to make metal-to-metal contacts in the MUMPs process. A vertical heat-drive actuator was developed specifically to support the vertical motion of the hinge switch. This actuator worked extremely well for devices with POLY1 lengths shorter than 112 μm. It was determined that the 170 μm and 150 μm long hinges combined with vertical heat-drive actuators with a POLY1 section shorter than 112 μm provided the most consistent actuation and the lowest contact resistances. The vertical heat-drive actuators worked well enough that they may be useful for other applications as well.. The only disadvantage to the hinge actuator is the difficulty in flipping them over after etching release. Clearly, use of the aero-duster can is not feasible for this purpose except for die containing only hinge actuators.

It was determined that the switches based upon electrostatic forces have the least potential for low-power, high-fidelity switches with wide bandwidths. The thick polysilicon layers (either 2.0 μm or 1.5 μm) and the 2.0 μm minimum feature size design rule forced most electrostatic devices to employ voltages of between 50 and 100 volts to move. Such high voltages caused problems with nearby dust and debris shorting electrostatic gaps and thereby making the devices inoperational. Despite the disadvantages, electrostatic switches developed in the MUMPs process, such as the microbridge switch, may have some use as one-time programmable switches because of their propensity to stick down after actuation. Devices utilizing electrostatic forces would be more useful in fabrication processes where the minimum feature size is less than 1 μm or in processes in which very high aspect ratio structures may be created.

6.2. MEM Fabrication Processing.

The most important conclusion of this thesis research is the utmost importance of the fabrication facilities and processing available to AFIT for MEMs research. In order to optimize many designs it is necessary that the designs be fabricated with desired layer thicknesses, resistivities, etc. The MUMPs and LIGA processes are beneficial in that they provide a means to fabricate MEMs designs for a great many users. Although adequet for "proof of concept" device fabrication and early prototyping, these processes are not adequet if custom made devices are desired

Specific to MEM switching, a specialized process with features not available in MUMPs, is necessary to create high fidelity switches. The ability to use many layers of

both highly conductive material and highly insulative material is required for good switching characteristics. No commercially available process provide this flexibility. As seen throughout Chapter 5, the electrical limitations of the polysilicon structural layers often forced contact resistances well up into the 10s of kΩ range. Additionally, the upper 3 dB frequencies for many devices low (generally < 1 MHz) due to process limitations. The only way to avoid these kinds of problems is to use structural layers with better electrical qualities (namely low resistivity). For production type MEM microswitch development, different processes are necessary.

6.3. Recommendations.

Based upon the results of this thesis, it is recommended that future research in the area of MEM high fidelity switching center around using the heat-drive actuator and the hinge switch. As discussed in section 6.1, these devices have the most potential in the MUMPs process which is currently available to AFIT. Perhaps some way can be found to combine the predictable motion of the heat-drive actuator with the metal-to-metal contact ability of the hinge switch.

Continued research on the physical modeling of the heat-drive actuator would be beneficial for the development of MEM devices for almost any application. This thesis was able to determine that an exponential empirical relation between the applied current and resulting deflection exists, but a good theoretical model for predicting the deflection for a given current based on the dimensions of the actuator is needed.

The most major recommendation for the development of MEM switches is to try and find other fabrication processes that may be more suited towards switching. Processes with large numbers of highly conductive layers and isolation layers would be ideal. The MUMPs process is good for exploratory research and some basic prototyping, but not much more (perhaps with the exception of the hinge switch) as far as MEM high-fidelity switching is concerned.

Additionally, it is recommended that some time be spent analyzing the devices that were designed in the LIGA process, but have not yet been returned to AFIT. The high-aspect ratio and high conductivity of the structural layers may prove beneficial for electrostatic devices and MEM switching.

Appendix A: Layout Plots not Shown in Chapter 4

Device: Microbridge Switch
Version: MUMPs 7, ver. 5

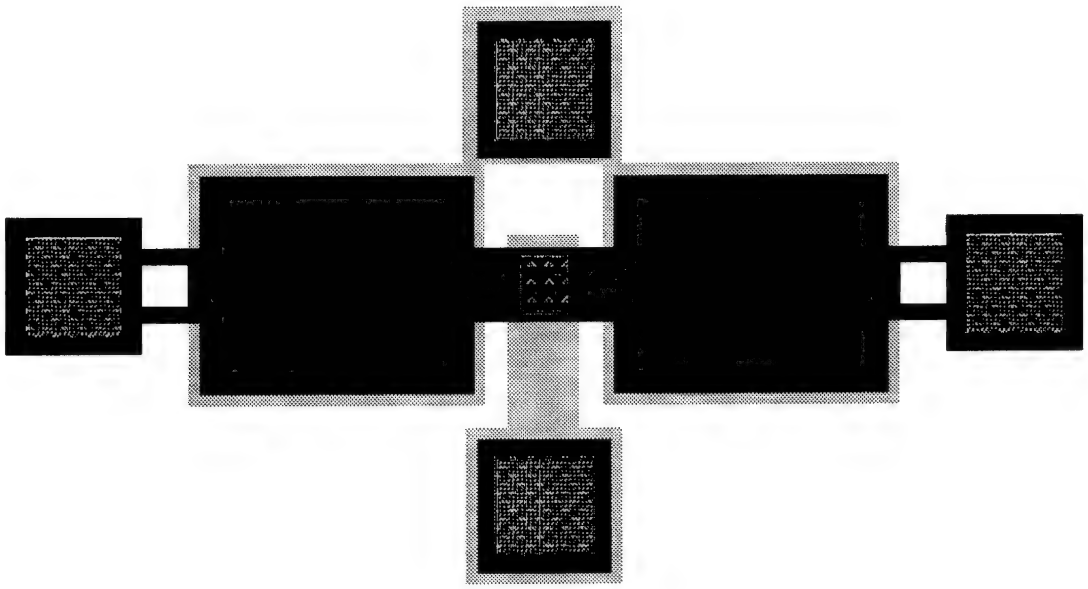

Device: Cantilever Beam Switch
Version MUMPs 5, ver. 8, 9

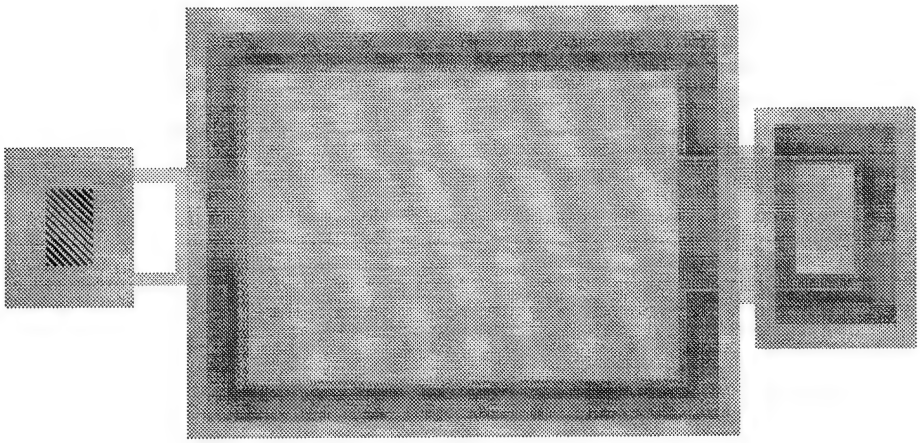

Device: Cantilever Beam Switch
Version MUMPs 5, ver. 8, 9

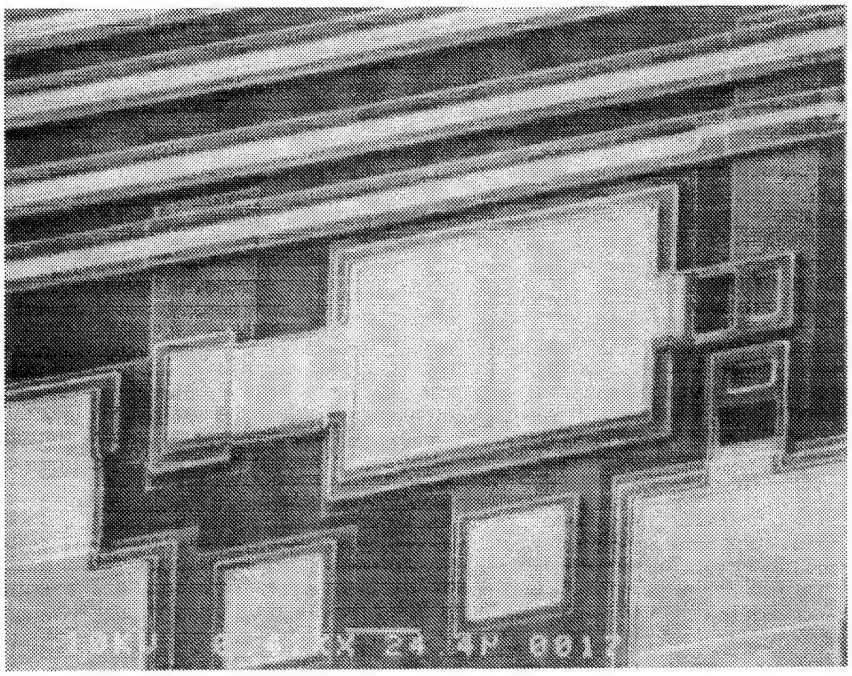

Device: Push-Lock Switch
Version: MUMPs 4, ver. 1

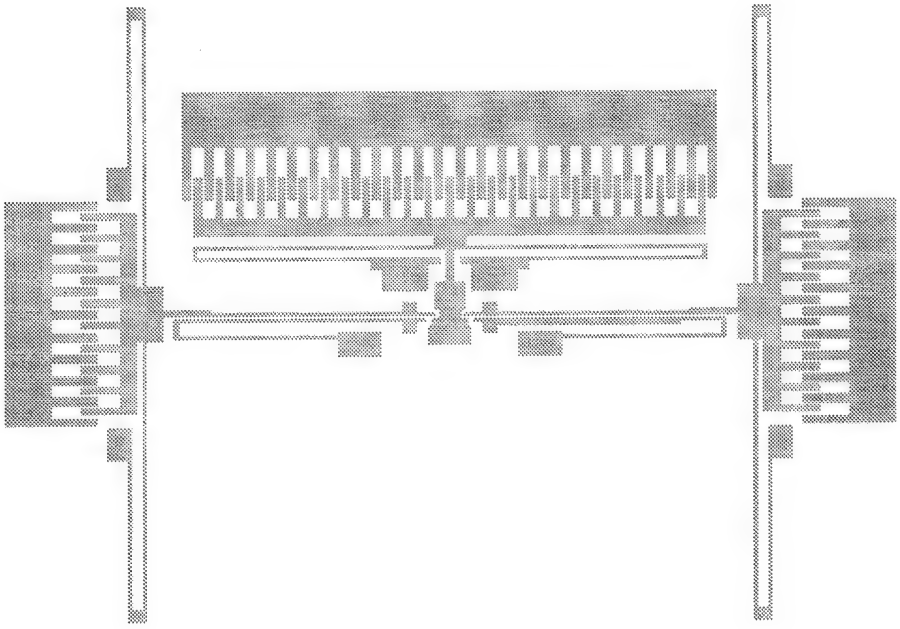

Device: Push Lock Switch
Version: MUMPs 5, ver. 4

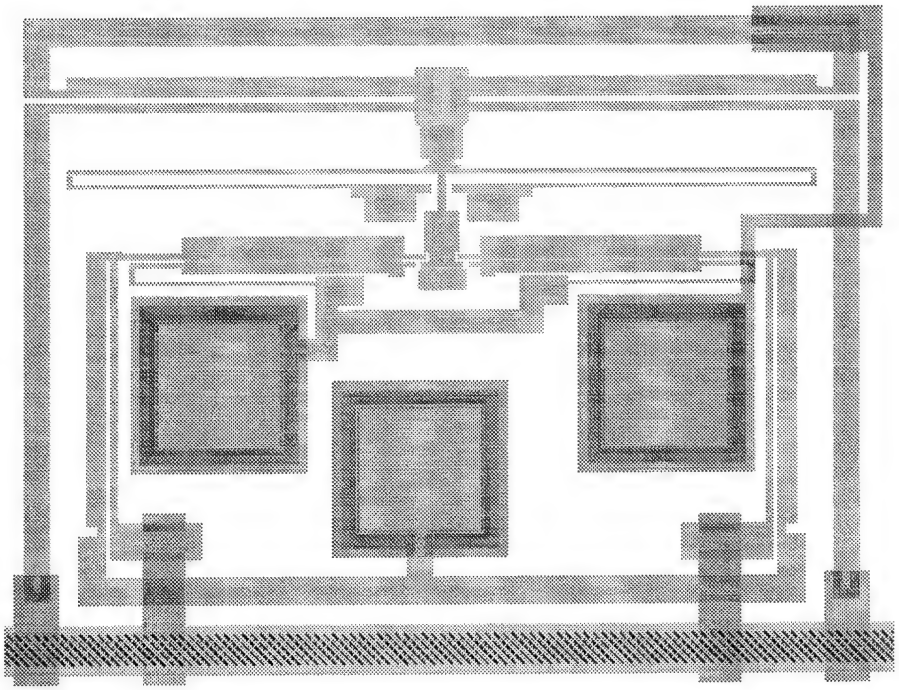

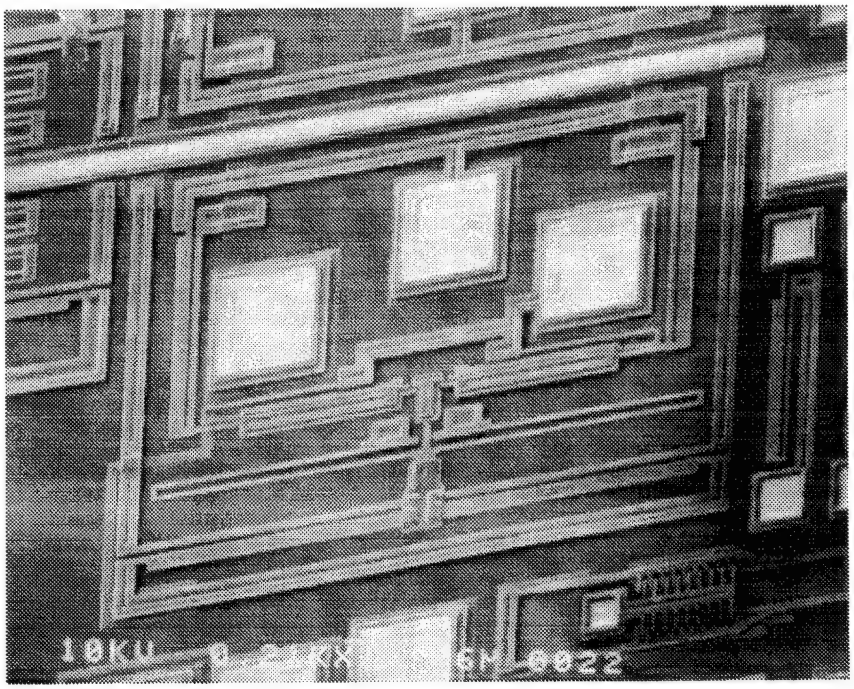

Device: Heat-Spring Switch
Version: MUMPs 6, ver. 3

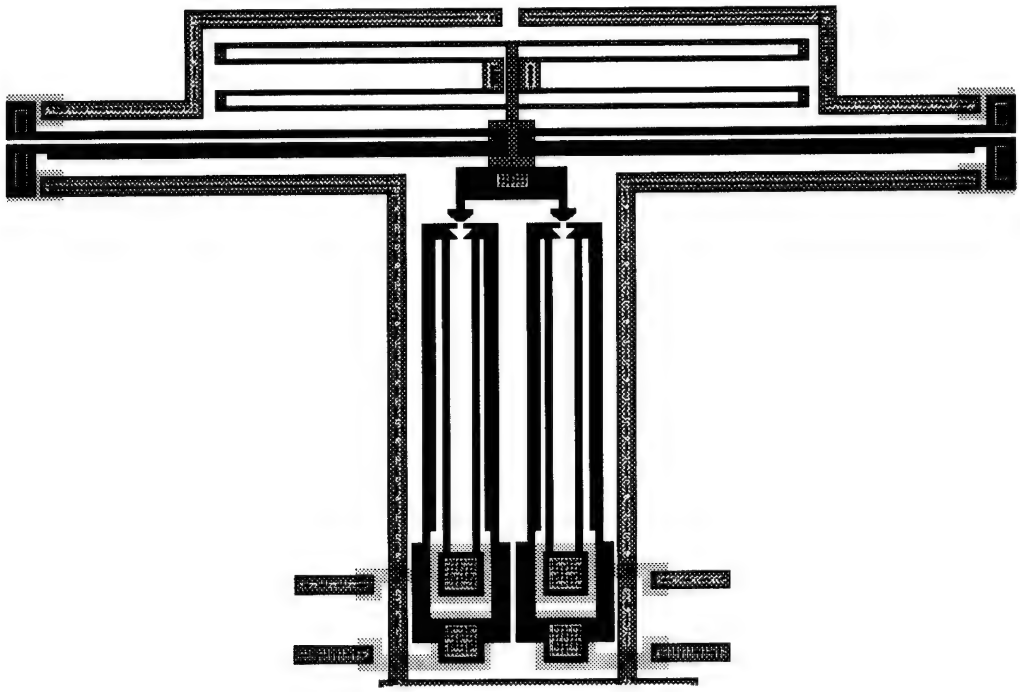

Device: Electrostatic Cantilever-Lock Switch
Version: MUMPs 5, ver. 2

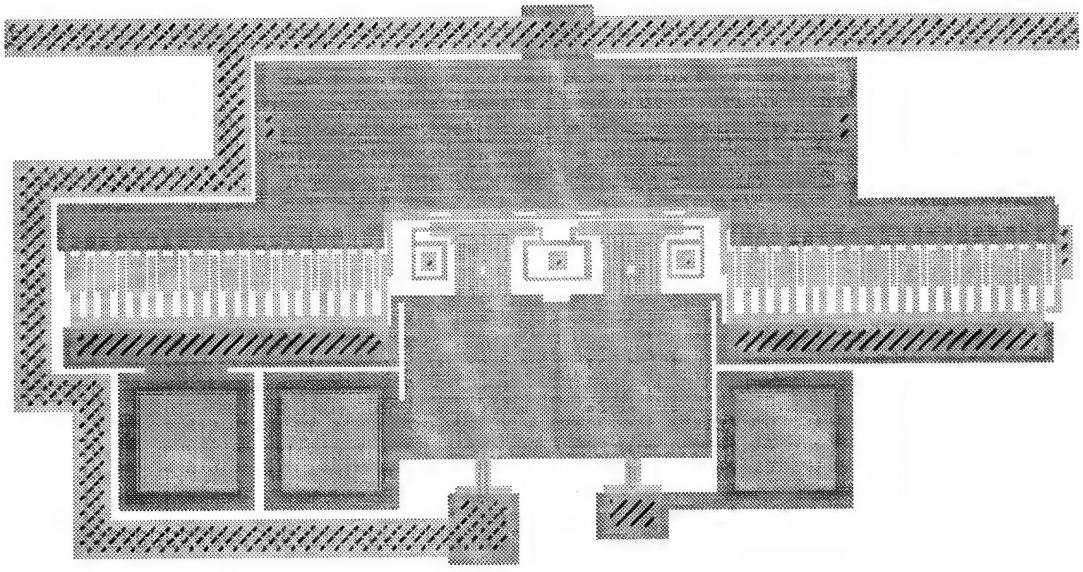

Device: Electrostatic Cantilever-Lock Switch
Version: MUMPs 5, ver. 2

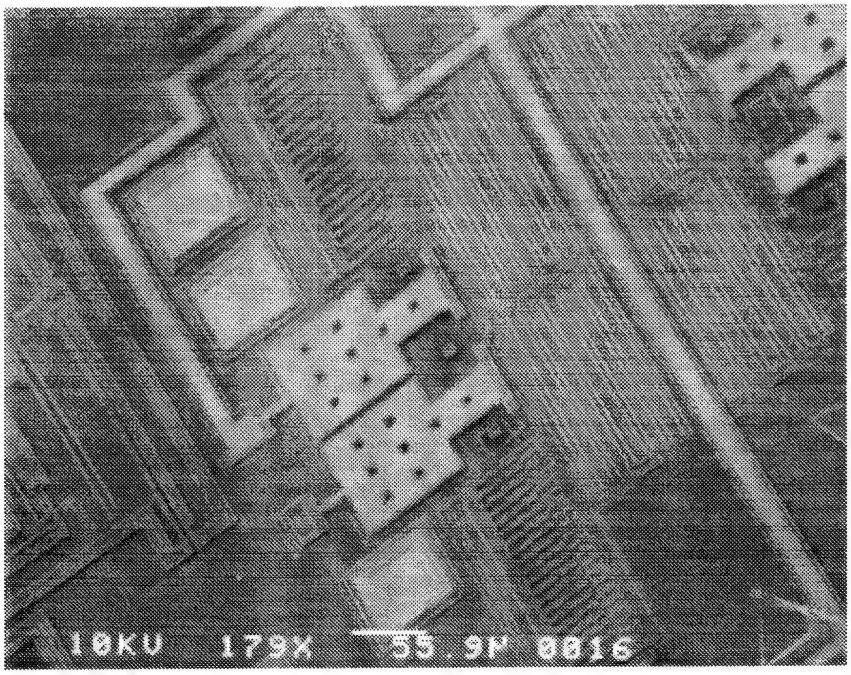

Device: Electrostatic Cantilever-Lock Switch
Version: MUMPs 5, ver. 3

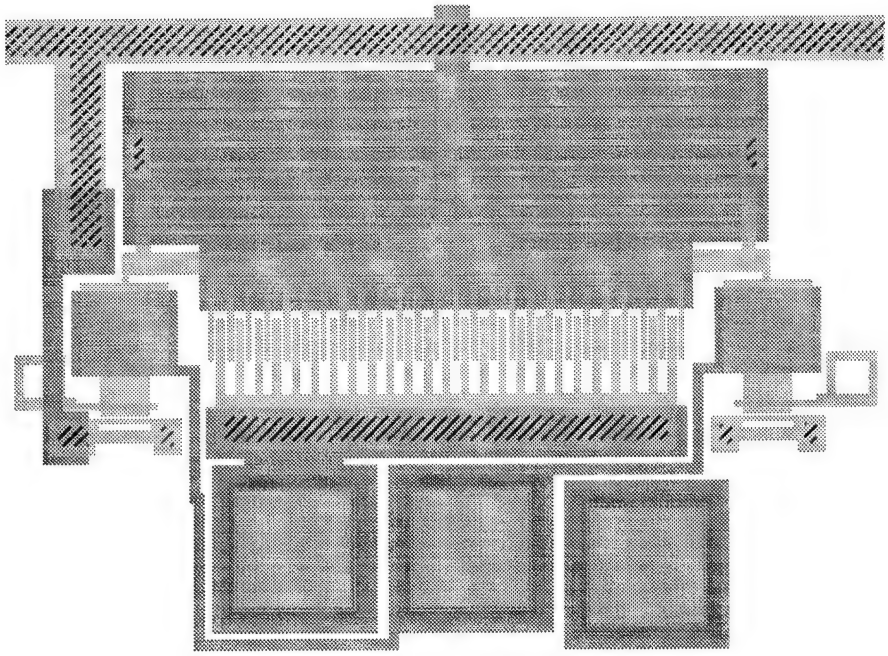

Device: Electrostatic Cantilever-Lock Switch
Version: MUMPs 5, ver. 3

Device: Electrostatic Cantilever-Lock Switch
Version: MUMPs 5, ver. 4

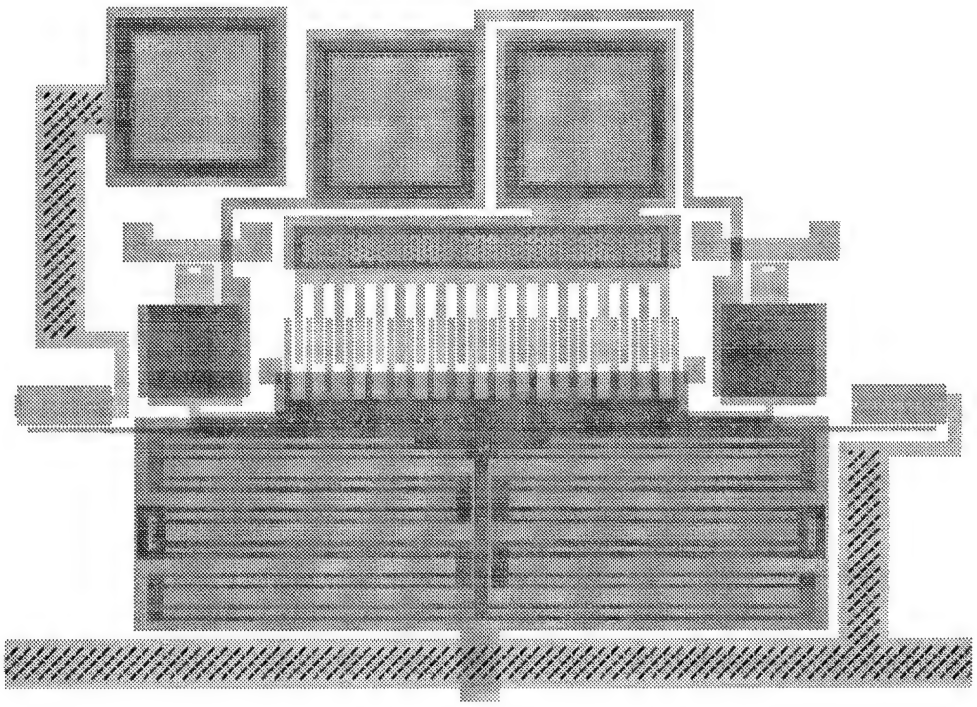

Device: Electrostatic Comb-Lock Switch
Version: MUMPs 5, ver. 5

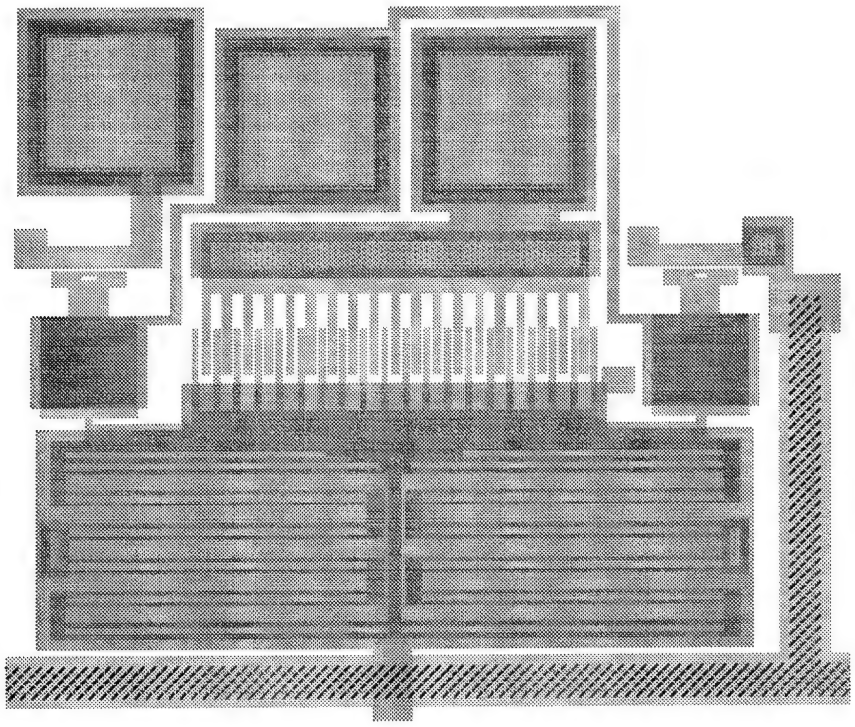

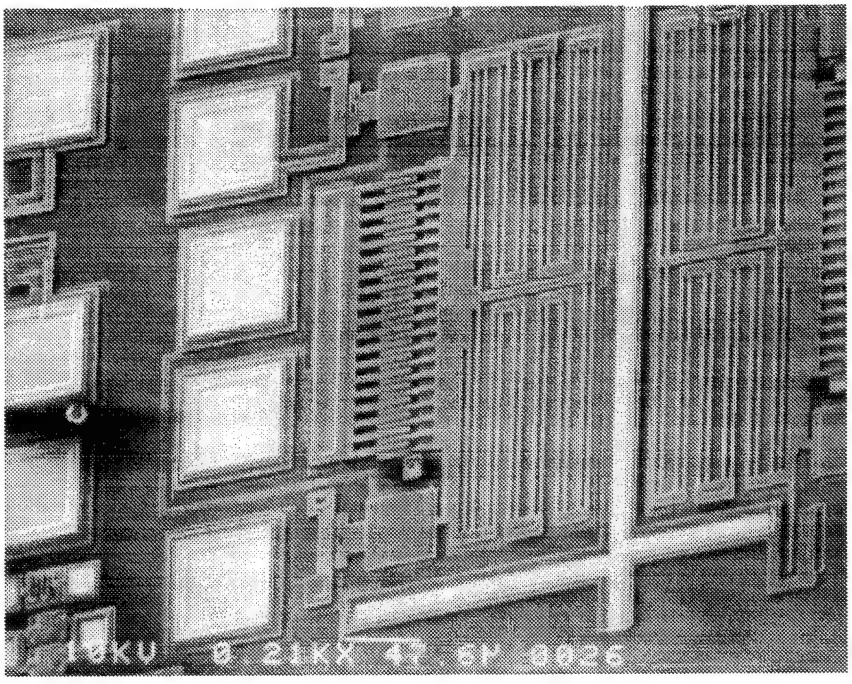

Device: Vertical Heat-Drive Actuator
Version: MUMPs 7, ver. 9, 10

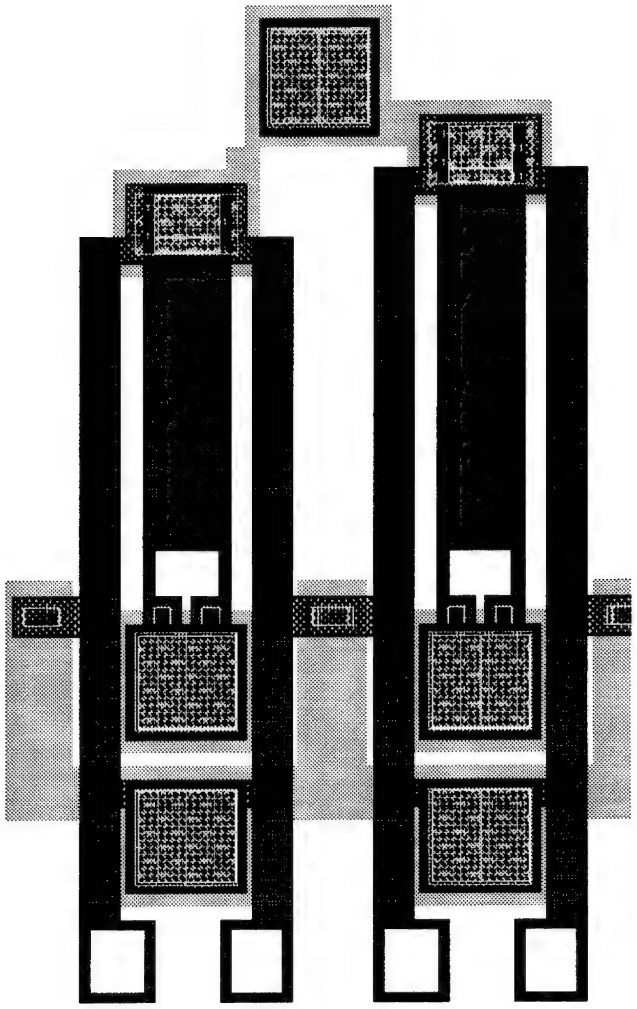

Appendix B: Heat-Drive Actuator Array Graphs

Array # 1: Deflection vs Applied Current

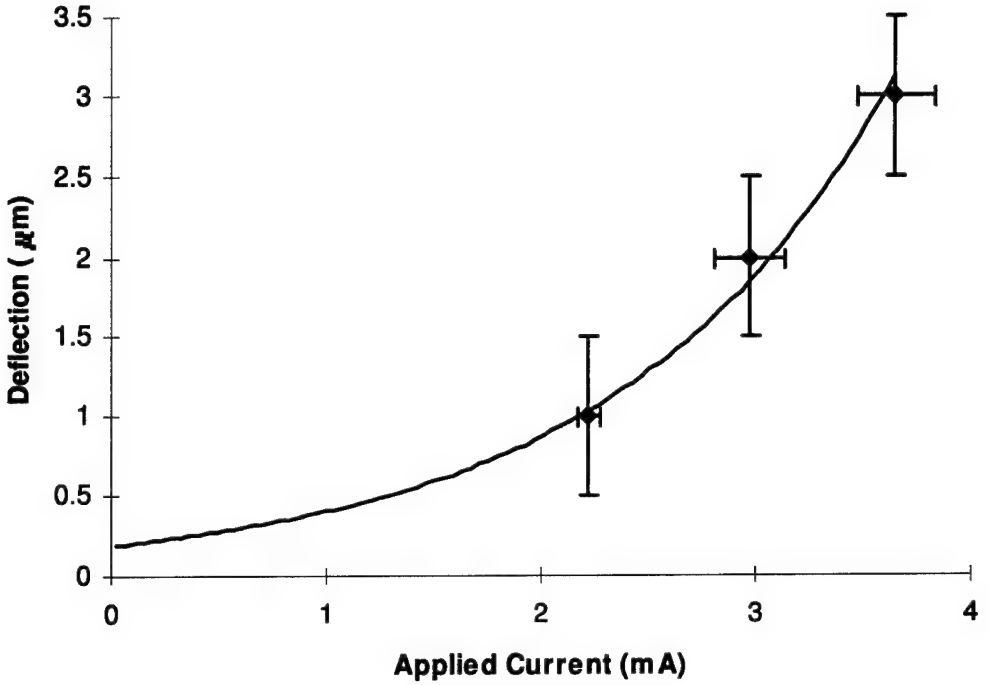

Array # 1: ΔT vs. Applied Current

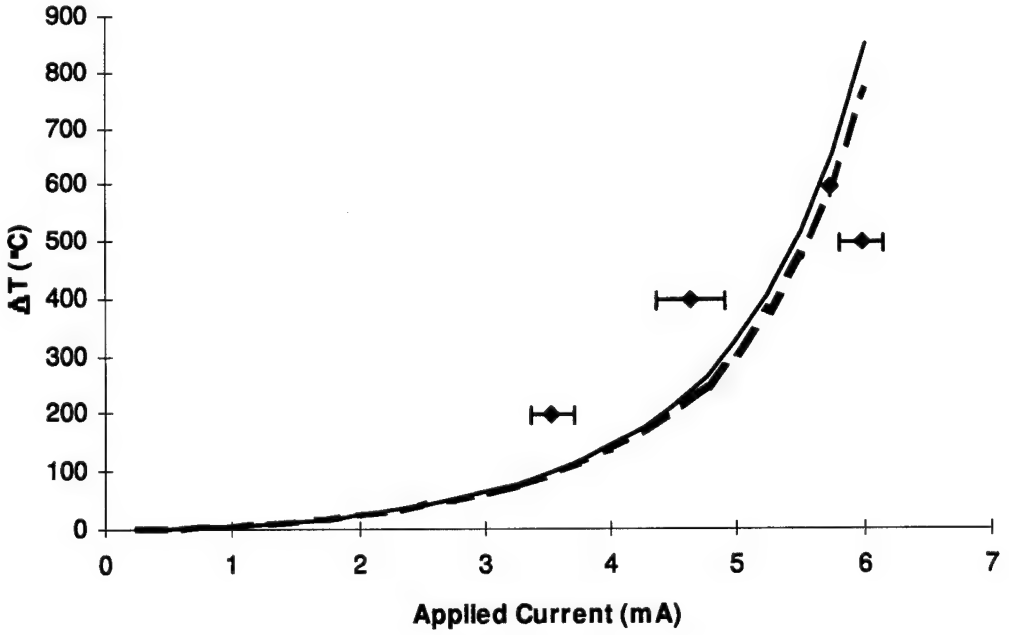

Array # 2: Deflection vs. Applied Current

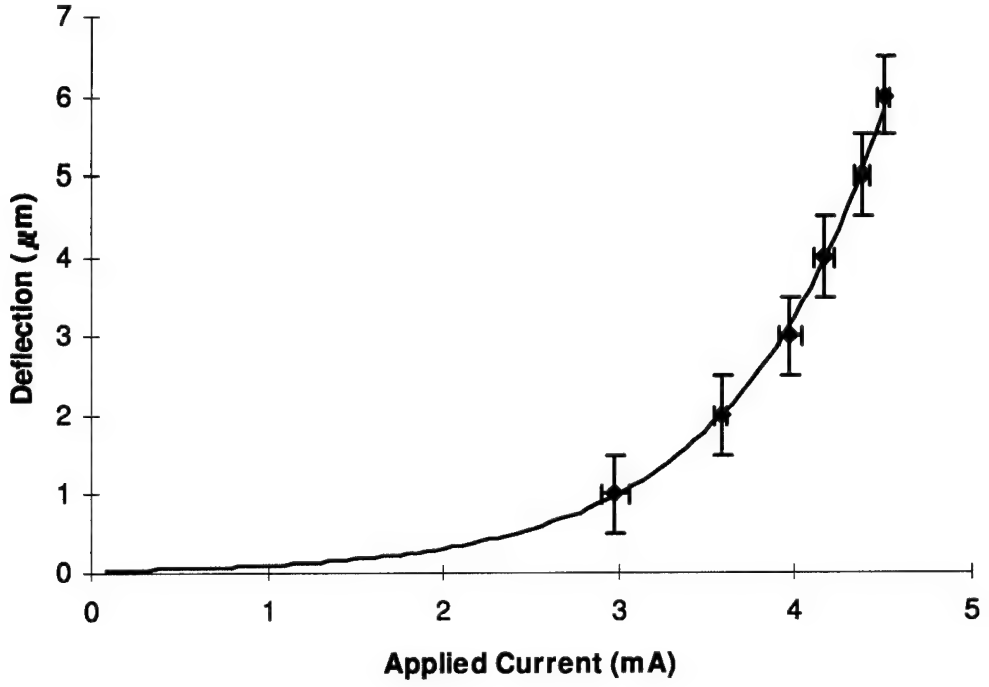

Array # 2: ΔT vs. Applied Current

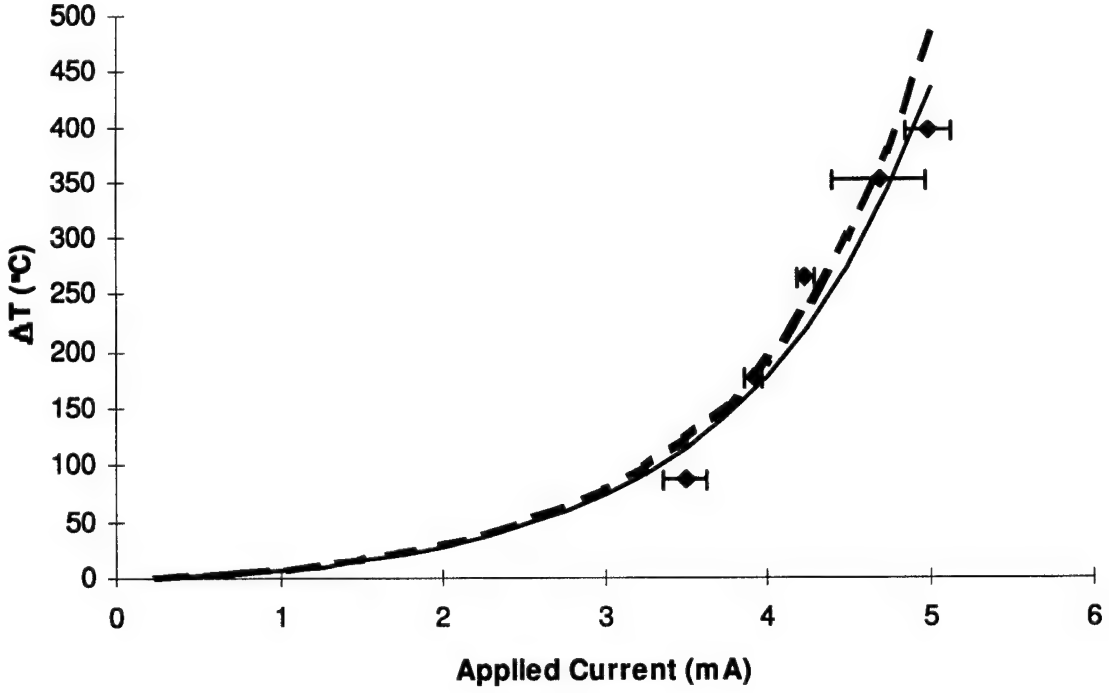

Array #3: Deflection vs. Applied Current

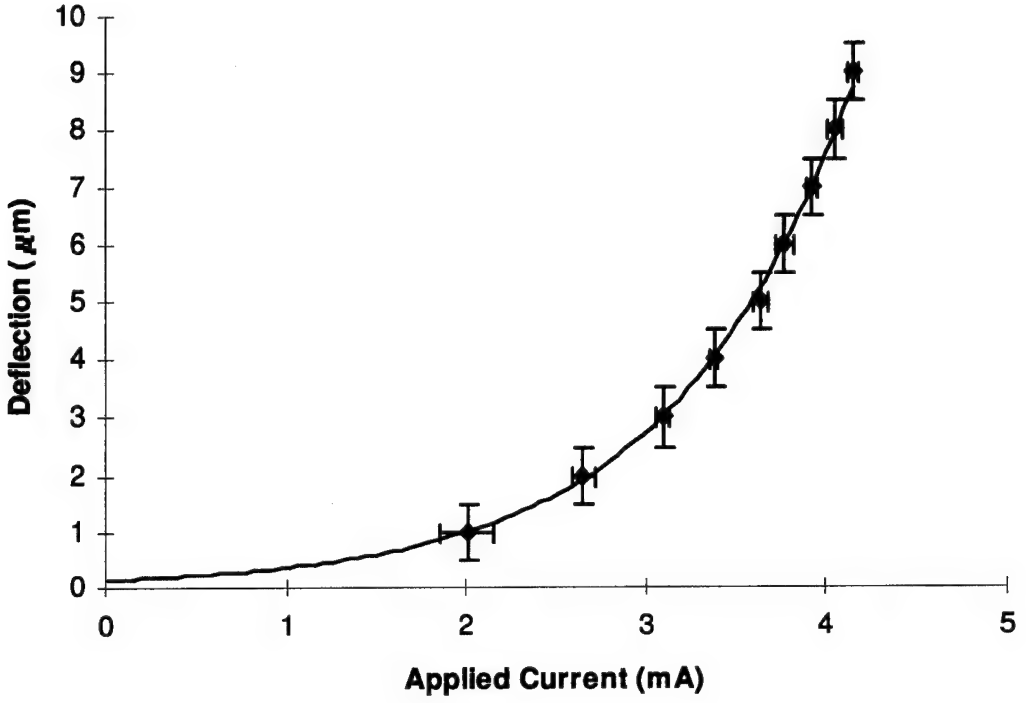

Array #3: ΔT vs. Applied Current

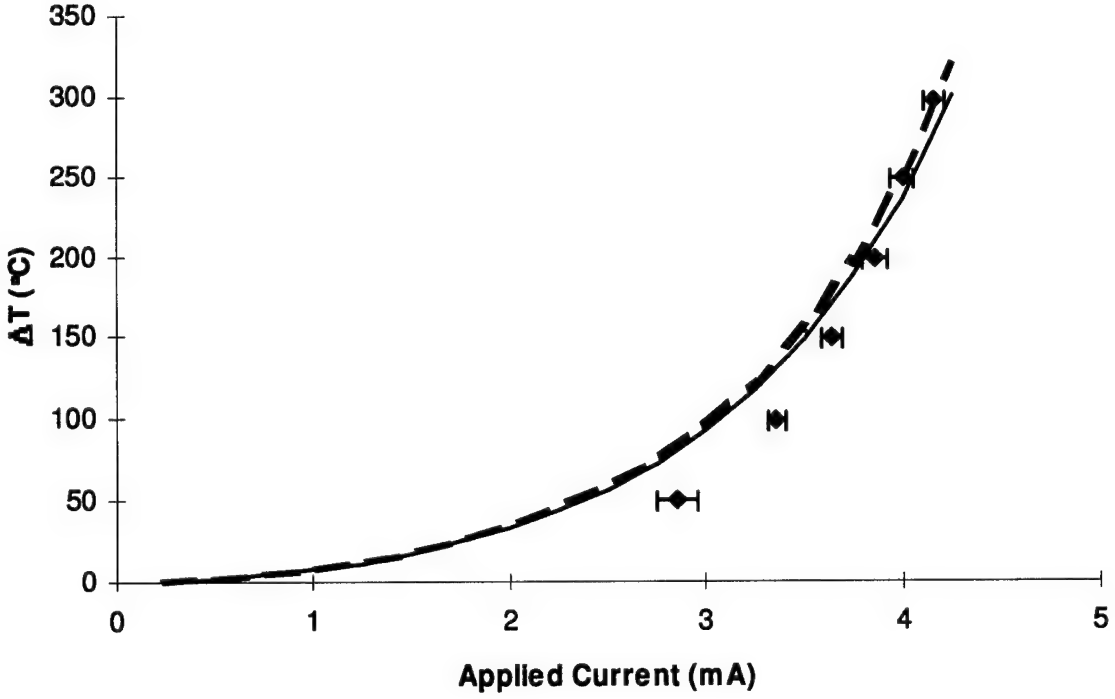

Array # 4: Deflection vs. Applied Current

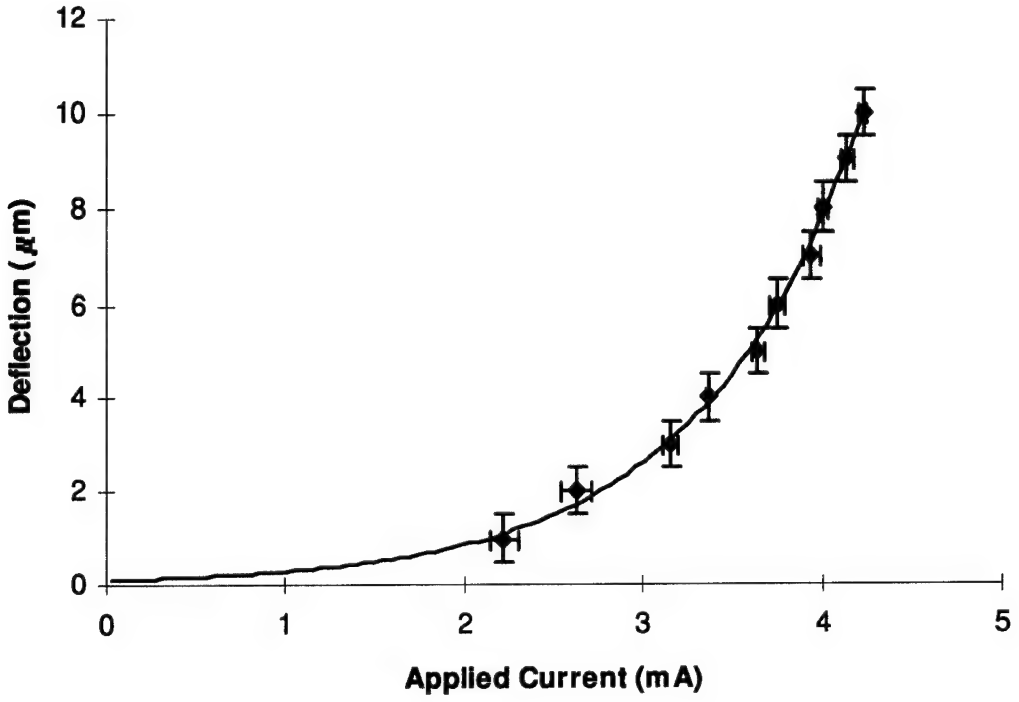

Array # 4: ΔT vs. Applied Current

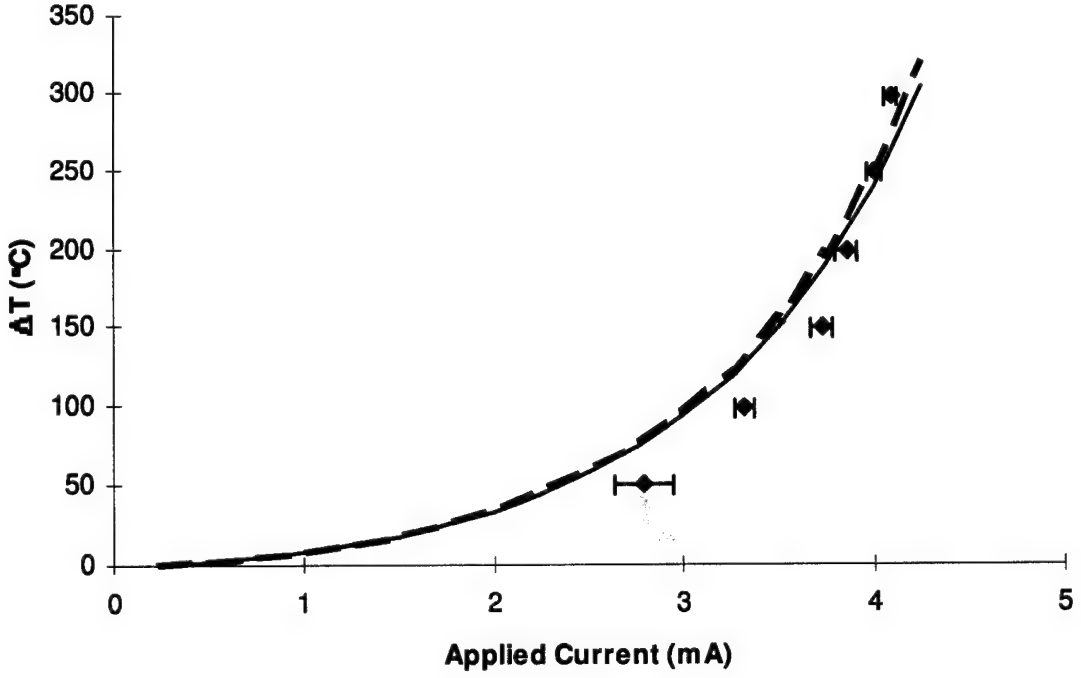

Array # 5: Deflection vs. Applied Current

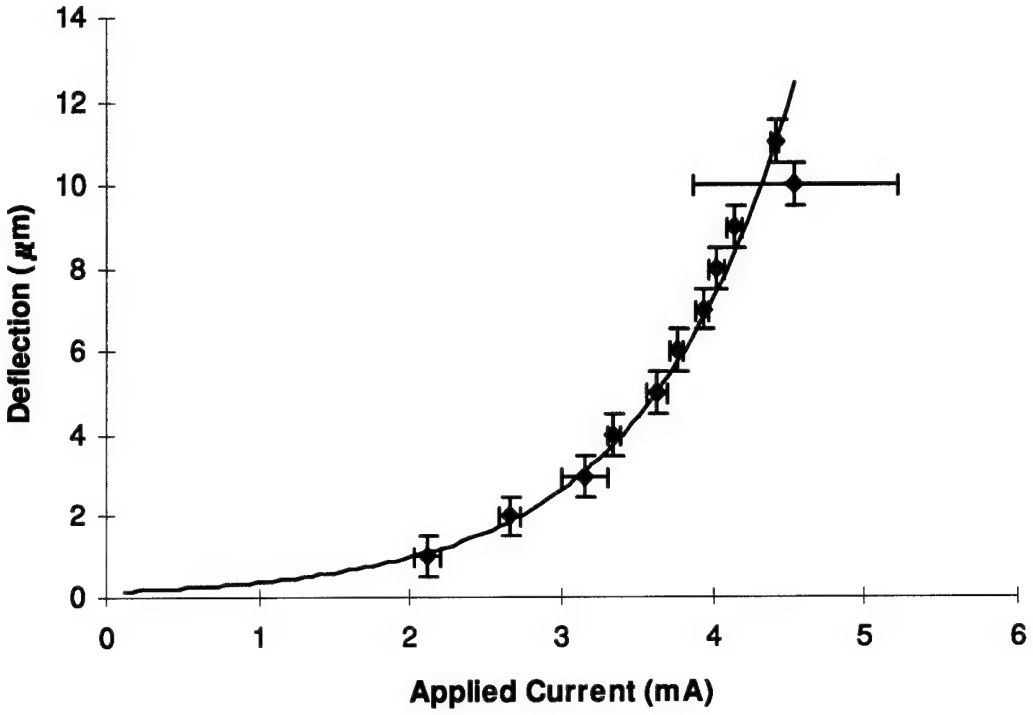

Array # 5: ΔT vs. Applied Current

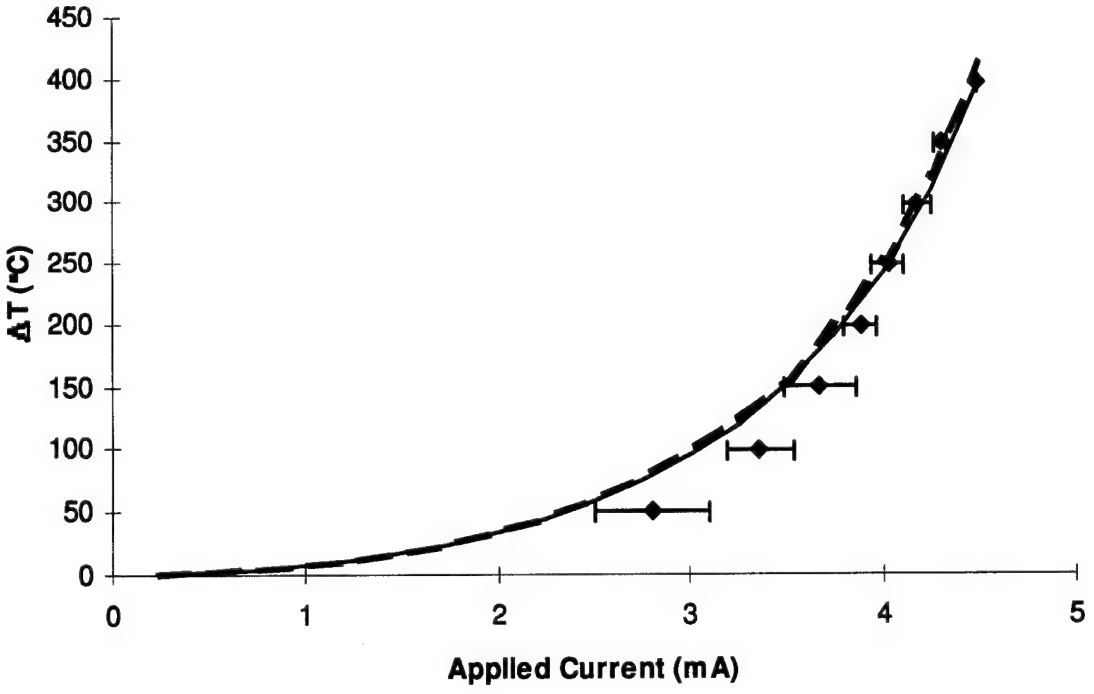

Array # 6: Deflection vs. Applied Current

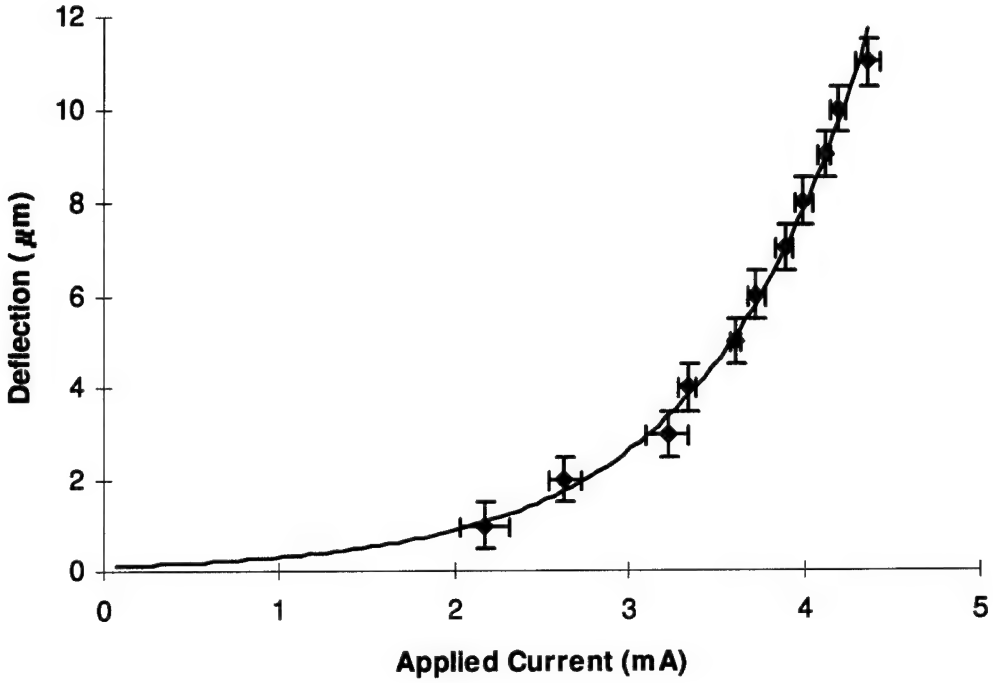

Array # 6: ΔT vs. Applied Current

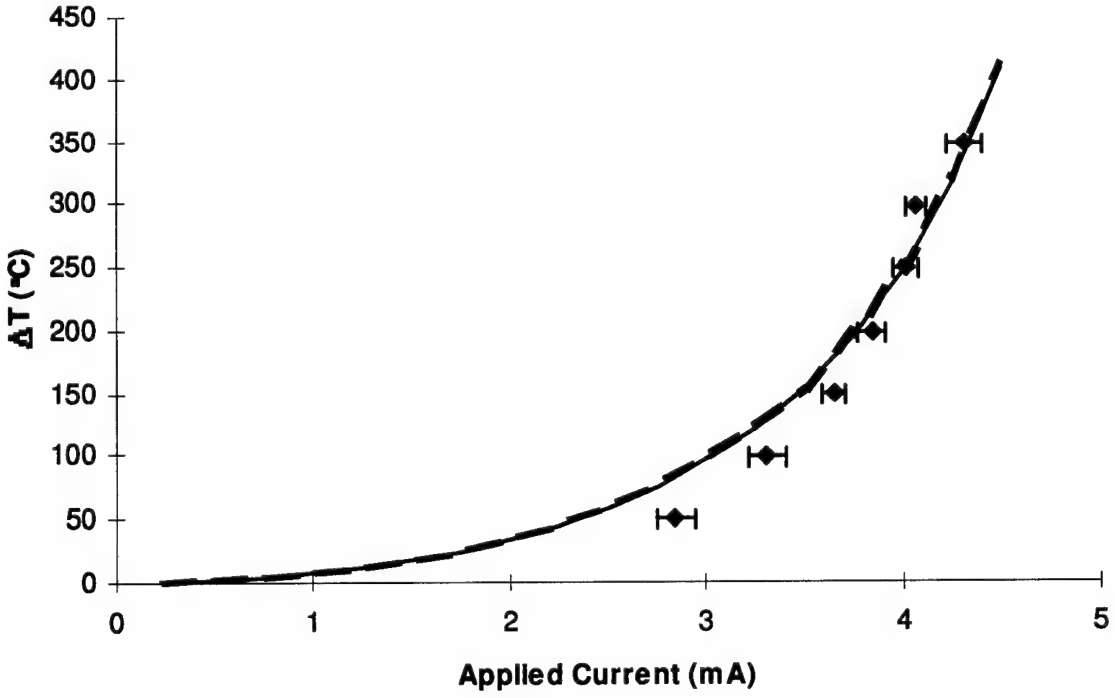

Array # 7: Deflection vs. Applied Current

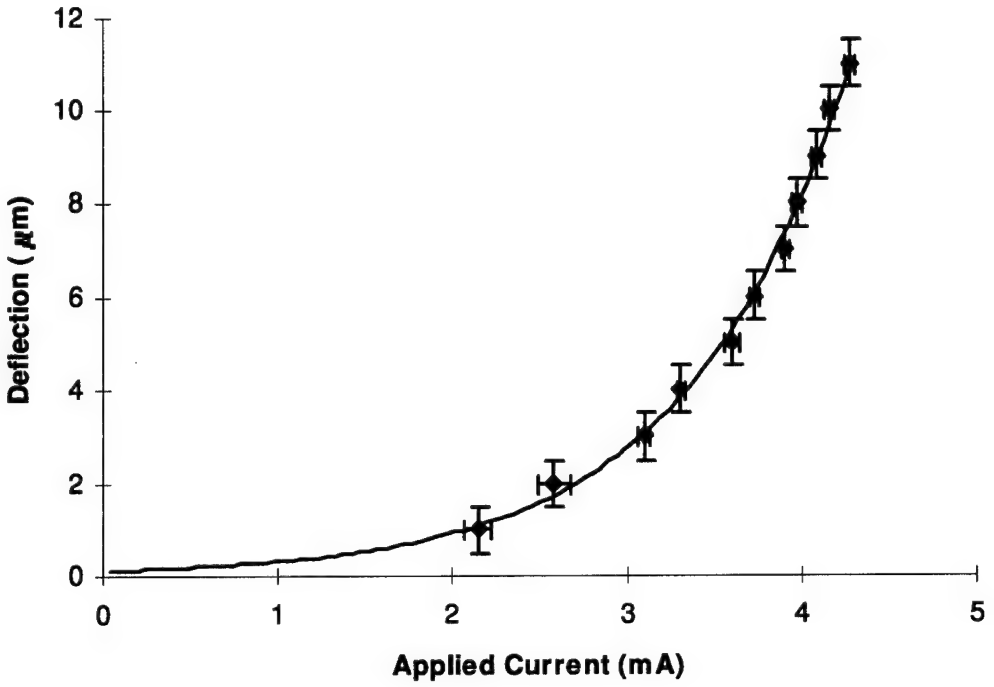

Array # 7: ΔT vs. Applied Current

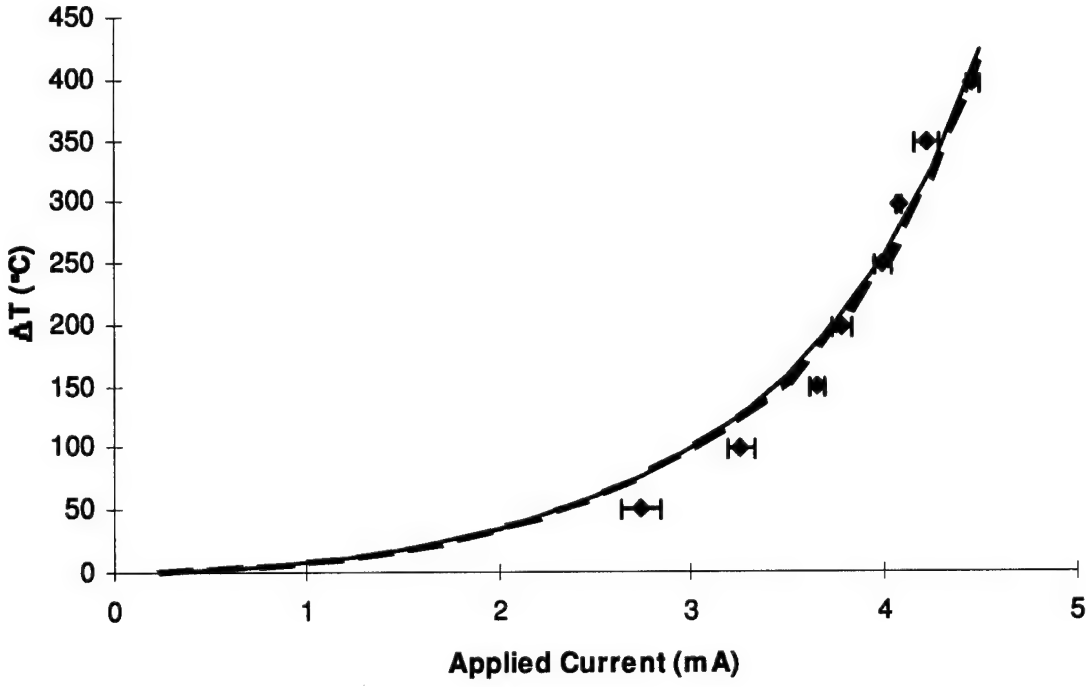

Array # 8: Deflection vs. Applied Current

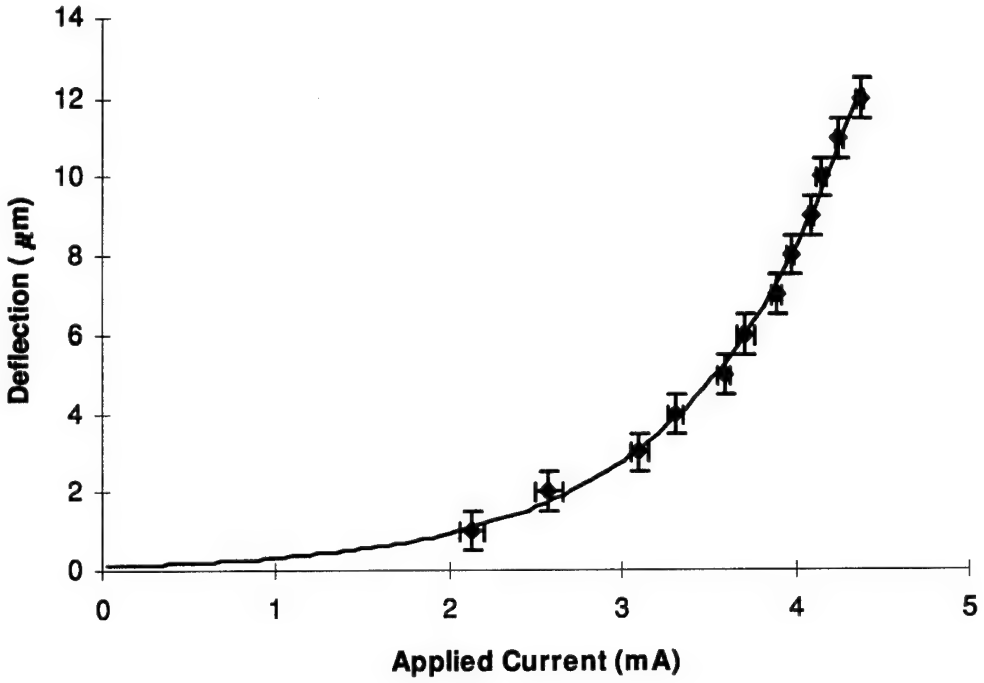

Array # 8: ΔT vs. Applied Current

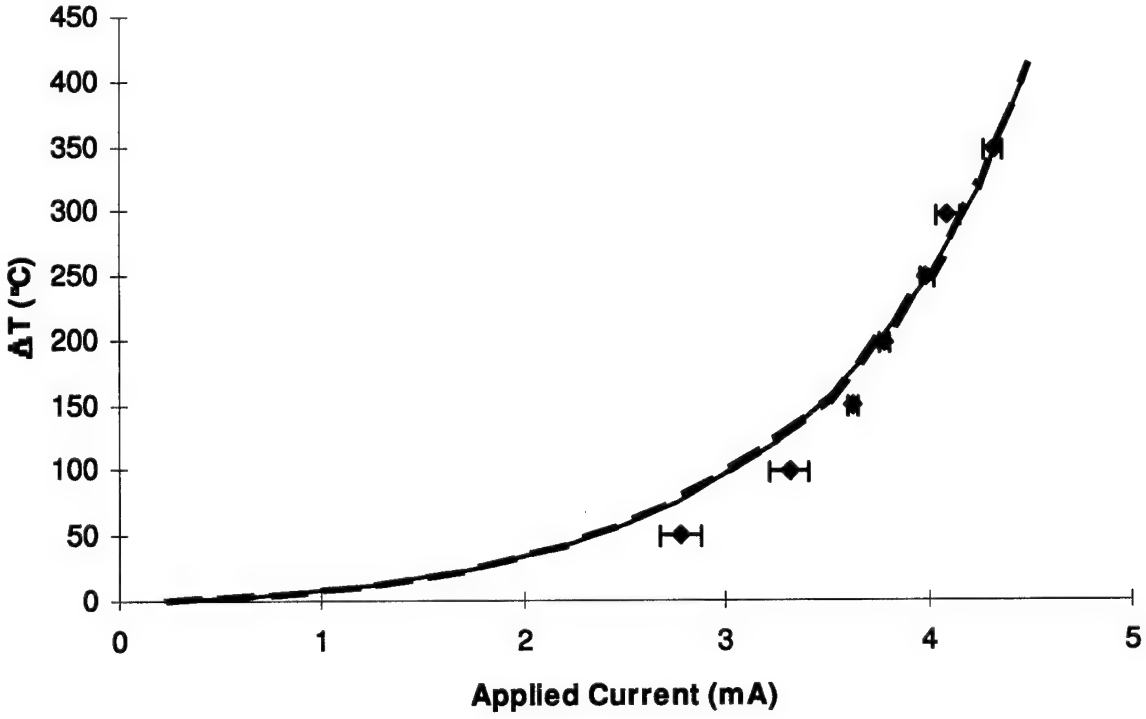

Array # 9: Deflection vs. Applied Current

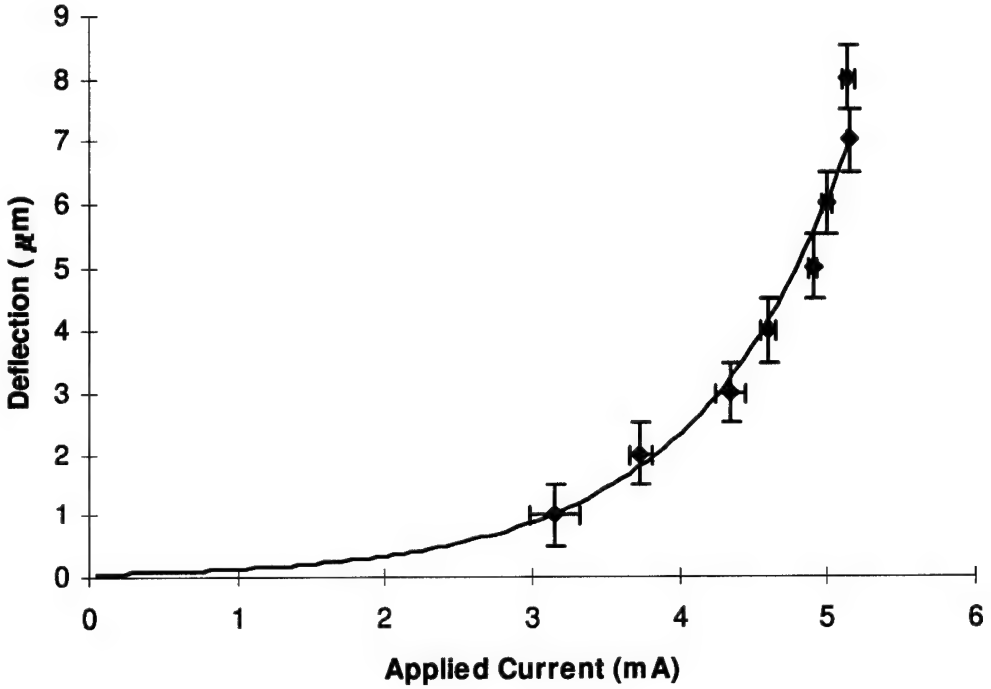

Array # 9: ΔT vs. Applied Current

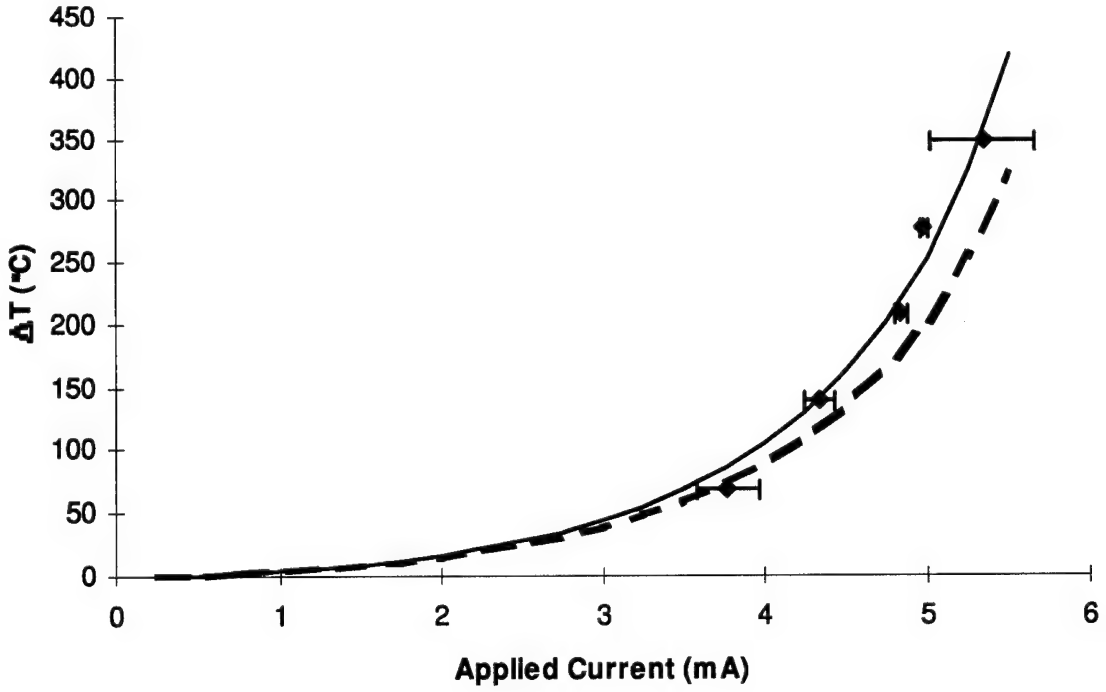

Array # 10: Deflection vs. Applied Current

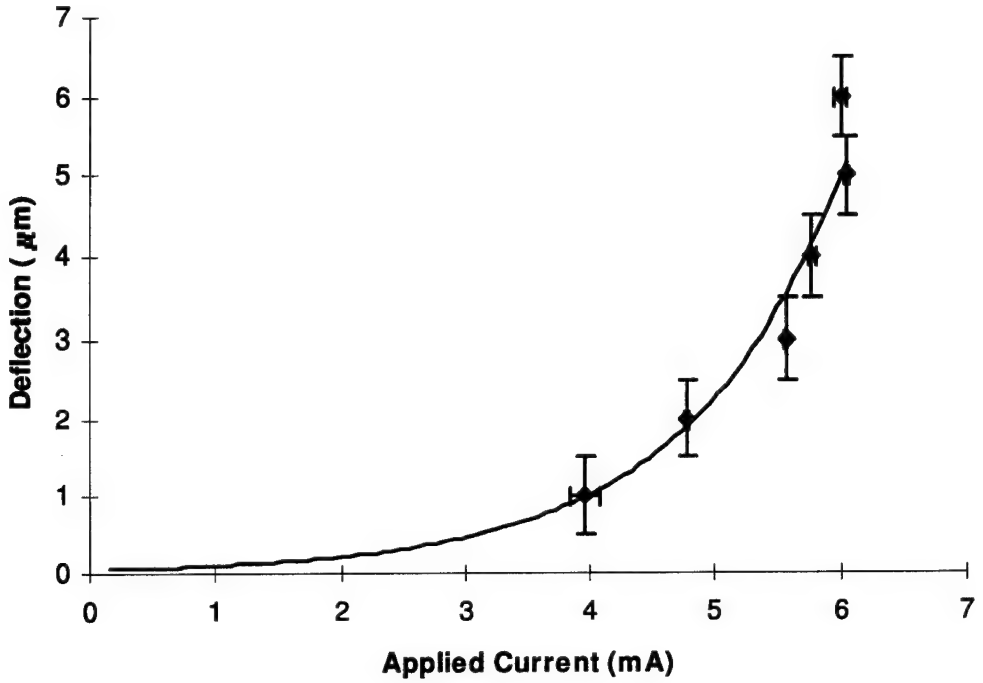

Array # 10: ΔT vs. Applied Current

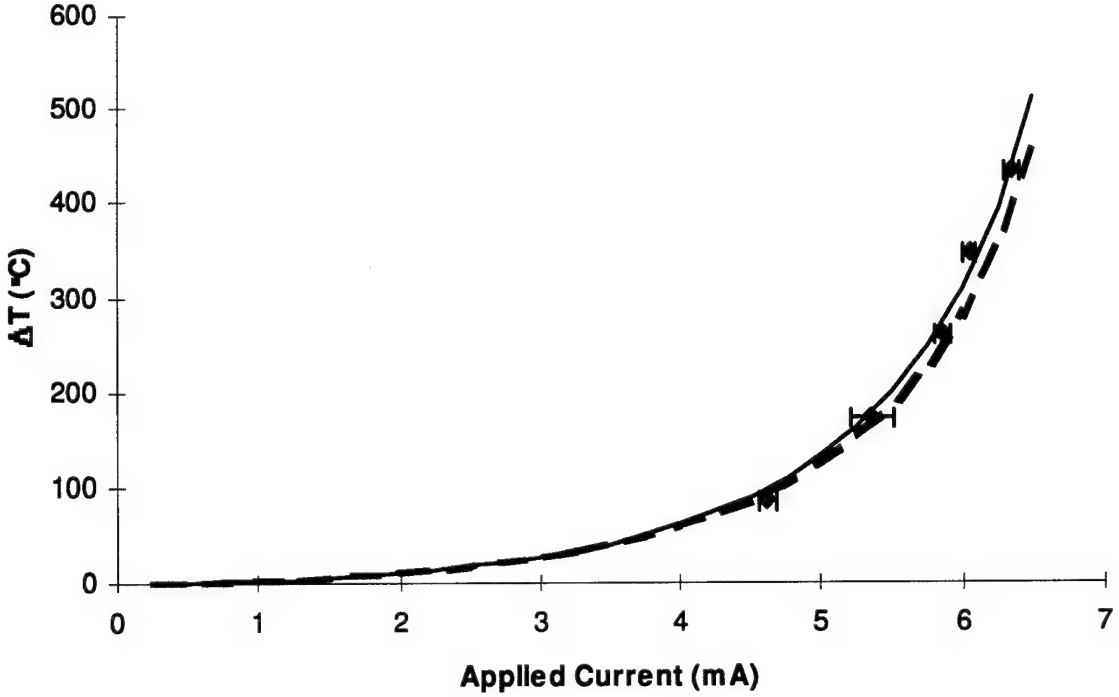

Array # 11: Deflection vs. Applied Current

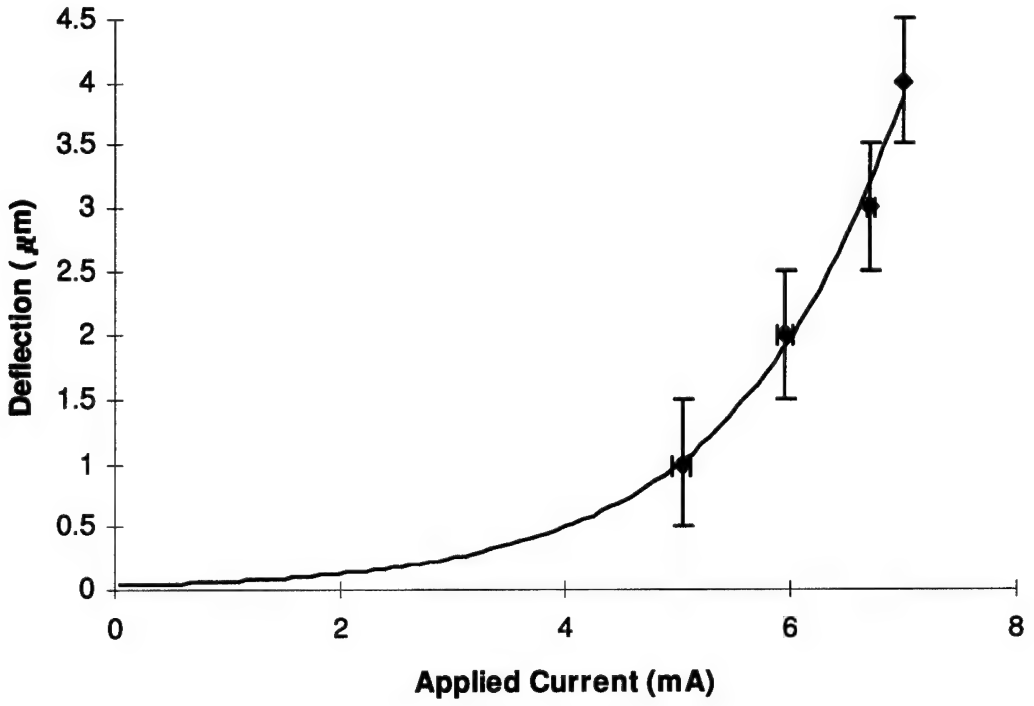

Array # 11: ΔT vs. Applied Current

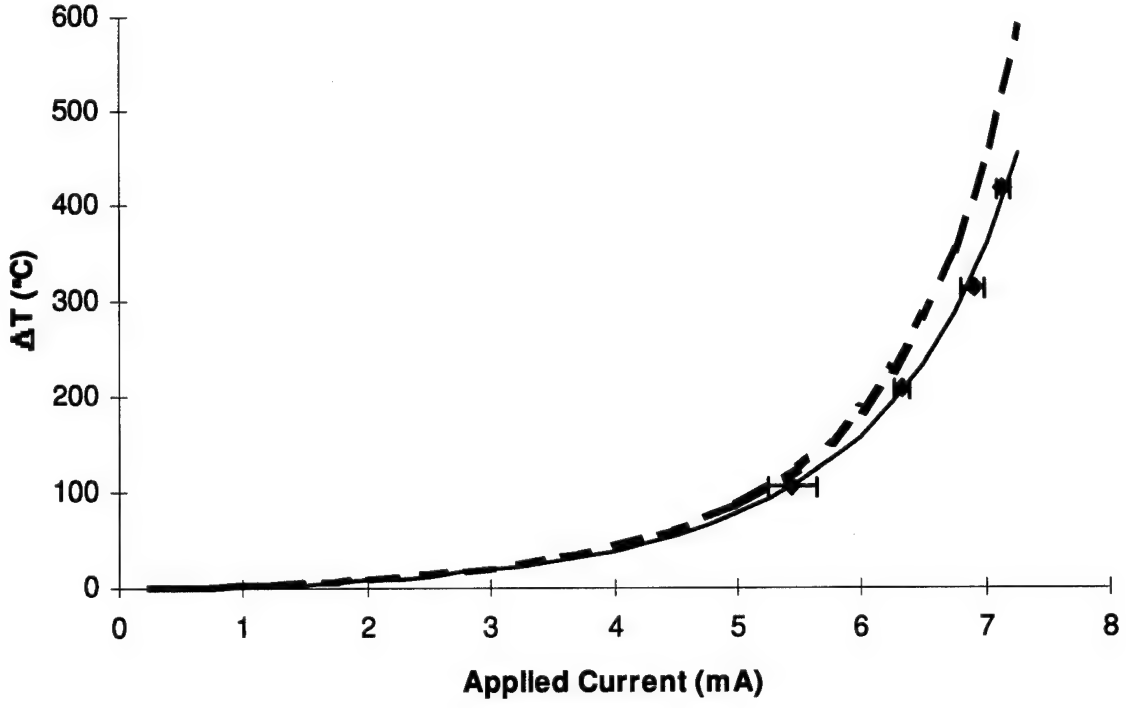

Array # 12: Deflection vs. Applied Current

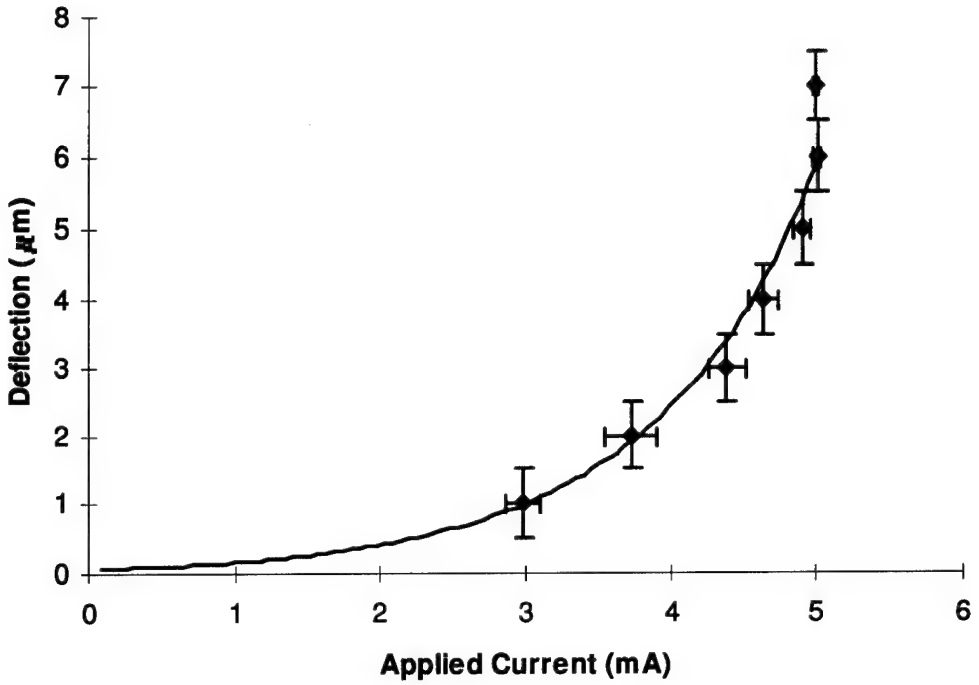

Array # 13: Deflection vs. Applied Current

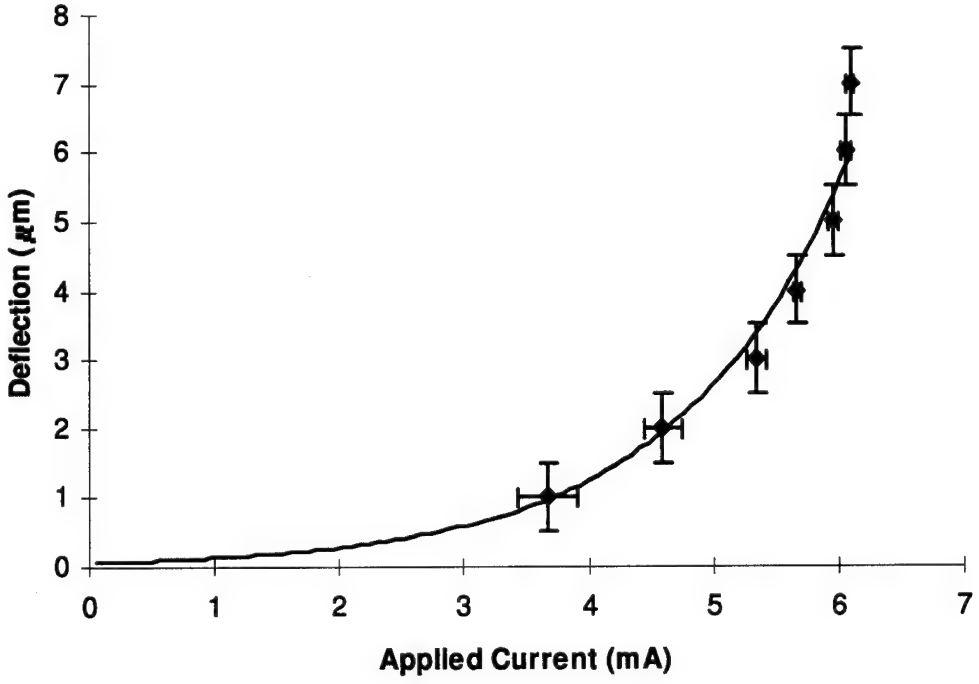

Array # 14: Deflection vs. Applied Current

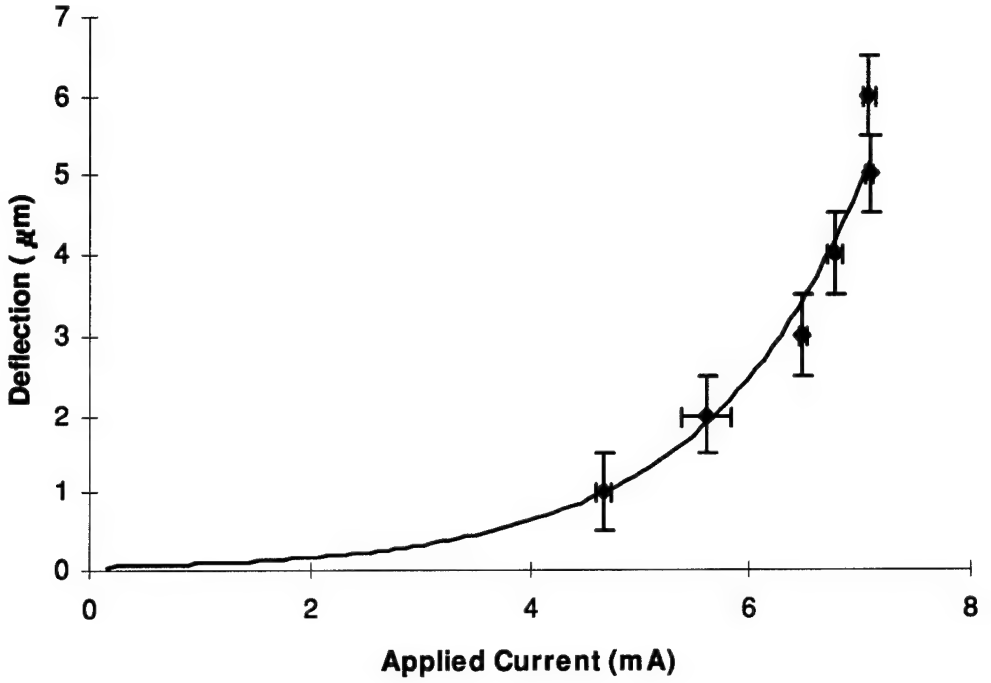

Array # 15: Deflection vs. Appplied Current

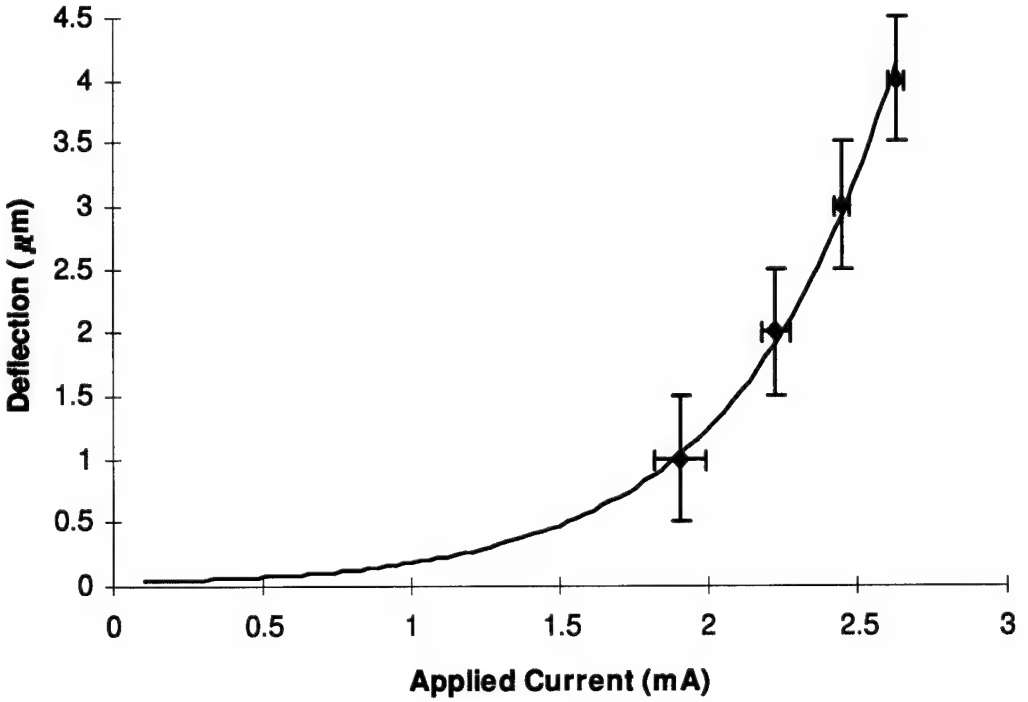

Array # 15: ΔT vs. Applied Current

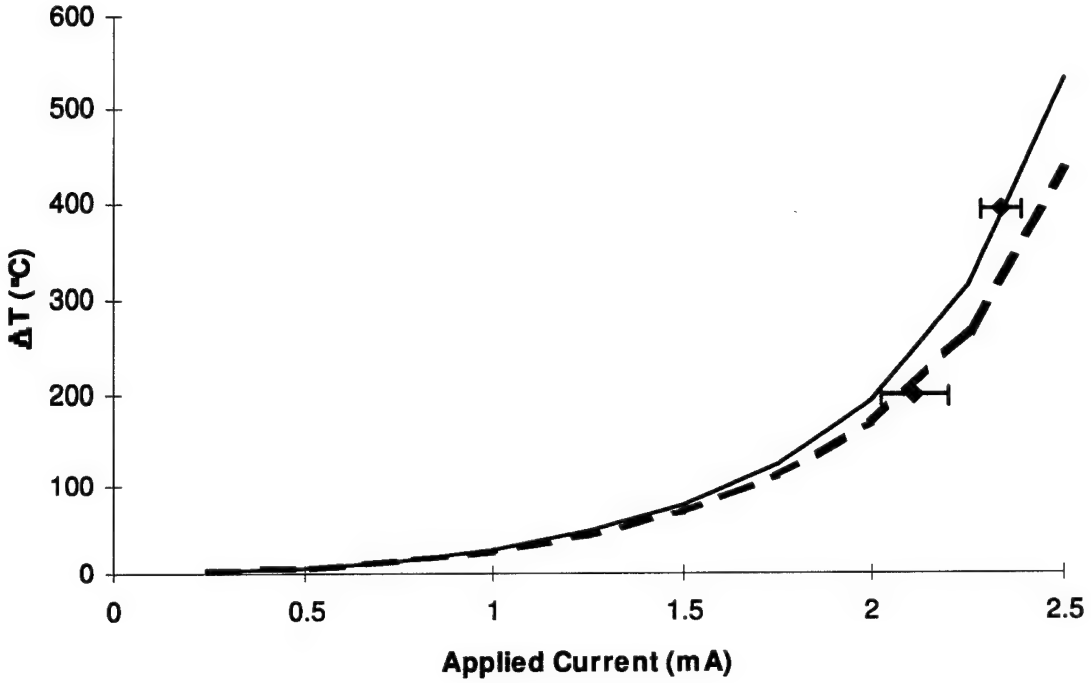

Array # 16: Deflection vs. Applied Current

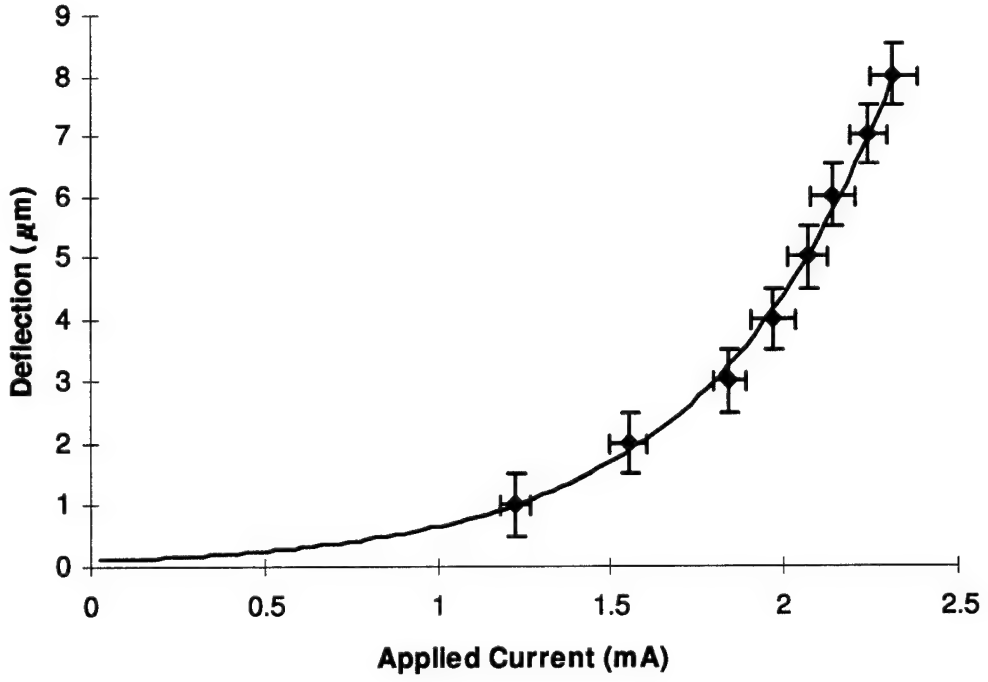

Array # 16: ΔT vs. Applied Current

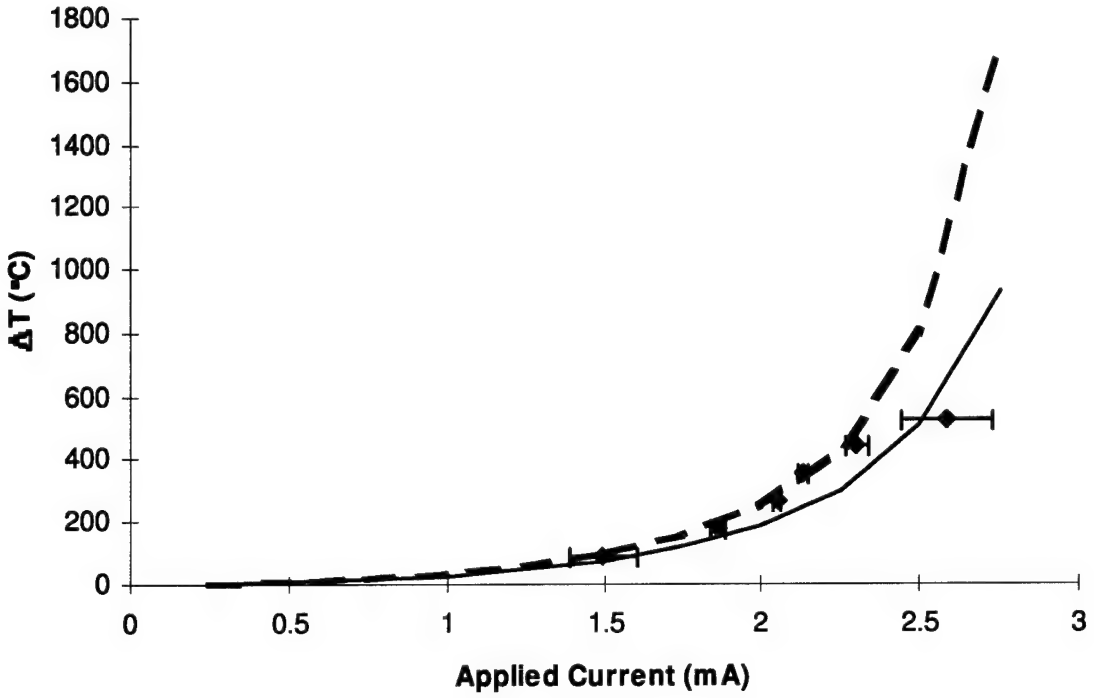

Array # 17: Deflection vs. Applied Current

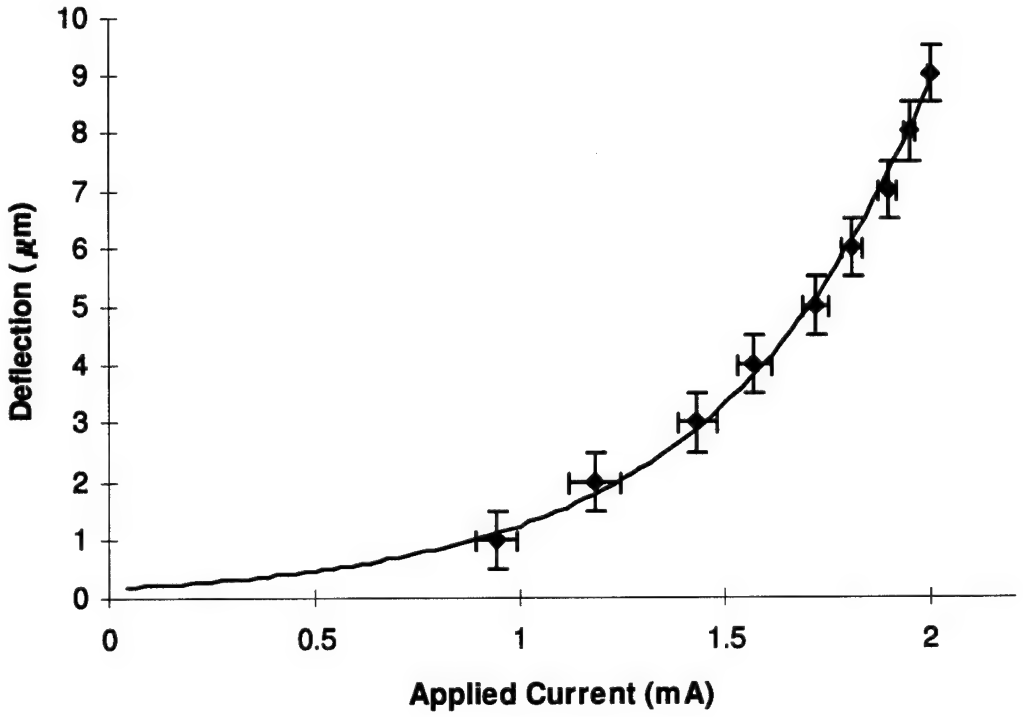

Array # 17: ΔT vs. Applied Current:

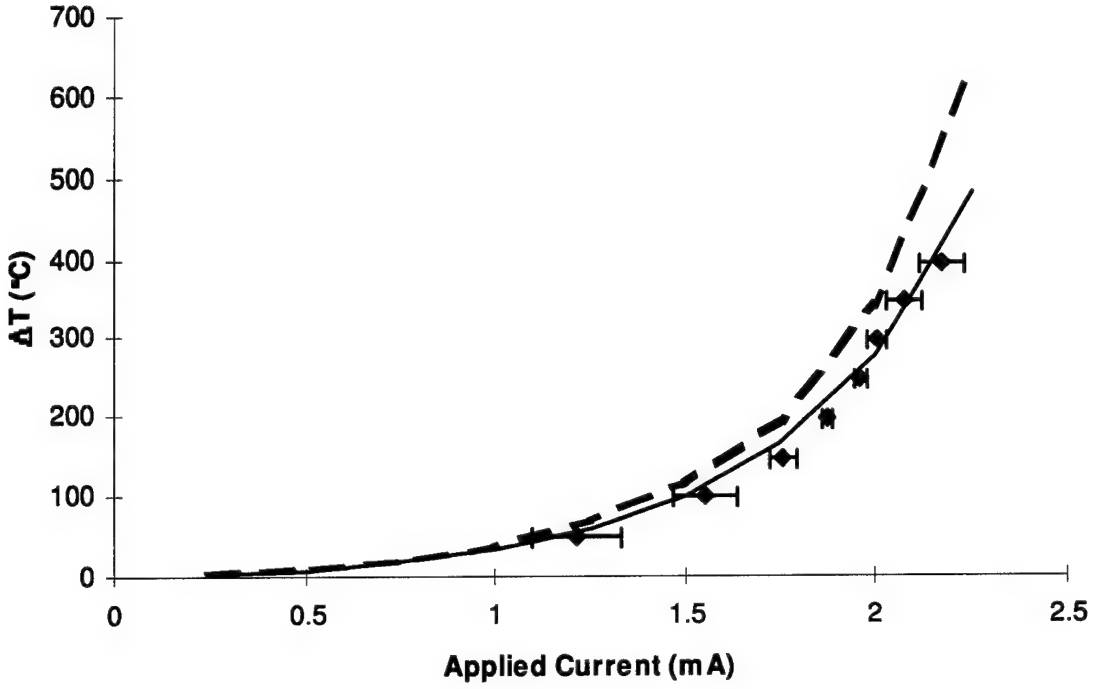

Bibliography

[1] J. Gaitan, M. Parameswaran, M. Zaghloul, J. Marshall, D. Novotny, and J. Suehle, "Design methodology for micromechanical systems at commercial CMOS foundries through MOSIS," *in Proceedings of the 35th Midwest Symposium on Circuits and Systems*, Washington D.C., Aug. 1992.

[2] A. S. Brown, "MEMS: Macro growth for micro systems," *Aerospace America*, pp. 32-37, Oct. 1994.

[3] R. Nass, "Tiny accelerometer IC reaches high sensitivity," *Electronic Design*, pp. 170-172, Sep. 1988.

[4] J. M. Younse, "Mirrors on a chip," *IEEE Spectrum*, pp. 27-31, Nov. 1993.

[5] Keithley Instruments, Inc., *Keithley Switching Cards and Accessories: Reference and Product Guide*, Kiethley Instruments, Inc. No. 1518, 1991.

[6] G. Stix, "Micron machinations," *Scientific American*, pp. 106-117, Nov. 1992.

[7] Lj. Ristic, H. Hughes, and F. Shemansky, *Sensor Technology and Devices*, Chapter 3: Bulk Micromachining Technology, Artech House, 1994.

[8] J. C. Marshall, M. Parameswaran, M. E. Zaghloul, and M. Gaitan, "High-level CAD melds micromachined devices with foundries," *Circuits and Devices*, vol. 8, pp. 10-15, Nov. 1992.

[9] M Parameswaran, H. Baltes, L. Ristic, A. Dhaded, and A. Robinson, "A new approach for the fabrication of micromechanical structures," *Sensors and Actuators*, vol. 19, pp. 289-307, 1989.

[10] Lj. Ristic, H. Hughes, and F. Shemansky, *Sensor Technology and Devices*, Chapter 4: Surface Micromachining Technology, Artech House, 1994.

[11] D. A. Koester, R. Mahadevan, K. W. Markus, *Multi-User MEMS Processes (MUMPs) Introduction and Design Rules*, rev. 3., MCNC MEMS Technology Applications Center, NC, Oct 1994.

[12] A. Rogner, J. Eicher, D. Munchmeyer, R-P Peters, and J. Mohr, "The LIGA technique--what are the new opportunities," *J. Micromech. Microeng.*, vol. 2, pp. 133-140, 1992.

[13] A. Rogner, W. Ehrfeld, D. Munchmeyer, P. Bley, C. Burbaum, and J. Mohr, "LIGA-based, flexible microstructures for fiber-chip coupling," *J. Micromech. Microeng.*, vol. 1, pp. 167-170, 1991.

[14] C-J. Kim, A. P. Pisano, R. S. Muller, and M. G. Lim, "Polysilicon micro-gripper," *Sensors and Actuators A*, vol. 33, pp. 221-227, 1992.

[15] K. S. J. Pister, M. W. Judy, S. R. Burgett, and R. S. Fearing, "Microfabricated hinges," *Sensors and Actuators A*, vol. 33, pp. 249-256, 1992.

[16] V. M. Bright, and R. L. Ewing, EENG 636 course notes, Microelecromechanical Systems. School of Engineering, Air Force Institute of Technology, Wright-Patterson AFB, OH, July 1994.

[17] W-H. Chu, M. Mehregany, and R. L. Mullen, "Analysis of tip deflection and force for a bimetallic cantilever microactuator," *J. Micromech. Microeng.* vol. 3, pp. 4-7, 1993.

[18] H. Guckel, J. Klein, T. Christeson, K. Skrobis, M. Laudon, E. G. Lovell, "Thermo-magnetic metal flexure actuators," *in Proceedings of Transducers* '92, San Fransisco, pp. 73-75, June 1992.

[19] S. F. Bar, T. A. Lober, R. T. Howe, J. H. Lang, and M. F. Schlecht, "Design considerations for micromachined electric actuators," *Sensors and Actuators A*, vol. 14, pp. 269-292, 1988.

[20] K. E. Peterson, "Dynamic micromechanics on silicon: techniques and devices," *IEEE Transactions on Electron Devices*, vol. ED-25, pp. 1242-1249, 1978.

[21] C. Linder, L. Paratte, M-A Gretillat, V. P. Jaecklin, and N. F. de Rooij, "Surface micromachining," *J. Micromech. Microeng.*, vol. 2, pp. 122-132, 1992.

[22] C. Linder, and N. F. de Rooij, "Investigations on free-standing polysilicon beams in view of their application as transducers," *Sensors and Actuators A*, vol. A21-A23, pp. 1053-1059, 1990.

[23] X-Q. Sun, L. Zhijian, X. Zheng, and L. Litian, "Study of fabrication process of a micro electrostatic switch and its application to a micromechanical V-F converter," *Sensors and Actuators A*, vol. A32, pp. 189-192, 1993.

[24] W. C. Tang, T-C Nguyen, and R. T. Howe, "Laterally driven polysilicon resonant microstructures," *Sensors and Actuators*, vol. 20, pp. 25-32, 1989.

[25] W. C. Tang, T-C. H. Nguyen, M. W. Judy, and R. T. Howe, "Electrostatic comb-drive of lateral polysilicon resonators," *Sensors and Actuators A*, vol. A21-A23, pp. 328-331, 1990.

[26] V. P. Jaecklin, C. Linder, N. F. de Rooij, and J. M. Moret, "Micromechanical comb actuators with low driving voltage," *J. Micromech. Microeng.* vol. 2, pp. 250-255, 1992.

[27] V. P. Jaecklin, C. Linder, N. F. de Rooij, and J. M. Moret, "Comb actuators for xy-microstages," *Sensors and Actuators A*, vol. 39, pp. 83-89, 1993.

[28] H. Hosaka, H. Kuwano, and K. Yanagisawa, "Electromagnetic microrelays: concepts and fundamental characteristics," *Sensors and Actuators A*, vol. 40, pp. 41-47, 1994.

[29] F. Cardot, J. Gobet, M. Bogdanski, and F. Rudolf, "Fabrication of a magnetic transducer composed of a high-density array of microelectromagnets with on chip electronics," *Sensors and Actuators A*, vol. 43, pp. 11-16, 1994.

[30] S. Bouwstra, H. A. C. Tilmans, A. Selvakumar, and K. Najafi, "Base driven micromechanical resonators," *IEEE Trans. on Electron Devices*, ED-14, pp. 148-151, 1992.

[31] H. Fujita, and K. J. Gabriel, "New opportunities for micro actuators," *IEEE Trans. on Electron Devices*, ED-35, pp. 14-20, 1991.

[32] D. J. Griffiths, *Introduction to Electrodynamics* (2nd Edition). Englewood Cliffs, NJ: Prentice-Hall, Inc., 1989.

[33] W. Griffel, *Handbook of Formulas for Stress and Strain*, New York, NY: Frederick Ungar Publishing Co., 1966.

[34] S. H. Crandall, N. C. Dahl, and T. J. Lardner, *An Introduction to the Mechanics of Solids*, New York, NY: McGraw-Hill Book Co., 1978.

[35] P. Osterberg, H. Yie, X. Cai, J. White, and S. Senturia, "Self-consistent simulation and modeling of electrostatically deformed diaphragms," *MEMS 94 Conference*, Oiso Japan.

[36] J. Mohr, P. Bley, M. Strohrmann, and U. Wallrabe, "Microactuators fabricated by the LIGA process," *J. Micromech. Microeng*, vol. 2, pp. 234-241, 1992.

Vita

Lieutenant Mark W Phipps was born on August 6, 1971, in Grand Junction, Colorado. After graduating form Plateau Valley High School in Mesa, Colorado in 1989, he accepted an appointment to the United States Air Force Academy in Colorado Springs, Colorado. In 1993 he graduated with a B.S. in Physics and was commissioned a Second Lieutenant in the United States Air Force. Following graduation, he moved to Wright Patterson Air Force Base, Ohio where he was assinged to the Air Force Institute of Technology to pursue a Masters Degree in Electrical Engineering.

Permanent Address: 5111 KE Road
Mesa, Colorado, 81643

REPORT DOCUMENTATION PAGE

Form Approved
OMB No. 0704-0188

Public reporting burden for this collection of information is estimated to average 1 hour per response, including the time for reviewing instructions, searching existing data sources, gathering and maintaining the data needed, and completing and reviewing the collection of information. Send comments regarding this burden estimate or any other aspect of this collection of information, including suggestions for reducing this burden, to Washington Headquarters Services, Directorate for Information Operations and Reports, 1215 Jefferson Davis Highway, Suite 1204, Arlington, VA 22202-4302, and to the Office of Management and Budget, Paperwork Reduction Project (0704-0188), Washington, DC 20503.

1. AGENCY USE ONLY (Leave blank)	2. REPORT DATE	3. REPORT TYPE AND DATES COVERED
	June 1995	Master's Thesis

4. TITLE AND SUBTITLE

DESIGN AND DEVELOPMENT OF MICROSWITCHES FOR MICRO-ELECTRO-MECHANICAL RELAY MATRICES

5. FUNDING NUMBERS

6. AUTHOR(S)

Mark W. Phipps, 2nd Lieutenant, USAF

7. PERFORMING ORGANIZATION NAME(S) AND ADDRESS(ES)

Air Force Institute of Technology, WPAFB OH 45433-6583

8. PERFORMING ORGANIZATION REPORT NUMBER

AFIT/GE/ENG/95J-02

9. SPONSORING / MONITORING AGENCY NAME(S) AND ADDRESS(ES)

Captain James Lyke, Phillips Laboratory (PL/VTEE)
3550 Aberdeen Ave. SE, Kirtland AFB, NM 87117-5776

10. SPONSORING / MONITORING AGENCY REPORT NUMBER

11. SUPPLEMENTARY NOTES

12a. DISTRIBUTION / AVAILABILITY STATEMENT

Distribution Unlimited

12b. DISTRIBUTION CODE

13. ABSTRACT *(Maximum 200 words)*

Many different micro-electro-mechanical switches were designed in the Multi-User MEMS processes (MUMPs) and deep x-ray lithography and electroforming (LIGA) processes. The switches were composed of actuators that operated based upon either electrostatic forces or thermal forces. A thermally activated beam flexure actuator that operated based upon differential hetaing was used extensively. This actuator, which was fabricated in the MUMPs process, was able to deflect up to 12 μm with a total input power of less than 25 mW. The thermal resistance, which was needed to model this actuator, was determined from a material constant, 1.9 +/- 0.08 $m^{1.5}$-°C-W^{-1} for the POLY1 layer in MUMPs and 7.4 +/- 0.88 $m^{1.5}$-°C-W^{-1} for the POLY2 layer in MUMPs, which was extracted from 1020 actuator test cases. A switch using a hinge mechanism that allowed metal-to-metal contacts to be formed was also developed in the MUMPs process. The contact resistance of these devices was determined to be 9.91 +/- 6.22 kΩ. An electrostatically deformable microbridge structure (2 mm thick, 40 mm wide, 332 mm long, and with a capacitive gap of 2mm) was also employed as a switch. A voltage of 53.3 volts applied between the microbridge and two drive electrodes was able to force the center of the microbridge to touch a sense electrode. The observed contact resistance for this connection was 300 +/- 89.7 Ω.

14. SUBJECT TERMS

micro-electro-mechanical, MEM, MEMS, MUMPs, LIGA, matrix switching, micromechanical switches, thermally activated beam flexure, heat-drive actuator, microbridge.

15. NUMBER OF PAGES

255

16. PRICE CODE

17. SECURITY CLASSIFICATION OF REPORT	18. SECURITY CLASSIFICATION OF THIS PAGE	19. SECURITY CLASSIFICATION OF ABSTRACT	20. LIMITATION OF ABSTRACT
UNCLASSIFIED	UNCLASSIFIED	UNCLASSIFIED	UL